Bridging COVID-19-mediated Myocardial Inflammation and the Epicardial Adipose Tissue in Heart Failure: ACE2 Regulation at Center Stage

by

Anissa Marie Viveiros

A thesis submitted in partial fulfillment of the requirements for the degree of

Doctor of Philosophy

Department of Physiology

University of Alberta

Abstract

ACE2 was discovered as the primary effector enzyme of the protective, counter-regulatory arm of the renin-angiotensin system (RAS). The canonical RAS, comprising the angiotensin-converting enzyme (ACE)/angiotensin II (Ang II)/AT 1 receptor (AT_1R) axis, mediates proinflammatory, profibrotic, and hypertensive effects. Rather, ACE2 deactivates Ang II to Ang-(1-7), which acts on the Mas receptor (MasR) to exert protective, anti-inflammatory, and antifibrotic action. However, beyond this primary neurohumoral function, the understanding of the role of ACE2 has broadened to a regulator of multiple peptide cascades, as a chaperone for the transport of amino acids, and, more recently, as the host receptor hijacked for the cellular infection of SARS-CoV and SARS-CoV-2: the causative agents of SARS and COVID-19, respectively. Here, we aimed to understand the diverse roles of ACE2 as the receptor for SARS-CoV-2 and as a protective molecule in heart failure (HF). Further, we aimed to phenotype the epicardial adipose tissue (EAT) in HF and to tease apart the RAS's function and the role of ACE2 in this adipose tissue depot.

Wild-type (WT) male and female C57BL/6J mice were divided into three age groups: young (3 months), adult (12 months), and aged (18 months). We assessed the heart, lungs, kidney, and small intestine using reverse transcription polymerase chain reaction (RT-PCR) for mRNA expression (*Ace2* and transmembrane protease serine 2 (*Tmprss2*)), protein levels by immunoblot (ACE2 and TMPRSS2) and activity (ACE2) to determine if differences in viral entry factors could explain the increased older male susceptibility to COVID-19 that was recognized clinically. We further assessed ACE2 expression, protein levels and activity in young and aged male and female human donor hearts. Next, we utilized SARS-CoV-2 infected Syrian hamsters to assess lung pathology, myocardial inflammation and ACE2

levels using immunoblot, immunohistochemistry and histological staining. We mirrored this analysis in the hearts of autopsied patients who died of COVID-19. As ACE2 was found to be altered in physiology and disease, we assessed candidate modes of ACE2 regulation in myocardial samples from non-failing controls and patients with HF. We employed immunoblot, activity assays and RT-PCR to identify the levels and expression of ACE2, a disintegrin and metalloprotease 17 (ADAM17), and micro RNAs (miRNAs) anticipated to regulate ACE2. Finally, we characterized the EAT from non-failing controls and patients with HF using single nucleus RNA sequencing (snRNA Seq), histology, a multiplexed cytokine assay, and immunoblot.

Taken together, we identified that increased tissue ACE2 may enhance older male susceptibility to severe COVID-19 and that myocardial ACE2 downregulation and myeloid dominant recruitment are common pathological features of COVID-19 in hamsters and humans. Further, post-transcriptional and post-translational regulation of ACE2 is likely etiology specific, whether in physiology or the pathophysiology of HF. Finally, we identify EAT dysregulation as a possible contributor to myocardial dysfunction in HF due to alterations in adipose tissue storage, EAT infiltration into the myocardium, aberrant adipogenesis, and, possibly, canonical RAS overactivation. The compilation of our efforts suggests that understanding the regulation of ACE2 is crucial to combating COVID-19 and HF, to ultimately finding novel therapeutic strategies to address these topical public health concerns.

Preface

This thesis includes writing and data from published and unpublished manuscripts. Specific contributions to the listed projects are outlined below.

Part of published reviews adopted for Chapter 1

Viveiros, A., Rasmuson, J., Vu, Jennie., Mulvagh, S.L., Yip, C.Y.Y., Norris, C.M., Oudit, G.Y. Sex differences in COVID-19: candidate pathways, genetics of ACE2, and sex hormones. *Am J Physiol Heart Circ Physiol*. 320: H296-H304. (2021).

Role of A.V.: Drafted the manuscript, obtained and incorporated epidemiological data into figures, created the remaining figures, and integrated contributions and edits from coauthors.

Rafeh, R.,* **Viveiros, A**.,* Oudit, G.Y., El-Yazbi, A.F. Targeting perivascular and epicardial adipose tissue inflammation: therapeutic opportunities for cardiovascular disease. *Clin Sci (Lond)*. 134(7): 827-851. (2020).

*indicates the authors contributed equally

Role of A.V.: Wrote half of the review, created the second figure (included in this thesis), edited and approved the final version of the manuscript.

Published manuscript adapted for Chapter 3

Viveiros, A., Gheblawi, M., Aujla, P.K. Sosnowski, D.K., Seubert, J.M., Kassiri, Z., Oudit, G.Y. Sex- and Age-Specific Regulation of ACE2: Insights into Severe COVID-19 Susceptibility. *Journal of Molecular and Cellular Cardiology*. 164:13-16. (2022). doi: 10.1016/j.yjmcc.2021.11.003.

Role of A.V.: Performed and analyzed most of the experiments, drafted the manuscript, prepared the figures and illustrations, and integrated contributions and edits from coauthors.

Published manuscript adapted for Chapter 4

Viveiros, A., Noyce, R., Gheblawi, M., Colombo, D., Bilawchuk, L.M., Clemente-Casares, X., Marchant, D.J., Kassiri, Z., Del Nonno, F., Evans, D.J., Oudit, G.Y. SARS-CoV-2 Infection Downregulates Myocardial ACE2 and Potentiates Cardiac Inflammation in Humans and Hamsters. *Am J Physiol Heart Circ Physiol*. 323:H1262-H1269. (2022). doi: 10.1152/ajpheart.00578.2022.

Role of A.V.: Performed and analyzed most of the experiments, drafted the manuscript, prepared the figures and illustrations, and integrated contributions and edits from coauthors.

Unpublished manuscript adapted for Chapter 5

Viveiros, A., Addo, P., Srinivasan, K., Zhang, A., Chen, H., Kassiri, Z., Prasad, V., Oudit, G.Y. The Role of miRNAs and ADAM17 in ACE2 Regulation.

Role of A.V.: Performed and analyzed the majority of the experiments, drafted the manuscript, and prepared the figures and illustrations.

Unpublished manuscript adapted for Chapter 6

Viveiros, A.*, Brown, K.J.*, Chen, H., Zhang, A., Khoramjoo, M., Kim, Y., Seidman, J.G., Seidman, C.E., Oudit, G.Y. Phenotyping the Epicardial Adipose Tissue in Heart Failure: Novel Targets for Drug Discovery.

*indicates authors contributed equally

Role of A.V.: Performed and analyzed most of the experiments, drafted the manuscript, and prepared the figures and illustrations.

Acknowledgements

I was fortunate for the opportunity to perform graduate studies within the Department of Physiology at the University of Alberta. Several people have made this work possible, and I am honoured to thank them.

First of all, thank you to my supervisor, Dr. Gavin Oudit, for accepting me into his laboratory and for the guidance throughout my Doctoral program. Gavin has taught me invaluable lessons in critical thinking, comprehending and disseminating scientific knowledge, as well as offering numerous opportunities to participate in collaborative projects. I have learned an incredible amount both in the laboratory and beyond the bench, and that is thanks to him.

Thank you to my remaining supervisory committee, Dr. Zamaneh Kassiri and Dr. John Seubert. I appreciate all your suggestions, insightful comments, and constructive advice throughout my Doctoral program. Thank you to Dr. Mark Chappell and Dr. Gina Rayat for serving as my external examiners and for providing excellent and thorough comments to improve this thesis.

Thank you to the present and former members of the Oudit laboratory, specifically Dr. Hao Zhang, Dr. Pavel Zhabyeyev, Dr. Faqi Wang, Mahmoud Gheblawi, Dr. Huachen Chen, Anran Zhang, Kaiming Wang, Mobin Khoramjoo, and Abby Ewasiuk for their assistance in the completion of this thesis, scientific discussions and for providing an always enjoyable work and learning environment. In addition, I am fortunate for the opportunity to participate in collaborative projects with the laboratory of Dr. Jonathan Seidman and Dr. Christine Seidman, and their constructive feedback, scientific discussions, inspiration, and

for offering their expertise. Accordingly, I would like to thank Dr. Kemar Joseph Brown for his invaluable work dedicated to completing my final PhD project.

I would like to acknowledge the incredible effort of all the present and former team members of the Human Explanted Heart Program (HELP) program established by Dr. Oudit. This work would not be possible without this strong dedication and support. Most importantly, we sincerely thank the participation of altruistic organ donors and their families. We consider the opportunity to work with human tissue samples as incredibly valuable, and we are fortunate for the support of donors in allowing us to capture these precious samples. It is always an honour to hear stories from patients and families, and I will always treasure every conversation and each encounter.

This research would not have been possible without funding from the Faculty of Medicine and Dentistry (Motyl Graduate Studentship in Cardiac Sciences, Dean's Doctoral Student Award, Violet Killburn Graduate Scholarship, Faculty of Medicine & Dentistry/ Alberta Health Services Graduate Student Recruitment Studentship (GSRS)), the University of Alberta (Friends of the Faculty of Graduate Studies and Research Scholarship, Doctoral Recruitment Scholarship), and the Government of Alberta (Alberta Graduate Student Excellence Scholarship (AGES)). I would further like to acknowledge the Canadian Institute of Health Research (CIHR) operating grant(s) under Dr. Oudit.

Finally, I am thankful to my family and friends for their unending support, their patience with this process, and for reminding me that I always have them to fall back on.

Table of Contents

CHAPTER 1 ..... **1**

INTRODUCTION **1**

1.1 Introduction to ACE2: from the RAS and beyond 2

1.2 Regulation of ACE2 6

1.3 ACE2 and Heart Failure 10

1.4 ACE2 and COVID-19 11

1.5 Sex Differences in Heart Failure and COVID-19 14

1.6 CVD and COVID-19 15

1.7 Candidate Pathways for Sex Differences 21

1.7.1 Innate Immunity *21*

1.7.2 Counter-regulatory RAS: ACE2 ..... *24*

1.8 Mechanism of Sex Differences 25

1.8.1 Sex Chromosomes *25*

1.8.2 Sex Hormones *27*

1.9 Impact of Gender 31

1.10 Limitations of Epidemiological Data 32

1.11 Adipose Tissue in Obesity and Heart Failure 33

1.12 Adipose Tissue of the Heart and Coronary Vasculature: Perivascular Adipose Tissue 34

1.12.1 Structural and functional roles *34*

1.12.2 PVAT and vascular dysfunction in metabolic disorders *37*

1.13 Adipose Tissue of the Heart: Epicardial and Pericardial depots 37

1.13.1 EAT Secretasome *39*

1.13.2 EAT Facilitates and Potentiates Local Inflammation *40*

1.14 EAT and cardiac dysfunction in metabolic disease 42

1.14.1 Obesity, Diabetes and EAT *42*

1.14.2 HFpEF and EAT *43*

1.15 Adipose Tissue RAS 44

1.16 Hypothesis and Objectives 49

CHAPTER 2 ..... **51**

MATERIALS AND METHODS **51**

2.1 Materials 52

2.2 Human Explanted Heart Protocol 52

2.2.1 Tissue Collection from Dilated Cardiomyopathy *53*

2.2.2 Tissue Collection from Ischemic Heart Disease *53*

2.3 Hematoxylin and Eosin 56

2.4 Trichrome Staining 56

2.5 Immunohistochemical Staining 57

2.6 Picrosirius Red (PSR) Staining 57

2.7 Fresh-Frozen Immunofluorescent Staining 58

2.8 Formalin-Fixed Paraffin Embedded (FFPE) Immunofluorescent Staining 59

2.9 Immunoblot Analysis 60

2.10 ACE2 Activity Assay 63

2.11 ADAM17 Activity Assay 64

2.12 RNA Extraction 64

2.13 TaqMan RT-PCR 65

2.14 MicroRNA (miRNA) RT-PCR 65

2.15 Single-nucleus RNA Sequencing (snRNA Seq) 66

2.15.1 Sample preparation and nuclei extraction *66*

2.15.2 Library preparation using the 10X genomics platform and sequencing *67*

2.16 Genotyping 67

2.17 Quantification of Hydroxyproline Content 68

2.18 Removal of Excess Lipids (RELi) Protein Extraction 69

2.19 MULTIPLEX CYTOKINE ASSAY 70
2.19.1 Sample preparation and Data Acquisition *70*
2.19.2 Data visualization *71*
2.19.3 Network analysis and pathway enrichment *72*
2.20 STATISTICS 73
CHAPTER 3 ..... **74**
SEX- AND AGE-SPECIFIC REGULATION OF ACE2: INSIGHTS INTO SEVERE COVID-19 SUSCEPTIBILITY **74**
3.1 ABSTRACT 76
3.2 INTRODUCTION 77
3.3 MATERIALS AND METHODS 78
3.3.1 Animal Studies *78*
3.3.2 Human Explanted Hearts *78*
3.3.3 Gene Expression *78*
3.3.4 Immunoblot *79*
3.3.5 Immunofluorescence *79*
3.3.6 ACE2 Enzyme Activity Assay *80*
3.3.7 Statistical Analysis *80*
3.4 RESULTS 80
3.5 DISCUSSION 87
3.6 CONCLUSION 89
3.7 ACKNOWLEDGEMENTS 89
3.8 DISCLOSURES 89
CHAPTER 4 ..... **100**
SARS-COV-2 INFECTION DOWNREGULATES MYOCARDIAL ACE2 AND POTENTIATES CARDIAC INFLAMMATION IN HUMANS AND HAMSTERS **100**

4.1 Abstract 102
4.2 New and Noteworthy 102
4.3 Introduction 103
4.4 Materials and Methods 104
4.4.1 Cells and viruses 104
4.4.2 In vivo hamster infections 104
4.4.3 Virus titrations 105
4.4.4 Human Samples 105
4.4.6 Immunohistochemical Staining 106
4.4.7 RT-PCR 107
4.4.8 Protein Extraction 108
4.4.9 Immunoblot 108
4.4.10 Statistical Analysis 109
4.5 Results 109
4.6 Discussion 116
4.7 Conclusion 122
4.8 Funding 122
4.9 Conflicts of Interest 122
CHAPTER 5 125
THE ROLE OF MIRNAS AND ADAM17 IN ACE2 REGULATION 125
5.1 Abstract 127
5.2 Introduction 128
5.3 Methods 129
5.4 Results 129
5.4.1 Study cohort 129
5.4.2 LV remodeling in HF 132
5.4.3 ACE2 in HF 132

5.4.4 ACE2 Regulation in HF *137*

5.5 DISCUSSION 137

5.6 CONCLUSION 142

5.7 ACKNOWLEDGEMENTS 142

5.8 DISCLOSURES 142

CHAPTER 6 155

PHENOTYPING THE EPICARDIAL ADIPOSE TISSUE IN ADVANCED HEART FAILURE: NOVEL TARGETS FOR DRUG DISCOVERY 155

6.1 ABSTRACT 157

6.2 INTRODUCTION 158

6.3 METHODS 160

6.4 RESULTS 161

6.4.1 Study cohort *161*

6.4.2 Region-associated cell type composition *161*

6.4.3 The EAT in HF *162*

6.4.4 HF possesses unique adipocyte cell states *165*

6.4.5 Infiltrative epicardial adipose tissue in HF *169*

6.4.6 Phenotyping the EAT *169*

6.4.7 Assessing the molecular signature of the EAT *172*

6.4.8 Computational PPI Network construction and pathway analysis *173*

6.4.9 MAPK pathway activation in the EAT *177*

6.4.10 Examining the RAS in HF EAT *181*

6.5 DISCUSSION 181

6.5.1 Different origins of IMAT in NFC and HF *181*

6.5.2 Perivascular IMAT in NFC *182*

6.5.3 Infiltrative IMAT in HF *183*

6.5.4 Cytokine profile in HF EAT *184*

6.5.5 Enhanced Adipogenesis in HF EAT *185*

6.5.6 p38 pathway *185*

6.5.7 ERK pathway *186*

6.5.8 JNK pathway *187*

6.5.9 RAS in the EAT *188*

6.6 CONCLUSION 188

6.7 ACKNOWLEDGEMENTS 189

6.8 DISCLOSURES 189

CHAPTER 7 201

DISCUSSION AND FUTURE DIRECTIONS 201

7.1 DISCUSSION AND RESEARCH IMPACT 202

7.2 LIMITATIONS 205

7.3 FUTURE DIRECTIONS 209

7.4 CONCLUSION 214

REFERENCES 216

List of Tables

Table 1.1. Epicardial adipose tissue-derived bioactive molecules and alteration in conditions of chronic systemic inflammation including obesity, type 2 diabetes mellitus (T2DM), and heart failure with preserved ejection fraction (HFpEF)…….……..41

Table 2.1. Source and dilutions of antibodies used in experiments……....61

Table 3.1. Human heart donor characteristics and grouping (young vs aged) ……...90

Table 4.1. Patient clinical characteristics……...…...119

Table 5.1. Baseline clinical characteristics of non-failing control (NFC) donors and patients with advanced heart failure secondary to dilated cardiomyopathy (DCM) or ischemic heart disease (IHD) ……...…….130

Table 6.1. Baseline clinical table of included non-failing control donors and patients with advanced Heart Failure……...…….….190

Table 6.2. KEGG pathways upregulated in DCM EAT compared to NFC..……...….192

Table 6.3. KEGG pathways upregulated in IHD EAT compared to NFC..……..…...193

Table 6.4. Gene Ontology pathways upregulated in DCM EAT compared to NFC……...194

Table 6.5. Gene Ontology pathways upregulated in IHD EAT compared to NFC…….....197

List of Figures

Figure 1.1. Expression, structure, and enzymatic function of ACE2……..…...…..4

Figure 1.2. Transcriptional, post-transcriptional, and post-translational regulation of ACE2……..…...…7

Figure 1.3. SARS-CoV-2 viral entry……...……...……12

Figure 1.4. Global reported COVID-19 epidemiological data of percent of cases disaggregated by sex……16

Figure 1.5. Global reported COVID-19 epidemiological data of percent of deaths disaggregated by sex……19

Figure 1.6. Global sex- and age- disaggregated data on COVID-19 across countries……...…22

Figure 1.7. Candidate mechanisms of sex-specific susceptibility of males to COVID-19….28

Figure 1.8. The adipose tissue depots of the heart……..35

Figure 1.9. The local RAS of the adipose tissue……...……..46

Figure 2.1. Schematic depiction of the collection and dissection of explanted human hearts by the Human Explanted Heart Program (HELP) protocol……...……..54

Figure 3.1. Assessment of ACE2 and TMPRSS2 across sex and aging…….……..……..82

Figure 3.2. Sex- and age-differences in ACE2 levels in mouse and human hearts…...……..85

Figure 3.3. Raw and uncropped western blot images from Figure 3.1A and Figure 3.1C…92

Figure 3.4. Raw and uncropped western blot images from Figure 3.1E…….……....94

Figure 3.5. Raw and uncropped western blot images from Figure 3.1E…….……....96

Figure 3.6. Raw and uncropped western blot images from Figure 3.2…….…….....98

Figure 4.1. SARS-CoV-2 infection induces lung injury and upregulates cytokine expression in hamsters……....……110

Figure 4.2. SARS-CoV-2 infection downregulates myocardial ACE2 and induces immune cell infiltration in hamsters……....……...…113

Figure 4.3. Severe COVID-19 leads to myocardial ACE2 downregulation and immune cell infiltration in humans……....…….……...…117

Figure 4.4. Raw and uncropped western blot images from Figure 4.2……..…123

Figure 5.1. Remodeling of the LV myocardium in HF…….133

Figure 5.2. ACE2 expression, protein levels and activity in NFC and HF……...…135

Figure 5.3. Assessing modes of ACE2 regulation: miRNAs and ADAM17……138

Figure 5.4. Regional differences in ACE2 expression, protein levels and activity in IHD……....…….……..……143

Figure 5.5. Regional differences in the modes of ACE2 regulation in IHD patients……...145

Figure 5.6. Immunoblot for ACE2 in DCM…….147

Figure 5.7. Immunoblot for ACE2 in IHD……...…149

Figure 5.8. Immunoblot for ADAM17 in DCM……...…151

Figure 5.9. Immunoblot for ADAM17 in IHD…….....…153

Figure 6.1. Pilot single-nucleus RNA sequencing study in the EAT and contiguous LV…163

Figure 6.2. Unique properties of the intramyocardial adipose tissue (IMAT) in HF……...166

Figure 6.3. Adipocyte hypertrophy and adipose tissue fibrosis in the EAT…….....170

Figure 6.4. Phenotyping the EAT in HF using a multiplexed cytokine analysis.....174

Figure 6.5. Assessing putative altered EAT pathways in HF.....178

Figure 6.6. Raw and uncropped western blot images from Figure 6.5.....199

Figure 7.1. Overview of thesis research and key findings.....206

Figure 7.2. Current snRNA sequencing samples and future directions……211

List of Abbreviations

Abbreviation is defined at first use in parentheses within each chapter.

ACE	angiotensin-converting enzyme
ACE2	angiotensin-converting enzyme 2
ACEi	angiotensin-converting enzyme inhibitor
ADAM17	a disintegrin and metalloproteinase 17
ADRF	adipocyte-derived relaxing factor
AF	atrial fibrillation
AGT	angiotensinogen
AKI	acute kidney injury
AMPK	AMP-activated protein kinase
Ang I	angiotensin I
Ang II	angiotensin II
Ang-(1-7)	angiotensin 1-7
AR	androgen receptor
ARB	ang II receptor blocker
ARDS	acute respiratory distress syndrome
ARE	androgen response element
AT_1R	angiotensin II receptor type 1
AT_2R	ang II receptor 2
β-blocker	beta adrenergic blocker
BMI	body mass index
BSA	bovine serum albumin

C/EBPβ	CCAAT-enhancer-binding protein beta
CAD	coronary artery disease
cDNA	complementary DNA
CKD	chronic kidney disease
CM	cardiomyocytes
CMR	cardiac magnetic resonance
COPD	chronic obstructive pulmonary disease
CTACK	cutaneous T-cell-attracting chemokine
CVA	cerebrovascular accident
CVD	cardiovascular disease
DAPI	4′,6-diamidino-2-phenylindole
DEG	differentially expressed genes
DPP-4	dipeptidyl-peptidase-four
EAT	epicardial adipose tissue
EC	endothelial cell
ECM	extracellular matrix
eGRF	estimated glomerular filtration rate
ERE	estrogen response element
ERK	extracellular signal-related kinases 1/2
FA	fatty acid
FB	fibroblast
FC	fold change
GLP-1	glucagon-like peptide 1

HELP	human explanted heart program
HF	heart failure
HFD	high-fat diet
HFpEF	heart failure with preserved ejection fraction
HFrEF	heart failure with reduced ejection fraction
HOPE	human organ procurement and exchange program
Htn	hypertension
IFN	interferon
IHD	ischemic heart disease
IHD-Per	ischemic heart disease, peri-infarct region
IHD-Rm	ischemic heart disease, remote region
IL	interleukin
IP-10	interferon-gamma-inducible protein 10
IRF	interferon regulatory factor
ISG	interferon-stimulated genes
JNK	c-jun amino (N)-terminal kinases 1/2/3
kDa	kilodaltons
LMNA	lamin A/C
lncRNA	long non-coding RNA
LV	left ventricle
LVEF	left ventricular ejection fraction
Lym	lymphoid
MAPK	mitogen-activated protein kinase

MasR	mas receptor
MC	mural cell
MCP-1	monocyte chemotactic protein-1
MDC	macrophage-derived chemokine
MDM2	murine double minute 2
MI	myocardial infarction
MIG/CXCL9	monokine induced by interferon-gamma
miRNA	micro RNA
MMP	matrix metalloproteinases
MRA	mineralcorticoid receptor antagonist
mRNA	messenger RNA
MSC	mesenchymal stem cell
MVC	motor vehicle collision
Mye	myeloid
NC	neuronal cell
NFC	non-failing control
NK	natural killer cells
NO	nitric oxide
OD	overdose
PAMP	pathogen-associated molecular pattern
PAT	pericardial adipose tissue
PCA	principle component analysis
PCR	polymerase chain reaction

PI3K	Phosphoinositide 3-kinase
PPARy	peroxisome proliferator-activated receptor gamma
PRR	pattern recognition receptor
PSR	picrosirius red
PVAT	perivascular adipose tissue
RAS	renin-angiotensin system
RLR	RIG-I-like receptors
RV	right ventricle
SAH	subarachnoid hemorrhage
scRNA Seq	single cell RNA sequencing
snRNA Seq	single nucleus RNA sequencing
SDH	subdermal hemorrhage
T2DM	type 2 diabetes mellitus
TIMP	tissue inhibitor of metalloproteinases
TLR	toll-like receptors
TMPRSS2	transmembrane serine protease 2
TRAIL	TNF-related apoptosis-inducing ligand
TTN	titin
UMAP	uniform manifold approximation and projections
UTR	untranslated region
VAD	ventricular assist device
VSMC	vascular smooth muscle cells
WGA	wheat germ agglutinin

WT	wild-type
XACT	X-active specific transcript
XIST	X-inactivation specific transcript

Chapter 1

Introduction

1.1 Introduction to ACE2: from the RAS and beyond

Angiotensin-converting enzyme 2 (ACE2) is a type I transmembrane monocarboxypeptidase with a single extracellular catalytic domain. ACE2 was discovered as the homologue of angiotensin-converting enzyme (ACE), which is a monomeric, membrane-bound dipeptidase. *ACE2* is ubiquitously expressed, with highest expression in the intestinal enterocytes, renal proximal tubules, cardiomyocytes, pulmonary type II alveolar cells, fibroblasts, endothelial cells, and mural cells; predominantly in the pericytes (**Figure 1.1A**).[1-4] The biological function of ACE2 was first discerned in a study of *Ace2*-deficient mice exhibiting impaired cardiac function that was rescued with concomitant *Ace* deletion.[5] Therefore, ACE2 controls heart function as a negative regulator of the canonical renin-angiotensin system (RAS), where ACE activity dictates the generation of the pathogenic peptide angiotensin II (Ang II).

The canonical RAS pathway involves sequential catalytic steps that culminate in Ang II formation, promoting vasoconstriction, sodium reabsorption, and fluid retention to trigger a pressor response. Ang II imparts these effects by binding and activating the angiotensin II receptor type 1 (AT_1R).[6] The RAS pathway is initiated by renal renin secretion; in response to sympathetic stimulation, hypotension, hyponatremia, and renal hypoperfusion, which cleaves angiotensinogen (AGT) to produce angiotensin I (Ang I). The latter is converted by ACE to Ang II, which activates angiotensin II receptor types 1 or 2 (AT_1R and AT_2R), the latter opposing the action of the classic AT_1R.[7]

Alternatively, ACE2 deactivates Ang II by conversion to Ang-(1-7), a peptide with anti-inflammatory, anti-fibrotic, and vasodilatory properties through activation of the Mas receptor (MasR) (**Figure 1.1B**).[8-11] Whereas exaggerated Ang II activity led to hypertension due to vasoconstriction and sodium and water retention, in addition to cardiac remodeling and

inflammation, Ang-(1-7) reduced blood pressure in hypertensive animals, produced vasodilation, and improved cardiac remodeling and fibrosis.[12,13] Disturbances of RAS activation and function are implicated in many cardiovascular disorders including hypertension, myocardial ischemia, atherosclerosis, aortic aneurysms, cardiac arrhythmias, and heart failure (HF).[14] Here, we will focus on ACE2 in HF.

The role of ACE2 has expanded to the modulation of many other peptide cascades essential for multi-organ homeostasis resulting from ACE2's substrate promiscuity.[15,16] As far as cascades central to the cardiovascular system, ACE2 cleaves: i) Ang I and Ang II to Ang-(1-9) and Ang-(1-7), respectively as part of the RAS pathway (as indicated above), ii) apelin-13/apelin-17 to apelin-12/apelin-16 of the apelin pathway, and iii) des-Arg9 bradykinin as part of the kallikrein-kinin pathway (**Figure 1.1B**).[15,17] Beyond its proteolytic role, ACE2 functions as a chaperone for the intestinal absorption of neutral amino acids. ACE2 harbours a collectrin-homology domain that stabilizes the sodium-dependent neutral amino acid transporter (B^0AT1) at the luminal brush border of enterocytes (**Figure 1.1C**).[18] Impairments in the ACE2-B^0AT1 interaction, by either mutations in *SLC6A19,* encoding B^0AT1, or ACE2 deficiency, result in impaired amino acid uptake and disruption of the gut microbiome.[19,20]

More recently, ACE2 gained notoriety as the receptor for the viral entry of SARS-coronaviruses, namely SARS-CoV and SARS-CoV-2[21,22] – a topic that will be discussed further in subsequent sections.

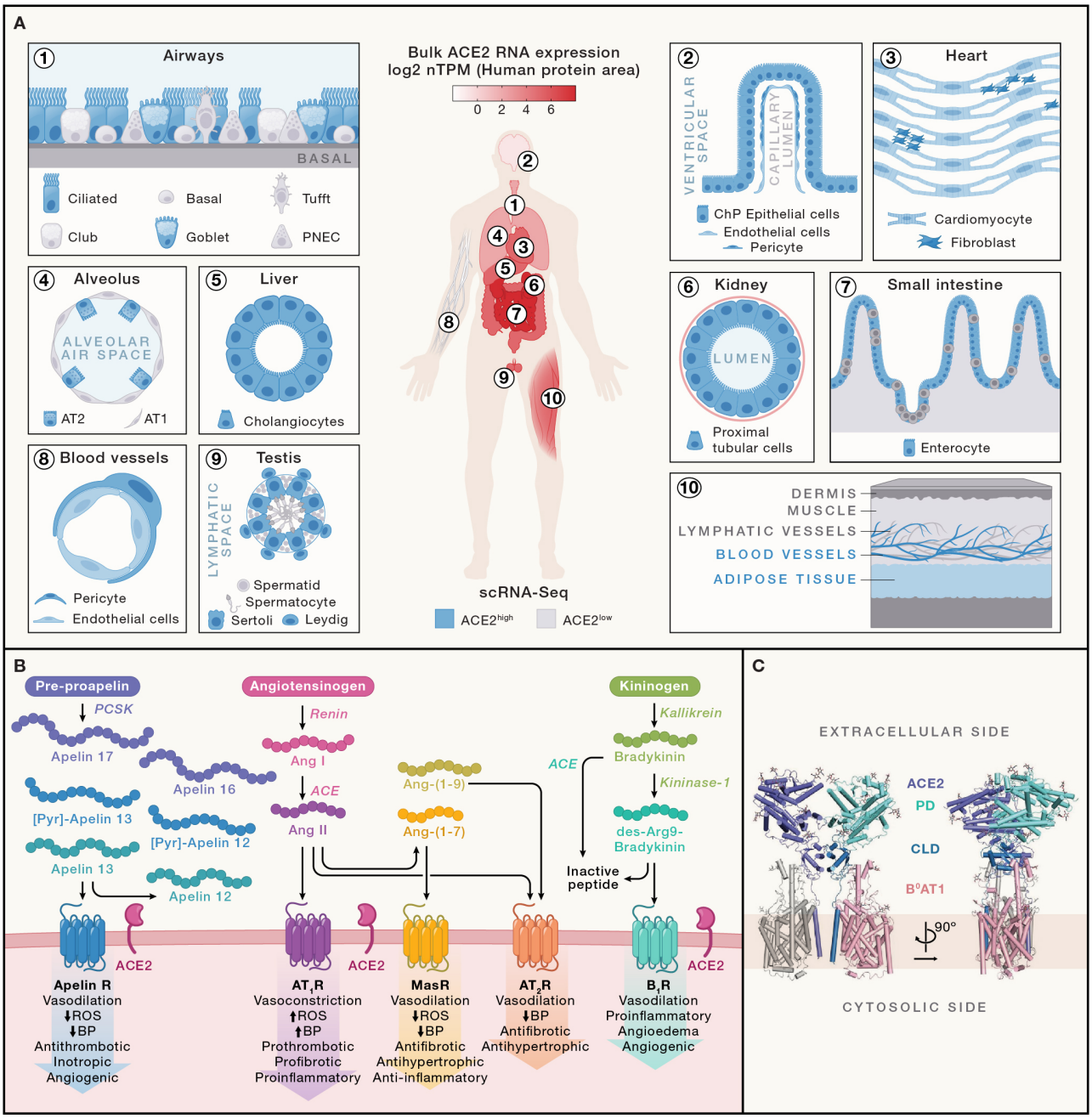

Figure 1.1. *Legend on next page*

Figure 1.1. Expression, structure and enzymatic function of ACE2.

A. *ACE2* is predominantly expressed in the small intestine, kidney, adipose tissue, heart, respiratory system, and, to a limited extent, in brain in data from bulk RNA sequencing (red). Findings are corroborated by single cell RNA sequencing (scRNA Seq) studies for the cell-type specific expression in each organ. High-confidence data sets were collated to determine $ACE2^{high}$ (blue) and $ACE2^{low}$ (grey) cell types. **B.** The canonical RAS results in Angiotensin II (Ang II) generation, which promotes vasoconstriction, inflammation, and fibrosis through activating the angiotensin II receptor type 1 (AT_1R). ACE2 deactivates Ang II to Ang-(1-7), which opposes the actions of Ang II to promote vasodilation and inhibit fibrosis or inflammation by acting on the Mas receptor. ACE2 deactivates the apelin pathway by converting apelin 17, pyr-apelin 13, and apelin 13 into apelin 16, pyr-apelin 12, and apelin 12, respectively. Finally, ACE2 deactivates des-Arg9 bradykinin, which acts on the B1 receptor (B1R) to potentiate inflammation and vasodilation. **C.** The N-terminal domain of ACE2 is positioned on the extracellular leaflet of the plasma membrane, with a C-terminal, or collectrin-like, transmembrane domain. The N-terminal domain contains the catalytic site of ACE2. The non-enzymatic collectrin domain of ACE2 operates as a chaperone protein for the neutral amino acid transporter B^0AT1. The ACE2- B^0AT1 complex exists as a dimer of heterodimers and is involved in the absorption of neutral amino acids in the small intestine. Taken from Yan *et al* without modification.[23] https://www.science.org/doi/10.1126/science.abb2762. *Adapted from Oudit, G.Y., Wang, K., **Viveiros, A**., Kellner, M.J., Penninger, J.M. Angiotensin-converting enzyme 2- at the heart of the COVID-19 pandemic. Cell. 186(5): 906-922. (2023).*

1.2 Regulation of ACE2

Given ACE2's physiological function in maintaining homeostasis of the RAS and as the endogenous entry receptor for SARS-coronaviruses, deciphering the regulation of ACE2 is critical to informing physiology and disease susceptibilities (**Figure 1.2**). As an X-linked gene capable of escaping X-chromosome inactivation, dimorphic expression of *ACE2* would be anticipated to contribute to sex differences in physiology and disease.[5,24,25] However, *ACE2* expression is fine-tuned by gonadal steroids. Androgen receptor (AR) agonists, testosterone for instance, upregulates *ACE2* expression, whereas estrogen negatively controls *ACE2* expression (**Figure 1.2**).[26-28] Aside from sex hormones that we will explore further in latter sections, the apelin pathway mediates transcriptional control of ACE2 as a feedback loop. Although the mechanism is not elucidated entirely, stimulation of the apelin receptor induces *ACE2* expression through the nuclear translocation of GATA transcription factors (**Figure 1.2**).[29,30] In accordance, exogenous administration of apelin restores *Ace2* expression in the failing hearts of *Apelin* knockout animals subjected to transthoracic aortic constriction.[29] Nevertheless, the transcriptional regulation of *ACE2* is incompletely understood, and remains an active area of basic and translational research.

DNA methylation and histone modifications epigenetically modulate *ACE2* (**Figure 1.2**). As described in essential hypertension, aberrant DNA hypermethylation at CpG4 and CpG5 within the *ACE2* promoter presumably promotes transcriptional repression,.[31,32] Histone post-translational modifications, namely lysine-specific histone demethylase 5B (KDM5B), which demethylates lysine 4 of histone 3 (H3K4), positively correlates with lung *ACE2* expression.[33] Conversely, in human embryonic stem cells, enhancer of zeste homolog 2 (EZH2) catalyzes H3K27 trimethylation (H3K27me3) to reduce *ACE2* expression.[34]

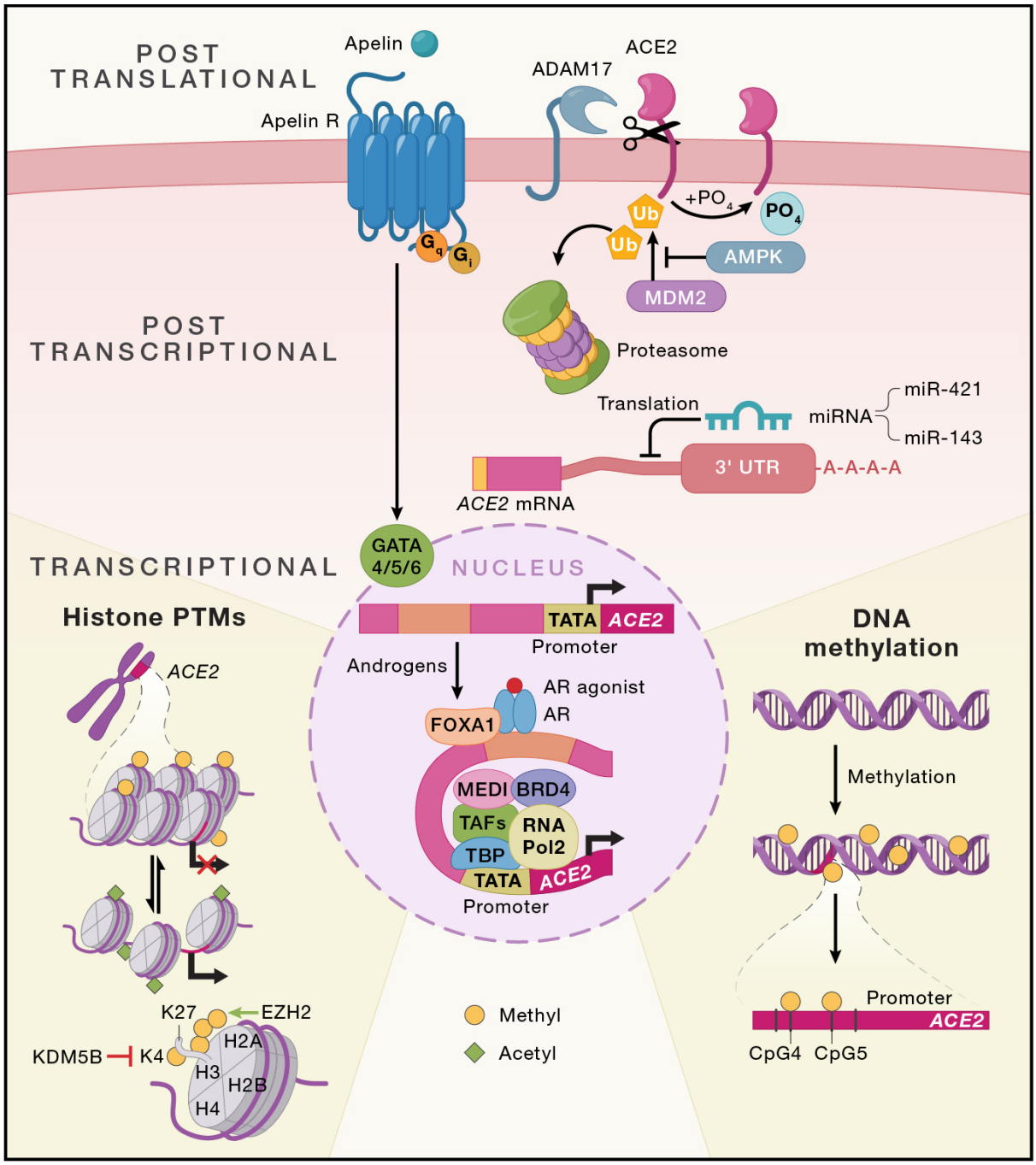

Figure 1.2. *Figure legend on next page*

Figure 1.2. Transcriptional, post-transcriptional, and post-translational regulation of ACE2. Nuclear translocation of GATA transcription factors and binding to the ACE2 promoter increases *ACE2* expression, though the specific GATA family members have yet to be elucidated. Agonists binding to the androgen receptor, namely testosterone, signals nuclear translocation and association with *ACE2* enhancer elements. Assembly of the enhanceosome complex, consisting of BRD4, MED1, and other accessory proteins, links the promoter bound RNA polymerase machinery (consisting of TATA-binding protein (TBP), TBP-associated factors (TAFs), and additional factors), initiating transcription. Epigenetic control of *ACE2* is a result of methylation and acetylation of histone tails, which repress and promote gene transcription, respectively. Lysine-specific histone demethylase 5B (KDM5B) upregulates *ACE2* expression by catalyzing the removal of a methyl group from lysine 4 (K4) of the histone H3 tail. In contrast, enhancer of zeste homolog 2 (EZH2) trimethylates lysine 27 (K27) to represses *ACE2* expression. DNA methyltransferases hypermethylate CpG4 and CpG5 within the *ACE2* promoter. Circles represent the addition of a methyl group, whereas triangles represent acetylation. Post-transcriptional control by miRNAs, namely miR-421 and miR-143, target *ACE2* mRNA transcripts for degradation or prevent their translation. At the post-translational level, fine-tuning of membrane-bound ACE2 is mediated by phosphorylation, ubiquitination, proteolytic cleavage, and glycosylation. Murine double minute 2 (MDM2), an E3 ubiquitin ligase, ubiquitinates and targets ACE2 for proteasomal degradation. AMP-activated protein kinase (AMPK)-mediated phosphorylation stabilizes ACE2 at the plasma membrane and prevents ubiquitination. Finally, ADAM17 cleaves and releases ACE2 from the cell membrane. *Adapted from Oudit, G.Y., Wang, K.,* ***Viveiros, A****., Kellner, M.J., Penninger, J.M. Angiotensin-converting enzyme 2- at the heart of the COVID-19 pandemic. Cell. 186(5): 906-922. (2023).*

Finally, micro RNAs (miRNAs) post-transcriptionally control *ACE2* through translational repression. *In silico* modeling of the miRNA binding domains on the 3' untranslated region (UTR) predicted miR-125a-5p, miR-200c, and miR-200b and miR-429 as putative *ACE2* regulators.[35] In a study investigating human aerobic exercise training, miRNA-143 was inversely associated with ACE2.[36] In cells, miR-421 reduced ACE2 protein levels and activity.[37]

ACE2 protein levels are controlled post-translationally by targeted degradation and proteolytic shedding (**Figure 1.2**). E3 ubiquitin ligase Murine double minute 2 (MDM2) ubiquitinates ACE2 and targets it for proteasomal degradation; a mechanism described in pulmonary arterial hypertension.[38] Phosphorylation of ACE2's intracellular domain by AMP-activated protein kinase (AMPK) stabilizes its membrane expression and prevents ubiquitination.[38,39]

A Disintegrin and Metalloproteinase-17 (ADAM17) facilitates ectodomain shedding and loss of ACE2 from the plasma membrane, which is then detectable as soluble, plasma ACE2.[40,41] As with most membrane proteins, correct conformational folding, N-glycosylation at the endoplasmic reticulum, and subsequent membrane-directed transport must occur for proper localization of ACE2. Thus, controlling ACE2 translocation to the plasma membrane may be another mechanism of regulation; however, the accessory proteins required for this process remain to be elucidated.[42] In all, ACE2 is subject to transcriptional, post-transcriptional, and post-translational regulation. The regulation of ACE2 may be further altered in different cell types based on sex and age, and in the pathogenesis of heart failure, hypertension, diabetes, and obesity.[3,40,43]

1.3 ACE2 and Heart Failure

Heart failure (HF) remains a leading cause of morbidity and mortality worldwide, with an estimated prevalence of 1.5-1.9% in Canada and the United States.[44] HF is a multifactorial clinical syndrome resulting from functional or structural abnormalities leading to impaired ventricular filling or ejection of blood. HF can be divided into three distinct classes – those with preserved left ventricular ejection fraction (LVEF) (HFpEF; LVEF ≥50%), a mid-range ejection fraction (HFmrEF; LVEF 41-49%), or those with a reduced ejection fraction (HFrEF; LVEF ≤ 40%).[45] Here, we will focus on HFrEF and may use this term interchangeably with HF unless specified. Clinically, HFrEF is characterized by a reduced LVEF (<40%) that presents with dyspnea, peripheral edema, and fatigue. HFrEF is further classified as non-ischemic, dilated cardiomyopathy (DCM) or as ischemic heart disease (IHD) secondary to myocardial infarction or chronic coronary artery disease (CAD).[46-48] The progression of HFrEF is characterized by extensive myocardial remodeling; the cumulative result of cardiomyocyte cell death, cardiomyocyte hypertrophy and fibrotic replacement.[49,50]

Neurohumoral activation in HFrEF is extensively described, of which we will focus on the RAS pathway. Ang II mediates age-dependent cardiomyopathy in *Ace2* deficient mice, a mechanism attributed to enhanced oxidative stress and inflammation.[13] Administration of recombinant human ACE2 (rhACE2) rescued this phenotype, ameliorating Ang II-induced superoxide production, myocyte hypertrophy, fibrotic deposition, and cardiac dysfunction.[51] Two independent studies found higher soluble ACE2 concentrations are associated with all-cause mortality and adverse clinical outcomes independent of traditional cardiac risk factors in HFrEF.[52,53] Indeed, many of the targets of HF therapy include blocking these pathways, namely ACE inhibitors (ACEi) and AT_1R blockers (ARBs) that target the canonical RAS.[45] As a

negative regulator of the RAS, ACE2 is implicated in maintaining cardiac function and reversing the pathogenic effects of excess Ang II and canonical RAS activity in HFrEF.

1.4 ACE2 and COVID-19

ACE2 was identified as the candidate cell-surface receptor for the novel SARS-CoV in 2003 *in vitro*,[54] confirmed *in vivo* with *Ace2* knockout mice who did not succumb to infection.[55] In close succession following SARS-CoV-2 being attributed as the causative virus of COVID-19, ACE2 was identified as its entry receptor in cells and human organoids.[56,57] Again, *Ace2*-deficient mice were protected from infection with a mouse-adapted SARS-CoV-2 strain,[58] confirming that ACE2 is the indispensable viral entry factor for both SARS-CoV and SARS-CoV-2. Prior to cellular infection, binding of the viral spike protein to ACE2 follows with spike protein priming by a handful of candidate accessory proteins, namely cathepsin L, cathepsin B, furin, and, notably, transmembrane protease serine 2 (TMPRSS2) (**Figure 1.3**).[40]

SARS-CoV-2's viral tropism and clinical manifestations outside the pulmonary system reflect ACE2's ubiquitous tissue distribution, including that of the heart and cardiovascular system within pericytes, vascular smooth muscle cells, and fibroblasts,[2] suggesting a probable mechanism of direct cardiac infection.[59,60] Consistently, in post-mortem autopsy heart tissues from twenty patients who succumbed to SARS-CoV, seven heart samples (35%) had detectable viral SARS-CoV genome, associated with increased fibrosis, inflammation and, notably, reduced myocardial ACE2.[21]

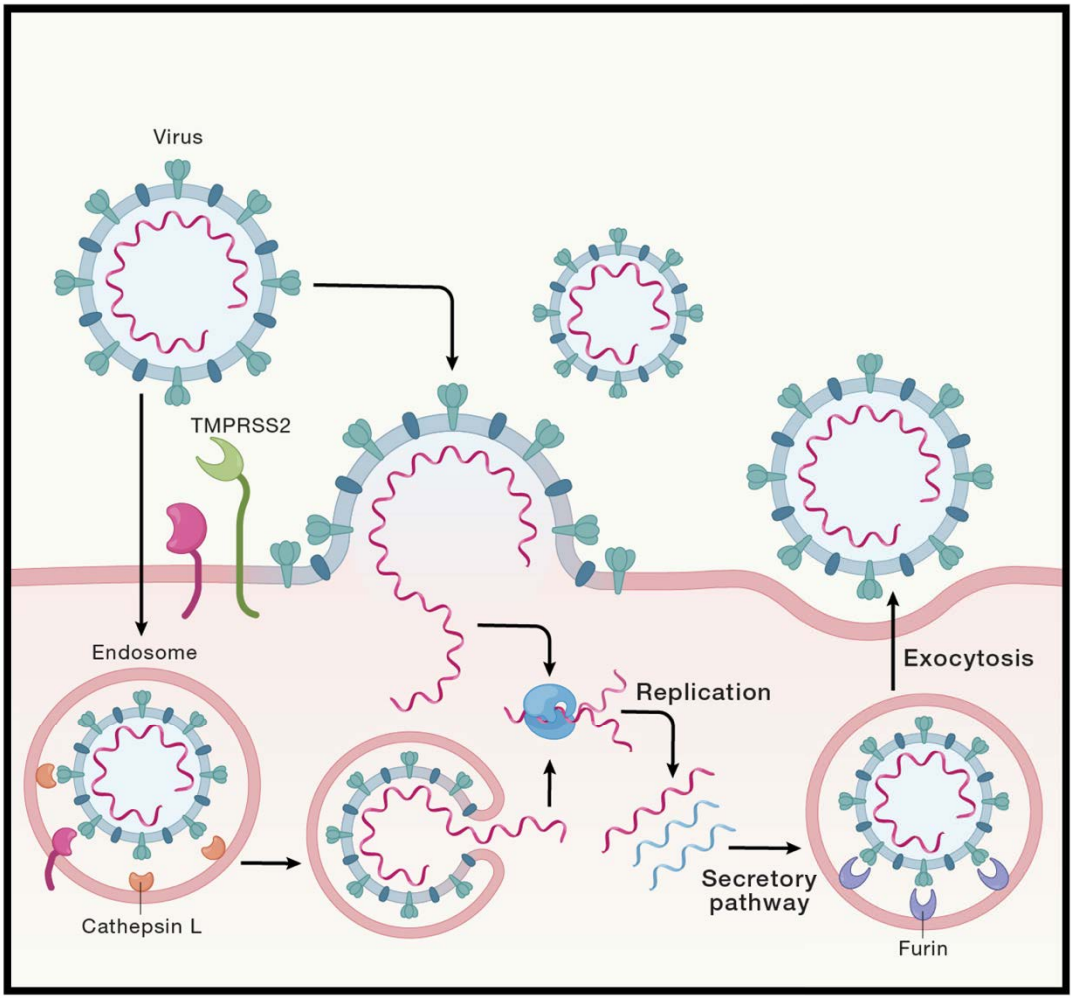

Figure 1.3. *Figure legend on next page*

Figure 1.3. SARS-CoV-2 viral entry.

Following SARS CoV-2 infection, the viral spike protein binds to ACE2. Endogenous proteases, namely transmembrane serine protease 2 (TMPRSS2), which is not required for Omicron, prime the viral spike protein. The viral membrane fuses directly with the target cell membrane and releases the viral single-stranded RNA (ssRNA) into the cytosol, which represents the cell surface entry process for SARS-CoV-2. Alternatively, the entire viral particle is endocytosed, followed by acidification of the endosome for spike protein cleavage by cathepsins, allowing the fusion of the viral and intracellular membranes to release the viral RNA. The ssRNA is subsequently replicated and translated into viral proteins, which are then assembled into mature, infectious viral particles through the secretory pathway. The spike protein can then be pre-processed by furin prior to exocytosis. *Adapted from Oudit, G.Y., Wang, K., **Viveiros, A**., Kellner, M.J., Penninger, J.M. Angiotensin-converting enzyme 2- at the heart of the COVID-19 pandemic. Cell. 186(5): 906-922. (2023).*

1.5 Sex Differences in Heart Failure and COVID-19

The importance of sex differences in clinical disease outcomes is increasingly recognized. A field that has pioneered this dialogue is cardiovascular disease (CVD), including HF, myocardial infarction, and hypertension.[61,62] Sex differences underlie the manifestation of HF; aged women preferentially develop HF with preserved left ventricular ejection fraction (HFpEF) with a background of hypertension, whereas men present with HF with reduced ejection fraction (HFrEF) associated with CAD.[63,64] Furthermore, women with HF have improved survival compared to men after adjusting for age in the Framingham study.[63] Acute myocardial infarction commonly presents with chest pain in both sexes; however, health care providers are more likely to associate symptoms in women with heart-independent conditions in the prodromal stage.[65] Hypertension incidence is higher for men than age-matched, pre-menopausal women.[66]

Similarly, sex differences are implicated in the severity of COVID-19 caused by the SARS-CoV-2 virus (**Figure 1.4, Figure 1.5**). Epidemiological data from the related 2002-2003 SARS epidemic suggested sex-dependency in clinical disease outcomes, including intensive care unit (ICU) admission and death favouring men, a pattern maintained after adjusting for age.[67,68] The sex disparity in COVID-19 is consistent in most countries, with a similar incidence of infection (percent of cases) in both sexes; however, men consistently demonstrate a more severe phenotype and increased mortality across age groups on a global level (**Figures 1.4-1.6**).[69,70] We will investigate the relationship between CVD and COVID-19 and provide a rationale for the involvement and targeting of two candidate pathways in the pathogenesis of COVID-19, namely immune responses and the counter-regulatory branch of the renin-angiotensin system (RAS). We will highlight sex hormones and sex chromosomes as two potential explanations for sexual

dimorphism in these pathways. Finally, we will briefly discuss the added challenges of gender in the COVID-19 pandemic.

1.6 CVD and COVID-19

The relationship between CVD and COVID-19 is multifaceted; a significant complication in COVID-19 is the development of acute and chronic cardiac injuries, including myocarditis, conduction abnormalities, and HF,[71,72] while pre-existing CVD enhances the probability of detrimental outcomes in SARS-CoV-2 infection.[73-76] Vascular effects are prominent in COVID-19 patients with endothelial damage, intussusceptive angiogenesis, and microthrombi formation following lung morphological examination.[77,78] Notably, the pathogenesis of CVD and COVID-19 overlap in key signaling pathways, namely the innate immune system and the RAS.

Extensive immune activation is implicated in severe cases of COVID-19 and predicts severity and mortality.[79] In accordance, chronic immune activation is implicated in the pathogenesis of CVD in some instances. In fact, autoimmune diseases, such as rheumatoid arthritis and periodontal disease, are associated with increased cardiovascular risk from accelerated atherosclerosis and subsequent premature CAD.[80] As women are more susceptible to inflammatory and autoimmune diseases, autoimmunity-associated CVD is of particular concern.[81] The emerging role of the innate immune system in CVD is characterized by Toll-like receptors (TLR) signaling that contributes to myocardial damage and adverse remodeling when stress-activated cytokine production is sustained. Further, the expression profile of innate immune genes is distinct in the failing heart compared to non-failing explanted human hearts, whereby the data suggests an increase in innate immune system activation in heart failure.[82,83]

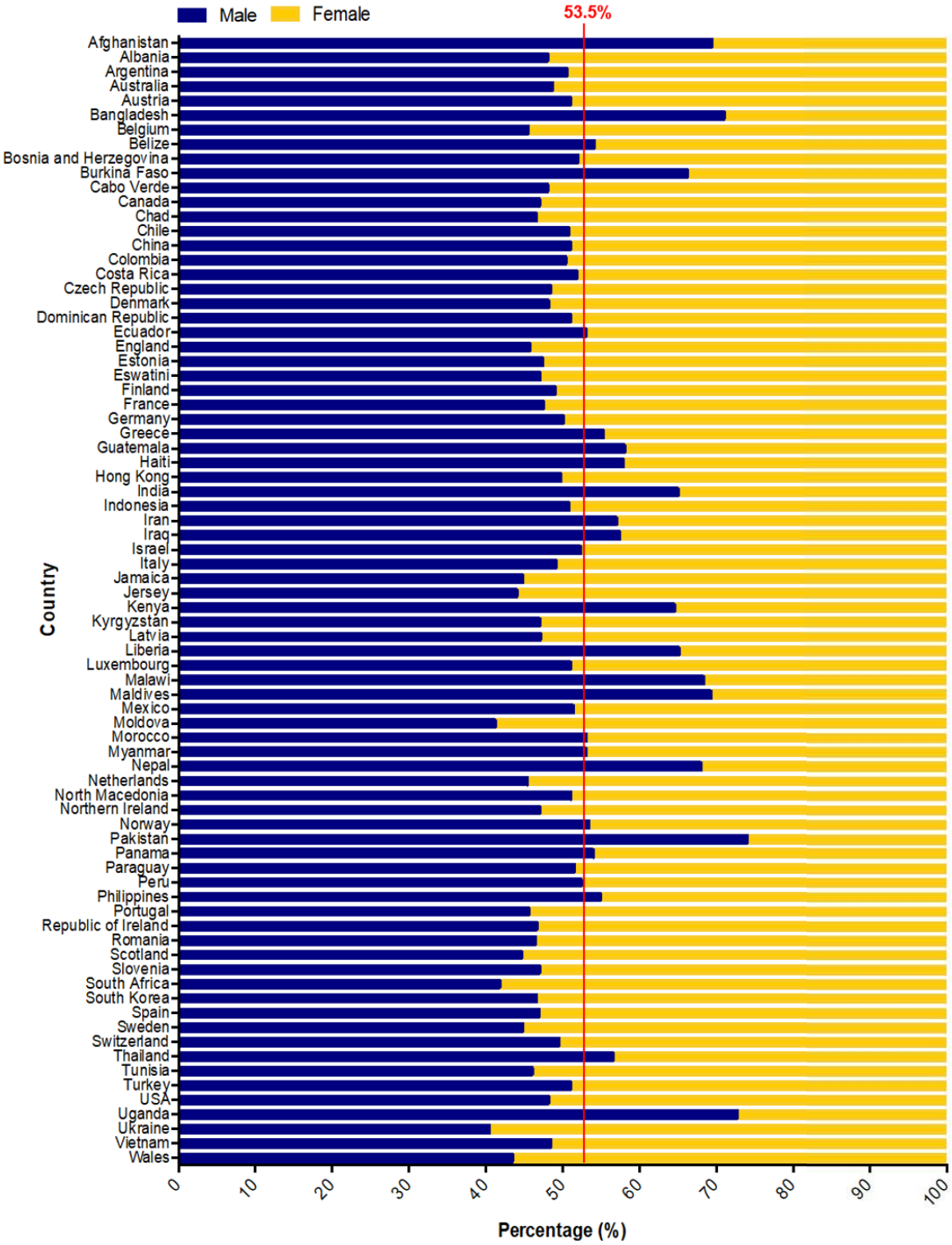

Figure 1.4. *Figure legend on next page*

Figure 1.4. Global reported COVID-19 epidemiological data of percent of cases disaggregated by sex.

The red line represents the average cases for males across all countries (53.5%). All countries with available and complete sex-disaggregated data were included (78 in total). The list of included countries and raw data plotted can be accessed as Supplementary Data S1 (https://figshare.com/s/2d52921a0b00e648199c). The data presented is a summary of publicly available data compiled by Global Health 5050. The compiled data is from various sources, which include: national governments, official media/social media communications, national surveillance centres, global/regional coordinating bodies. Figures created are based on data directly from data source (no calculations were made). Numbers presented may not reflect the actual current cases since not all the available data is disaggregated by sex. Data accessed November 11th, 2020. *Adapted from* ***Viveiros, A****., Rasmuson, J., Vu, Jennie., Mulvagh, S.L., Yip, C.Y.Y., Norris, C.M., Oudit, G.Y. Sex differences in COVID-19: candidate pathways, genetics of ACE2, and sex hormones. Am J Physiol Heart Circ Physiol. 320: H296-H304. (2021).*

COVID-19 and CVD share another common feature in that ACE2 is implicated in the pathogenesis of both. As described, ACE2 is protective in CVD to counteract the canonical renin-angiotensin system (RAS), and loss of this protein (genetic knockout or proteolytic cleavage) exacerbates dysfunction.[8,9,41,84,85] In accordance, increased plasma ACE2 concentration was correlated with a worsened prognosis in HF, and male sex was the strongest predictor of elevation.[86] Pre-menopausal women are protected from developing CVD and hypertension, including stroke; however, male androgens may contribute to these conditions' incidence and progression.[66,87]

Therapies indicated for the prevention, treatment, or management of CVD include drugs targeting the RAS, namely angiotensin-converting enzyme inhibitors (ACEi) or angiotensin II type 1 receptor blockers (ARBs).[88] Interestingly, despite common clinical manifestations of HF, treatment response in men and women is variable: women may be incorrectly dosed in HFrEF with ACEi,[89] women are more likely to have cough-induced intolerance of ACEi, and women are twice as likely as men to develop HFpEF- a clinical phenotype without adequate therapy.[46,90] Overall, there is substantial evidence for inflammation and immunity and aberrant RAS activity in the pathogenesis of CVD, which we will explore in the context of delineating sex differences in COVID-19.

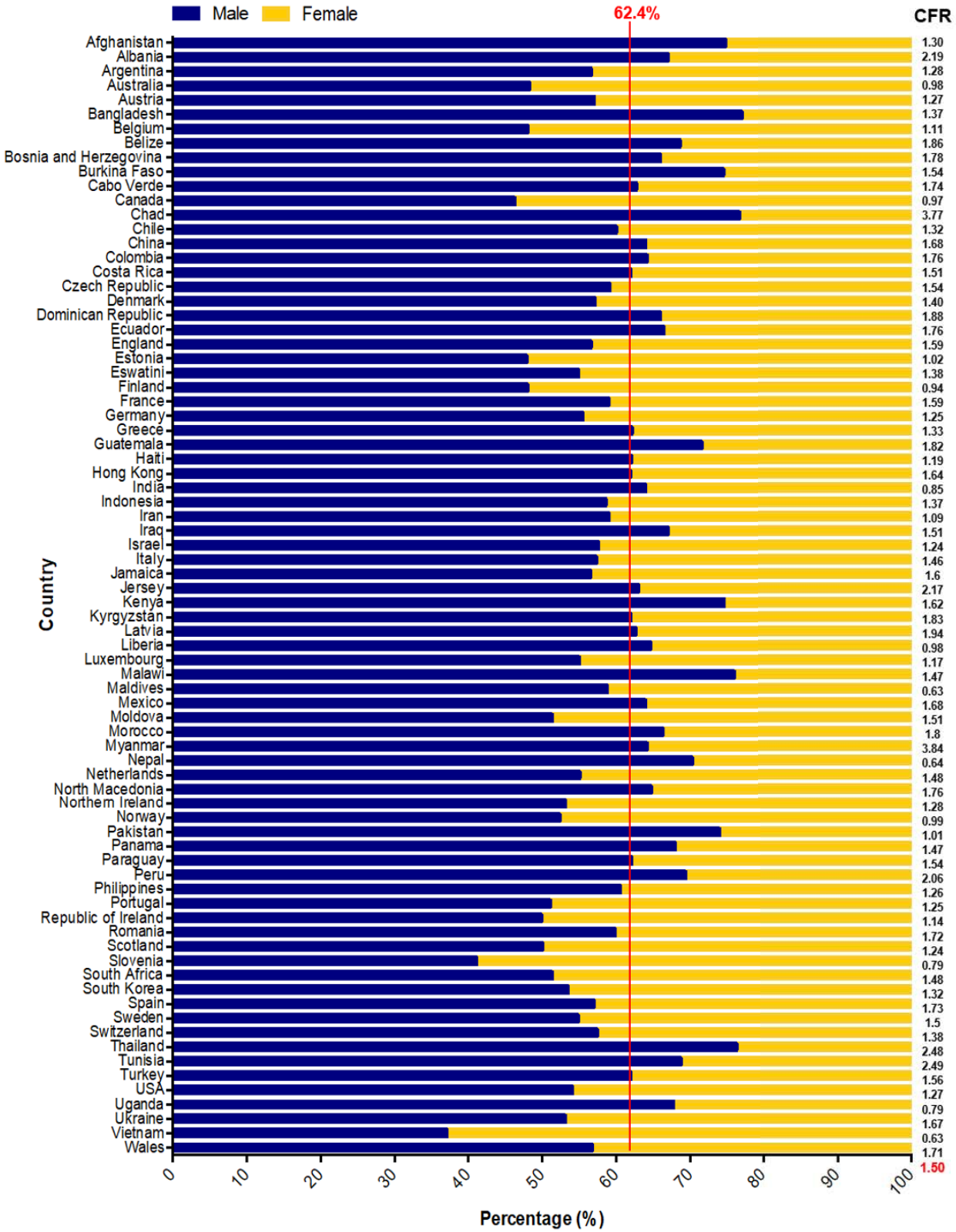

Figure 1.5. *Figure legend on next page*

Figure 1.5. Global reported COVID-19 epidemiological data of percent of deaths disaggregated by sex.

Deaths are reported as percent of total male or total female cases. The red line represents the average cases for males across included countries (62.4%). The case fatality ratio (CFR) for each is included adjacent to the countries' corresponding bar graph. The average CFR for included countries is indicated in red (1.50). All countries with available and complete sex-disaggregated data were included (78 in total). The list of included countries and raw data plotted can be accessed as Supplementary Data S1 (https://figshare.com/s/2d52921a0b00e648199c). The data presented is a summary of publicly available data compiled by Global Health 5050. The compiled data is from various sources, which include: national governments, official media/social media communications, national surveillance centres, global/regional coordinating bodies. Figures created are based on data directly from data source (no calculations were made). Numbers presented may not reflect the actual current cases since not all the available data is disaggregated by sex. Data accessed November 11th, 2020. *Adapted from* ***Viveiros, A****., Rasmuson, J., Vu, Jennie., Mulvagh, S.L., Yip, C.Y.Y., Norris, C.M., Oudit, G.Y. Sex differences in COVID-19: candidate pathways, genetics of ACE2, and sex hormones. Am J Physiol Heart Circ Physiol. 320: H296-H304. (2021).*

1.7 Candidate Pathways for Sex Differences

1.7.1 Innate Immunity

The innate immune system drives the initial response to viral infection. It is initiated when host-cell pattern recognition receptors (PRRs), such as RIG-I-like receptors (RLRs) and Toll-like receptors (TLRs), identify pathogen-associated molecular patterns (PAMPs) of viral components, subsequently activating a signaling cascade to combat the infection.[91] Immunological sex differences play a substantial role in the prevalence, severity, and pathogenesis of infectious diseases. Adult women mount a rapid and aggressive innate and adaptive immune response to combat invading pathogens.[81] In contrast, men have a dampened immune response and are more susceptible to viral infections.[81,92]

In accordance, in SARS-CoV infection, the innate immune response is a primary driver of viral clearance and pathogenesis if activity is uncoordinated and prolonged.[91] Specifically, type I interferons (IFN), including IFNα, limit viral infection, initiate tissue repair, and programs the adaptive immune system to foster viral elimination. The robust, delimited, and timely IFN-I response is considered protective; however, left unchecked, aberrant cytokine and chemokine production (many of which are interferon stimulated genes (ISGs)) contribute to dysfunction in SARS-CoV infection, including the development of acute respiratory distress syndrome (ARDS).[91,93] In the context of SARS-CoV-2, enhanced severity in men is correlated with increased plasma cytokine levels of the innate immune system, including proinflammatory interleukin (IL)-8 and IL-18. In contrast, reduced severity in females corresponds with higher T-cell activation.[70] Further, increases in tumour necrosis factor alpha (TNFα) and IL-6 immunological activation are significant and independent predictors of severity and mortality in COVID-19.[79]

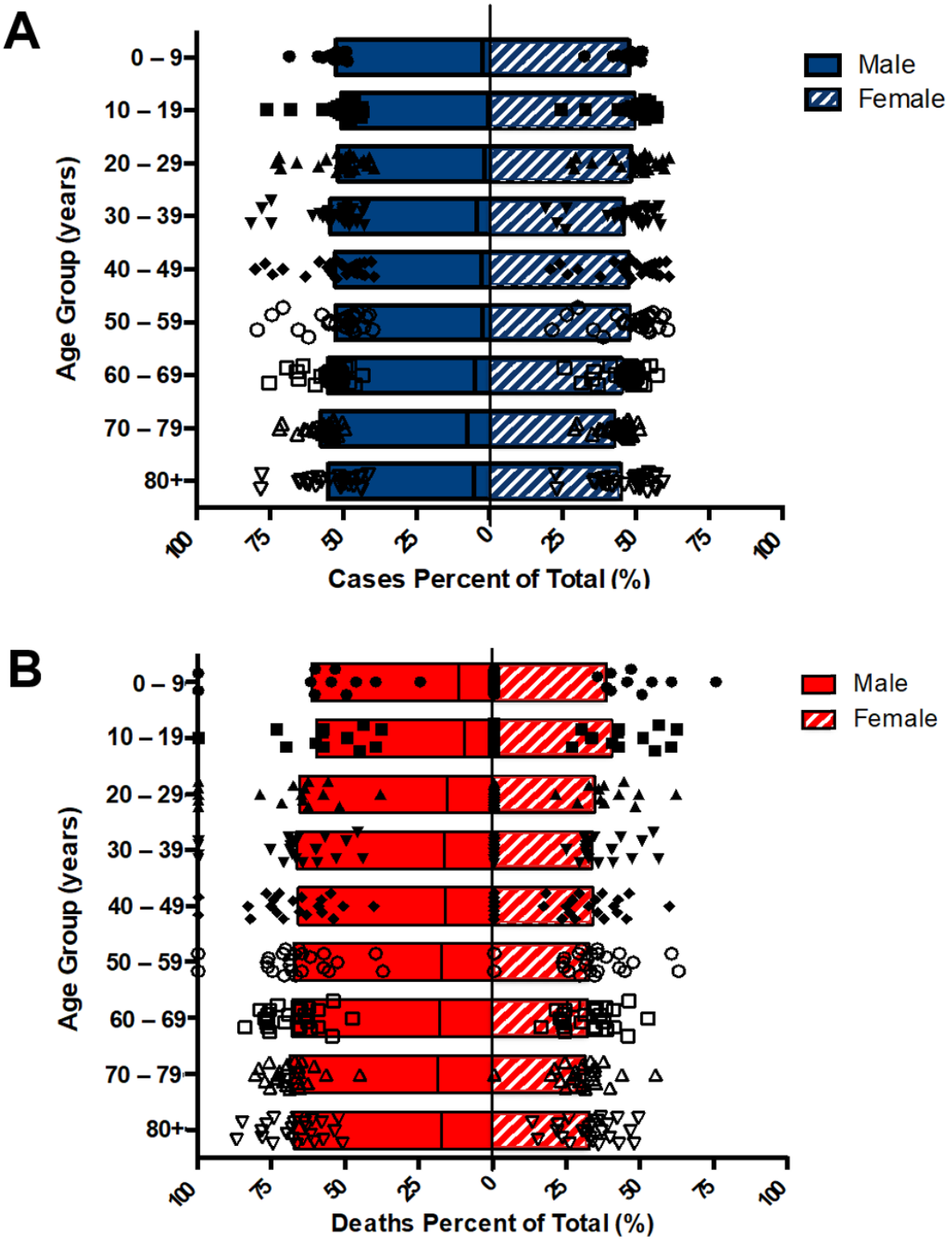

Figure 1.6. *Figure legend on next page*

Figure 1.6. Global sex- and age- disaggregated data on COVID-19 across countries.

A. Data represents the percent of the total rate of cases in males and females. The line in each bar represents the mean to visually indicate the direction each data set is skewed. Data was pooled from all available countries with complete sex- and age- disaggregated records for cases and organized by decade (29 in total). **B.** Data represents the percent of the total rate of deaths in males and females. The line in each bar represents the mean to visually indicate the direction each data set is skewed. Data was pooled from all available countries with complete sex- and age- disaggregated records for deaths and organized by decade (24 in total). The list of included countries and raw data plotted can be accessed as Supplementary Data S1 (https://figshare.com/s/2d52921a0b00e648199c). The data presented is a summary of publicly available data compiled by Global Health 5050. The compiled data is from various sources, including: national governments, official media/social media communications, national surveillance centres, global/regional coordinating bodies. Data accessed November 11th, 2020. *Adapted from* ***Viveiros, A****., Rasmuson, J., Vu, Jennie., Mulvagh, S.L., Yip, C.Y.Y., Norris, C.M., Oudit, G.Y. Sex differences in COVID-19: candidate pathways, genetics of ACE2, and sex hormones. Am J Physiol Heart Circ Physiol. 320: H296-H304. (2021).*

1.7.2 Counter-regulatory RAS: ACE2

ACE2, has garnered enhanced interest as the receptor for SARS-CoV-2.[8,9,56] However, the negative connotation should be refrained, as ACE2 is essential to deactivate the detrimental effects of the RAS, reported particularly in the context of CVD.[41] ACE2 is ubiquitously expressed and exerts protective effects in the cardiovascular system, lungs, kidneys, and gut. Indeed, symptoms of SARS-CoV-2 are intimately linked with the expression pattern of ACE2.[9,94] SARS-CoV-2 requires ACE2 for cellular entry and downregulates protective ACE2.[56]

Following viral entry, SARS-CoV and SARS-CoV-2 activate A Disintegrin and Metalloproteinase (ADAM)17; a cellular event that differentiates mild and severe coronavirus infections.[9,95] Specifically, Haga *et al.* examined the differences in activated signaling cascades between SARS-CoV and HNL63-CoV, the latter a coronavirus that causes mild symptoms attributed to the common cold. Despite commonly binding to ACE2, the HNL63-CoV spike protein does not induce ACE2 shedding or ADAM17 activation.[95] Further, ADAM17 mobilizes and activates TNFα and determines IL-6 signaling through cleavage of the IL-6 receptor alpha.[96] Activation of the canonical RAS (ACE-Ang II-AT_1R) pathway leads to enhanced ADAM17 activity.[9] Therefore, RAS overactivity would promote disease severity, especially for patients with comorbid CVD.[59] ADAM17 may provide the critical link between aberrant immune system activation and exacerbating the loss of protective ACE2, thus fostering enhanced susceptibility to severe COVID-19.

1.8 Mechanism of Sex Differences

1.8.1 Sex Chromosomes

The female advantage lies in harbouring an additional X-chromosome than males, therefore conferring the benefit of mosaicism, skewed inactivation, and escaping X-inactivation to bypass the deleterious effects of X-linked mutations and offer functional diversity in responses.[97] We will focus on X-linked genes escaping silencing, as this mechanism is relevant for both the innate immune system and *ACE2* in females (**Figure 1.7A**). Physiologically X-inactivation occurs for dosage compensation; however, approximately 15% of X-genes escape inactivation in humans, thus they are found at a higher copy number in females over males.[81] Although not elucidated entirely, one mechanism of X-inactivation is dominantly controlled by two long noncoding RNAs (lncRNAs), namely X-inactivation specific transcript (XIST) and X-active specific transcript (XACT) responsible for X-silencing and maintaining an active X-chromosome, respectively.[97] The probability of escape from X-chromosome inactivation is determined by the specific gene's dosage sensitivity and location on the X-chromosome.[97] Generally, X-inactivation of the maternal or paternal X-chromosome occurs randomly, thereby producing a mosaic in females, whereas skewed inactivation describes the genetic selection of the inactivated chromosome. A skewed inactivation pattern confers a sex-specific phenotype in females, and this phenomenon increases with age. Therefore, this may offer females a protective mechanism against deleterious mutations by restricting their expression.[97]

Many immune-associated genes are X-linked, including but not limited to PRRs (such as *TLR7*, *TLR8*) and fundamental regulators of TLR signaling (interleukin-1 receptor-associated kinase 1 (*IRAK1*) for example) with females having two copies of these genes.[97] We will focus on TLR7, a receptor localized to dendritic cells that responds to single-stranded viral RNA, thus

relevant for SARS-CoV-2 infection. Increased *TLR7* gene expression has been detected in females over males, thus suggesting the *TLR7* gene, as it is X-linked, may escape inactivation.[81,98] Similarly, IFNα production is enhanced by female-derived peripheral blood mononuclear cells (PMBCs) stimulated *in vitro* with TLR7 ligands.[81,99] However, despite this increase, Berghofer *et al.* reported anticipated gene silencing of one of the *TLR7* alleles in females; therefore, the differences were not attributed to X-gene escape in this study.[99] However, female upregulation of TLR7 is estradiol-dependent.[81]

The *ACE2* gene resides in the Xp22.2 region of the X-chromosome and is recognized as an escape gene. As described, X-gene escape generally confers a female-bias in expression.[24] Therefore, in theory, females have a double dose of ACE2 that may compensate for SARS-CoV-2 mediated loss of membrane ACE2. In fact, heterozygous knockout of *Ace2* is sufficient to enhance heart disease susceptibility and reduce ACE2 protein levels in female mice, demonstrating a gene-dosing effect fundamentally dependent on the *ACE2* locus.[100] Further research efforts are required to investigate the putative female bias in ACE2 expression; however, sex hormones may modulate this mechanism.[24,28] Of note, many articles draw conclusions based exclusively on expression profiles of *ACE2*, which may limit our complete understanding of the impact on the ACE2 protein and its function. Indeed, *ACE2* expression may not correlate with enzyme activity,[101] as ACE2 is highly regulated by proteolytic cleavage[41] and is predicted to be regulated by microRNAs (miRNAs).[35] The ability of ACE2 to deactivate the RAS is complex, and the sex-specific function and control of ACE2 requires investigation at the transcriptional, post-transcriptional, and post-translational levels.

1.8.2 Sex Hormones

Sex hormones confer differential susceptibility of the sexes to viral infections, which we will discuss in the context of innate immunity and the counter-regulatory RAS (ACE2) pathway. Immunological differences between males and females are exemplified by the fact that androgen response elements (AREs) and estrogen response elements (EREs) reside in the promoters of several genes of the innate immune system.[81,102] Seoul hantavirus challenge in female rats saw transcriptional upregulation of genes associated with the innate immune system, namely *TLR7*, *TLR3*, *RIG-I,* as well as proinflammatory genes including *IFNβ*, *IFNAR1,* and interferon regulatory factor 7 (*IRF7*); a transcription factor for the induction of type I interferons.[102] The enhanced antiviral response in females resulted in a reduced viral RNA copy number and reduced expression of viral antigens, thus improved viral handling over males in a sex hormone-dependent manner.[81,102] In accordance, male mice infected with SARS-CoV demonstrated increased viral load, vascular permeability, and alveolar edema compared to age-matched females, an effect attributed to sex-hormone dependent innate immunity.[103]

17β-estradiol possesses cell-type dependent effects, namely fostering an increased neutrophil number in response to viral infection[104] and an increased number of natural killer (NK) cells, yet reduces their cytotoxicity.[105] Further, 17β-estradiol demonstrates a bipartite effect on monocytes and macrophages: at low doses the hormone stimulates the release of IL-1, IL-6 and TNFα; however, at high concentrations, it limits the production of proinflammatory cytokines.[81] In contrast, androgens are immunosuppressive; exogenous testosterone administration reduced TLR4 in isolated mouse macrophages, effectively diminishing the propensity to activate the innate immune response.[92]

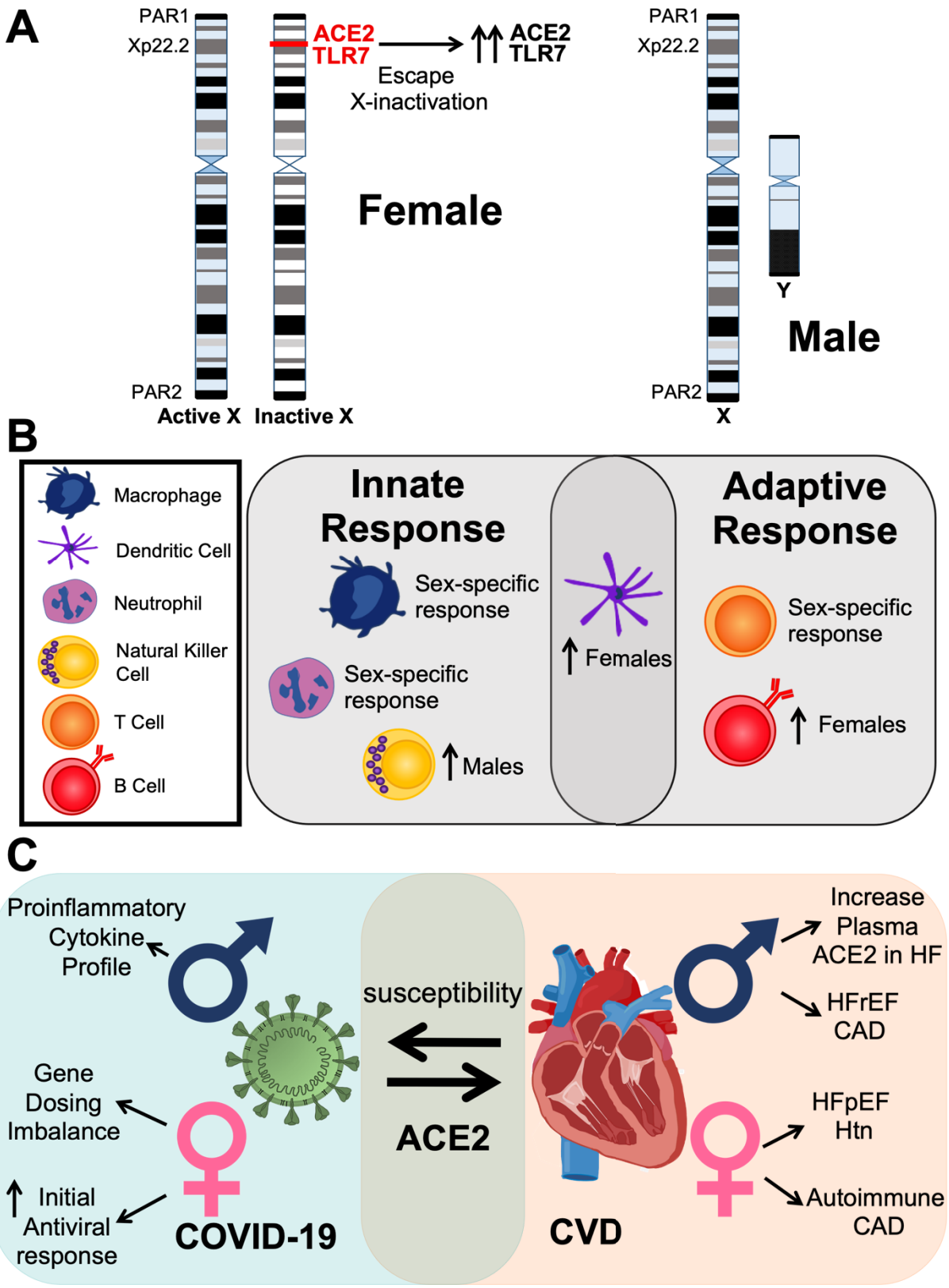

Figure 1.7. *Figure legend on next page*

Figure 1.7. Candidate mechanisms of sex-specific susceptibility of males to COVID-19.

A. *TLR7* and *ACE2* are localized to the Xp22.2 region of the X-chromosome and escape X-chromosome inactivation in females. **B.** Differences in the innate and adaptive immune response between males and females. In general, neutrophils in females have a higher phagocytic capacity, however males have higher TLR4 expression and TNF production. Therefore, a sex-specific response exists for neutrophils. Macrophages from females have higher activation, phagocytic capacity, and IL-10 production, whereas males have increased proinflammatory cytokine generation, indicating sex-specific responses. Dendritic cells from females have higher TLR7 and Type 1 interferon activity, exhibiting a sex-bias favouring females. Males have an increased number of Natural Killer Cells. Females have generally higher B cell numbers and antibody production. Females have a higher number of $CD4^+$ T cells, activated T cells and T cell proliferation than males. Rather, males possess higher frequencies of $CD8^+$ T cells, indicating sex-specific responses in the profile of T lymphocytes.[81] **C.** Summarized sex differences and bidirectional susceptibility in COVID-19 and CVD. In COVID-19, females have an increased IFN-α secretion and early virus sensing and prompt antiviral response upon TLR7 stimulation in dendritic cells. Gene dosing imbalances in females result from innate immune genes escaping X-inactivation. Males have increased proinflammatory cytokine and chemokine production in COVID-19 associated with enhanced severity, specifically IL-8 and IL-18. In CVD, males have higher incidence of HFrEF with a background of CAD, whereas females are more likely to have HFpEF with a background of hypertension (Htn) and autoimmune-related coronary artery disease (CAD). *Adapted from* ***Viveiros, A****., Rasmuson, J., Vu, Jennie., Mulvagh, S.L., Yip, C.Y.Y., Norris, C.M., Oudit, G.Y. Sex differences in COVID-19: candidate pathways, genetics of ACE2, and sex hormones. Am J Physiol Heart Circ Physiol. 320: H296-H304. (2021).*

Therefore, although sex hormones elicit cell type-specific effects, the hormonal modulators, genetics, and environmental factors culminate in female bias in both the innate and adaptive immune response (**Figure 1.7B**).[69,81]Although the role of sex hormones is compelling, in the context of SARS-CoV-2 infection, this mechanism would be absent upon reproductive senescence; a period characterized by a rapid decline of sex hormones (estrogens) in females and a progressive decline of androgens in males.[81] Therefore, sex hormones may not entirely explain the sex discrepancy, as differences persist in aged males and females (**Figure 1.6)**, Supplementary Data S1 (https://figshare.com/s/2d52921a0b00e648199c).

Interestingly, ACE2 expression and enzyme activity changes throughout life in a sex-specific manner. Normal aging is characterized by increased *ACE2* expression in both sexes; however, only males demonstrated an increase in ACE2 activity from studies in sheep.[101] In support, *ACE2* had a male-biased expression pattern in humans, which is counterintuitive to *ACE2* escaping X-gene inactivation.[24] In this case, the female bias in escape is counteracted by sex-hormone dependent regulation. Renal ACE2 mRNA, protein levels, and activity are increased in male mice under basal conditions. Further, 17β-estradiol inhibited ACE2 activity post-transcriptionally.[24,28] In contrast, 17β-estradiol upregulated ACE2 and conferred renal protection in animal models of hypertension- an effect lost in ovariectomized rats and restored upon exogenous administration of Ang-(1-7) or 17β-estradiol.[106] In another study investigating sex differences in response to high-fat diet (HFD)-induced obesity, females exhibited an estrogen-dependent increase in adipose ACE2 activity and Ang-(1-7) despite increased body weight and fat mass compared to males. In contrast, male animals exhibited increased plasma Ang II, decreased Ang-(1-7), and reduced renal ACE2 activity, thus greater susceptibility to obesity-induced hypertension.[107] Taken together, these studies suggest that a male-bias in ACE2 expression and

activity is characteristic of normal aging; however, females may harbour a sex hormone-dependent compensatory mechanism to upregulate ACE2 in disease.

The positive feedback mechanism of ACE2 downregulation driven by aberrant RAS and ADAM17 activation may explain the enhanced susceptibility of males to COVID-19. As described, RAS pathogenesis is contingent on Ang II activating AT_1R. Although the expression of AT_1R followed no sex-specific pattern in a mouse model of vascular injury, studies demonstrated that females have a greater capacity to upregulate expression of the antagonistic AT_2R, which elicits anti-inflammatory and protective effects in CVD.[108] Ovariectomy in spontaneously hypertensive rats increases the expression of AT_1R in mesenteric vascular beds, and reduces kidney AT_2R expression in Wistar-Hanover rats. Exogenous supplementation of estradiol decreases AT_1R and increases AT_2R expression. Testosterone may mediate opposing effects, however, the evidence remains controversial.[66] Female mice have a greater capacity to upregulate ACE2 than males following Ang II infusion-induced hypertension, resulting in enhanced catabolism of Ang II and reduced glomerular AT_1R expression.[109] Although these associations have not been addressed directly in COVID-19, this suggests females have attenuated RAS activation in disease, which may correspond to reduced activation of the ADAM17-mediated positive-feedback pathway that augments ACE2 loss. Altogether, sex differences exist in the gene dosing effects of X-chromosome linked genes and the immune responsiveness between males and females. The bidirectional susceptibility of COVID-19 and CVD is fundamentally dependent on ACE2 shedding, thus highlighting ADAM17 as a potential therapeutic target (**Figure 1.7C**).

1.9 Impact of Gender

Gender plays a fundamental role in health and disease outcomes. Considering the COVID-19 pandemic, gender norms, culture, and societal roles collectively influence viral exposure, infection

susceptibility and treatment access. Differences in the incidence of infectious diseases, such as SARS-CoV-2, are more likely to be impacted by alternate exposure rather than differences in biological immunity.[68] Examples of differing exposure include occupational risk and gender roles in providing care, resulting in discrepancies in contracting viral infections. Women constitute the majority of frontline healthcare workers globally, with 70% of the world's healthcare staff comprised of women.[110] Moreover, women are exposed in care-giving roles and care-taking occupations, whereas men have greater exposure outside the home.[68] Additional strain is placed on women in childcare roles due to the existing family structure.[68,111] Differential exposure may be particularly relevant in SARS-CoV-2 infection due to the modest positive association between viral load and shedding duration with the degree of COVID-19 severity.[112] In summary, the interplay between gender and biological sex represents an added challenge to delineate COVID-19 outcomes.

1.10 Limitations of Epidemiological Data

Sex-disaggregated data is not available from all countries, and consistent reporting of data based on sex and age interaction is limited.[113] All cases documented are both reported and confirmed cases; therefore, if non-severe or access to testing is limited, these will not be included. Further, asymptomatic cases will not likely be reported. Outbreaks in long-term care facilities are substantial and may lead to a bias in statistics due to women's higher life expectancy and the overrepresentation of women in these facilities. However, the discrepancy in male severity is still represented across age groups, including the aged cohorts (**Figure 1.6B**), and the number of cases does not favour older women (**Figure 1.6A**). Additional limitations include a lack of reliable test

rate data and varying test methods with different specificity and sensitivity, thus challenging the ability to draw conclusions based on globally reported statistics.

1.11 Adipose Tissue in Obesity and Heart Failure

Metabolic disorders, including type 2 diabetes (T2DM) and obesity, are steadily rising global health threats associated with significant morbidity and mortality. T2DM is a major risk factor for CAD, stroke and peripheral vascular diseases,[114] as well as microvascular dysfunction leading to renal failure and blindness.[115] Obesity predicts the incidence of HF,[116-118] most notably in women towards HFpEF.[119,120] Therefore, increased adiposity is a major driving force for the development of cardiovascular complications in metabolic disorders. The concept of adipose tissue as a neutral storage organ for triglycerides has been challenged. In fact, adipose tissue as an endocrine organ is increasingly recognized, especially as it pertains to glucose and lipid homeostasis.[121] Studies have shown that adipose tissue inflammation contributes to insulin resistance and poor glycemic control.[122-124] Prolonged caloric excess triggers chronic inflammatory changes in adipose tissue with several implicated immune cells and inflammatory cytokines involved.[125] However, the mechanistic and temporal association between adipose tissue inflammation and cardiovascular dysfunction triggered by metabolic disease has only been recently recognized. The heterogeneity of adipose tissue depots of the body and the breadth of signaling pathways involved are underscored by each unique location, biochemical, developmental, and structural properties.[126,127] This offers a valuable therapeutic opportunity to intervene with cardiovascular complications of metabolic disease by harnessing adipose depot-specific targets or modulating the signaling pathways of adipose tissue dysfunction.

1.12 Adipose Tissue of the Heart and Coronary Vasculature: Perivascular Adipose Tissue

1.12.1 Structural and functional roles

Perivascular adipose tissue (PVAT) is an adipose tissue depot that is contiguous with the tunica externa of most arteries and veins with an internal diameter greater than 100 μm, including small vessels like subcutaneous small arteries and coronary arteries, as well as large systemic vessels like the aorta, with the exception of the cerebral and micro-vasculature (**Figure 1.8A**).[128,129] The physical proximity of this adipose layer to blood vessels and its intertwinement with fibrous adventitia provides a cushioning effect that both protects vessels and insulates them from their surroundings.[130] Initially, the role of PVAT has been limited to this structural function, but in 1991 Soltis *et al.* demonstrated that aortas with intact periaortic fat displayed a decrease in norepinephrine-induced contractility compared to those in which the PVAT has been removed.[131]

The anti-contractile effect remained when vessels without adipose tissue were treated with PVAT-conditioned media.[132] The name adipocyte-derived relaxing factor (ADRF) was coined, and since then the ability of PVAT to reduce the contractility of vascular smooth muscle cells (VSMCs) has been well documented.[133-137] This suggests a mechanistic pathway by which PVAT secretes a complex array of factors to modulate vascular tone at the level of the tunica externa, thus regulating cells of the tunica media and intima, and ultimately vascular health and disease. Like other adipose tissue depots, the PVAT plays a fundamental role as an endocrine organ, secreting a myriad of cytokines, chemokines, and hormones collectively referred to as adipokines.[138]

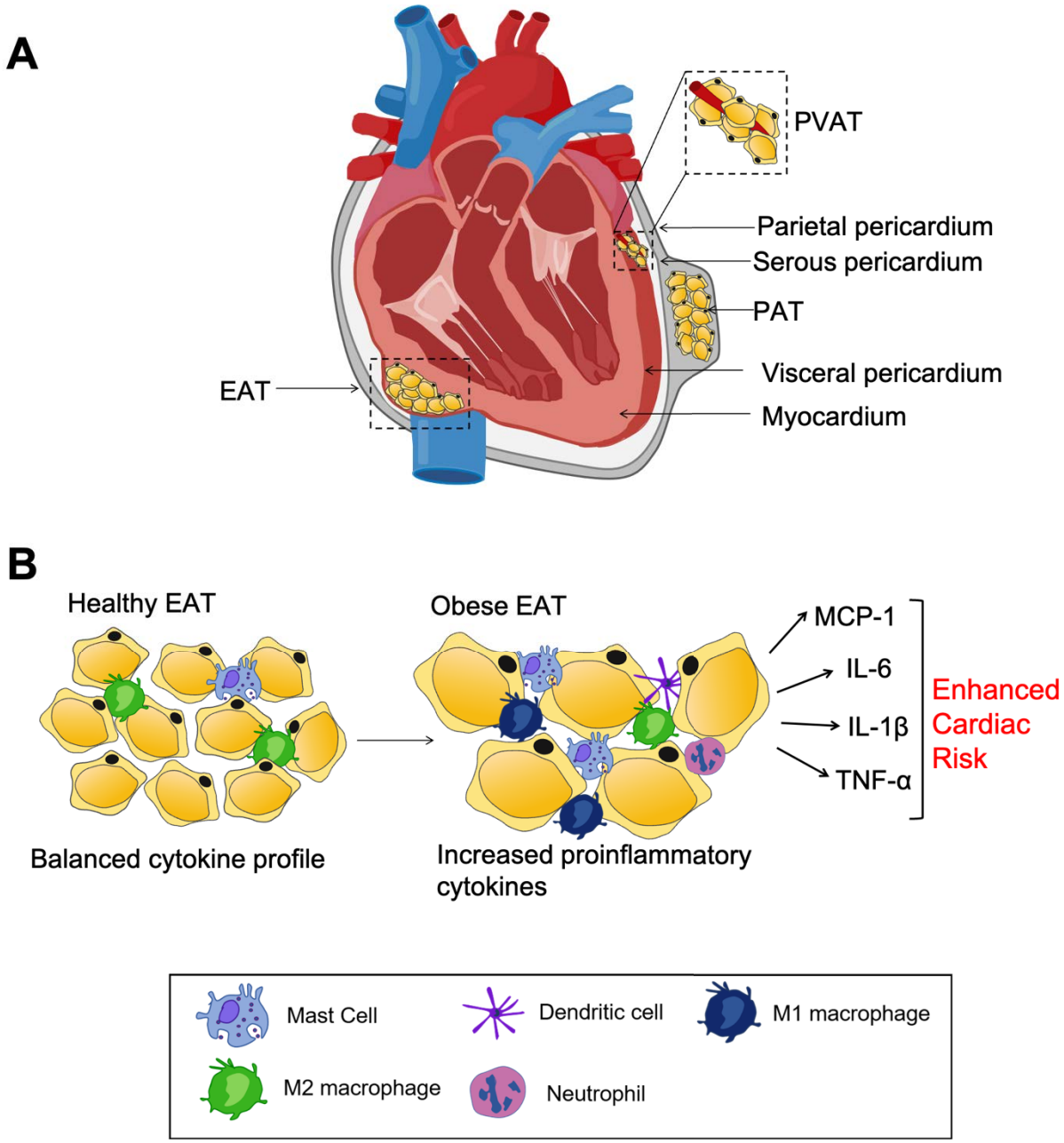

Figure 1.8. *Figure legend on next page*

Figure 1.8. The adipose tissue depots of the heart.

A. Localization of perivascular (PVAT), epicardial (EAT), and pericardial (PAT) adipose tissue. The PVAT denotes the adiose tissue of the vasculature. The EAT denotes the fat depot between the myocardium and the visceral pericardium. The PAT denotes the adipose tissue in the pericardial cavity. **B.** Increased visceral adiposity in obesity induces EAT expansion and promotes inflammation. Infiltration of mast cells, macrophages, neutrophils, and dendritic cells promotes the release of proinflammatory cytokines and disrupts cytokine profile. Increased cardiovascular risk is associated with obesity and chronic inflammation. *Adapted from Rafeh, R.,* **Viveiros, A**.,* Oudit, G.Y., El-Yazbi, A.F. Targeting perivascular and epicardial adipose tissue inflammation: therapeutic opportunities for cardiovascular disease. Clin Sci (Lond). 134(7): 827-851. (2020).*

The location of PVAT confers the unique ability to communicate with VSMCs and endothelial cells in a paracrine manner. This localized interaction provides a direct mechanism through which diseases involving adipose dysfunction, such as T2DM and metabolic syndrome, may impair vascular function.

1.12.2 PVAT and vascular dysfunction in metabolic disorders

Several epidemiological studies examined the relationship between PVAT dysfunction and several vascular disorders. Not only was thoracic peri-aortic fat correlated with markers of metabolic risk, including glucose intolerance, dyslipidemia, and diabetes, but it also appeared tightly associated with vascular diseases such as atherosclerosis, hypertension, peripheral artery disease, thoracic and abdominal aortic calcification, and CAD.[139,140] In the context of CAD, extensive research showed that changes in coronary artery PVAT are tightly associated with pathological changes leading to myocardial infarction.[141,142] Indeed, multiple changes in the adipokine secretory profile and inflammatory cytokine expression in the coronary PVAT are associated with CAD or coronary arterial dysfunction.[143] These data highlight the role of PVAT in transducing metabolic dysfunction to vascular pathologies.

1.13 Adipose Tissue of the Heart: Epicardial and Pericardial depots

Other than that of the coronary vasculature, the adipose tissue of the heart is distinguished based on anatomic location into two layers: 1) the epicardial adipose tissue (EAT) and 2) the pericardial adipose tissue (PAT). Inconsistencies in the anatomic location of the EAT and PAT is prevalent in the literature; therefore, findings from different studies should be examined thoroughly to understand the specific depot assessed.[144,145] The EAT is a visceral fat depot localized between the

visceral pericardium and myocardium, whereas the PAT resides within the pericardial cavity on the outer surface of the parietal pericardium (**Figure 1.8A**).[146,147] Therefore, the PAT does not share physical proximity with the myocardium. In contrast, the EAT lies adjacent to the myocardium without structural boundary; therefore, these two layers share a common microcirculation,[146,148-150] allowing local modulation of both the myocardium and coronary vessels.[151,152] In contrast, the PAT is supplied by a branch of the internal thoracic artery termed the pericardiacophrenic artery.[153]

Anatomically, the EAT contributes to approximately 15% of cardiac mass in physiological conditions.[149] It is primarily located in the atrioventricular and interventricular grooves; however, as the amount of epicardial fat increases, it progressively expands to cover the ventricles and the epicardial surface in its entirety.[146] Interestingly, ventricular mass is positively correlated with EAT mass, and no such correlation exists with overall adiposity (BMI). Therefore, myocardial hypertrophy is a better predictor of EAT mass than both overweight and obesity.[149] However, studies also demonstrate the clinical association between EAT thickness or volume with metabolic syndrome and atherosclerosis.[144,154] Indeed, clinical imaging studies with echocardiography indicate that obesity predisposes the accumulation of epicardial fat; however, they concluded that fat distribution, specifically abdominal fat accumulation (determined by waist circumference), was a stronger correlate for the amount of epicardial fat.[155] Taken together, these studies indicate that fat distribution is the essential parameter, and increased waist circumference positively correlates with EAT deposition. The EAT and PAT also differ by embryologic origin and biochemical properties. The EAT originates from the splanchonopleuric mesoderm of the gut; therefore, it is of the same embryologic origin as mesenteric and omental adipocytes.[147] In contrast, the pericardial fat is derived from the primitive thoracic mesenchyme, which divides to form the parietal

pericardium and the external thoracic wall.[150] The EAT is a heterogeneous tissue consisting of adipocytes, nervous and nodal tissue and resident immune cells.[147,156]

The EAT is distinct from other fat depots with a smaller adipocyte size, high protein content, and higher rates of fatty acid incorporation and triglyceride synthesis.[157] Physiologically, the EAT maintains fatty acid homeostasis, acting as a local source of free fatty acids (FFA) and mediating their sequestration when levels escalate. As fatty acid (FA) oxidation meets 50-70% of the metabolic demand of the heart, the EAT may maintain the energy demand and incorporate excess FA to circumvent lipotoxicity.[158] In contrast, in advanced HF, this balance shifts towards a glycolytic and carbohydrate source of ATP production to limit oxygen consumption; thus, FA oxidation is significantly reduced.[159,160]

1.13.1 EAT Secretasome

The EAT is a source of bioactive molecules, including adiponectin, leptin, apelin and cytokines;[127,148,161] therefore, it plays a role in determining the inflammatory status of the surrounding myocardium in physiology and disease. As discussed previously, adiponectin inhibits platelet aggregation and macrophage activation and is responsible for insulin sensitivity, glucose uptake and lipid catabolism through its activation of AMPK.[162-164] On the other hand, leptin signaling in the cardiovascular system is associated with pro-angiogenic activity and the promotion of atherosclerotic lesions.[127,162] Apelin, a factor secreted by adipocytes, vascular stromal cells and the myocardium, confers cardioprotection, vasodilation, is anti-atherosclerotic, and improves cardiac metabolism in obesity-related HF.[127,162] Physiologically, a balance is sustained between harmful and protective factors; however, pathology denotes an alteration that favours inflammation.

1.13.2 EAT Facilitates and Potentiates Local Inflammation

Under physiological conditions, the EAT mediates positive effects, such as regulating FA homeostasis to circumvent lipotoxicity, serving as a fuel source for the myocardium, and secreting anti-inflammatory and anti-atherogenic adipokines.[147,154] However, as the metabolic profile shifts in obesity, the EAT secretasome is altered, and the EAT becomes pathogenic – shifting the adipokine balance toward an upregulated release of FA and proinflammatory cytokines (**Table 1.1**).[147,158] Indeed, resident immune cells of the adipose tissue demonstrate significant plasticity, allowing the transition from a protective to a detrimental phenotype. The context is essential as mast cells, macrophages and neutrophils can both potentiate inflammation or promote its resolution depending on the presence of extrinsic pathogens or danger signals.[165,166] As the EAT expands, extensive immune cells infiltrate and generate a proinflammatory microenvironment; a discovery that prompted the investigation of specific immune cells and cytokine profile of adipose tissue as key to metabolic inflammation.[147,166,167] Key alterations in cytokine and adipokine profile as a result of EAT inflammation are summarized in **Table 1.1**.[127,156,168-173]

The EAT harbours mast cells,[156] macrophages,[174] dendritic cells,[175] and lymphocytes[176] **(Figure 1.8B)**. Mazurek *et al.* characterized the presence of inflammatory cells in the EAT compared with subcutaneous fat. They identified the presence of T lymphocytes (CD3+), macrophages (CD68+) and mast cells (tryptase+) unique to EAT compared to subcutaneous adipose tissue. No cellular retention was observed in subcutaneous fat in these studies.[156] Further, the specific cytokine and chemokine profile was assessed from plasma and conditioned media of cultured adipose tissue from both subcutaneous and epicardial adipose tissue of patients with CAD. Protein and mRNA levels of IL-6, IL-1β, monocyte chemotactic protein-1 (MCP-1) and TNFα were significantly elevated in EAT.[156]

Table 1.1. Epicardial adipose tissue-derived bioactive molecules and alteration in conditions of chronic systemic inflammation including obesity, type 2 diabetes mellitus (T2DM), and heart failure with preserved ejection fraction (HFpEF).

Category	Factor	Alterations	Role	Expression	References
Cytokine	TNF-α	Increased	Proinflammatory	protein, mRNA	[155, 167, 168]
	MCP-1	Increased	Proinflammatory (chemoattractant)	protein, mRNA	[155]
	IL-1β	Increased	Proinflammatory	protein, mRNA	[155]
	IL-6	Increased	Proinflammatory (angiogenesis)	protein, mRNA, secretion	[155, 168, 169]
	IL-10	Decreased	Anti-inflammatory	protein, mRNA	[167]
	FGF-β	Decreased	Anti-inflammatory	mRNA	[170]
Adipokine	Adiponectin	Decreased	Anti-inflammatory	protein, mRNA	[168, 169, 171]
	Leptin	Increased	Proinflammatory	mRNA, secretion	[167, 168]
	Resistin	Increased	Proinflammatory	mRNA	[171]
	Visfatin	Increased	Proinflammatory	protein	[168]
	Apelin	Decreased	Cardioprotective, Anit-atherosclerotic	protein	[126, 172]

However, this study was limited to patients with CAD undergoing coronary bypass surgery; therefore, the physiological immune cells of healthy patients were not assessed.[156]

In a more recent study, the impact of macrophages on EAT inflammation has been investigated in CAD and non-CAD patients undergoing elective cardiac surgery. Macrophage polarization was examined by immunohistochemical staining of CD11c and CD206: two macrophage markers indicative of proinflammatory M1 phenotype and anti-inflammatory M2 phenotype, respectively.[177] CAD patients demonstrated an increased M1/M2 phenotype ratio compared to non-CAD. Further, this ratio was positively correlated with the severity of CAD.[177] A causal relationship was later demonstrated in murine experiments whereby the EAT M1/M2 macrophage ratio was increased in high-fat-fed mice compared to controls, further indicating a relationship between obesity and adipose tissue inflammation.[174]

1.14 EAT and cardiac dysfunction in metabolic disease

1.14.1 Obesity, Diabetes and EAT

The EAT is considered a transducer of local and systemic inflammation in obesity, exemplified as adiposity exacerbates chronic inflammatory conditions, including rheumatoid arthritis, psoriasis and multiple sclerosis.[178-180] This connection is bidirectional, as obesity, rheumatoid arthritis, psoriasis, and multiple sclerosis are associated with accelerated CAD and/or an increased risk of myocardial infarction.[181-183] Interestingly, EAT thickness and volume are also elevated in these patients and patients with other chronic inflammatory disorders, including inflammatory bowel disease.[184-186] The pathological shift in obesity and chronic inflammation highlights the intimacy between these two phenotypes.

Patients with T2DM are likely to have concomitant obesity and enhanced visceral adiposity with a marked increase of EAT thickness and are predisposed to develop HFpEF.[187,188] Although the association with enhanced EAT and systemic inflammation is likely the driving force, another risk factor may be the pharmacological treatment of T2DM. The side effect of weight gain accompanied with certain anti-hyperglycemic drugs have been associated with a higher incidence of HF in randomized clinical trials.[189] Insulin, for example, increases the amount of epicardial fat and is associated with an enhanced risk of HF.[188] In contrast, newer glucose-lowering medications such as dipeptidyl-peptidase-4 (DPP-4) inhibitors are also associated with an increased risk of HFpEF despite a neutral effect on adiposity.[189] Interestingly, DPP-4 inhibitors were reported to reduce EAT volume;[190] however, they may potentiate EAT inflammation.[188,191] Another class of incretin-based antidiabetics includes the glucagon-like peptide-1 (GLP-1) receptor antagonists. Although these drugs reduce EAT volume rapidly and substantially[192] and promote weight loss, they did not ameliorate EAT dysfunction;[193] thus, no improvements were observed for the rate of HF-related adverse events with GLP-1 receptor antagonists.[188,194,195]

1.14.2 HFpEF and EAT

HFpEF is characterized by LV diastolic dysfunction with retained systolic function and represents greater than 50% of heart failure patients.[196,197] HFpEF is associated with considerable morbidity and mortality and is increasing in prevalence despite recent advances in HF treatment.[198] In fact, clinical trials for patients with HFpEF have failed to meet their primary endpoints, limiting the availability of efficacious therapeutic approaches for HFpEF.[46] Impaired LV filling results from physical restriction from limited pericardial space or a result of fibrosis, which enhances LV stiffness, thus limiting the capacity to relax and fill.[199] Clinically, patients with HFpEF present

signs and symptoms of HF with preserved LV ejection fractions (≥50%), reduced cardiac output and impaired longitudinal strain.[200,201] HFpEF is frequently associated with comorbidities, including obesity and T2DM.[84,198] Multiple lines of evidence suggest proinflammatory adipocytokines released from EAT may contribute to the comorbidities observed with HFpEF, especially with obesity and T2DM. In obese patients, the accumulation of EAT is accompanied by diastolic filling abnormalities, enhanced vascular stiffness, and impaired coronary microcirculation.[202-205] Further, patients with concomitant obesity and HFpEF demonstrate increased EAT thickness with a cytokine profile shift to a proinflammatory state. Indeed, this inflammatory phenotype and diastolic filling irregularities precede the clinical diagnosis of HFpEF.[188] Therefore, as EAT expansion facilitates inflammation and fibrosis of the adjacent myocardium, this provides a mechanistic link between HFpEF related to obesity and T2DM, particularly given the close connection with weight gain and accumulation of EAT in these conditions.[127,158,188]

1.15 Adipose Tissue RAS

The adipose tissue possesses a local RAS with the machinery to produce and respond to effector angiotensin peptides. Specifically, human and rodent adipose tissue expresses angiotensinogen (AGT),[206,207] renin or renin-like activity,[207-209] ACE,[207,210] ACE2,[211-213] and angiotensin receptors (AT_1R and AT_2R) (**Figure 1.9**).[214,215] Moreover, studies in human adipose tissue demonstrated the expression of cathepsin D, which generates Ang I, and chymase and cathepsin G, which generate Ang II.[206,207] Although the roles of each enzyme in the adipose tissue RAS have yet to be established, administration of perindopril, an ACEi, did not inhibit the formation of Ang II

from rat periaortal adipose tissue, reinforcing that multiple enzymes contribute to adipose tissue-generated Ang II.[216]

Ang II has many biological consequences on the adipose tissue that have been extensively studied in the context of metabolic syndrome and obesity. In mouse models of obesity, AT_1R blockade reduced oxidative stress, inflammation, and the development of atherosclerosis in subcutaneous and visceral adipose tissue.[217,218] Caloric excess or genetic obesity increased local angiotensinogen (AGT) expression or production in adipose tissue in humans and rodents.[219-221] Moreover, *Agt* mRNA expression was 68% of that in the liver, the dominant AGT-producing organ, which further supports the role of adipose tissue as an alternative contributor in downstream Ang II production.[222] However, none of these studies investigated the systemic conversion of AGT to Ang II nor the release into the systemic circulation. The impact of adipocyte AGT on blood pressure regulation, thus a surrogate measure of Ang II production, was assessed in a study that harnessed a mouse model in which *Agt*-expression is restricted to adipose tissue, or *Agt* is overexpressed in adipose tissue.[223] Animals in which *Agt* expression is restricted to the adipose tissue had measurable plasma AGT, were normotensive, and recovered renal function compared to *Agt* knockout animals. In contrast, mice overexpressing *Agt* in adipocytes had higher circulating AGT and were hypertensive.[223] Thus, adipose tissue AGT was sufficient to compensate for the loss of hepatic production, and elevated adipocyte AGT induced a pressor response.

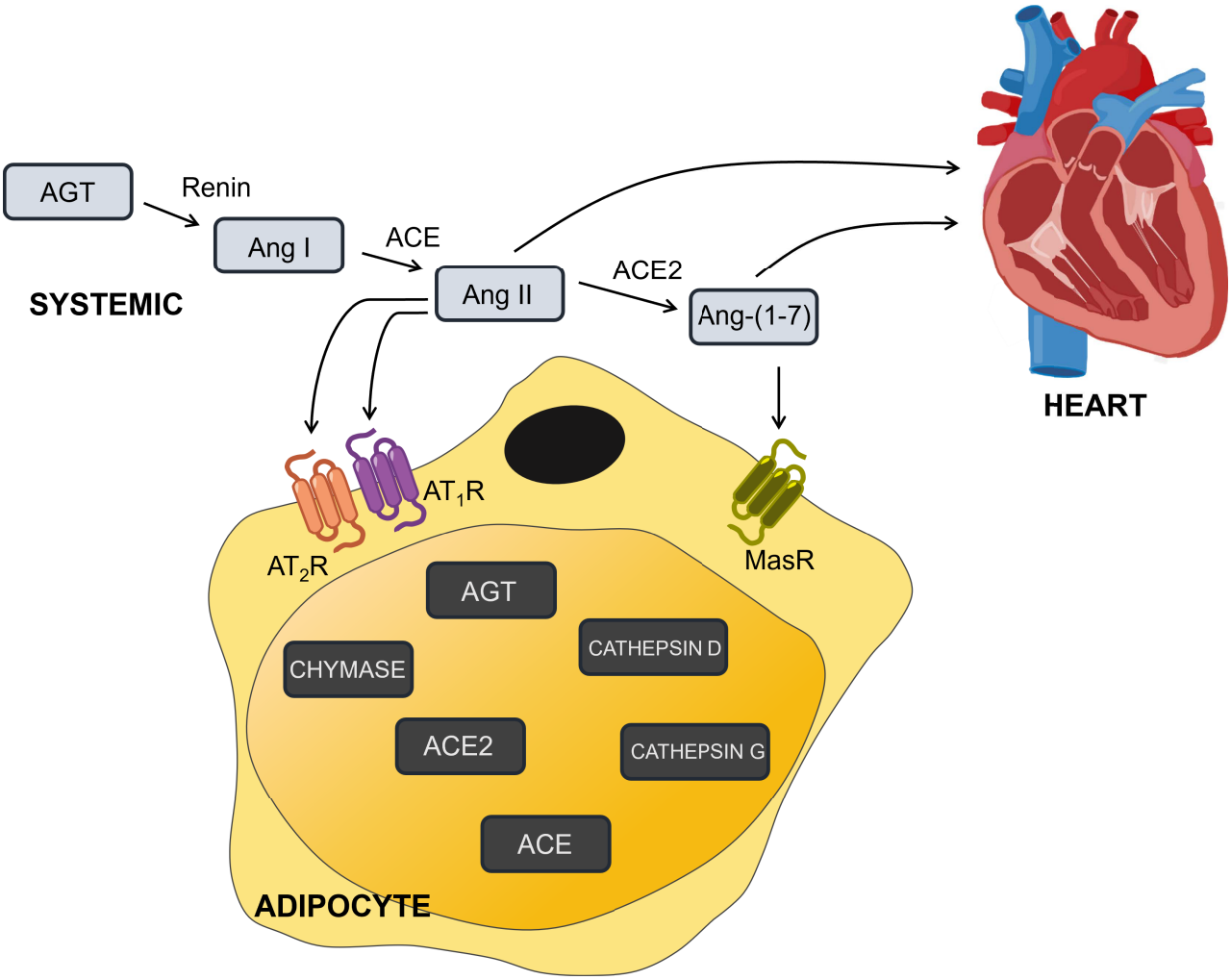

Figure 1.9. *Figure legend on next page*

Figure 1.9. The local RAS of the adipose tissue.

The classical RAS pathway occurs in the systemic circulation (light grey boxes); rather, the adipose tissue harbours a local tissue RAS that is proposed to affect the systemic system. The dark grey boxes within the adipocyte dictate mRNA expression of enzymes that can generate RAS peptides. The precursor angiotensinogen (AGT) is converted to Ang I by Renin in the systemic circulation. In the adipocyte, Cathepsin D and G are expressed, and may also mediate the conversion from AGT to Ang I, or directly to Ang II in the case of Cathepsin G. Ang I is then converted to Ang II by ACE, which is also expressed in the adipocyte. Chymase is an alternative enzyme that hydrolyzes Ang I to Ang II and is expressed in adipocytes. Ang II can act by a paracrine mechanism on the adipocyte, promoting lipogenesis and blocking lipolysis through actions on the AT_2R and AT_1R, respectively. Ang II can be deactivated by ACE2 to Ang-(1-7), reducing oxidating stress and improving glucose uptake in the adipocyte. It has been proposed that adipose tissue-generated Ang II and Ang 1-7 can act through autocrine and paracrine mechanisms within the adipose tissue. The implications of an adipose tissue RAS is the possibility to contribute to systemic RAS peptide levels and impact other organs, such as the heart.

Interestingly, the adipocyte-specific *Agt* expression and overexpression of *Agt* in adipocytes had a 1.5-fold and two-fold increase in adipose tissue mass, respectively.[223] Consistently, stimulation of 3T3-L1 preadipocytes and primary human adipocytes with Ang II increases lipogenesis and triglyceride accumulation,[224] and Ang II antagonism in rats reduced adipocyte size.[225] Moreover, genetic deletion of AGT,[226] the AT_2R,[227] or the AT_1R[228] in mice protected from diet-induced obesity.

Ang II promotes lipid storage and adipocyte hypertrophy by two mechanisms. Ang II acts on the AT_2R receptor to promote lipogenesis in human and murine adipocytes,[224] and murine *Agtr2* knockout exhibited lower adipose tissue glucose uptake following insulin stimulation.[227,229] On the other hand, Ang II is an antilipolytic hormone through its actions on the AT_1R in human primary adipocytes.[230-232] Overall, the downstream consequence of Ang II on adipocytes is adipocyte hypertrophy.[233] Alternatively, Ang II can be deactivated by ACE2 locally in the adipocytes to produce Ang-(1-7). In diabetes, Ang-(1-7) fosters favourable effects in the adipocyte, including suppressing oxidative stress, improving glucose uptake, and promoting insulin sensitivity.[234,235]

Limited research has investigated the local RAS in the adipose tissue of the heart and vasculature. Despite the reported expression of all RAS component proteins in PVAT,[236] there is a gap of knowledge regarding changes in the RAS activity localized to PVAT, as well as alterations in the status of ACE2 activity, Ang-(1-7) production, and Mas receptor function in metabolic disorders. Few studies examined the vascular consequences of PVAT-specific modulation of the RAS during inflammation. Interestingly, *in vitro* simulation of PVAT hypoxia in small arterioles led to a loss of its anti-contractile effect that recovered after exposure to ARBs.[237] Deletion of AT_1R in peri-aortic PVAT in mice reduced macrophage infiltration and aneurysm formation.[238] Significantly, a recent study demonstrated that PVAT-derived Ang-(1-7) contributed to its anti-

contractile effect under normal conditions through the Mas receptor-mediated activation of phosphoinositide 3-kinase (PI3K)/Akt pathway and subsequent increase in nitric oxide (NO) activity.[239] However, whether this was altered in conditions of PVAT inflammation was not examined.

In the EAT, fewer studies exist investigating the role of the local RAS. With human cardiac surgery as an acute stressor, *AGT* expression increases in the EAT but not in the subcutaneous adipose tissue.[240] Genetic loss of ACE2 in diet-induced obesity triggered adipocyte cell death, increased expression of proinflammatory cytokines (TNFα, IL-1β and IL-6), and an enhanced polarization towards proinflammatory macrophages.[174] However, *Ace2*-knockout was not adipose tissue-specific; therefore, the contribution of the EAT RAS towards this phenotype is unknown.

1.16 Hypothesis and Objectives

Maintaining tissue levels of ACE2 is critical for cardiovascular function and homeostasis.[5] A gap of knowledge exists in both delineating the regulation of ACE2 and in recognizing sex differences in ACE2 expression, protein levels and activity, all of which are critical for the understanding physiology and disease susceptibilities, such as that of heart failure (HF) and COVID-19. The epicardial adipose tissue (EAT) is a novel modulator of heart function and possesses its own tissue RAS.[240] As the EAT is contiguous with the myocardium without fascial separation and shares a common microcirculation,[148] understanding the influence of the EAT on the heart is of paramount importance.

Hypothesis: ACE2 is a double-edged sword in COVID-19, as increased ACE2 enhances susceptibility to severe disease in acute infection, yet SARS-CoV-2-mediated ACE2 downregulation is detrimental to the heart. As a critical cardioprotective enzyme, loss of ACE2 contributes to the pathogenesis of HF and EAT dysfunction.

Objectives:

1. To identify sex differences in ACE2 expression, protein levels and activity in physiology to inform COVID-19 susceptibility of older males
2. To study whether SARS-CoV-2 exhibits direct cardiac infection and its implications on ACE2 and myocardial inflammation
3. To explore the regulation of ACE2 in physiology and the pathophysiology of HF
4. To phenotype and assess ACE2 and the local RAS in the EAT of HF patients

Chapter 2

Materials and Methods

2.1 Materials

Protease and phosophotase inhibitor cocktail tablets were from Roche. Clarity™ Western ECL Substrate (#170-5060) and Detergent Compatible (*DC*™) Protein Assay kit (#500-0111) were purchased from Bio-Rad. All horseradish peroxidase-conjugated secondary antibodies were from Cell Signaling Technology (Denver, Massachusetts, United States). Trichrome Stain Kit (ab150686), and 3,3'Diaminobenzidine (DAB) Substrate Kit (ab64238) were purchased from Abcam (Cambridge, United Kingdom). Pierce® RIPA Lysis and Extraction Buffer (#89900) was purchased from Thermo Fisher Scientific (Montreal, Quebec, Canada). Immobilon® polyvinylidene fluoride (PVDF) membrane (IPVH00010), CelLytic™ MT Cell Lysis Reagent, Harris Modified Hematoxylin Solution (HHS32), and all chemicals were purchased from MilliporeSigma (Burlington, Massachusetts, United States).

2.2 Human Explanted Heart Protocol

Human explanted hearts were obtained following cardioplegic arrest according to the Human Organ Procurement and Exchange (HOPE) program protocol (healthy donors) or the Human Explanted Heart Program (HELP) protocol (failing hearts) and stored in the HELP biobank for future analysis (**Figure 2.1A**). All methods were approved by the Health Research Ethics Board of the University of Alberta. Transmural left ventricle specimens were procured from diseased (DCM or IHD) and aged matched donor hearts (NFC). For molecular analysis, the epicardial adipose tissue was carefully removed from the left ventricle (LV), avoiding the peri-coronary and peri-atrial adipose tissue.[241] For immunohistochemistry and histology, the epicardial adipose tissue was not removed from the contiguous LV. Tissues were flash-frozen in liquid nitrogen for molecular approaches, or formalin-fixed and paraffin embedded for histological staining.

2.2.1 Tissue Collection from Dilated Cardiomyopathy

Collection of hearts with dilated cardiomyopathy (DCM), or non-ischemic hearts, are collected based on anatomic location of different regions of the whole heart. First, the major branches of the coronary arteries are identified from the ostia within the ascending aorta above the aortic valve. The right coronary artery (RCA) is carefully dissected first, followed by the left anterior descending (LAD) and left circumflex (LCx) arteries. The leaflets of the aortic valve and aorta are also collected. Next, the left and right atria are removed, followed by the anterior and posterior right ventricle. Four samples in total were obtained from the left ventricle free wall: anterior basal, anterior middle, posterior basal, and posterior middle. The interventricular septum and apex are next removed. Finally, the mitral valve is removed. All samples are cut cross-sectionally and embedded in optimal cutting temperature compound (OCT), fixed in 10% neutral buffered formalin, and the remaining tissue flash frozen in liquid nitrogen (**Figure 2.1B-C**).

2.2.2 Tissue Collection from Ischemic Heart Disease

Cases with an ischemic cause of heart failure are collected based on the proximity to the infarct area for left ventricular specimens. As for the non-ischemic group, the major branches of the coronary arteries are first identified and collected, followed by the aorta and the aortic valve. The right and left atria, and anterior and posterior right ventricle are then collected. Informed by pre-transplant imaging studies and angiography, the location of the infarct area is visually identified upon collection. Samples from the infarct area (entirety fibrotic), peri-infarct (adjacent to the infarct), and the non-infarct or remote region (no proximity to the infarct) are captured. Finally, the interventricular septum, apex and mitral valve are then collected. Cross-sectional pieces of all regions are collected in OCT, 10% formalin, or flash-frozen in liquid nitrogen (**Figure 2.1B-C**).

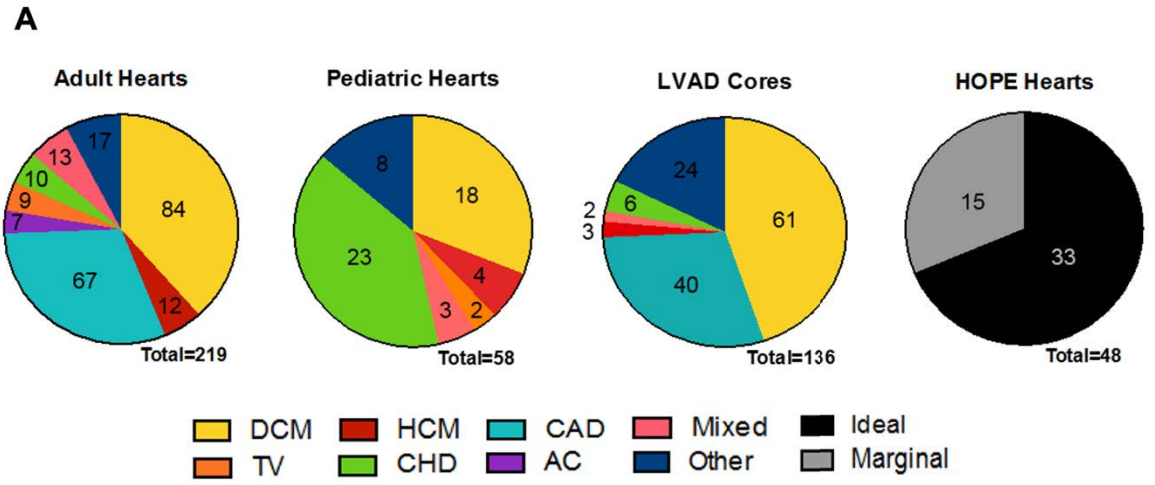

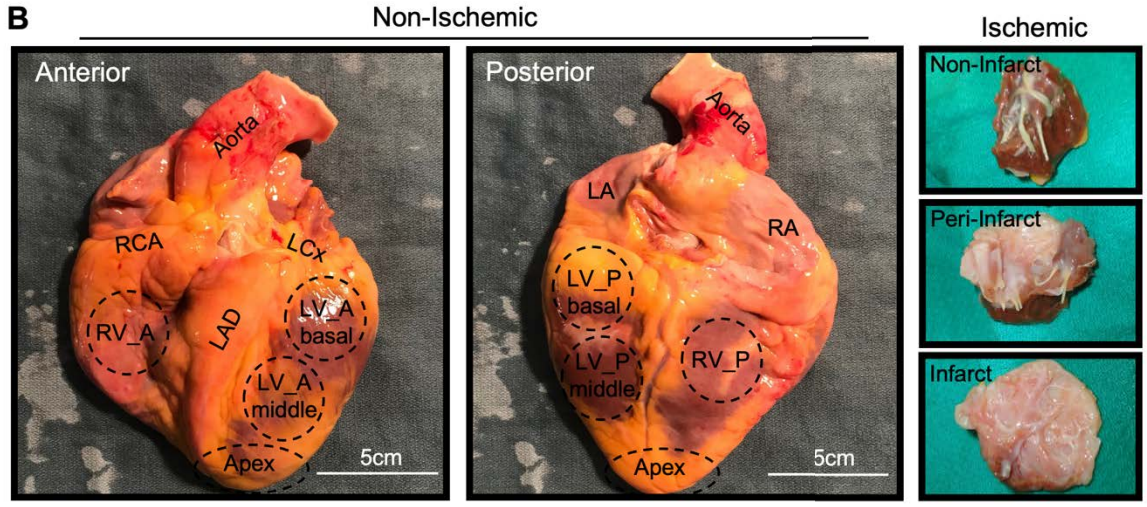

C

Non-Ischemic

Myocardium	RV	Anterior		Frozen 2xOCT Formalin EM
		Posterior		
	LV	Anterior	Basal	
			Middle	
		Posterior	Basal	
			Middle	
	Septum			
	Apex			

Ischemic

Myocardium	RV	Anterior	Frozen 2xOCT Formalin EM
		Posterior	
	LV*	Infarct	
		Peri-Infarct	
		Non-Infarct	
	Septum		
	Apex		

Non-Ischemic and Ischemic

Atria	RA	Free Wall	Frozen 2xOCT Formalin EM
	LA	Free Wall	
		Appendage	
Arteries	Large Vessels	Aorta	Frozen OCT Formalin
	Coronary Arteries	RCA	
		LAD	
		LCx	
Valves	Mitral Valve	Anterior	
		Posterior	
	Aortic Valve	NCC/RCC/LCC	
EAT	RV		
	LV		

Figure 2.1. *Figure legend on next page*

Figure 2.1. Schematic depiction of the collection and dissection of explanted human hearts by the Human Explanted Heart Program (HELP) protocol

A. Collection of explanted human hearts and apical core samples divided by etiology of heart disease. Mixed etiology describes patients that hold two or more heart disease diagnoses, and "other" describes rare collections that do not fall into the above categories (i.e. restrictive cardiomyopathy) **B.** Visual depiction of the systematic dissection of explanted human hearts. Non-ischemic collections, such as that for dilated cardiomyopathy, are acquired based on anatomic location. Rather, collections for ischemic heart disease are collected based on proximity to the infarct area **C.** Cross-sectional samples are obtained from each region of the heart and kept in one of three ways: flash-frozen in liquid nitrogen, embedded in optimal cutting temperature compound (OCT), or fixed in 10% neutral buffered formalin. Reproduced without modification from *Zhang, H., **Viveiros, A**., Nguyen, Q., Wang, K., Wang, W., Freed, D.H., Mullen, J.C., MacArthur, R., Kim, D.H., Tymchak, W., Sergi, C.M., Kassiri, Z., Wang, S., Oudit, G.Y. The Human Explanted Heart Program: A translational bridge for cardiovascular medicine. Biochimica et Biophysica Acta (BBA)-Molecular Basis of Disease. 1867: 165995 (2021).*

2.3 Hematoxylin and Eosin

Formalin-fixed paraffin embedded tissue were sectioned onto slides at 5 μm thickness. Hematoxylin and Eosin (H&E) staining was performed according to a standard protocol. Briefly, slides were de-waxed, and brought to distilled water by alcohol gradient. Nuclei were stained with Harris Hematoxylin for 15 seconds, rinsed, and differentiated with 1% acid alcohol. Bluing was achieved by rinsing in Scott's tap water substitute (20 mM Sodium Bicarbonate, 166 mM Magnesium Sulfate), then slides were stained with Eosin for two minutes. Slides were dehydrated, cleared and mounted. Imaging was performed with a Leica DM4000 B LED microscope system. Quantification of adipocyte size was performed using the Adiposoft plugin in ImageJ.

2.4 Trichrome Staining

Masson's trichrome staining was performed using a commercially available kit (Abcam). Deparrafinized and rehydrated slides were incubated in pre-heated Bouin's Fluid, cooled, and rinsed. Sections were stained in Weigert's iron hematoxylin working solution (equal parts of solutions A and B) and rinsed under tap water. Slides were then stained in Biebrich Scarlet/Acid Fuchsin solution and washed with distilled water. Slides were differentiated in Phosphomolybdic/Phosphotungstic acid solution until collagen was no longer red, then transferred directly to Aniline Blue solution. Slides were rinsed, then differentiated in 1% acetic acid. Slides were quickly dehydrated, cleared in xylene, and mounted with a resinous mounting medium. Images were captured with a Leica DM4000 B LED microscope system.

2.5 Immunohistochemical Staining

Immunohistochemical (IHC) staining was performed on formalin-fixed paraffin embedded tissues. Tissues were sectioned onto slides at 5 μm thickness, de-waxed, and rehydrated by ethanol gradient. Heat induced epitope retrieval was performed with sodium citrate buffer (10 mM Sodium Citrate, 0.05% Tween 20, pH 6.0). Slides were cooled to ambient temperature then blocked with 10% goat serum in 1% bovine serum albumin (BSA) for one hour. The blocking buffer was removed, and slides incubated with primary antibody diluted in 1% BSA. Endogenous peroxidases were blocked with 10% H_2O_2 for 10 minutes, then slides were incubated with HRP-conjugated secondary antibodies (Cell Signaling Technology). Positive staining was visualized with freshly prepared DAB (3,3'Diaminobenzidine) substrate (Abcam) for 10 minutes. Slides were counterstained with regressive Harris Hematoxylin for 15 seconds and differentiated with 1% acid alcohol. Slides were dehydrated by washing step-wise with increasing concentrations of ethanol, cleared, and mounted with organic mounting medium. Positive staining was visualized as brown precipitates. Imaging was performed with a Leica DM4000 B LED microscope system, or the Leica Aperio ScanScope CS.

2.6 Picrosirius Red (PSR) Staining

Formalin-fixed paraffin embedded slides were cut at 5 μm thickness and warmed for 15 minutes in a 65 oven to melt the wax. Dewaxing was achieved with xylene, and slides rehydrated by ethanol gradient. Slides were incubated in PMA (0.2% Phosphomolybdic Acid in ddH_2O) in the dark for 30 minutes. The slides were transferred to the Picrosirius Red (PSR) solution (0.01% Sirius red in Picric Acid) for one hour. Slides were washed in acidified water (0.05% acetic acid

in ddH_2O) and dehydrated, cleared, and mounted with organic mounting media. Images were captured with a Leica DM4000 B LED microscope system.

2.7 Fresh-Frozen Immunofluorescent Staining

Immunofluorescent staining was performed on OCT-embedded samples for the left ventricle. Fresh-frozen, OCT-embedded tissues were sectioned onto slides at 5 µm thickness and air dried for five minutes at ambient temperature. Slides were fixed in 4% paraformaldehyde for 20 minutes, then washed three times with phosphate-buffered saline (PBS) (137 mM NaCl, 2.7 mM KCl, 10 mM Na_2HPO_4, 1.8 mM KH_2PO_4, 1 mM $CaCl_2$, 0.5 mM $MgCl_2$). Tissues were permeabilized by incubation with 0.1% Triton-X100 in PBS for five minutes, then washed with PBS again three times for five minutes each. TrueBlack® Lipofuscin Autofluorescence Quencher (#23007) (Biotium; Fremont, California, United States) was freshly diluted to 1X in 70% ethanol and applied to the tissue for 30 seconds. The solution was removed by washing in PBS three times for five minutes each. Slides were blocked in 4% BSA for one hour at ambient temperature, then incubated with primary antibody at 4˚C. Next, the primary antibody was washed off with three changes of PBS for five minutes each, and the slides incubated in the dark with fluorophore-conjugated secondary antibodies (Invitrogen; Waltham, Massachusetts, United States) diluted in 2% BSA at 1:1000. The slides were washed in three changes of PBS for five minutes each then incubated in the dark with Wheat Germ Agglutinin (WGA) conjugated to Alexa Fluor™ 488 (W11261) or to Alexa Fluor™ 350 (W11263) (Invitrogen; Waltham, Massachusetts, United States) at 1:100 in 2% BSA for thirty minutes. The slides were washed with three changes of PBS for five minutes each, then mounted with Prolong™ Gold Antifade mountant containing DAPI (P36931) (Thermo Fisher Scientific; Montreal, Quebec, Canada).

Slides were imaged with the Olympus IX81 inverted fluorescent microscope. Cardiomyocyte cross-sectional area was quantified with ImageJ using WGA-stained sections.

2.8 Formalin-Fixed Paraffin Embedded (FFPE) Immunofluorescent Staining

Immunohistochemical (IHC) staining was performed on formalin-fixed paraffin embedded tissues (FFPE) for the epicardial adipose tissue. Tissues were sectioned onto slides at 5 μm thickness, de-waxed, and rehydrated by ethanol gradient. Heat induced epitope retrieval was performed with sodium citrate buffer (10 mM Sodium Citrate, 0.05% Tween 20, pH 6.0), then the slides were cooled to ambient temperature. Following two washes with 0.025% Triton-X100 diluted in PBS, the slides were incubated for 30 seconds in freshly prepared TrueBlack® Lipofuscin Autofluorescence Quencher (#23007) (Biotium; Fremont, California, United States) diluted in 70% ethanol. The slides were washed with PBS and blocked in 4% BSA for one hour at ambient temperature, then incubated with primary antibodies for Perilipin-1 (Abcam, ab3526), and cardiac Troponin T (MA5-12960, Invitrogen) at 4˚C. Next, the slides were washed in three changes of PBS for five minutes each and incubated in the dark with fluorophore-conjugated secondary antibodies (Invitrogen; Waltham, Massachusetts, United States) diluted in 2% BSA at 1:1000. The slides were washed in three changes of PBS for five minutes each then incubated in the dark with Wheat Germ Agglutinin (WGA) conjugated to Alexa Fluor™ 488 (W11261) (Invitrogen; Waltham, Massachusetts, United States) at 1:100 in 2% BSA for thirty minutes. The slides were washed with three changes of PBS for five minutes each, then mounted with Prolong™ Gold Antifade mountant containing DAPI (P36931) (Thermo Fisher Scientific; Montreal, Quebec, Canada). The slides were imaged using a Leica SP5 laser scanning confocal microscope.

2.9 Immunoblot Analysis

Transmural left ventricle samples were cut for immunoblot analysis. Approximately 60 mg of tissue was placed in a 2 mL round bottom tube with 300 µL 1×RIPA buffer (140 mM NaCl, 20 mM Tris, 1% SDS, 0.1% NP40, 0.5% Sodium deoxycholine, pH 7.4) with protease and phosphatase inhibitor cocktail (Roche). Samples were pulverized with the TissueLyser II (Qiagen; Hilden, Germany) following the addition of a 5 mm metal bead to the tube for two rounds of three minutes at 25 Hz. Homogenized tissue samples were incubated on ice for one hour and vortexed every 15 minutes. Lysates were cleared by centrifugation at 14,000 × *g* for 15 minutes and protein quantified using the *DC*™ protein assay kit. Lysates were normalized to achieve the same amount of protein in each sample prior to western blot analysis (40-80 µg). Normalized samples were denatured with 4× sample buffer (60 mM Tris, 25% glycerol, 2% SDS, 5% 2-mercaptoethanol, 0.1% bromophenol blue pH 6.8) and boiled for five minutes prior to loading and running gels. Proteins were resolved by SDS-PAGE with 10% polyacrylamide gels containing 0.1% SDS. Gels were transferred to PVDF membranes overnight at 4°C in transfer buffer (25 mM Tris, 192 mM glycine and 20% methanol, (pH 8.3)). Membranes were washed three times with TBS (200 mM Tris, 1.37 M NaCl, pH 7.4) containing 0.1% Tween 20 (TTBS) then blocked for one hour in TTBS containing 5% non-fat milk (blocking buffer). Membranes were incubated with primary antibodies diluted in TTBS containing 5% bovine serum albumin (BSA) overnight at 4°C.

Table 2.1. Source and dilutions of antibodies used in experiments.

Antibody	Supplier	Catalogue #	Host	Reactivity	Dilution	Purpose (Chapter)
ACE2	Abcam	ab108252	Rabbit	Human	1:1000	WB (**3-6**)
ACE2	R&D Systems	AF933	Goat	Human, Hamster	1:50	Staining (**3,4**)
ADAM17/ TACE	Santa Cruz Biotechnology	sc-390859	Mouse	Human	1:1000	WB (**5**)
cTnT	Thermo Fisher Scientific	MA5-12960	Mouse	Human	1:200	Staining (**6**)
CD4	Millipore Sigma	MABF415	Rat	(Hamster)	1:50	Staining (**4**)
CD4	Abcam	ab133616	Rabbit	Human	1:100	Staining (**4**)
CD8	Biolegend	200702	Mouse	(Human), (Hamster)	1:50	Staining (**4**)
CD15	Abcam	ab135377	Rabbit	Human, (Hamster)	1:50	Staining (**4**)
CD68	AbD Serotec	MCA1957	Rat	(Hamster)	1:100	Staining (**4**)
CD68	ThermoFisher Scientific	MA5-13324	Mouse	Human	1:100	Staining (**4**)
p-ERK	Cell Signaling Technology	9101	Rabbit	Human	1:1000	WB (**6**)
ERK	Cell Signaling Technology	9102	Rabbit	Human	1:1000	WB (**6**)
p-JNK	Cell Signaling Technology	4668	Rabbit	Human	1:1000	WB (**6**)
JNK	Cell Signaling Technology	9252	Rabbit	Human	1:1000	WB (**6**)
NG2	Abcam	ab129051	Rabbit	Mouse, Human	1:50	Staining (**3**)
Nucleocapsid	Bioss	bs-41408R	Rabbit	SARS-CoV-2 Virus	1:1000	Staining (**4**)
Perilipin-1	Abcam	ab3526	Rabbit	Human	1:50	Staining (**6**)
p-p38	Cell Signaling Technology	4511	Rabbit	Human	1:1000	WB (**6**)
p38	Cell Signaling Technology	9212	Rabbit	Human	1:1000	WB (**6**)
TMPRSS2	Abcam	ab92323	Rabbit	Mouse	1:1000	WB (**3**)

Antibodies used for Western blot are indicated (WB). Antibodies used for staining represents either IF, IHC-Fr, and IHC-P. Please refer to the specific chapter for more information on the staining protocol employed. Reactivity in brackets indicates that the antibody was not tested for this application by the company, rather we tested this antibody for its specificity in house. The chapter each antibody was used for is indicated in brackets in the final column.

The following day, membranes were washed twice with TBS, twice with TTBS and twice again with TBS followed by a one-hour incubation with secondary antibody (1:2000 in blocking buffer, Cell Signaling Technology) at ambient temperature with gentle agitation. Membranes were washed again two times for five minutes with TBS, TTBS and TBS respectively. Immunoreactivity was detected with Clarity™ Western ECL Substrate (Bio-Rad) and visualized with ImageQuant LAS 4000 (GE Healthcare; Chicago, Illinois, United States). Signal was normalized to MemCode reversible total protein stain (Thermo Fisher Scientific; Montreal, Quebec, Canada). Band densitometry was quantified with Image Studio Software (LI-COR Biosciences; Lincoln, Nebraska, United States).

2.10 ACE2 Activity Assay

ACE2 activity assays were performed as previously described with modification for tissue analysis.[242] Briefly, 150 µg of LV tissue lysates were diluted in 1× Assay buffer (75mM Tris, 5mM $ZnCl_2$, 1M NaCl, pH 6.5) with EDTA-free protease inhibitors, 10µM captopril and 5µM amastatin. Specificity was assessed by incubating samples in the presence and absence of ACE2 inhibitor 30 µM DX-600 (Cayman Chemical Company, Ann Arbor, Michigan, United States) for thirty minutes. Fluorogenic Peptide Substrate VI (ES007, R&D Systems) was subsequently added (final concentration of 50 µM in Assay buffer), and kinetic measurements obtained immediately following (350/405nm). Fluorogenic standards (R&D Systems) were run in parallel to generate a conversion factor (pmol/RFU) to calculate the specific activity of ACE2.

2.11 ADAM17 Activity Assay

ADAM17 activity assays were performed as previously described.[41] Briefly, 150 µg of LV tissues were diluted in 1×Assay buffer (25 mM Tris, 2.5 mM $ZnCl_2$, 0.005% Brij-35 (w/v), pH 9.0) with EDTA-free protease inhibitors. Specificity was assessed by incubating samples in the presence and absence of 200 nM TAPI-2 (Cayman Chemical Company, Ann Arbor, Michigan, United States) for thirty minutes. Fluorogenic Peptide Substrate VI (ES003, R&D Systems) was subsequently added (final concentration of 20 µM in Assay buffer), and kinetic measurements obtained immediately following (350/405nm). Fluorogenic standards (R&D Systems) were run in parallel to generate a conversion factor (pmol/RFU) to calculate the specific activity of ADAM17.

2.12 RNA Extraction

RNA was isolated from the left ventricle using a TRIzol®-chloroform based extraction method. Briefly, 1 mL of ice cold TRIzol® was added to a 60 mg piece of transmural left ventricle tissue in a 2.0 mL round bottom Eppendorf tube. A 5mm metal bead was carefully added, and the tissue homogenized at 25 Hz twice for three minutes. Samples were left at ambient temperature for five minutes, then centrifuged at 12,000 × *g* for ten minutes at 4˚C. The resulting supernatant was transferred to a 1.5 mL Eppendorf tube and 200 µL of chloroform was added. The tubes were shaken vigorously by hand for fifteen seconds, then incubated at ambient temperature for three minutes. The tubes were then centrifuged at 12,000 × *g* for ten minutes at 4˚C and the upper colourless phase was carefully transferred to a new 1.5 mL Eppendorf tube. 500 µL of isopropanol was then added with the tubes inverted several times for thorough mixing. The samples were incubated for 48 hours at -20˚C for RNA extraction. Next, the samples were centrifuged at 12,000 × *g* for ten minutes at 4˚C, the supernatant discarded, and pellet gently

resuspended in 1 mL of 75% ethanol. The samples were centrifuged at 7,500 × *g* for ten minutes at 4˚C. The supernatant was removed, and pellets air dried for 5-10 minutes until solvent was no longer present. The RNA was dissolved in 2 µL of RNase-free water.

2.13 TaqMan RT-PCR

Complementary DNA (cDNA) was reverse transcribed from 1µg of RNA template using SuperScript® II Reverse Transcriptase from Invitrogen (Thermo Fisher Scientific; Montreal, QC, Canada). Real-time quantitative polymerase chain reaction (RT-PCR) with TaqMan premixed assays (Thermo Fisher Scientific; Montreal, QC, Canada) and 2.5 ng of cDNA was used to quantify genes of interest, unless otherwise stated. 18S (Mm04277571_s1) or hypoxanthine-guanine phosphoribosyltransferase (HPRT) (Cg04448432_m1) were quantified as housekeeping genes.

2.14 MicroRNA (miRNA) RT-PCR

Total RNA from 60 mg of LV samples were extracted using the mirVana™ miRNA Isolation Kit (AM1560, Invitrogen) according to the manufacturer's protocol for the preservation of small RNA. Reverse transcription was performed using the TaqMan™ MicroRNA Reverse Transcription kit (4366597, Applied Biosystems™) and the 5x RT stem loop primers for the miRNA specific assays, according to the manufacturer's instructions. RT-PCR was performed using the TaqMan™ MicroRNA specific assays for miR-421 (hsa-miR-421, Assay ID 002700), miR-125a-5p (hsa-miR-125a-5p, Assay ID 002198), and miR-200c (has-miR-200c, Assay ID 002300), and miR-191 (hsa-miR-191, Assay ID 002299) as a housekeeping control. The miRNA RT-PCR was performed using the TaqMan™ Universal Master Mix II without UNG (4440040,

Applied Biosystems™) combined with the TaqMan™ miRNA specific premixed assays. 0.67 µL of cDNA template was loaded into a 384-well white PCR plate for a total RT reaction volume of 10 µL. The plate was sealed with optical adhesive film, centrifuged briefly to bring the reaction mix to the bottom of the wells, and loaded into the LightCycler® 480 (Roche Holding AG; Basel, Switzerland).

2.15 Single-nucleus RNA Sequencing (snRNA Seq)

2.15.1 Sample preparation and nuclei extraction

The epicardial adipose tissue (EAT) was carefully removed from the flash-frozen left ventricle free wall into an individual 1.5 mL cryogenic vial. A transmural sample of the contiguous left ventricle tissue was also separated into another 1.5 mL cryogenic vial. Samples were sent to Boston for subsequent analysis. Nuclei isolation and library preparation were performed at the Harvard Medical School, as previously described.[243-245] Briefly, a transmural left ventricle tissue specimen of approximately 100 mg was removed from the -80˚C immediately onto ice. The tissue was homogenized in 1 mL homogenization buffer (1× NIM2, 40 U/µL RNaseI, 20 U/µL SuperaseI, 10% Triton X-100) containing 10× Nuclei Isolation buffer 2 (NIM2) (1.5 M sucrose, 2 M KCl, 1 M MgCl, 1 M Tris-HCl, 1mM DTT, pH 8) with protease inhibitors. Samples were homogenized in the Qiagen TissueLyser II for one minute at 25 Hz and allowed to lyse on ice for five minutes. The tissue was then filtered through 40-µm cell strainer into a 50 mL falcon tube. The samples were centrifuged for five minutes at 500 × *g* to pellet the nuclei. The nuclei were resuspended in 500 µL storage buffer (1× PBS, 4% BSA, 40 U/µL RNaseI) and filtered through a 35 µm filter. The purity of extracted nuclei was then assessed by flow cytometry. Two drops of NucBlue™ live cell stain (Thermo Fisher Scientific; Montreal, Quebec, Canada) was added to

the filtered solution, vortexed for five seconds, and incubated on ice for 15 minutes. Nuclei were sorted by Fluorescence Activated Cell Sorting (FACS) into a new 1.5 mL Eppendorf tube containing 150 µL of storage buffer using the BD FACSAria II instrument. A negative control of unstained nuclei was analyzed in parallel to set parameters. Following sorting, the samples were centrifuged at 500 × *g* for five minutes at 4˚C and the supernatant removed without disturbing the nuclei-containing pellet.

2.15.2 Library preparation using the 10X genomics platform and sequencing

The 3' gene expression libraries were prepared using the v3 Chromium Single Cell Reagent Kits (10X Genomics; Pleasanton, California, United States), according to the manufacturer's instructions. The final cDNA library was subject to quality control using Bioanalyzer High Sensitivity DNA Analysis (Agilent Technologies; Santa Clara, California, United States) and the KAPA Library Quantification kit. Libraries were sequenced on an Illumina HighSeq 4000 or NovaSeq with a read number target of 30,000-50,000 reads per nucleus.

2.16 Genotyping

The genomic DNA from patient samples was extracted from frozen left ventricle tissue using the Genomic DNA Extraction Kit (Qiagen; Hilden, Germany). Following exome enrichment, Whole Exome Sequencing (WES) was performed on the Illumina NovaSeq 6000 system. The genomic DNA of patients who were not identified to have a pathogenic variant on WES was further subject to Whole genome sequencing (WGS) on the Illumina HiSeq instrument. For WES, sequencing reads were mapped to the human reference genome hg19/CRCh37 and for WGS to hg38/CRCh38 using the BWA-MEM aligner (BWA v0.7.15).[246] Single nucleotide variants and

small insertions or deletions (indels) were identified using the Genome Analysis Tool Kit (GATK) Haplotype Caller tool[247], and filtered for high quality variants. Criteria for high quality variants includes passing GATK, Variant Score Quality Recalibration (VSQR) with a truth sensitivity threshold of 99.5 for single nucleotide variants, and 99.0 for indels, a minimum depth of 10, and genotype quality of ≥ 20. The data were further filtered for protein-altering variants and annotated as pathogenic or likely pathogenic on ClinVar.[248]

2.17 Quantification of Hydroxyproline Content

Hydroxyproline is a modified amino acid selectively incorporated into collagen which facilitates its structure and stability.[249] Hydroxyproline quantification as a surrogate measure of the collagen content was assayed as previously described,[250] with some modifications for the analysis of the epicardial adipose tissue. 120 mg of EAT was lyophilized for 24 hours with the FreeZone 2.5 L -50˚C Benchtop Freeze Dryer (Labconco Corporation; Kansas City, Missouri, United States) run on auto mode. 300 µL of 6 M HCl was added to the tissue and hydrolyzed at 110˚C for 16 hours in a heat compatible tube. The acid was then neutralized with 300 µL of 6 M NaOH and centrifuged at 14,000 × *g* for fifteen minutes. A serial dilution of 4-hydroxy-L-proline at concentrations of 1.25 µg/mL – 80 µg/mL was created to create the standard curve. 500 µL of the collagen fractions and standards were removed into a new 1.5 mL Eppendorf tube and 250 µL of chloramine T solution (1.4% (w/v) chloramine T dissolved in 0.2 citrate acetate buffer (5% citric acid, 1.2% glacial acetic acid, 12% sodium acetate trihydrate, pH 6.5) with 10% n-propanol) was added and incubated for 20 minutes at ambient temperature to oxidize the hydroxyproline. 250 µL of Ehrlich reagent was added (3.75% (w/v) 4-(Dimethylamino)benzaldehyde in 60% n-propanol and 24% perchloric acid) and heated at 60˚C

for 20 minutes to neutralize the chloroamine T. The samples were loaded into a clear-bottom 96 well plate. The absorbance was measured at 550 nm using the SpectraMax iD5 Multi-Mode microplate reader (Molecular Devices; San Jose, California, United States).

2.18 Removal of Excess Lipids (RELi) Protein Extraction

Proteins were extracted from the epicardial adipose tissue using the Removal of Excess Lipids (RELi) method with minor modifications.[251] Briefly, 120 mg of epicardial adipose tissue was carefully removed from the flash-frozen left ventricle free wall and placed in a 2.0 mL round bottom Eppendorf tube. 300 μL of RIPA buffer containing protease and phosphatase inhibitors was added to tube, along with a 5 mm metal bead and the tissue subject to two rounds of homogenization at 25 Hz for three minutes using the Qiagen TissueLyser II. The samples were incubated for a minimum of one hour on ice, then centrifuged at 20,000 × *g* for 15 minutes at 4˚C. The interphase was carefully separated from the tube while avoiding the top solidified lipid cap and pellet. The extraction was repeated an additional two times to adequately deplete the resulting sample of excess lipids. Protein was then quantified in the lysate using the *DC*™ assay (Bio-Rad; Hercules, California, United States), and subject to immunoblot analysis for ACE2 (Abcam, ab108209); TACE/ADAM17 (B6) (Santa Cruz, sc-390859), phospho-p38 MAPK (Thr180/Tyr182) (3D7) (Cell Signaling Technology, #9215); p38 MAPK (Cell Signaling Technology, 9212); phospho-p44/42 MAPK (Erk1/2) (Thr202/Tyr204) (Cell Signaling Technology, #9101); p44/42 MAPK (Erk1/2) (Cell Signaling Technology, #9102); Phospho-SAPK/JNK (Thr183/Tyr185) (81E11) (Cell Signaling Technology, #4668), and SAPK/JNK (Cell Signaling Technology, #9252).

2.19 Multiplex Cytokine Assay

2.19.1 Sample preparation and Data Acquisition

Protein was extracted from EAT samples and normalized to a concentration of 2.5 µg/mL and analyzed by Eve Technologies Corp. (Calgary, Alberta, Canada). For the study, the Luminex xMAP technology was used for multiplexed quantification of eighty-nine Human cytokines, chemokines, and growth factors in three separate assays performed according to the manufacturer's protocol. The multiplexing analysis was performed using the Luminex™ 200 system (Luminex; Austin, Texas, United States).

Seventy-one markers were measured simultaneously in the samples using Eve Technologies' Human Cytokine 71-Plex Discovery Assay® comprised of two separate kits: one 48-plex (HD48; #HCYTA-60K) and one 23-plex (HD23; #HCYP2MAB-62K) (MilliporeSigma, Burlington, Massachusetts, USA). The 48-plex consisted of sCD40L, EGF, Eotaxin, FGF-2, FLT-3 Ligand, Fractalkine, G-CSF, GM-CSF, GROα, IFN-α2, IFN-γ, IL-1α, IL-1β, IL-1RA, IL-2, IL-3, IL-4, IL-5, IL-6, IL-7, IL-8, IL-9, IL-10, IL-12(p40), IL-12(p70), IL-13, IL-15, IL-17A, IL-17E/IL-25, IL-17F, IL-18, IL-22, IL-27, IP-10, MCP-1, MCP-3, M-CSF, MDC, MIG/CXCL9, MIP-1α, MIP-1β, PDGF-AA, PDGF-AB/BB, RANTES, TGFα, TNF-α, TNF-β, and VEGF-A. The 23-plex consisted of 6CKine, BCA-1, CTACK, ENA-78, Eotaxin-2, Eotaxin-3, I-309, IL-16, IL-20, IL-21, IL-23, IL-28A, IL-33, LIF, MCP-2, MCP-4, MIP-1δ, SCF, SDF-1α+β, TARC, TPO, TRAIL, and TSLP. Assay sensitivities of these markers range from 0.14 – 55.8 pg/mL for the 71-plex. Individual analyte sensitivity values are available in the MILLIPLEX® MAP protocol. Samples were run undiluted.

Thirteen markers were simultaneously measured in the samples using Eve Technologies' Human MMP/TIMP 13-Plex Discovery Assay® which consists of two separate kits: one 9-plex

and one 4-plex (R&D Systems, Inc., Minneapolis, Minnesota, United States). The 9-plex consisted of MMP-1, MMP-2, MMP-3, MMP-7, MMP-8, MMP-9, MMP-10, MMP-12 and MMP-13. The 4-Plex consisted of TIMP1, TIMP2, TIMP3 and TIMP4. Assay sensitivities of these markers range from 0.28 – 253 pg/mL for the 13-plex. Individual analyte sensitivity values are available in the product datasheet for the 4-Plex and by building the panel on the R&D Systems Magnetic Luminex Performance product page for the 9-Plex. Samples were run undiluted.

Five markers were simultaneously measured in the samples using Eve Technologies' Human Adipokine 5-Plex Discovery Assay® (HDADK5) (MilliporeSigma; Burlington, Massachusetts, United States). The 5-plex consisted of Adiponectin, Adipsin, Lipocalin-2/NGAL, Resistin, PAI-1(total). Assay sensitivities of these markers range from 1.7 – 11 pg/mL for the 5-plex. Individual analyte sensitivity values are available in the MilliporeSigma MILLIPLEX® MAP protocol. Samples were diluted 50× for this panel.

2.19.2 Data visualization

Data visualization by Heatmap and Principal Component Analysis (PCA) for the analyte profile was performed using MetaboAnalyst 5.0 software.[252] The heatmap was constructed on the normalized data with feature autoscaling, Euclidean distance measuring, and Ward's linkage clustering method. Both samples and features (cytokines) were clustered. The top fifty features were displayed for the comparisons (DCM and NFC; IHD and NFC).

2.19.3 Network analysis and pathway enrichment

To identify the biological relationship between upregulated molecules between two groups, the proteins were mapped using the open-source search tool, Search Tool for the Retrieval of Interacting Genes/Proteins (STRING, V11.0; https://string-db.org/) that provides a schematic delineating the interaction between proteins. We analyzed major upregulated effector molecules and their biological pathways within cells using Kyoto Encyclopedia of Genes and Genomes (KEGG). Term description describes the annotated pathways that are upregulated. Observed gene count refers to the genes (of the corresponding proteins) input in the pathway analysis that contribute to the terms. Background gene count refers to the total number of genes within the pathway. Strength refers to how large the enrichment effect is compared to other pathways (Log10(observed/expected)). It denotes a ratio between i) the number of proteins in the network annotated with a term and ii) the number of proteins expected to be annotated with the term in a random network of the same size. The false discovery rate (FDR) describes the significance of enrichment corrected for multiple testing using the Benjamini-Hochberg method.

We further analyzed the protein-protein interaction network by enriching these proteins using Gene Ontology (GO), a bioinformatics classification database. GO annotates genes or proteins into predicted biological processes, molecular functions, and cellular components. GO pathway enrichment was performed with g:Profiler.[253] Observed gene count refers to the genes (of the corresponding proteins) input in the pathway analysis that contribute to the terms. Background gene count refers to the total number of genes within the pathway. Strength refers to how large the enrichment effect is compared to other pathways (Log10(observed/expected)). It denotes a ratio between i) the number of proteins in the network annotated with a term and ii) the number of proteins expected to be annotated with the term in a random network of the same size.

The false discovery rate (FDR) describes the significance of enrichment corrected for multiple testing using the Benjamini-Hochberg method.

2.20 Statistics

Statistics were performed in Graphpad Prism version 9.5.0. Paired analyses were performed with paired t-test. With multiple comparisons, one-way ANOVA was applied with Tukey multiple comparisons *post hoc* test. With multiple comparisons comparing to a control group, one-way ANOVA was applied with Dunnet multiple comparisons *post hoc* test. For multiple comparisons with multiple variables, two-way ANOVA was applied with Tukey *post hoc* test. In data with high variability, an unbiased method of outlier elimination was performed using the ROUT method with Q=0.1%. Statistical significance was determined at *$p<0.05$, **$p<0.01$, ***$p<0.001$ and ****$p<0.0001$.

Chapter 3

Sex- and Age-Specific Regulation of ACE2: Insights into Severe COVID-19 Susceptibility

Sex- and Age-Specific Regulation of ACE2: Insights into Severe COVID-19 Susceptibility

Anissa Viveiros[1,2], Mahmoud Gheblawi[1], Preetinder K. Aujla[1], Deanna K. Sosnowski[3], John M. Seubert[3,4], Zamaneh Kassiri[1], and Gavin Y. Oudit[2,5*]

[1]Department of Physiology, Faculty of Medicine and Dentistry, University of Alberta, Edmonton, Alberta, Canada
[2]Mazankowski Alberta Heart Institute, University of Alberta, Edmonton, Alberta, Canada
[3] Faculty of Pharmacy and Pharmaceutical Sciences, University of Alberta, Edmonton, Alberta, Canada
[4]Department of Pharmacology, Faculty of Medicine and Dentistry, University of Alberta, Edmonton, Alberta, Canada
[5]Division of Cardiology, Department of Medicine, Faculty of Medicine and Dentistry, University of Alberta, Edmonton, Alberta, Canada

A version of this chapter has been published as: ***Viveiros, A**., Gheblawi, M., Aujla, P.K. Sosnowski, D.K., Seubert, J.M., Kassiri, Z., Oudit, G.Y. Sex- and Age-Specific Regulation of ACE2: Insights into Severe COVID-19 Susceptibility. Journal of Molecular and Cellular Cardiology. 164:13-16. (2022). doi: 10.1016/j.yjmcc.2021.11.003.* This chapter has been modified from the article above.

Author Contributions

Conceptualization: ZK, JMS, ZK, GYO; Methodology: AV, MG, GYO; Animals: MG, PKZ, DKS; Human donor tissue procurement: AV; Sample processing: AV, MG; Histology and molecular work: AV, MG; Data analysis: AV, MG; Writing: AV, GYO; Review and editing: AV, MG, PKA, DKS, JMS, ZK, GYO; Supervision: JMS, ZK, GYO; Funding: JMS, ZK, GYO.

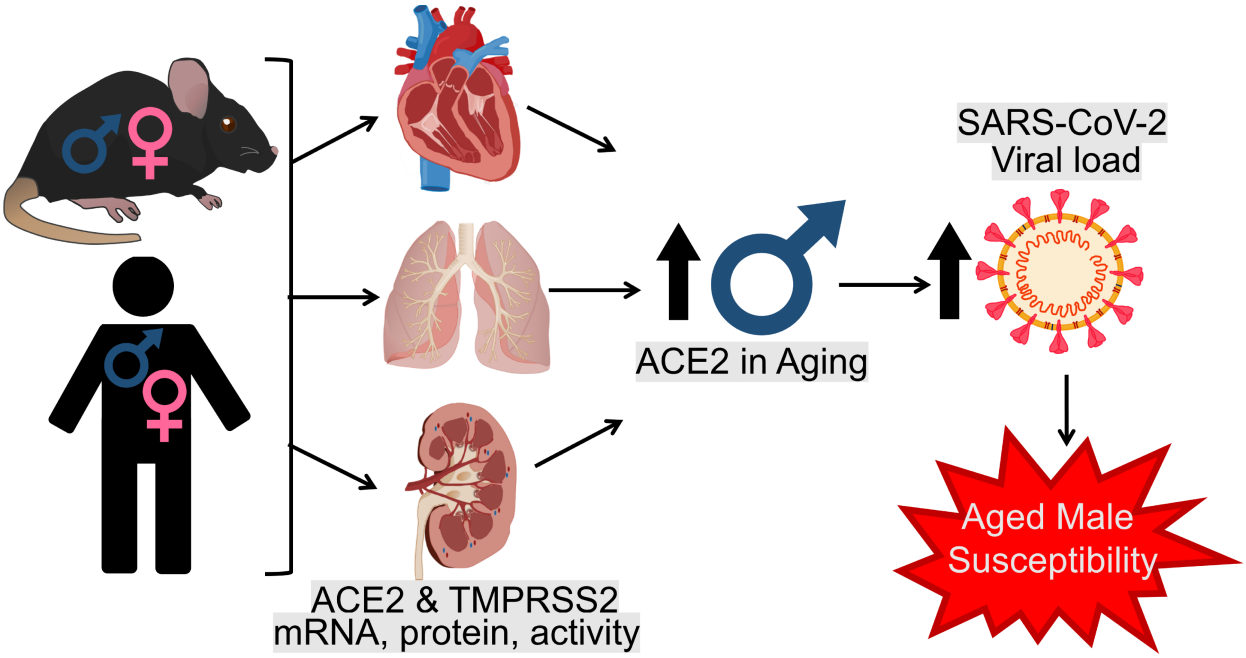

3.1 Abstract

Aged males disproportionately succumb to increased COVID-19 severity, hospitalization, and mortality compared to females. Angiotensin-converting enzyme 2 (ACE2) and transmembrane protease, serine 2 (TMPRSS2) facilitate SARS-CoV-2 viral entry and may have sexually dimorphic regulation. As viral load dictates disease severity, we investigated the expression, protein levels, and activity of ACE2 and TMPRSS2. Our data reveal that aged males have elevated ACE2 in both mice and humans across organs. We report the first comparative study comprehensively investigating the impact of sex and age in murine and human levels of ACE2 and TMPRSS2, to begin to elucidate the sex bias in COVID-19 severity.

Keywords: COVID-19, Sex, Age, ACE2, TMPRSS2, Heart

3.2 Introduction

The COVID-19 pandemic predominately finds aged males experiencing worsened disease severity and adverse outcomes.[25] Current experimental data are limited in explaining this sex bias. The SARS-CoV-2 virus predominantly hijacks two broadly-expressed endogenous proteins to facilitate infection, namely angiotensin-converting enzyme 2 (ACE2) and transmembrane protease, serine 2 (TMPRSS2).[40,254] A meta-analysis of thirty-six clinical studies found that a higher viral load at symptom onset is associated with disease severity, ICU hospitalization, and mortality.[255] Therefore, it is likely that increased viral load confers susceptibility to severe COVID-19; thus, the sex discrepancy may result from differences in levels of viral entry factors.

ACE2 demonstrates sexually dimorphic expression dependent on sex chromosomes and sex hormones.[25] Interestingly, *Ace2* is an X-linked gene that escapes X-chromosome inactivation, which may confer a "double-dosage" of ACE2 mRNA.[25,40] However, the female hormone 17β-estradiol (E2) reduces ACE2 expression *in vitro*, but does not affect TMPRSS2.[256] In the kidney, basal ACE2 activity is reduced in females compared to males in an E2-dependent manner.[28,257] However, E2 upregulates ACE2 in a model of intrauterine growth restriction, thereby complicating the relationship between E2 and ACE2 in disease.[258] Further, ACE2 is regulated downstream by micro RNAs (miRNAs) and proteolytic cleavage.[25] Finally, the TMPRSS2 gene is positively regulated by androgens in the prostate, thus may demonstrate male-biased expression elsewhere.[259] In all, the regulation of ACE2 and TMPRSS2 are complex and organ-specific, and the role of sex and age have yet to be elucidated.

Our recent review highlights the global pattern of sex- and age-bias in COVID-19 severity to favour older males.[25] Here, we aimed to delineate the impact of sex and aging on the expression,

protein levels, and activity of viral entry factors ACE2 and TMPRSS2 to begin to explain this discrepancy.

3.3 Materials and Methods

3.3.1 Animal Studies

Animals were maintained at the University of Alberta, and animal protocols were performed in compliance with the guidelines of the Animal Care and Use Committee and the Canadian Council of Animal Care. Kidney, lung, heart, and small intestine (SI) were harvested from male and female wild-type (WT) mice (background C57BL6/J) at three months (young), twelve months (adult), and eighteen months of age (aged) under ketamine-xylazine anesthesia.

3.3.2 Human Explanted Hearts

Explanted human hearts were obtained following cardioplegic arrest according to the Human Organ Procurement and Exchange (HOPE) program protocol and approved by the Health Research Ethics Board of the University of Alberta. Transmural left ventricle specimens were procured from young (median age 23/23; M/F) and aged (median age 55/56; M/F) human donors with no history of cardiovascular disease (**Table 3.1**).

3.3.3 Gene Expression

RNA isolation from mouse and human tissue was performed by Trizol-chloroform extraction. Isolated RNA (1 μg) was reverse transcribed with random primers (Invitrogen), and cDNA synthesized using SuperScript® II Reverse Transcriptase (Invitrogen). Real-time quantitative PCR was performed with TaqMan premixed assays (ThermoFisher Scientific) for gene expression in

mice for TMPRSS2 (Mm00443687_m1 and ACE2 (Mm01159009_m1), and human ACE2 (Hs00222343_m1).

3.3.4 Immunoblot

Cross-sectional tissue sections from each organ were homogenized in CelLytic™ Lysis reagent (ThermoFisher) and normalized by bicinchoninic acid protein assay (BCA). Proteins were resolved by SDS-PAGE on a 12% gel and transferred to polyvinylidene fluoride membranes in 25mM Tris, 192mM glycine, and 20% methanol (pH 8.3). Membranes were blocked in 5% non-fat milk and probed for ACE2 (Abcam) (1:1000) and TMPRSS2 (Abcam) (1:1000) in 5% bovine serum albumin (BSA). HRP-conjugated secondary antibodies (1:2000, Cell Signaling Technology) were used for detection. Lanes were normalized to MemCode™ total protein staining (ThermoFisher). Immunoreactivity was detected with Clarity™ Western ECL substrate (BioRad), and band densitometry measured with Image Studio (LI-COR Biosciences).

3.3.5 Immunofluorescence

Immunofluorescence was performed with Optimal Cutting Temperature (OCT)-embedded frozen transmural left ventricle tissue sections from both mice and humans. Sections were fixed in 4% paraformaldehyde, blocked with 4% BSA, and probed for ACE2 (R&D Systems) and NG2 (Abcam). Proteins were visualized with anti-goat Alexa-488 and anti-rabbit Alexa-594 secondary antibodies, respectively. Wheat Germ Agglutinin (WGA) conjugated to Alexa-405 (Invitrogen) was included to delineate the cell membrane.

3.3.6 ACE2 Enzyme Activity Assay

ACE2 activity assays were performed as previously described with modification for tissue analysis [242]. Briefly, tissue lysates were normalized (*2.3*), and equal protein (150ug heart/lung, 50ug SI/kidney) was diluted in 1x Assay buffer (75mM Tris, 5mM $ZnCl_2$, 1M NaCl, pH 6.5) with protease inhibitors, including 10μM captopril and 5μM amastatin. Specificity was assessed by incubating samples in the presence and absence of ACE2 inhibitor DX-600 (Cayman Chemical) for thirty minutes. Fluorogenic Peptide Substrate VI (ES007, R&D Systems) was subsequently added (final concentration of 50μM in Assay buffer), and kinetic measurements obtained immediately following (350/405nm). Fluorogenic standards (R&D Systems) were run in parallel to generate a conversion factor (pmol/RFU) to calculate the specific activity of ACE2.

3.3.7 Statistical Analysis

Statistics were performed using SPSS software and graphs plotted with GraphPad Prism. Data are represented as the mean ± SEM. Data that did not follow normal distribution were analyzed as independent samples with the Kruskal-Wallis test with pairwise comparison adjusted by Bonferroni correction. Two-way ANOVA with Tukey post hoc test was used to compare multiple groups. Unpaired student's t test was used to compare only two groups. *$p<0.05$; **$p<0.01$, ***$p<0.001$. Alternate symbols may be used to indicate significance among different comparisons, but the number of symbols indicates the level of significance.

3.4 Results

Gene expression for *Ace2* exhibits a tissue-specific pattern, with the highest expression in the small intestine (SI) and lowest expression in the heart and lungs (**Figure 3.1A**), demonstrating

a positive linear relationship with ACE2 protein levels and enzyme activity (**Figure 3.1B**). In contrast, *Tmprss2* mRNA is highest in the kidneys, whereas the highest TMPRSS2 protein level is in the SI, with undetectable mRNA and minimal protein in the heart (**Figure 3.1C**).

To analyze the impact of sex and aging across organs, we first examined the molecular signature for ACE2 and TMPRSS2 in mice. In the heart, *Ace2* mRNA was lowered in the aged animals (**Figure 3.1D**) with a lack of a difference in ACE2 protein levels and activities between males and females within age groups; however, ACE2 activity was elevated in aged animals (**Figure 3.1E-F**). In the lungs, *Ace2* mRNA expression was higher in adult females, whereas protein levels and activity were reduced in the aged females compared to males (**Figure 3.1D-F**).

In the kidneys, ACE2 levels and activity were higher in males than females across all age groups, thus corroborating studies demonstrating increased renal ACE2 activity in male rats.[257] No differences in ACE2 were observed in the SI. In both organs, *Ace2* mRNA expression did not show a sex-dependent variation (**Figure 3.1D-F**). In contrast, TMPRSS2 mRNA and protein levels did not vary between sexes and with aging in the lungs and SI; however, adult females had increased expression in the kidneys compared to males (**Figure 3.1D-E**).

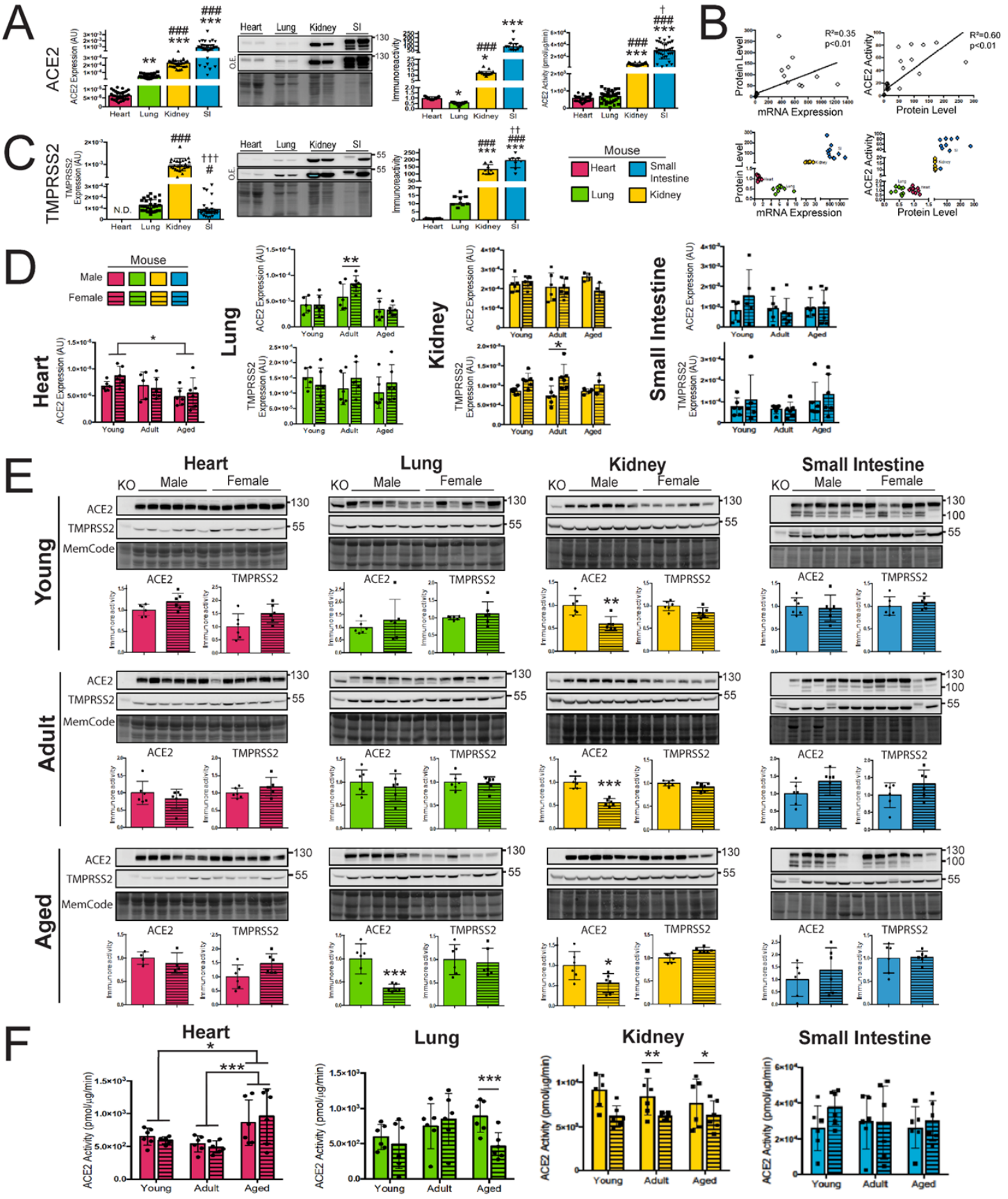

Figure 3.1. *Figure legend on next page*

Figure 3.1. Assessment of ACE2 and TMPRSS2 across sex and aging.

A. ACE2 mRNA expression (n=36, biological replicates), protein levels (n=11, biological replicates), and activity (n=36, biological replicates) are positively correlated across all organs in male and female animals (**B.**). **C.** TMPRSS2 mRNA (n=36, biological replicates) and protein levels (n=11, biological replicates). Data from A-C was generated from C57BL6/J mice using a pooled analysis of males and females. Levels are compiled from all sexes and age groups for expression and activity; however, protein levels are compiled from representative and three replicate gels sampled from a subset of all age groups (**Figure 3.3**). All organs were run on the same gel for comparison. Immunoblots were over-exposed (O.E.) to visualize low levels in the lung and heart. Expression and activity data were run one time in the same plate for quantification. Data are represented as median with interquartile range (IQR) and were analyzed as independent samples with the Kruskal-Wallis test with pairwise comparison adjusted by Bonferroni correction; * indicates differences from the heart; # indicates differences from the lung; and † indicates differences from the kidney. *$p<0.05$; **$p<0.01$, ***$p<0.001$ where the number of symbols indicates the level of significance. Analysis of mRNA expression (**D**.), protein levels (**E.**), and ACE2 activity (**F.**) of ACE2 and TMPRSS2 across sex and age in the heart (magenta), lung (green), kidney (yellow), and small intestine (SI) (blue) (n=6, biological replicates/group). ACE2 global knockout mice were analyzed as a negative control (KO) for western blots. Raw images are provided in **Figure 3.4-3.5**. Data are represented as the mean ± SEM and analyzed by two-way ANOVA with Tukey post hoc test (mRNA and activity), or unpaired student's t test (protein levels). For all experiments, young animals (n=12) were obtained from four litters and each litter was collected over two days. Adult and aged animals (n=12 /group) were obtained from five and three litters respectively, and each litter was collected over two days.

SARS-CoV-2 infection facilitates the loss of membrane ACE2 following initial infection.[40,260] The high burden of cardiovascular disease (CVD) in COVID-19 patients and the critical role of ACE2 in myocardial and vascular protection highlights this pathophysiological connection; thus, we next focused on examining ACE2 in the heart.[2,40] To determine the age-related pattern of myocardial ACE2 across age groups, we first measured murine protein levels by immunoblot. ACE2 was elevated in aged males and females compared to the younger age groups (**Figure 3.2A**), in accordance with ACE2 activity (**Figure 3.1F**), yet in contrast to mRNA expression (**Figure 3.1D**). Immunofluorescence demonstrated predominant pericyte and vascular distribution of ACE2 (colocalization with NG2) (**Figure 3.2B**).[2]

We next analyzed young and aged explanted human heart samples. ACE2 protein levels were elevated in aged males but not in aged females, as confirmed by ACE2 immunofluorescence (**Figure 3.2C-D**). Interestingly, no differences in *Ace2* mRNA expression were discernable; however, ACE2 activity was consistent with the immunoblot results, in which aged males were elevated (**Figure 3.1F**). Discordant mRNA and protein levels also characterized murine hearts (data not shown).

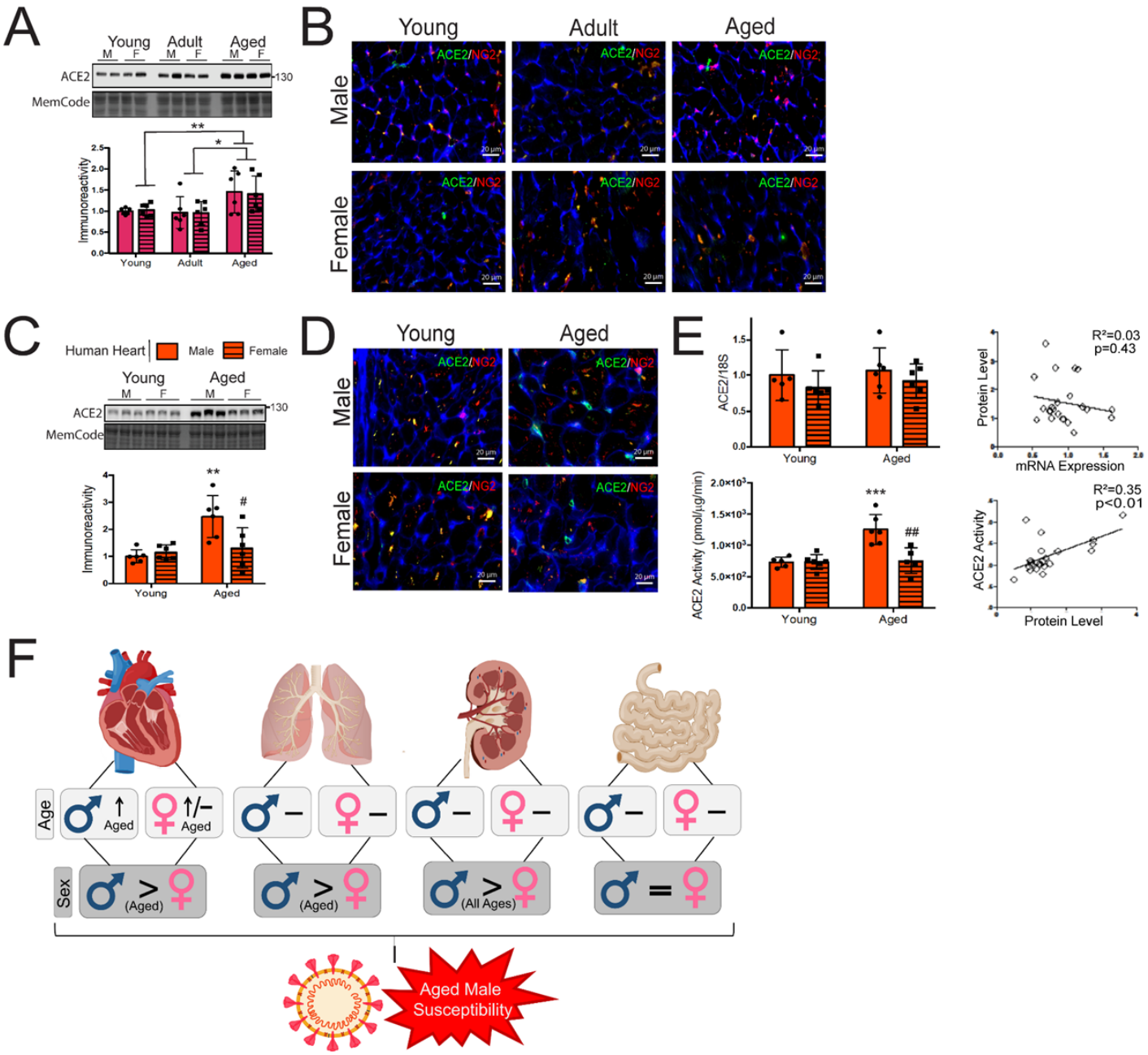

Figure 3.2. *Figure legend on next page*

Figure 3.2. Sex- and age-differences in ACE2 levels in mouse and human hearts.

A. Representative immunoblot of mouse hearts for ACE2 protein levels (n=6 biological replicates/group). Three gels were compiled for quantification (Figure 3.6). Data are represented as the mean ± SEM and were analyzed by two-way ANOVA with Tukey post hoc test; *p<0.05; **p<0.01, ***p<0.001. For all experiments, young animals (n=12) were obtained from four litters and each litter was collected over two days. Adult and aged animals (n=12 /group) were obtained from five and three litters respectively, and each litter was collected over two days. **B.** Immunofluorescence of ACE2 (green) and pericyte marker NG2 (red). Wheat Germ Agglutinin (WGA) (blue) was used to delineate the cell membrane. Qualitative images were captured from n=2 biological replicates and n=16 (8 images/animal) technical replicates for each age group. **C.** Representative immunoblot for ACE2 in human hearts (n=6, biological replicates/group). Two gels were compiled for quantification (Figure 3.6). Quantification represents the combined result from two western blots. Data are represented as the mean ± SEM and were analyzed by two-way ANOVA with Tukey post hoc test. * indicates differences from young males, and # indicates differences between aged males and aged females; *p<0.05; **p<0.01, ***p<0.001 where the number of symbols indicates the level of significance. **D.** Immunofluorescence of ACE2 (green) and NG2 (red). WGA (blue) was used to delineate the cell membrane. Qualitative images were captured from n=2 biological replicates and n=16 (8 images/donor) technical replicates for each age group. **E.** ACE2 protein levels and activity are positively correlated, but not mRNA expression. * indicates differences from young males, and # indicates differences between aged males and aged females. *p<0.05; **p<0.01, ***p<0.001 where the number of symbols indicates the level of significance. **F.** Schematic figure showing the multi-organ impact of sex and aging on ACE2 levels as a potential contributor to the increased male susceptibility to severe COVID-19.

3.5 Discussion

In this study, our data reveal an organ-, sex- and age-dependent difference in ACE2 regulation, with increased ACE2 in the lungs and hearts of aged males, and with a sex- rather than an age-dependent pattern in the kidneys favouring males. These changes can contribute to the increased severity and adverse outcomes reported in male COVID-19 patients (**Figure 3.2F**). As SARS-CoV-2 viral load is predictive of intensive care unit hospitalization and mortality,[255,261] we propose that aged males may be at an elevated risk partly due to the higher initial viral burden driven by the increased tissue ACE2, thus subject to pulmonary, myocardial, and renal injury. However, additional studies are necessary to delineate the relationship between viral load and the levels of ACE2 (and TMPRSS2). Further, as we confirmed the low levels of TMPRSS2 in the heart, other proteases, such as the cathepsins, may also facilitate spike protein priming and are worthy of investigation.[254] Our results also highlight that SARS-CoV-2 could target multiple organs beyond the respiratory system, including the heart, kidneys, and gut, mainly because ACE2 protein levels in these organs far exceed the levels in the lungs. In fact, gastrointestinal symptoms are common in COVID-19 patients and occasionally precede pulmonary manifestations.[260]

While a positive relationship exists between protein levels and activity of ACE2, *Ace2* mRNA and protein levels were uncoupled within organs. These findings, coupled with the observation that females have two functional copies of the X-linked *Ace2* gene, suggest a complex mechanism of transcriptional, translational, and proteolytic control of ACE2 that counteracts the predicted female-biased expression.[25] For example, given the impact of E2 on ACE2 levels and activity, the levels of gonadal steroids may also influence the observed sex differences.[28] Besides sex hormone-dependent regulation, ACE2 protein levels are subject to post-transcriptional and post-translational modulation, such as by proteolytic cleavage and miRNAs.

Proteolytic cleavage of ACE2 is linked to the pathogenesis of CVD.[25,40] Physiologically, ACE2 counteracts the canonical renin-angiotensin system (RAS), which promotes vasoconstriction and inflammation with angiotensin II as the effector molecule. Therefore, ACE2 is protective in CVD, where chronic elevation of the canonical RAS pathway is characterized.[40] A downstream consequence of RAS activity is the activation of a disintegrin and metalloprotease 17 (ADAM17), which cleaves and releases ACE2 from the plasma membrane. Therefore, aberrant canonical RAS and subsequent increase of ADAM17 activity generate soluble plasma ACE2, which is associated with detrimental outcomes in CVD.[25,40] Similarly, ADAM17-dependent ACE2 shedding may contribute to increased COVID-19 severity following initial viral endocytosis.[40] In accordance, increased plasma ACE2 is associated with worsened clinical outcomes in hospitalized COVID-19 patients.[40,262]

Finally, another mechanism of post-transcriptional control occurs by miRNAs, which suppress gene expression. Organ-specific miRNAs are predicted *in silico* to target ACE2 mRNA based on transcript sequences,[35] as well as validated experimentally in cardiomyocytes.[263] Therefore, the mechanisms of proteolytic cleavage and miRNAs further complicate the discourse on ACE2 regulation. Additional studies are required to delineate the contribution of miRNAs and proteolytic cleavage on ACE2 expression and activity. In all, the regulation of ACE2 is complex, and the homeostatic mechanisms controlling ACE2 should be assessed for modulation in health versus disease. Given the discordance between mRNA expression and protein levels, we emphasize the complicated regulation of viral entry proteins. Further, we demonstrate the need to assess all levels from transcriptional to post-translational to understand the biological consequences of all modes of regulation.

3.6 Conclusion

Our study highlights a novel sex- and age-specific bias in ACE2 protein levels and activity in the kidney, heart, and lung at basal conditions. To our knowledge, we present the first comparative analysis to comprehensively investigate the impact of sex and age on ACE2 and TMPRSS2 in both humans and mice. Given the global burden of the COVID-19 pandemic, our findings expand the knowledge of the tissue distribution of viral entry factors and begin to inform the sex-discrepancy in COVID-19 severity.

3.7 Acknowledgements

The authors acknowledge funding from the Canadian Institutes of Health Research (CIHR) and Heart and Stroke Foundation of Canada to GYO, and from the Heart and Stroke Foundation of Canada to JMS. The remaining authors have no funding sources to declare.

3.8 Disclosures

The authors have no conflict of interests to declare.

Table 3.1. Human heart donor characteristics and grouping (young vs aged).

Explanted human hearts were obtained according to the Human Organ Procurement and Exchange (HOPE) program protocol. All donors were declared brain dead (BDB).

Group	Age	Sex	BMI	Ethnicity	Cause of Death	Heart Weight (g)	EF	Comorbidities	Relevant Medications
Young	18	Male	19	Caucasian	Anoxia/ hypoxia	271	50-55%	None	None
Young	19	Male	21.4	multiracial	MVC	299	>60 %	None	None
Young	29	Male	22.6	Black	Gunshot to head	290	60%	Diabetes	None
Young	23	Male	23.9	Caucasian	Gunshot to the head	436	50%	None	None
Young	31	Male	22.6	Caucasian	Anoxia/ hypoxia Presumed drug OD	285	54%	None	None
Young	38	Male	N/A	N/A	Anoxia	371	>60 %	N/A	N/A
Young	16	Female	24.1	Asian	OD-multidrug	225	>60 %	None	None
Young	18	Female	N/A	East Indian	Anoxia suicide/ drug OD	227	65%	None	N/A
Young	25	Female	23.8	Caucasian	SAH, heroin OD	236	>60 %	No	None
Young	23	Female	25.2	Caucasian/ Indigenous	Primary CNS tumor	328	>70 %	No	None
Young	27	Female	26.8	Caucasian	Hypoxia/ anoxia (hanging)	298	>60 %	No	None
Young	26	Female	27.3	Caucasian	Anoxia/ hypoxia, drug OD	270	55-60%	No	None
Aged	52	Male	25.3	Caucasian/ Indigenous	Anoxia/ hypoxia (hanging)	394	55-60%	None	N/A
Aged	54	Male	27.9	N/A	Anoxia/ hypoxia aortic dissection	447	60%	None	None
Aged	61	Male	24.5	Caucasian	Trauma (fall)	423	>60 %	Mild Htn hyperlipidemia	None
Aged	61	Male	25.1	Caucasian	Trauma (fall-SDH)	326	55%	None	None

Aged	54	Male	23.4	Caucasian	Ruptured cerebral aneurysm	308	>60 %	None	None
Aged	57	Male	27.6	Caucasian/ Hispanic	CVA (stroke)	310	55-60%	None	N/A
Aged	48	Female	29.2	Caucasian	CVA (ischemic stroke)	316	>60 %	No	None
Aged	54	Female	24.7	Caucasian	Trauma (fell down stairs)	290	55-60%	Asthma	None
Aged	60	Female	22.1	Caucasian	CVA hemorrhagic stroke	287	>60 %	hypothyroid	N/A
Aged	58	Female	28.4	Caucasian	SAH	427	>60 %	Mild Htn	None
Aged	61	Female	23.9	Caucasian	CNS infection bacterial meningitis	335	55-65%	Htn	Metoprolol
Aged	38	Female	21.6	Caucasian	CO poisoning	328	50-55%	No	None

MVC, motor vehicle collision; OD, overdose; SAH, subarachnoid hemorrhage; SDH, subdermal hemorrhage; CVA, cerebrovascular accident; CO, carbon monoxide; CVA, cerebrovascular accident, Htn, hypertension.

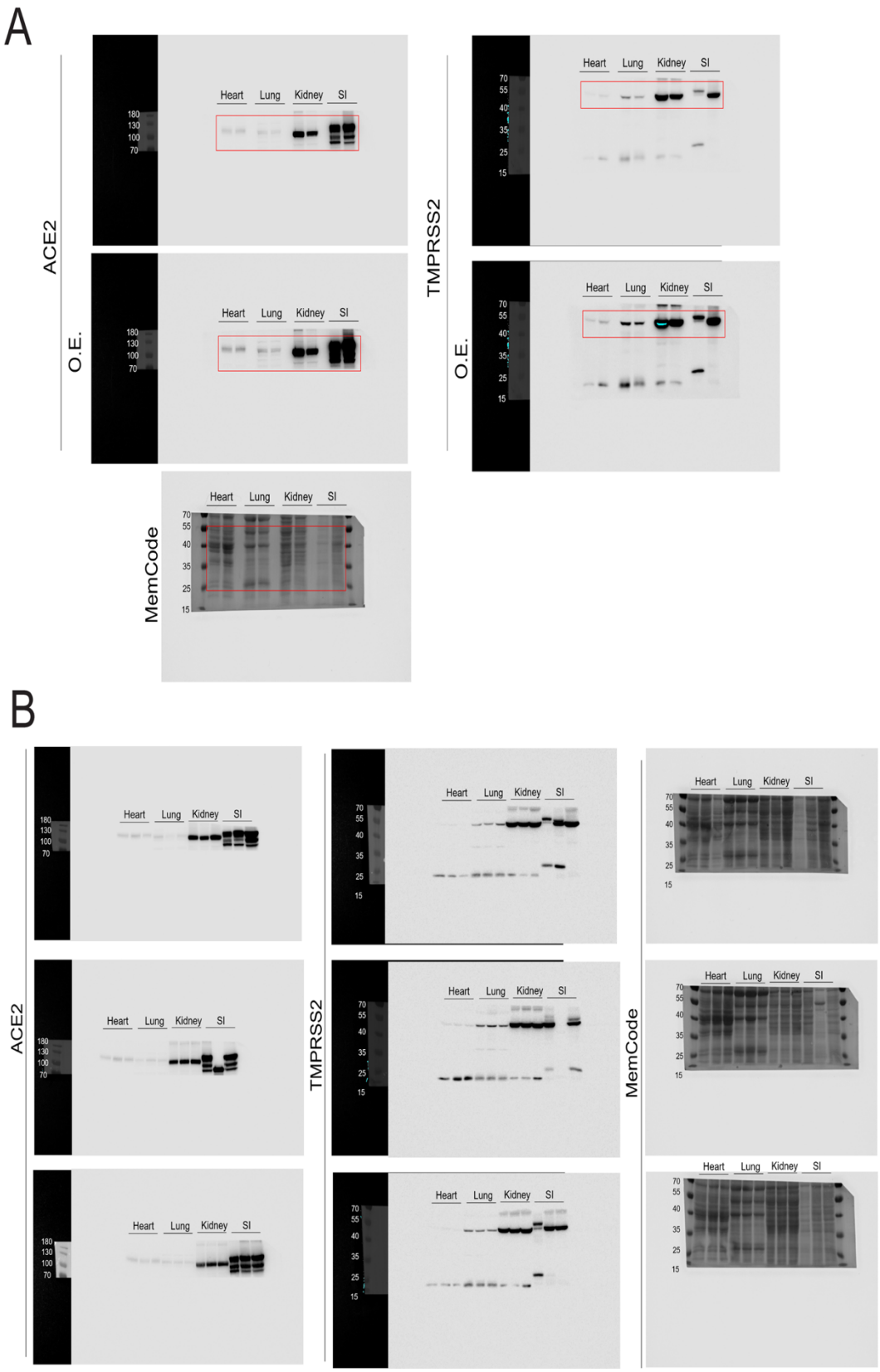

Figure 3.3. *Figure legend on next page*

Figure 3.3. Raw and uncropped western blot images from **Figure 3.1A and Figure 3.1C**.

A. Immunoreactivity of ACE2 (left) and TMPRSS2 (right). Proteins were resolved on a 12% gel and transferred to a PVDF membrane. Following transfer, the membrane was cut at 75 kDa to visualize ACE2 on the top half of the membrane (predicted molecular weight of 130 kDa), and TMPRSS2 on the bottom (predicted molecular weight of 55 kDa). For these representative blots, two samples were run for heart, lung, kidney and small intestine (SI) with a one-lane gap between each organ. The red rectangle represents the area cropped for the corresponding figure.

B. Replicate western blots used for quantification in graphs from **Figure 3.1A and Figure 3.1C**. Three samples for heart, lung, kidney and small intestine (SI) were run in each gel. In total, eleven animals (five young, three adult, and three aged) with four males and four females for each organ was analyzed across four western blot runs (including representative images in A.). Immunoreactivity was detected with Clarity™ Western ECL substrate and visualized with ImageQuant™ LAS 4000 (GE Healthcare). The chemiluminescent image is captured first, then a digitization image is captured by epi-illumination to visualize the molecular weight markers. The chemiluminescent image is overlayed onto the digitization image to visualize protein bands adjacent to molecular weight markers.

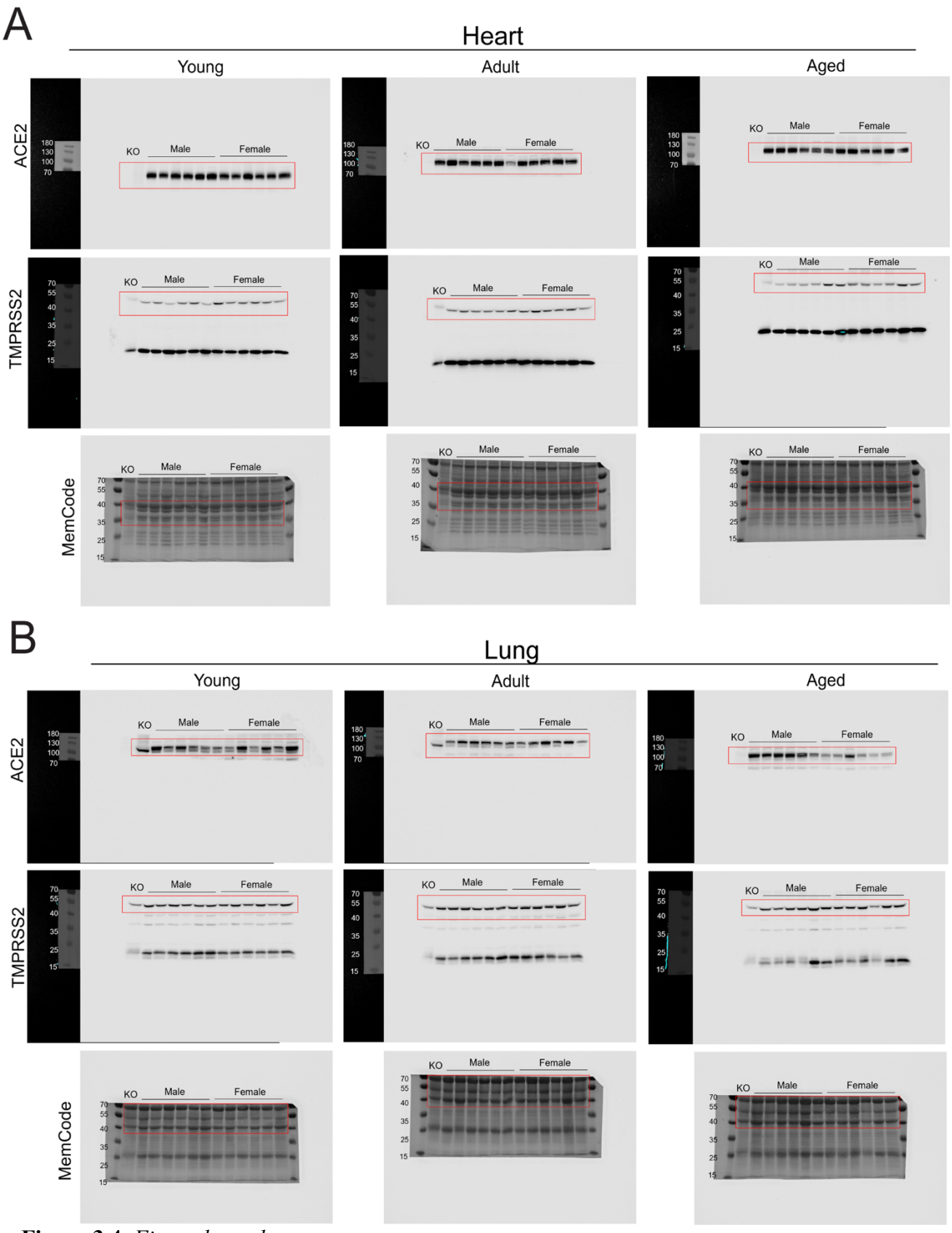

Figure 3.4. *Figure legend on next page*

Figure 3.4. Raw and uncropped western blot images from **Figure 3.1E**.

A. Immunoreactivity of ACE2 and TMPRSS2 in the heart of young (left) adult (middle) and aged (right) animals. Proteins were resolved on a 12% gel and transferred to a PVDF membrane. Following transfer, the membrane was cut at 75 kDa to visualize ACE2 on the top half of the membrane (predicted molecular weight of 130 kDa), and TMPRSS2 on the bottom (predicted molecular weight of 55 kDa). The bottom portion of the membrane was stained with MemCode™ to quantify of protein loading. Six samples were run for each male and female, with the heart from one ACE2 global knockout (KO) animal ran as a negative control for each gel. The red rectangle represents the area cropped for the corresponding figure. **B.** Immunoreactivity of ACE2 and TMPRSS2 in the lung of young (left) adult (middle) and aged (right) animals. Proteins were resolved on a 12% gel and transferred to a PVDF membrane. Following transfer, the membrane was cut at 75 kDa to visualize ACE2 on the top half of the membrane (predicted molecular weight of 130 kDa), and TMPRSS2 on the bottom (predicted molecular weight of 55 kDa). The bottom portion of the membrane was stained with MemCode™ to quantify of protein loading. Six samples were run for each male and female, with the lung from one ACE2 global knockout (KO) animal ran as a negative control for each gel. The red rectangle represents the area cropped for the corresponding figure. Immunoreactivity was detected with Clarity™ Western ECL substrate and visualized with ImageQuant™ LAS 4000 (GE Healthcare). The chemiluminescent image is captured first, then a digitization image is captured by epi-illumination to visualize the molecular weight markers. The chemiluminescent image is overlayed onto the digitization image to visualize protein bands adjacent to molecular weight markers.

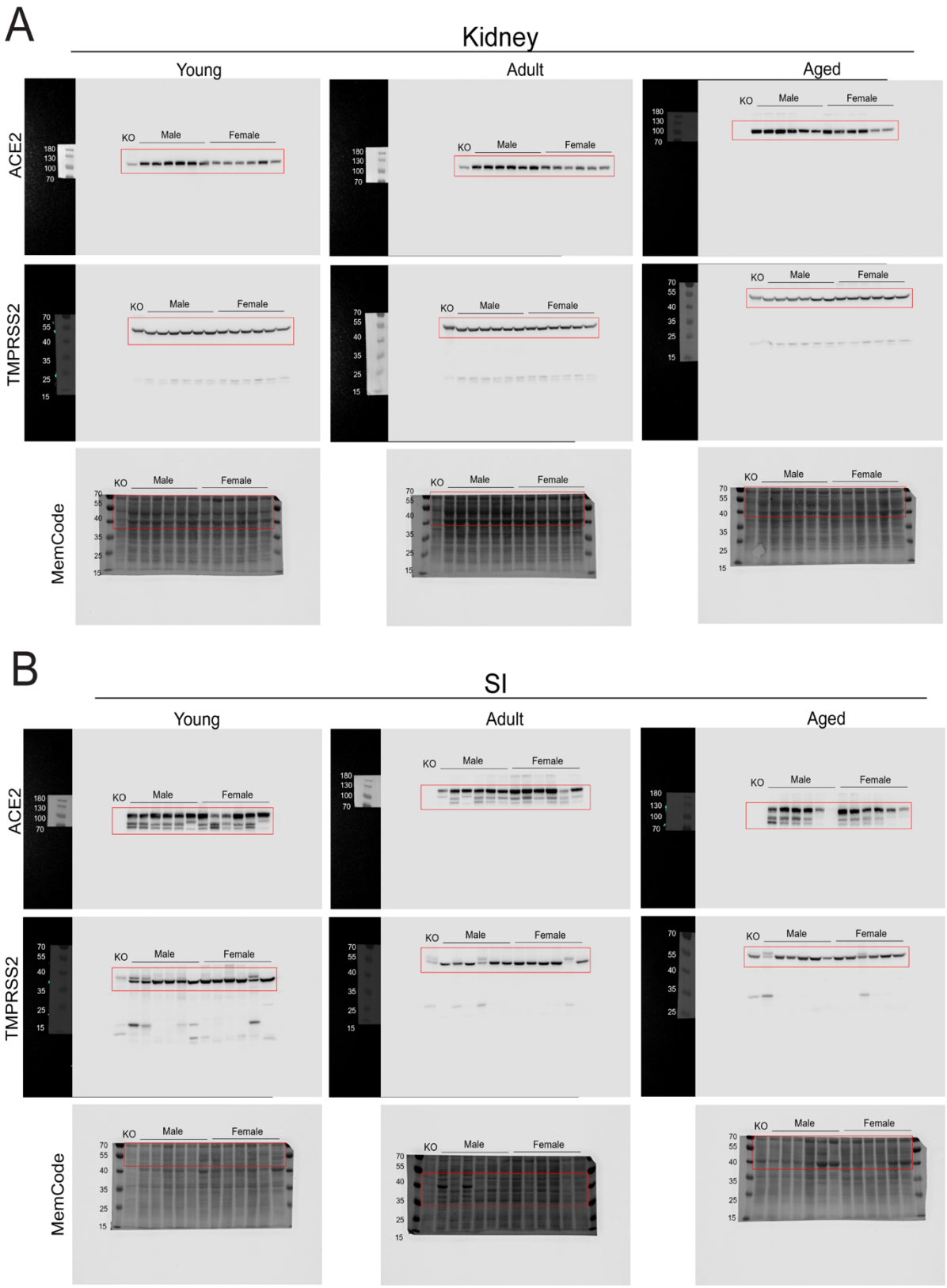

Figure 3.5. *Figure legend on next page*

Figure 3.5. Raw and uncropped western blot images from **Figure 3.1E**.

A. Immunoreactivity of ACE2 and TMPRSS2 in the kidney of young (left) adult (middle) and aged (right) animals. Proteins were resolved on a 12% gel and transferred to a PVDF membrane. Following transfer, the membrane was cut at 75 kDa to visualize ACE2 on the top half of the membrane (predicted molecular weight of 130 kDa), and TMPRSS2 on the bottom (predicted molecular weight of 55 kDa). The bottom portion of the membrane was stained with MemCode™ to quantify of protein loading. Six samples were run for each male and female, with the kidney from one ACE2 global knockout (KO) animal ran as a negative control for each gel. The red rectangle represents the area cropped for the corresponding figure. **B.** Immunoreactivity of ACE2 and TMPRSS2 in the small intestine (SI) of young (left) adult (middle) and aged (right) animals. Proteins were resolved on a 12% gel and transferred to a PVDF membrane. Following transfer, the membrane was cut at 75 kDa to visualize ACE2 on the top half of the membrane (predicted molecular weight of 130 kDa), and TMPRSS2 on the bottom (predicted molecular weight of 55 kDa). The bottom portion of the membrane was stained with MemCode™ to quantify of protein loading. Six samples were run for each male and female, with the SI from one ACE2 global knockout (KO) animal ran as a negative control for each gel. The red rectangle represents the area cropped for the corresponding figure. Immunoreactivity was detected with Clarity™ Western ECL substrate and visualized with ImageQuant™ LAS 4000 (GE Healthcare). The chemiluminescent image is captured first, then a digitization image is captured by epi-illumination to visualize the molecular weight markers. The chemiluminescent image is overlayed onto the digitization image to visualize protein bands adjacent to molecular weight markers.

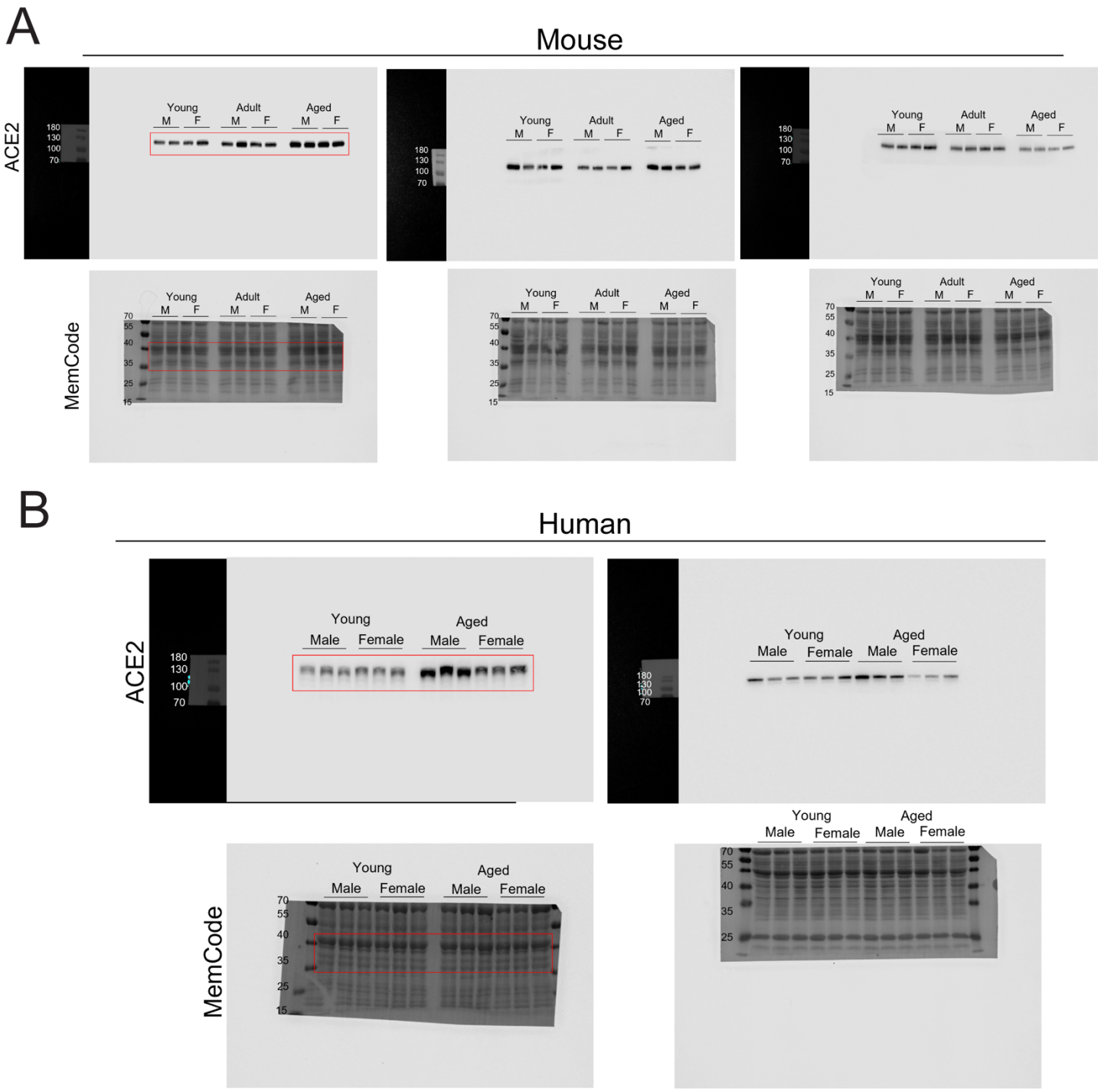

Figure 3.6. *Figure legend on next page*

Figure 3.6. Raw and uncropped western blot images from **Figure 3.2**.

A. Representative and replicate western blots for **Figure 3.2A**. Immunoreactivity of ACE2 in the the heart of mice across age groups. Proteins were resolved on a 12% gel and transferred to a PVDF membrane. Following transfer, the membrane was cut at 75 kDa to visualize ACE2 on the top (predicted molecular weight 130 kDa) and the bottom portion was stained with MemCode™ to quantify protein loading. Three gels were run with samples from thirty-six different animals (biological replicates) in total. For each blot, two males and two female animals were run in each young, adult, and aged groups, with a one-lane gap between the age groups. The red rectangle represents the area cropped for the corresponding figure. **B.** Representative and replicate western blots for **Figure 3.2C**. Immunoreactivity of ACE2 in the the heart of human donors across age groups. Proteins were resolved on a 12% gel and transferred to a PVDF membrane. Following transfer, the membrane was cut at 75 kDa to visualize ACE2 on the top (predicted molecular weight 130 kDa) and the bottom portion was stained with MemCode™ to quantify protein loading. Two gels were run with samples from twenty-four different human donors in total. For each blot, three male and three female donors were run in young and aged groups, with a one-lane gap between the age groups. The red rectangle represents the area cropped for the corresponding figure. Immunoreactivity was detected with Clarity™ Western ECL substrate and visualized with ImageQuant™ LAS 4000 (GE Healthcare). The chemiluminescent image is captured initially then a digitization image is captured by epi-illumination to visualize the molecular weight markers. The chemiluminescent image is overlayed onto the digitization image to visualize protein bands adjacent to molecular weight markers.

Chapter 4

SARS-CoV-2 Infection Downregulates Myocardial ACE2 and Potentiates Cardiac Inflammation in Humans and Hamsters

SARS-CoV-2 Infection Downregulates Myocardial ACE2 and Potentiates Cardiac Inflammation in Humans and Hamsters

Anissa Viveiros[1,2], Ryan S. Noyce[3,4], Mahmoud Gheblawi[1], Daniele Colombo[5], Leanne M. Bilawchuk[3,4], Xavier Clemente-Casares[4], David J. Marchant[3,4], Zamaneh Kassiri[1], Franca Del Nonno[5], David H. Evans[3,4], and Gavin Y. Oudit[1,2,6 *]

[1]Department of Physiology, Faculty of Medicine and Dentistry, University of Alberta, Edmonton, Alberta, Canada
[2]Mazankowski Alberta Heart Institute, University of Alberta, Edmonton, Alberta, Canada
[3]Li Ka Shing Institute of Virology, University of Alberta, Edmonton, Alberta, Canada.
[4]Department of Medical Microbiology and Immunology, University of Alberta, Edmonton, Alberta, Canada.
[5]Pathology Unit, National Institute for Infectious Diseases "Lazzaro Spallanzani," IRCCS, Rome, Italy
[6]Division of Cardiology, Department of Medicine, Faculty of Medicine and Dentistry, University of Alberta, Edmonton, Alberta, Canada

A version of this chapter has been published as: ***Viveiros, A**., Noyce, R., Gheblawi, M., Colombo, D., Bilawchuk, L.M., Clemente-Casares, X., Marchant, D.J., Kassiri, Z., Del Nonno, F., Evans, D.J., Oudit, G.Y. SARS-CoV-2 Infection Downregulates Myocardial ACE2 and Potentiates Cardiac Inflammation in Humans and Hamsters. Am J Physiol Heart Circ Physiol. 323:H1262-H1269. (2022). doi: 10.1152/ajpheart.00578.2022.* This chapter has been modified from the article above.

Author Contributions

Conceptualization: XCC, DJM, ZK, DHE, GYO; Methodology: RSN, DHE, GYO, DC, FDN; Animals: RSN, DHE; Human donor tissue procurement: DC, FDN; Sample processing: AV, RSN, MG, DC, FDN; Histology and molecular work: AV, MG, LMB; Data analysis: AV, RSN; Writing: AV, RSN, GYO; Review and editing: AV, RSN, MG, DC, XCC, DJM, ZK, FDN, DHE, GYO; Supervision: DC, XCC, DJM, ZK, FDN, DHE, GYO; Funding: DHE, GYO.

4.1 Abstract

Myocardial pathologies resulting from SARS-CoV-2 infections are consistently rising with mounting case rates and reinfections; however, the precise global burden is largely unknown and will have an unprecedented impact. Understanding the mechanisms of COVID-19 mediated cardiac injury is essential towards the development of cardioprotective agents that are urgently needed. Assessing novel therapeutic strategies to tackle COVID-19 necessitates an animal model that recapitulates human disease. Here, we sought to compare SARS-CoV-2 infected animals to COVID-19 patients to identify common mechanisms of cardiac injury. Two-month-old hamsters were infected with either the ancestral (D614) or Delta variant of SARS-CoV-2 for two days, seven days and/or fourteen days. We measured viral RNA and cytokine expression at the earlier time points to capture the initial stages of infection in the lung and heart. We assessed myocardial ACE2, the entry receptor for the SARS-CoV-2 virus and cardioprotective enzyme, as well as markers for inflammatory cell infiltration in the hamster hearts at days 7 and 14. In parallel, human hearts were stained for ACE2, viral nucleocapsid, and inflammatory cells. Indeed, we identify myocardial ACE2 downregulation and myeloid cell burden as common events in both hamsters and humans infected with SARS-CoV-2, and we propose targeting downstream ACE2 downregulation as a therapeutic avenue that warrants clinical investigation.

4.2 New and Noteworthy

Cardiac manifestations of COVID-19 in humans are mirrored in the SARS-CoV-2 hamster model, recapitulating myocardial damage, ACE2 downregulation and a consistent pattern of immune cell infiltration independent of viral dose and variant. Therefore, the hamster model is a valid approach to study therapeutic strategies for COVID-19 related heart disease.

4.3 Introduction

Cardiovascular complications in severe COVID-19, namely microvascular dysfunction, myocarditis, conduction abnormalities, and heart failure, represents an emerging global health crisis. Further, cardiovascular injury resulting from SARS-CoV-2, the causative virus of COVID-19, is complicated by the post-acute sequelae as also linked to an increased incidence of inflammatory heart disease and thrombotic disorders; thus, cardiac injury in COVID-19 is likely currently underestimated.[60] Reports of myocardial damage and the fact that angiotensin-converting enzyme 2 (ACE2), the indispensable viral entry receptor, is expressed in the heart and other affected organs suggests a probable mechanism of direct infection.[59,60] Therefore, in light of this public health emergency, it is of paramount importance to delineate the pathological mechanisms of myocardial inflammation and injury in COVID-19, and to discover novel cardioprotective interventions.

Studying SARS-CoV-2 mediated myocardial injury requires animal models to test therapeutic interventions: a feat challenged by the limited ability of small animal models to adequately recapitulate this human disease. Generally, mouse models are studied extensively and are readily available; however, have limited utility for COVID-19 studies since murine ACE2 does not effectively bind to the SARS-CoV-2 spike protein.[264] Strategies to overcome this limitation have been developed, including modifying the viral spike protein to bind mouse ACE2 or developing humanized mice that express the human ACE2 protein.[264] Despite these approaches, these mice can develop additional symptoms following SARS-CoV-2 infection, such as lethal encephalitis in humanized mice that are not captured in humans; yet, they do not develop cardiac symptoms. In addition, extensive manipulation of animals and the viral spike protein limits translational significance.[264] Alternatively, the Syrian hamster model superficially

resembles human COVID-19 disease, with low mortality, is readily available, and succumbs to infection by unmodified SARS-CoV-2; therefore, is a valuable tool for COVID-19 research.[265] To date; however, it is unclear if hamsters exhibit similar cardiac manifestations as in human COVID-19 patients.

Here, we provide evidence that the Syrian hamster is a suitable animal model to study the cardiovascular manifestations of COVID-19, thus providing a means of studying therapeutic interventions to prevent or treat myocardial injury in COVID-19 patients.

4.4 Materials and Methods

4.4.1 Cells and viruses

Vero cells (ATCC CCL-81) were maintained in minimum essential medium (MEM) supplemented with 100U/mL penicillin, 100U/mL streptomycin, 0.25µg/mL Amphotericin B, and 10% fetal bovine serum. An ancestral (D614) SARS-CoV-2 strain (GISAID # EPI_ISL_425177) and a SARS-CoV-2-Delta variant of concern strain (B.1.617.2) were used in these studies.

4.4.2 In vivo hamster infections

Animal experiments were approved by the University of Alberta Animal Care and Use Committee (AUP00001847 and AUP00003869). All SARS-CoV-2 infection studies were conducted in a certified BSL3 containment facility at the University of Alberta. Briefly, two month-old male Syrian hamsters were inoculated intranasally with the ancestral SARS-CoV-2 variant at a dose of 2.0 x10^3 PFU in a total volume of 100µL (50µL per nare). Nasal swabs were performed on days 1, 3, and 6 post challenge and collected for histopathology on day 7 or day 14

post infection. To determine cytokine responses following virus infection, another set of hamsters were inoculated at a viral dose of $1.0x10^6$ PFU with SARS-CoV-2-Delta (B.1.617.2) and heart and lung tissues were collected on day 2 and day 7. Control hamsters were inoculated with MEM containing no virus. Animals were randomized to either the infected or control groups. The hamsters were monitored daily for signs of infection and morbidity (**Figure 4.1A**). Animals who lost greater than 20% of their initial body weight were to be humanely euthanized and excluded from the study; however, no animals exceeded this threshold.

4.4.3 Virus titrations

For virus culture, 2×10^5 cells were seeded into each well of a 12-well tissue culture plate one day prior to titration. Ten-fold serial dilutions of the virus stock or nasal swab were plated in duplicate on Vero CCL-81 cells and cultured for 3 days at 37°C in MEM containing 0.5% carboxymethylcellulose (Sigma). Cells were fixed and stained with a solution containing 0.13% (w/v) crystal violet, 11% formaldehyde (v/v), and 5% ethanol (v/v) to visualize plaques.

4.4.4 Human Samples

Patients who succumbed to COVID-19 from the Lazio Region were autopsied in Rome, Italy. In parallel, hearts were procured from age and sex-matched donors following cardioplegic arrest according to the Human Organ Procurement and Exchange (HOPE) protocol. Control hearts were obtained from brain dead patients (DBD) with no known history of cardiovascular disease. Transmural myocardial sections were formalin-fixed and paraffin-embedded for histological analysis. All protocols are approved by the Health Research Ethics Board of the University of Alberta.

4.4.5 Histological Staining

Formalin-fixed paraffin-embedded tissue were sectioned onto slides at 5µm thickness. Hematoxylin and Eosin (H&E) staining was performed according to a standard protocol. Briefly, slides were de-waxed and rehydrated by decreasing alcohol gradient. Nuclei were stained with Harris Hematoxylin for 15 seconds, rinsed, and differentiated with 1% acid alcohol. Sections were rinsed in Scott's tap water substitute (20mM Sodium Bicarbonate, 166mM Magnesium Sulfate), then stained with Eosin. Sections were dehydrated, cleared and mounted. Masson's trichrome staining was performed using a commercially available kit (Abcam ab150686). Briefly, deparrafinized and rehydrated slides were incubated in pre-heated Bouin's Fluid, cooled, and rinsed. Next, sections were stained in Weigert's iron hematoxylin working solution (equal parts of solutions A and B) and rinsed under tap water. Next, slides were stained in Biebrich Scarlet/Acid Fuchsin solution and washed with distilled water. Slides were differentiated in Phosphomolybdic/Phosphotungstic acid solution until collagen was no longer red and transferred directly to Aniline Blue solution. Slides were rinsed, then differentiated in 1% acetic acid. Slides were quickly dehydrated, cleared in xylene, and mounted with a resinous mounting medium. Images were captured with a Leica DM4000 B LED microscope system.

4.4.6 Immunohistochemical Staining

Immunohistochemical (IHC) staining was performed on formalin-fixed paraffin-embedded tissues sectioned at 5µm thickness, then de-waxed and rehydrated by ethanol gradient. Heat-induced epitope retrieval was achieved with pre-heated sodium citrate buffer (10mM Sodium Citrate, 0.05% Tween 20, pH 6.0). Slides were blocked with 10% goat serum in 1% bovine serum albumin (BSA) and incubated with primary antibodies diluted in 1% BSA for ACE2

(1:50, R&D Systems AF933), SARS-CoV-2 nucleocapsid (1:1000, Bioss bs-41408R), CD15 (1:50, Abcam ab135377), CD68 (1:100, Thermo Fisher MA5-13324 (human); 1:100, AbD Serotec MCA1597 (hamster)), CD4 (1:100, Abcam ab133616 (human); 1:50, Millipore Sigma MABF415 (hamster)), and CD8 (1:50, Biolegend 200702). Antibody specificity was validated by staining control hamster and human hearts which do not have immune cell infiltration or virus. Antibody specificity for ACE2 was validated previously.[266] Further, antibody for ACE2 Endogenous peroxidases were blocked with 10% H_2O_2, then slides incubated with HRP-conjugated secondary antibodies (1:1000, Cell Signaling Technologies) and visualized with freshly prepared 3,3'Diaminobenzidine substrate (Abcam). Slides were counterstained with regressive Harris Hematoxylin, differentiated with 1% acid alcohol, then dehydrated by alcohol gradient, cleared, and mounted with organic mounting media. Staining was quantified as a percent area that the staining occupies over the total area of the image (Staining Area (%)) and as a count of positive staining regions per square millimeter (count/mm^2). Imaging and quantification were performed blinded to the experimental groups.

4.4.7 RT-PCR

RNA was extracted from the lung, and left ventricle of control and SARS-CoV-2-Delta infected hamsters using Trizol-chloroform. cDNA was reverse transcribed from 1µg of RNA template using SuperScript® II Reverse Transcriptase (Invitrogen). Real-time quantitative polymerase chain reaction (RT-PCR) with TaqMan premixed assays (ThermoFisher Scientific) and 25ng of cDNA was used to quantify ACE2 (Cg04585346_m1), TNF-α (Cg04607188_g1), IL-1β (Cg04576706_g1), IL-6 (Cg04486380_m1), with HPRT (Cg04448432_m1) as the housekeeping gene. Viral RNA copy number was quantified using the 2019-nCoV RUO kit (Integrated DNA

Technologies) and a serial dilution of the 2019-nCoV_N positive control (Integrated DNA Technologies). 2.5ng and 25ng of cDNA were analyzed for the lung and heart, respectively.

4.4.8 Protein Extraction

Immunoblot was performed from protein samples extracted in Trizol following removal of the aqueous phase for RNA extraction. DNA was precipitated from the organic phase with one third volume of ethanol then centrifuged at 2,000×g at 4°C for 5 minutes. Proteins were precipitated from the supernatant with ispropanol (1:1), then centrifuged at 12,000×g at 4°C. The pellet was washed with 0.3M guanidine hydrochloride in 95% ethanol and centrifuged at 12,000×g, then repeated, and then washed in ethanol by the same procedure. The supernatant was decanted and the protein pellet was dried under vacuum then re-solubilized in 500µL of CelLytic™ buffer (Sigma-Aldrich) supplemented with protease inhibitors (Roche). Samples were sonicated on ice using a tip ultrasonicator (Sonic Dismembrator Model 100, Fisher Scientific) set to level 2 in 4×20s bursts with 30s intervals.

4.4.9 Immunoblot

Extracted proteins were quantified with DC Protein Assay (BioRad), and 90µg of protein resolved by SDS-PAGE then transferred to polyvinyldene fluoride membranes in transfer buffer (25mM Tris, 192mM glycine, 20% methanol (pH 8.3)). Membranes were blocked in 5% non-fat milk and incubated with ACE2 (1:1000, Abcam) primary antibody overnight, and subsequently detected with HRP-conjugated secondary antibodies (1:4000, Cell Signaling Technology) and Clarity™ ECL substrate (BioRad). Lanes were normalized to MemCode™ total protein stain

(Thermo Fisher Scientific). Band densitometry was quantified with Image Studio Software (LI-COR Biosciences).

4.4.10 Statistical Analysis

Statistics were performed with SPSS software and graphs created with GraphPad Prism. Data are represented as mean ± SEM. Unpaired student's t-test was performed for comparisons of controls to COVID-19 patients. In comparisons exceeding two groups, cases that followed normal distribution were subject to One-way ANOVA with Dunnett's multiple comparisons test, rather nonparametric datasets were subject to Kruskal Wallis test with Dunn's multiple comparisons; *$p<0.05$, **$p<0.01$, ***$p<0.001$.

4.5 Results

Anthropometric assessment of SARS-CoV-2 infection in hamsters demonstrated weight loss compared to baseline over the course of the study and increased lung weight at the end of the 14-day period following ancestral SARS-CoV-2 infection (**Figure 4.1B**). Nasal swabs of control and ancestral SARS-CoV-2 infected animals were measured on days 1, 3 and 6 to assay viral burden (**Figure 4.1C**). Histologically, infected hamster lungs revealed multifocal parenchymal damage and thickening of the alveolar septa, indicating diffuse alveolar damage (DAD) (**Figure 4.1D**). Trichrome staining corroborated alveolar thickening; however, staining did not demonstrate substantive parenchymal fibrosis (**Figure 4.1D**). SARS-CoV-2 viral nucleocapsid staining was absent in control hamster lungs; however, SARS-CoV-2 treated hamsters displayed positive perivascular staining for viral proteins (**Figure 4.1E**).

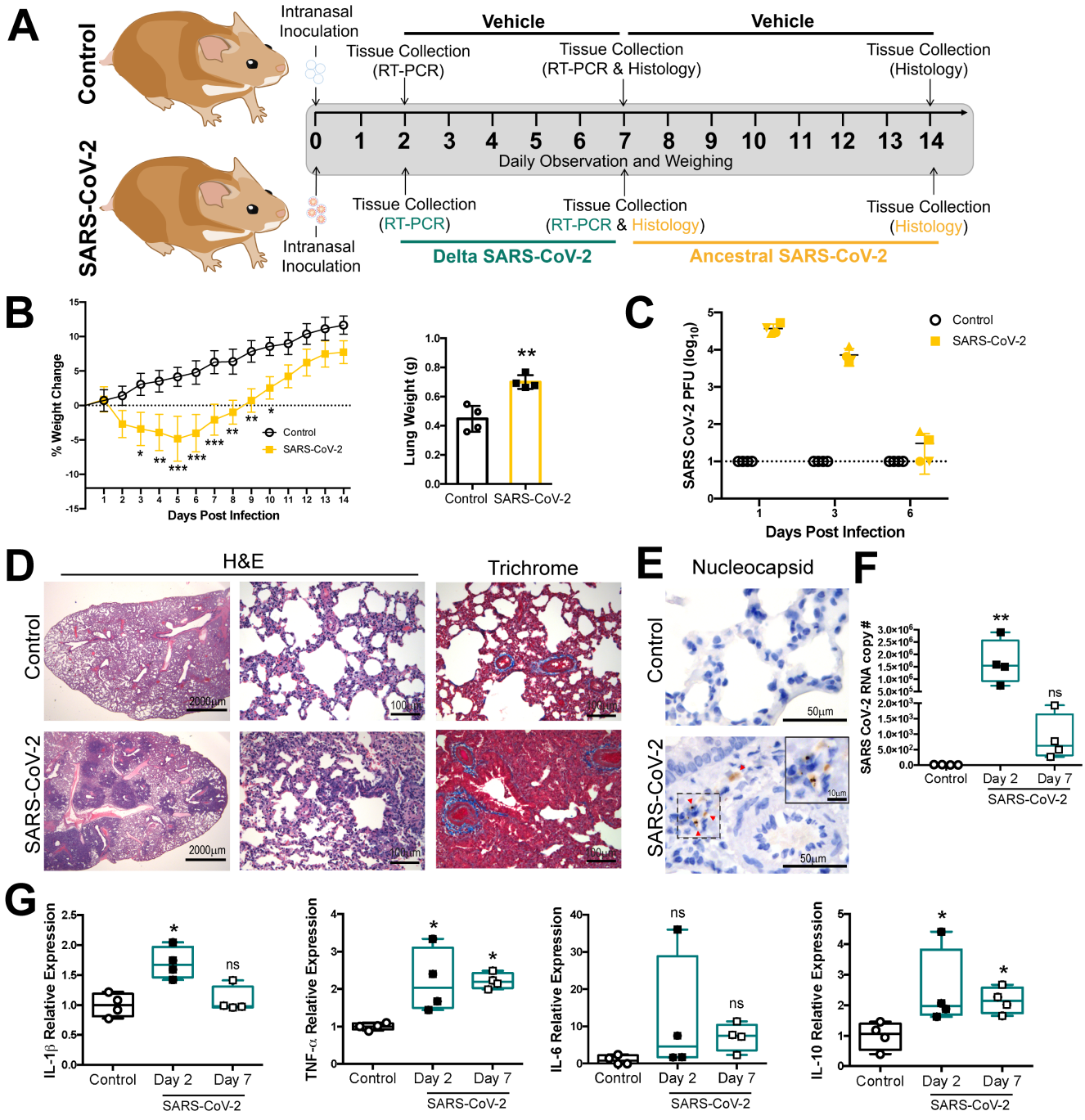

Figure 4.1. *Figure legend on next page*

Figure 4.1. SARS-CoV-2 infection induces lung injury and upregulates cytokine expression in hamsters.

A. Experimental timeline for Delta (collected at days 2 and 7 for RT-PCR) and ancestral (collected at day 7 and 14 for histopathology) SARS-CoV-2 infected hamsters. Vehicle inoculated control hamsters were analyzed in parallel. **B.** Anthropometric data of body weight and lung weight of ancestral SARS-CoV-2 infected hamsters. Body weight was measured and recorded daily, and reflected as percent of weight change relative to day 0. Time points were compared using Two-way repeated measures ANOVA and Sidak's multiple comparisons test. Lungs were harvested and weighed at the end of the 14-day study period. **C.** SARS-CoV-2 nasal swabs and plaque measurement **D.** Gross histopathological assessment of hamster lungs using Hematoxylin and eosin staining (H&E) and Masson's trichrome staining at day 7 post ancestral SARS-CoV-2 infection **E.** Staining for SARS-CoV-2 nucleocapsid protein in the lungs at day 7 post viral challenge **F.** SARS-CoV-2 viral RNA copies in the lung following SARS-CoV-2 Delta challenge **G.** Expression of IL-1β, TNF-α, IL-6 and IL-10 in hamster lungs at day 2 and day 7 following Delta SARS-CoV-2 infection. Cytokines are visualized as a relative expression compared to controls. Data are represented as mean ± SEM. Unpaired student's t-test was performed for comparisons of controls to SARS-CoV-2 treated animals. One-way ANOVA with Dunnett's multiple comparisons test or Kruskal Wallis test with Dunn's multiple comparisons were used to compare parametric or non-parametric data, respectively; *$p<0.05$, **$p<0.01$, ***$p<0.001$.

To examine earlier time points, we next analyzed control and Delta SARS-CoV-2 infected hamsters at day 2 and 7, which revealed positive amplification for SARS-CoV-2 viral RNA (**Figure 4.1F**), and increased expression of IL-1β, TNF-α, and IL-10 in lung homogenates (**Figure 4.1G**). Next, we examined myocardial changes in the hamster heart consequent of SARS-CoV-2 infection. Infected hamsters have infrequent regions of increased mononuclear infiltrates and focal fibrosis absent in control animals (**Figure 4.2A**). Further, the viral nucleocapsid was detected in the heart in ancestral SARS-CoV-2 infected animals (**Figure 4.2B**). This finding aligns with the positive amplification of SARS-CoV-2 viral RNA copies in the heart of SARS-CoV-2 Delta infected animals, supporting myocardial infection as strain and dose independent (**Figure 4.2C**). Following a basic assessment of myocardial damage and discovering SARS-CoV-2 viral proteins and RNA in the hamster heart, we aimed to investigate the consequence of infection on ACE2 levels. We first assessed the ancestral SARS-CoV-2 by histology, which demonstrated a reduction in ACE2 that persisted at both time intervals (7 and 14) (**Figure 4.2D**). Interestingly, when we examined early time points, *ACE2* expression was unchanged between control and Delta SARS-CoV-2 infected animals (**Figure 4.2E**); however, ACE2 protein levels were significantly reduced compared to controls as in the ancestral SARS-CoV-2 infected animals (**Figure 4.2F**). Next, due to the prominent myocardial inflammation present in certain COVID-19 cases,[267] we aimed to identify and quantify the immune cells of the heart following infection. Staining for mature neutrophils (CD15), macrophages (CD68), and T-cell antigens (CD4 and CD8) demonstrated a macrophage and neutrophil dominant pattern, with a mild increase in lymphocyte staining compared to control animals (**Figure 4.2G-H**). Congruently, expression of proinflammatory cytokines were mildly elevated in the heart, namely IL-1β and a trend towards an increase of TNF-α (**Figure 4.2I**).

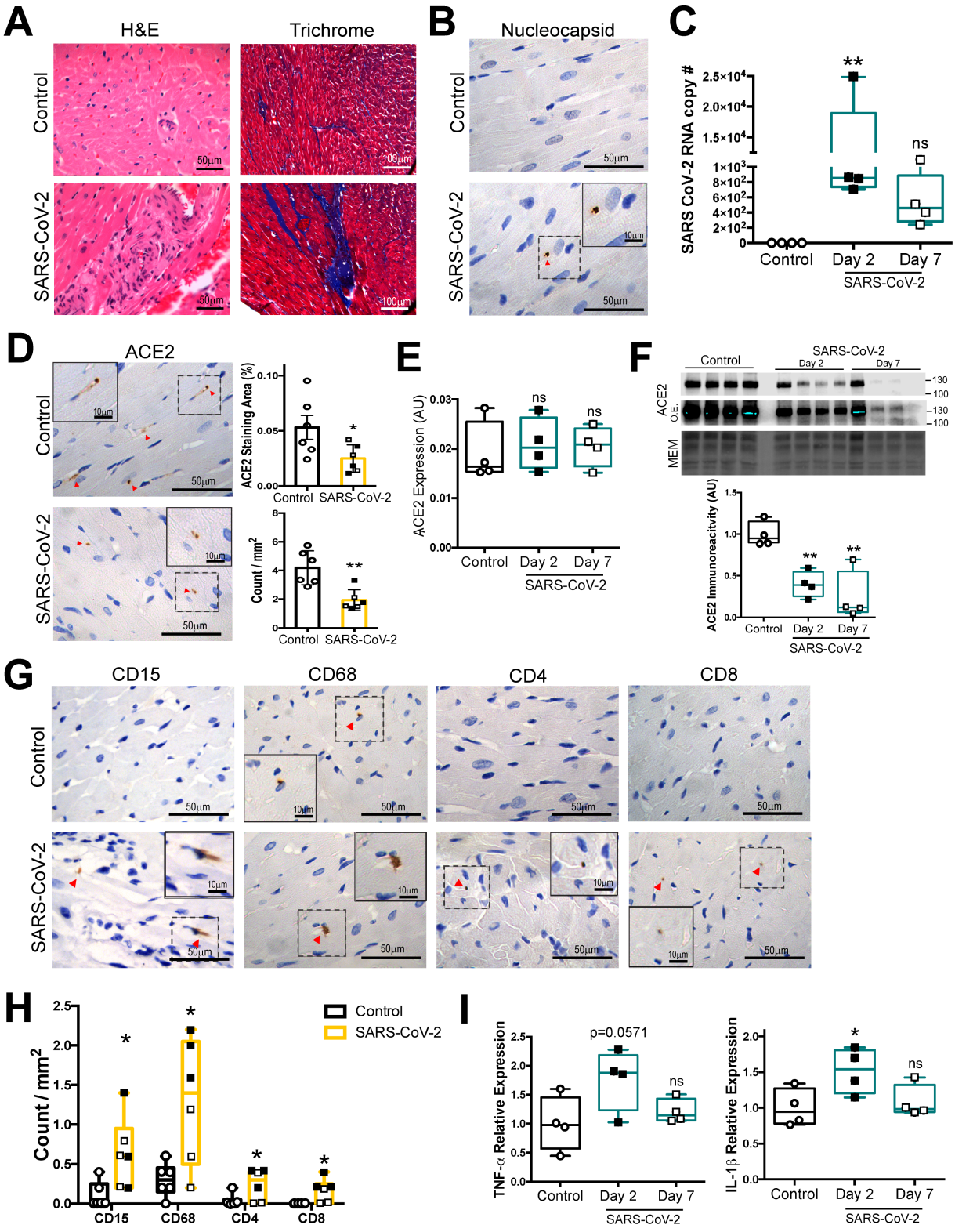

Figure 4.2. *Figure legend on next page*

Figure 4.2. SARS-CoV-2 infection downregulates myocardial ACE2 and induces immune cell infiltration in hamsters.

A. Histological assessment of hamster hearts using Hematoxylin and eosin staining (H&E) and Masson's trichrome staining 7 days following ancestral SARS-CoV-2 challenge **B.** SARS-CoV-2 nucleocapsid staining in the hamster heart at 14 days post ancestral SARS-CoV-2 infection **C.** SARS-CoV-2 viral RNA copies in the heart following SARS-CoV-2 Delta challenge **D.** Representative images and pooled analysis of ACE2 staining in the hamster heart at day 7 (empty squares) and day 14 (filled squares) following inoculation with ancestral SARS-CoV-2. ACE2 staining area (%) and the number of areas with positive staining (count/mm^2) are quantified. **E.** ACE2 mRNA expression by RT-PCR in the hamster heart at day 2 and day 7 after Delta SARS-CoV-2 infection **F.** Western blot analysis and quantification of immunoreactivity (band densitometry for protein levels) of ACE2 following Delta SARS-CoV-2 inoculation. Immunoblots were visualized at a standard exposure (*STD*), or overexposed (*O.E.*) to visualize low protein levels of ACE2. Band densitometry was quantified and normalized to MemCode™ total protein stain (MEM). **G.** Representative immune cell staining for neutrophils (CD15), macrophages (CD68), and T-cells (CD4 and CD8) in the hearts of vehicle (control) and ancestral SARS-CoV-2 inoculated hamsters at day 14, and immune cell quantification (**H**). Day 7 (empty squares) and day 14 (filled squares) are pooled for analysis **I.** Expression of TNF-α and IL-1β in hamster heart at day 2 and day 7 following Delta SARS-CoV-2 infection. IL-6 and IL-10 were below the limit of detection in the heart. Cytokines are visualized as a relative expression compared to controls. Data are represented as mean ± SEM. Unpaired student's t-test was performed for comparisons of controls to SARS-CoV-2 treated animals. One-way ANOVA with Dunnett's multiple comparisons test or Kruskal Wallis test with Dunn's multiple comparisons

were used to compare parametric or non-parametric data, respectively; *$p<0.05$, **$p<0.01$, ***$p<0.001$.

We next compared the hamster phenotype to myocardial samples of patients who died from COVID-19 (**Table 4.1**). Basic histological staining revealed extensive mononuclear infiltrates and interstitial and vascular fibrosis (**Figure 4.3A**). Viral nucleocapsid staining was predominantly perivascular in the myocardium (**Figure 4.3B**). ACE2 was significantly downregulated in COVID-19 patient's hearts compared to sex and age-matched controls (**Figure 4.3C**). Finally, the myocardium from COVID-19 patients demonstrated a significant inflammatory cell burden biased toward neutrophils and macrophages consistent with a pathological diagnosis of myocarditis in 60% of the autopsied hearts (**Figure 4.3D-E**; **Table 4.1**).

4.6 Discussion

Our data corroborate pulmonary histological findings in hamsters that mirror findings from human COVID-19 patients,[268] with a common mechanism of myocardial ACE2 downregulation that aligns with previous work from the SARS-CoV epidemic.[21] Although humans had a greater abundance of immune cell infiltrates, this difference likely reflects the enhanced severity of humans who died of COVID-19 compared to animals that survived and recovered. Nevertheless, the pattern of immune cell burden coincided in humans and hamsters, suggesting SARS-CoV-2 infection facilitates a consistent macrophage and neutrophil dominant recruitment. These findings are unexpected, as cell-mediated immune responses driven by T lymphocytes are implicated in typical cases of viral myocarditis, such as coxsackievirus B-mediated myocardial inflammation.[267]

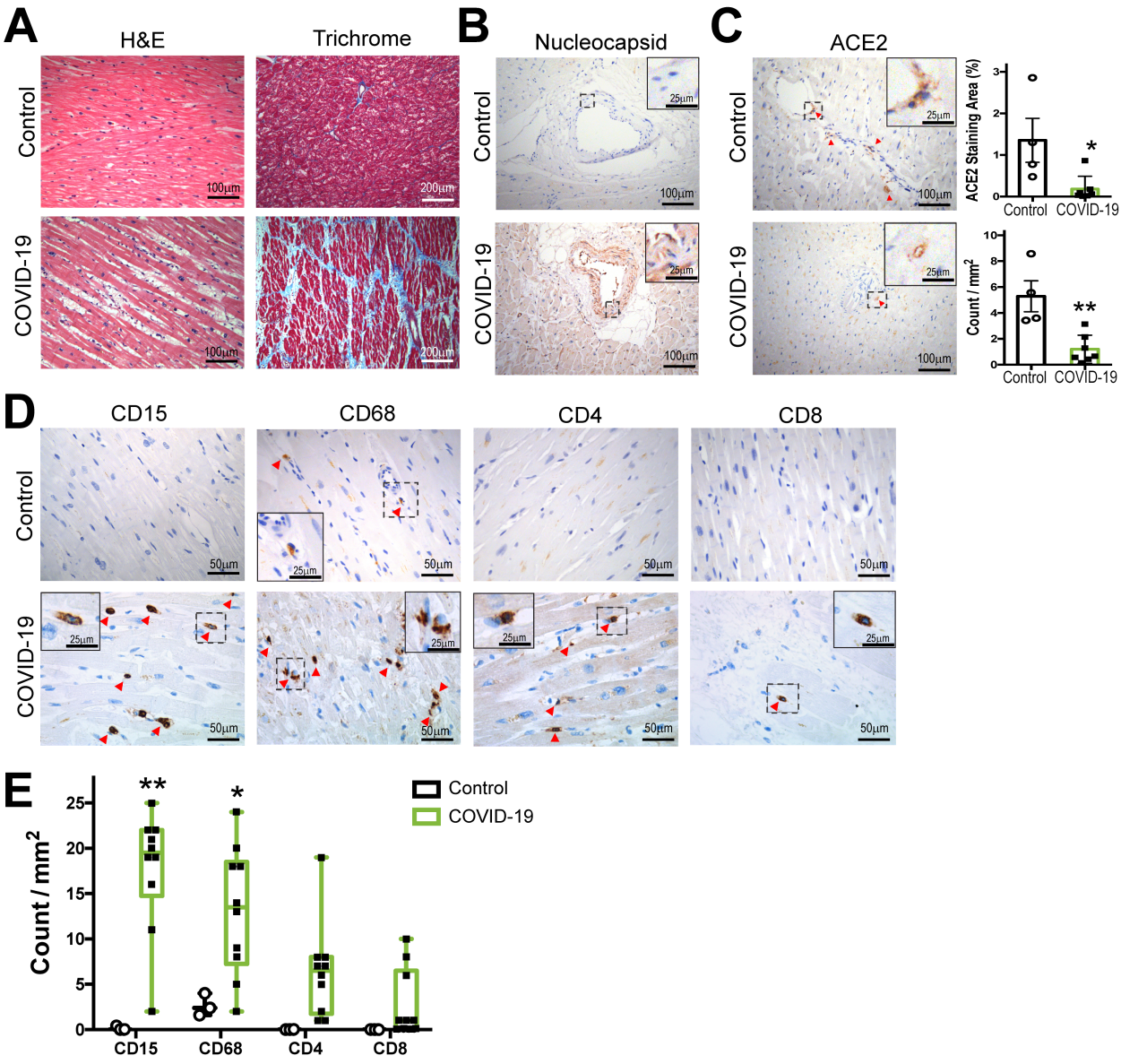

Figure 4.3. *Figure legend on next page*

Figure 4.3. Severe COVID-19 leads to myocardial ACE2 downregulation and immune cell infiltration in humans.

A. Routine histological assessment of human control and COVID-19 hearts with Hematoxylin and eosin staining (H&E) and Masson's trichrome staining **B.** SARS-CoV-2 nucleocapsid and ACE2 staining (**C**) in the human heart. ACE2 staining area (%) and the number of areas with positive staining (count/mm^2) are quantified. **D.** Immune cell staining for neutrophils (CD15), macrophages (CD68), and T-cells (CD4 and CD8) in the hearts of control and COVID-19 patients, and immune cell quantification (**E**). Data are represented as mean ± SEM. Unpaired student's t-test was performed for comparisons of controls to COVID-19 patients; *$p<0.05$, **$p<0.01$, ***$p<0.001$.

Table 4.1. Patient clinical characteristics

		Control (n=6)	COVID-19 (n=10)
Demographics			
Age, y		54.3 (47-67)	69.2 (44-86)
Sex, Male		3 (50.0)	7 (70.0)
Comorbidities			
Pre-existing Cardiac Conditions	Dilated Cardiomyopathy	0 (0)	1 (10.0)
	Ischemic Heart Disease	0 (0)	2 (20.0)
Hypertension		1 (16.7)	2 (20.0)
Diabetes Mellitus		0 (0)	1 (10.0)
Obesity		1 (16.7)	0 (0)
CKD		0 (0)	2 (20.0)
COPD		0 (0)	2 (20.0)
Acute Injury			
Myocarditis/Pericarditis		0 (0)	6 (60.0)
Arrhythmia		0 (0)	4 (40.0)
Coagulopathy		0 (0)	6 (60.0)
AKI		0 (0)	8 (80.0)
ARDS		0 (0)	10 (100)

Obesity is defined as a BMI ≥30 kg/m^2, CKD: chronic kidney disease; AKI: acute kidney injury; COPD: chronic obstructive pulmonary disease. Categorical variables are reported by count with percentage in parenthesis: sex, comorbidities, and diagnoses. Continuous variables are reported by mean with the range in parenthesis: age.

It remains unclear if SARS-CoV-2 predominately mediates direct cardiac injury because of ACE2 tropism or if myocarditis is consequent of indirect, cytokine-activated cardiotoxicity. However, we provide evidence of SARS-CoV-2 viral nucleocapsid and positive viral RNA amplification in the lungs and heart independent of viral strain and dose that appears preferentially localized to vessels. This corroborates the detectable myocardial SARS-CoV-2 viral load in the hearts of COVID-19 patients,[267] and work supporting a direct viral infection of the myocardium in a subset of post-mortem autopsy hearts in patients with SARS, which demonstrated increased fibrosis, inflammation and a reduction of myocardial ACE2.[21] Further, the localization of viral nucleocapsid and ACE2 is supported by single nucleus RNA sequencing studies that identify pericytes, vascular smooth muscle cells, and fibroblasts as harboring greatest ACE2 expression in the human left ventricle.[2]

Predominant myeloid recruitment aligns with tangential evidence emerging from the COVID-19 pandemic. Interstitial macrophages loaded with viral particles reside in the myocardium of a patient with COVID-19 mediated cardiogenic shock,[269] and macrophages are the primary cell for SARS-CoV viral replication.[270] Consistently, macrophage-derived cytokine interleukin 6 (IL-6) is part of a significant predictive signature of COVID-19 mortality.[271] Although IL-6 was below the limit of detection in hamster lung and myocardial tissue, we observed the paradoxical upregulation of anti-inflammatory cytokine IL-10 that was found to predict increased disease severity.[272]

As concomitant cardiovascular disease (CVD) in COVID-19 patients is a risk factor for severe disease, SARS-CoV-2 itself mediates myocardial damage, and SARS-CoV-2 exploits ACE2 for cellular entry, it is essential to delineate the role of ACE2 in CVD and COVID-19.[25,76,273] ACE2 is protective in CVD to counteract the proinflammatory, hypertensive arm of

the canonical renin-angiotensin system (RAS) mediated by Angiotensin (Ang) II. Specifically, ACE2 deactivates Ang II to Ang 1-7, a peptide that acts on the Mas receptor to promote vasodilation and anti-inflammatory effects.[25,60] A disintegrin and metalloprotease 17 (ADAM17) facilitates proteolytic ectodomain shedding of membrane-bound proteins, including ACE2; thus, deactivating and releasing it into the systemic circulation.[41,274] Indeed, ADAM17 is aberrantly activated in CVD, and may lead to a deficiency in membrane ACE2, which is associated with worsened outcomes in hypertension, heart failure, and coronary artery disease.[60]

SARS-CoV-2 also activates ADAM17 to foster ACE2 loss,[95] which is suggested to be critically involved in COVID-19 pathogenesis as coronaviruses that cause the common cold do not activate ADAM17.[95] We previously proposed that increased ACE2 in healthy males may confer susceptibility to SARS-CoV-2 infection;[275] however, the downstream consequence of SARS-CoV-2 is a reduction of membrane ACE2 (measured as an increase in plasma ACE2) as a result of ADAM17 activity.[60,95] Consistently, progressive elevation in soluble plasma ACE2 in an intra-individual serial sampling of hospitalized COVID-19 patients predicted cumulative mortality, similarly with increased surrogate markers of ADAM17 activity.[60] This highlights the double-edge sword of ACE2 in COVID-19, as higher ACE2 may increase SARS-CoV-2 viral load in the initial stages of infection, where viral load is positively associated with disease severity;[275] however, post-acute ADAM17 activity and viral endocytosis promotes ACE2 proteolytic shedding.[60] This suggests ADAM17 inhibition is likely a promising therapeutic target in SARS-CoV-2 infection to circumvent loss of protective membrane-bound ACE2**.**

4.7 Conclusion

Taken together, our comparative study demonstrates that hamsters exhibit similar downstream effects of SARS-CoV-2 infection as human COVID-19 patients, recapitulating myocardial damage, ACE2 downregulation, and a consistent pattern of immune cell infiltration. Therefore, ACE2 is a double-edged sword in COVID-19, such that increased ACE2 may enhance infection susceptibility in the initial stages, yet maintaining tissue levels of cardioprotective ACE2 will likely ameliorate myocardial injury. Critical to resolving the COVID-19 pandemic aftermath is screening novel therapeutic strategies; thus, the hamster model provides a means to target both the immune cell burden and loss of membrane ACE2 – two mechanisms that drive disease pathogenesis.

4.8 Funding

This study was supported by a Canadian Institutes of Health Research (CIHR) Grant – Grant Number PJT-451105.

4.9 Conflicts of Interest

The authors have no conflicts of interests to disclose.

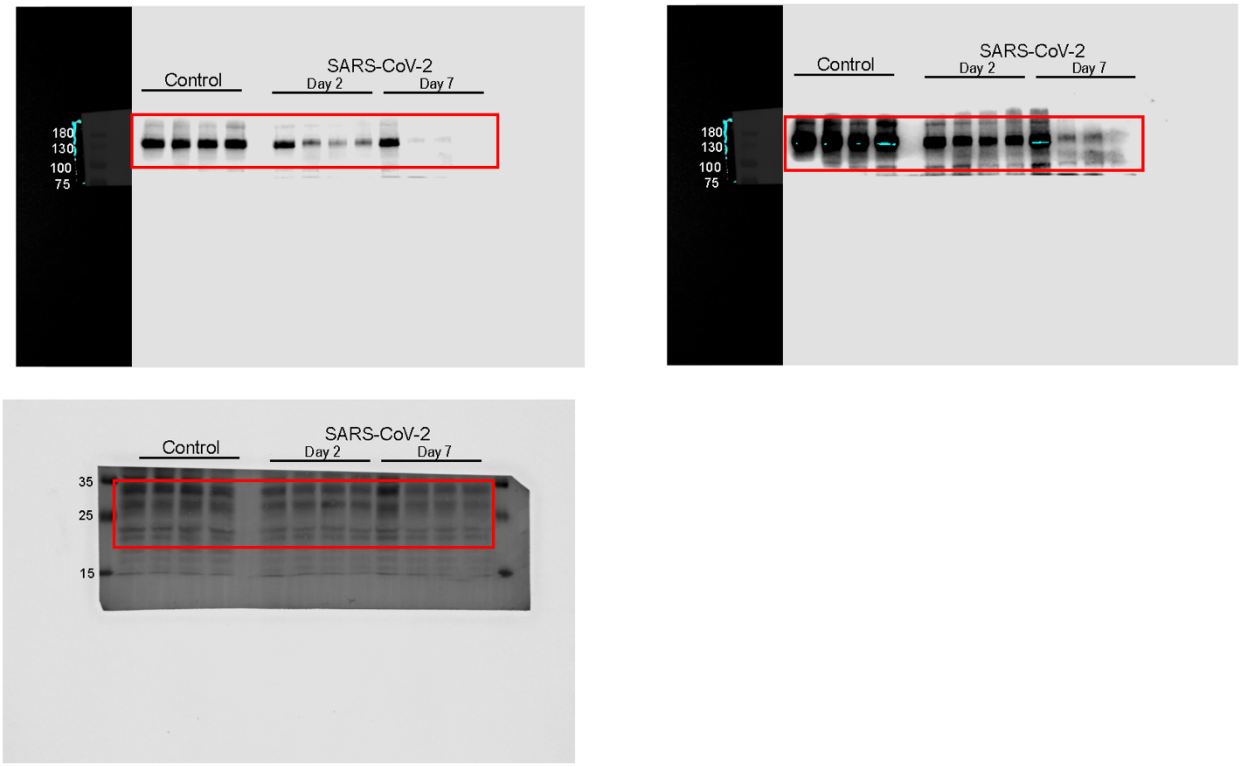

Figure 4.4. *Figure legend on next page*

Figure 4.4. Raw and uncropped western blot images from **Figure 4.2.**

Following transfer, the membrane was cut at 75 kDa to visualize ACE2 on the top (predicted molecular weight 130 kDa) and the bottom portion was stained with MemCode™ to quantify protein loading. One gel was run with samples from control, SARS-CoV-2 infected animals harvested on Day 2, and SARS-CoV-2 infected animals harvested on Day 7. The left ventricle (LV) was collected from four different animals (biological replicates) in each group. The red rectangle represents the area cropped for the corresponding figure. The standard exposure is shown on the top left, whereas the overexposed membrane is displayed on the top right

Chapter 5

The Role of miRNAs and ADAM17 in ACE2 Regulation

The Role of miRNAs and ADAM17 in ACE2 Regulation

Anissa Viveiros[1,2], Prince Addo[3], Karthik Srinivasan[3], Anran Zhang[1,2], Huachen Chen[1,2], Zamaneh Kassiri[1], Vinay Prasad[3], and Gavin Y. Oudit[1,2,4*]

[1]Department of Physiology, Faculty of Medicine and Dentistry, University of Alberta, Edmonton, Alberta, Canada
[2]Mazankowski Alberta Heart Institute, University of Alberta, Edmonton, Alberta, Canada
[3]Department of Chemical and Materials Engineering, Faculty of Engineering, University of Alberta, Edmonton, Alberta, Canada
[4]Division of Cardiology, Department of Medicine, Faculty of Medicine and Dentistry, University of Alberta, Edmonton, Alberta, Canada

A version of this chapter will be submitted to a peer-reviewed journal for consideration of publication as: ***Viveiros, A.****, Addo, P., Srinivasan, K., Zhang, A., Chen, H., Zhang, H., Prasad, V., Oudit, G.Y. The Role of miRNAs and ADAM17 in ACE2 Regulation.* This chapter has been modified from the article above.

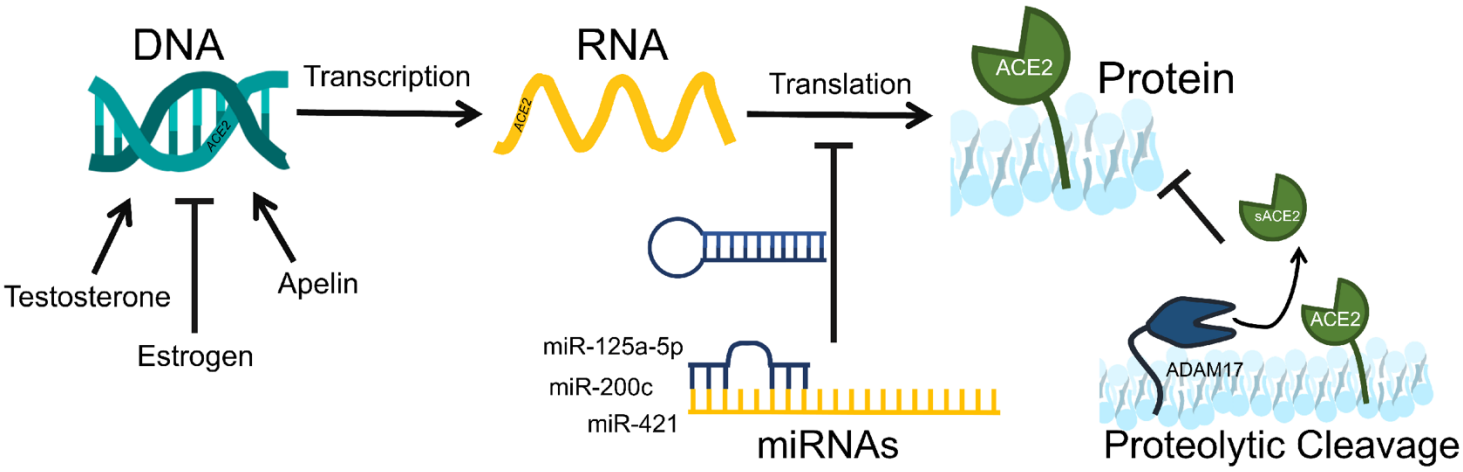

5.1 Abstract

Despite a recent resurgence in research efforts focused on ACE2 in light of serving as the endogenous receptor for SARS and SARS-CoV-2 viral entry, one of ACE2's dominant physiological roles is as the negative regulator of the renin-angiotensin system (RAS). As such, ACE2 is, first and foremost, a protective enzyme that is altered in many disease paradigms, including kidney disease, acute lung injury, and cardiovascular disease. Fundamental to targeting the counter-regulatory arm of the RAS is delineating the pathways that dictate ACE2 protein levels and activity. Here, we investigate some of the modes of regulation of ACE2, namely micro RNAs (miRNAs) and proteolytic cleavage, to begin to elucidate the contributing regulators of ACE2 in physiology and in the pathogenesis of heart failure.

Keywords: ACE2, Heart Failure, miRNAs, ADAM17

5.2 Introduction

The COVID-19 pandemic has made ACE2 one of biomedical history's most researched human molecules. However, before the discovery that SARS and SARS-CoV-2 hijack ACE2 as a cellular entry key, ACE2 was renowned as a cardioprotective enzyme.[5] ACE2 deactivates the canonical renin-angiotensin system (RAS), facilitating the breakdown of the vasoconstrictive, pro-fibrotic, and proinflammatory peptide Ang II to Ang1-7 – a peptide which opposes Ang II's effects.[5,51] Delineating the regulation of ACE2 is of paramount importance, both for understanding physiology and disease susceptibilities.

The transcriptional control of ACE2 is modified by gonadal hormones and apelin, for example.[25] However, our laboratory and others have shown that ACE2 expression does not correlate with protein levels and activity.[275,276] Analysis of the final protein levels and activity levels of ACE2 is complicated by extensive modes of post-transcriptional and post-translational regulation, two candidates of which are by micro RNAs (miRNAs) and by proteolytic cleavage.[25] miRNAs downregulate protein levels either by translational repression or by targeting mRNAs for degradation.[277] *In silico* modeling predicted miRNA 125a-5p and miRNA 200c to bind to *ACE2* mRNA.[35] In fact, transfection of miRNA 200c mimics reduced ACE2 protein levels, which was rescued upon administration of miRNA 200c inhibitors.[278] In isolated cardiac myofibroblasts, miRNA 421 also downregulates ACE2 protein levels.[37] Proteolytic cleavage is another mechanism that reduces ACE2 levels. Our laboratory and others have shown that ADAM17 cleaves the catalytic domain of ACE2 from the cellular membrane, releasing it as soluble plasma ACE2.[41,274]

Understanding how ACE2 may be impacted in heart failure is crucial for developing therapies that can upregulate the protective arm of the RAS. Here, we aim to elucidate the impact

of various nidus of control of ACE2, namely miRNAs and ADAM17-mediated proteolytic cleavage. In addition, we aim to determine if heart failure has a unique mechanism that ultimately controls final ACE2 protein levels and activity that may be distinct from non-failing controls, in an effort to understand the nuances of ACE2 regulation.

5.3 Methods

Please refer to **2.2 Human Explanted Heart Protocol**, **2.6 Picrosirius Red (PSR) Staining**, **2.7 Fresh-Frozen Immunofluorescent Staining**, **2.9 Immunoblot Analysis**, **2.10 ACE2 Activity Assay**, **2.11 ADAM17 Activity Assay**, **2.12 RNA Extraction**, **2.13 TaqMan RT-PCR** and **2.14 MicroRNA (miRNA) RT-PCR** for specific methods relevant for this chapter.

5.4 Results

5.4.1 Study cohort

We studied myocardial tissue from nineteen controls, fourty-nine patients with DCM and twenty-one patients with IHD (**Table 5.1**). Patients with HF were sex and age-matched with control donors. However, patients with IHD were moderately older than the remaining groups. The median age of control donors was 52.0 years, for DCM patients was 50.0 years, and 59.0 years for IHD patients. There was an approximately equal distribution of males and females across groups, with 52.6% male for NFC, 49.0% for DCM, and 52.4% male for IHD patients (**Table 5.1**). DCM and IHD patients had significantly increased heart weight, and a reduced left ventricular ejection fraction (LVEF) compared to the NFCs.

Table 5.1. Baseline clinical characteristics of non-failing control (NFC) donors and patients with advanced heart failure secondary to dilated cardiomyopathy (DCM) or ischemic heart disease (IHD).

	NFC (n=19)	DCM (n=49)		IHD (n=21)	
			p-value		p-value
Demographics					
Age, y	52.0 (37.0-57.5)	50.0 (39.0-58.0)	0.512	59.0 (54.0-63.0)	0.003*
BMI, kg/m^2	24.7 (23.6-27.8)	26.7 (24.1-32.1)	0.124	26.8 (24.9-31.0)	0.122
Male (%)	10 (52.6)	24 (49.0)	>0.999	11 (52.4)	>0.999
Cardiac Parameters					
VAD	0 (0.0)	19 (59.4)		28 (57.1)	
Heart Weight	324.5 (299.0-382.5)	454.0 (402.0-529.0)	<0.0001*	532.0 (597.0-667.0)	<0.0001*
LVEF	60.0 (60.0-60.0)	20.0 (15.0-30.0)	<0.0001*	20.0 (15.0-30.0)	<0.0001*
Comorbidities					
AF (%)	0 (0.0)	14 (28.6)	0.007*	1 (4.76)	>0.999
Obesity (%)	2 (10.5)	17 (34.7)	0.070	7 (33.3)	0.133
Dyslipidemia (%)	1 (5.26)	7 (14.6)	0.424	8 (38.1)	0.021*
T2DM (%)	0 (0.0)	5 (10.4)	0.312	7 (33.3)	0.009*
CKD (%)	0 (0.0)	25 (52.1)	<0.0001*	11 (52.4)	0.0002*
HTN (%)	4 (21.0)	8 (16.7)	0.729	4 (19.0)	>0.999
Medications					
ACE Inhibitors (%)	0 (0.0)	25 (54.3)		12 (63.2)	
ARB (%)	0 (0.0)	12 (30.8)		1 (6.67)	
β-Blocker (%)	0 (0.0)	38 (88.4)		14 (73.7)	
Loop diuretics (%)	0 (0.0)	40 (90.9)		15 (78.9)	
MRA (%)	0 (0.0)	39 (90.7)		10 (62.5)	
Statin (%)	0 (0.0)	20 (48.8)		14 (82.4)	
Antiarrhythmic (%)	0 (0.0)	18 (48.9)		5 (27.8)	

Obesity is defined as a BMI ≥30 kg/m^2. Chronic kidney disease (CKD) is defined as a estimated glomerular filtration rate (eGFR) of <60 mL/min/1.73 m^2. BMI: body mass index; VAD: ventricular assist device; LVEF: left ventricular ejection fraction; AF: atrial fibrillation; CKD:

chronic kidney disease; HTN: hypertension; ARB: angiotensin-receptor blockers; MRA: mineralocorticoid receptor antagonist. Categorical variables are reported by count with percentage in parenthesis: sex, comorbidities, devices, and medications. Continuous variables are reported by median with the interquartile range in parenthesis: age, BMI, heart weight. Statistical comparison was performed using Mann-Whitney U test compared to non-failing controls; *$p<0.05$.

There were no significant differences in the percentage of patients in each cohort with obesity or hypertension; however, there was a significant increase in the number of patients with dyslipidemia, diabetes, and kidney disease in the IHD group. The DCM cohort had significantly more instances of kidney disease and atrial fibrillation compared to controls (**Table 5.1**).

5.4.2 LV remodeling in HF

We confirmed increased interstitial fibrosis by picrosirius red (PSR) staining in DCM and IHD hearts (**Figure 5.1A-B**). Further, increased cardiomyocyte area was measured and quantified in DCM and IHD patients, indicative of cardiomyocyte hypertrophy (**Figure 5.1C-D**).

5.4.3 ACE2 in HF

We next aimed to assess the expression, protein levels and activity of ACE2 in HF. *ACE2* expression was significantly reduced in DCM patients compared to controls and not different in controls compared to IHD (**Figure 5.2A**). Substantial variation and no significant differences were observed with ACE2 protein levels between NFC and either DCM or IHD (**Figure 5.2B**). IHD patients demonstrated significantly higher ACE2 activity compared to controls; rather, there was no difference between patients with DCM or control donors in ACE2 activity (**Figure 5.2C**). The comparisons of NFC to IHD were made to the peri-infarct zone. As IHD is a regional disease, we next examined variations between the peri-infarct zone (adjacent to the infarct area) and the remote region (distant from the infarct area) from the hearts of patients with IHD. We noted no difference in ACE2 expression or activity; however, ACE2 protein levels were significantly reduced in the remote zone (**Figure 5.4A-C**).

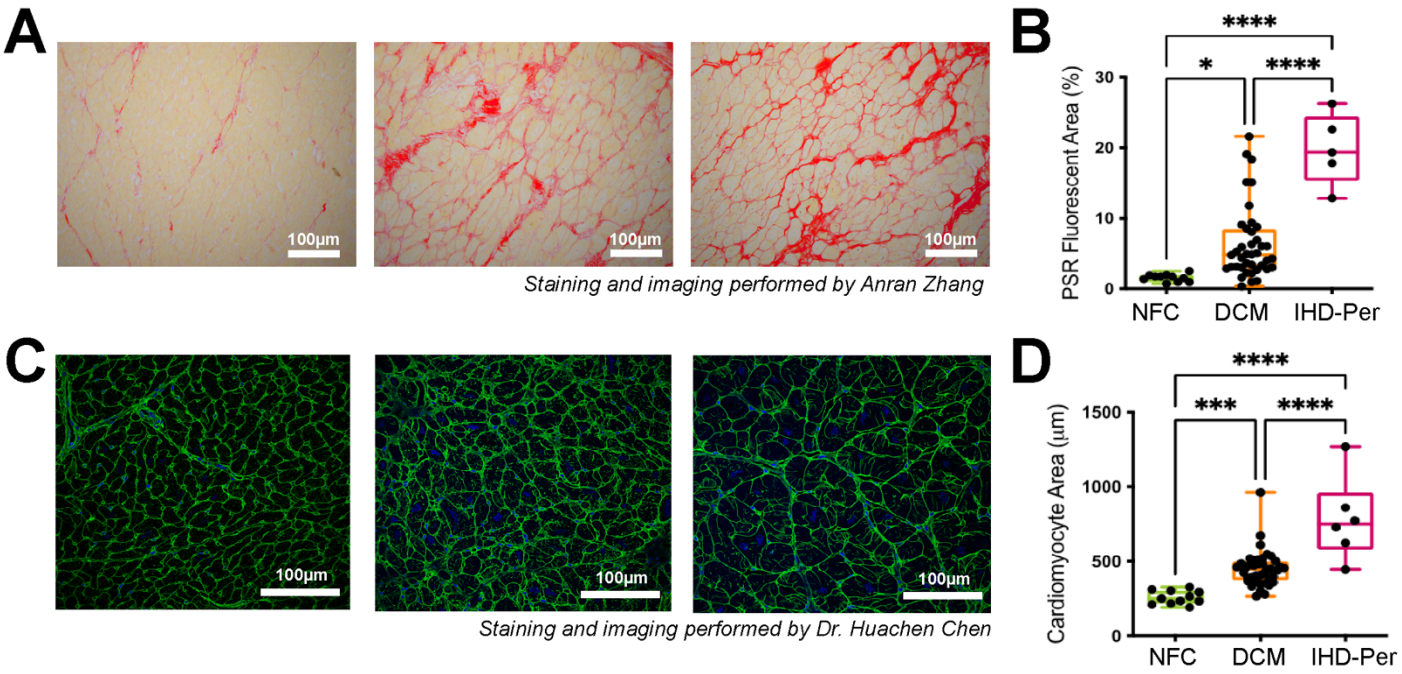

Figure 5.1. *Figure legend on next page*

Figure 5.1. Remodeling of the LV myocardium in HF.

A. Representative picrosirius red (PSR) staining of the LV myocardium in NFC, DCM and IHD patients. The peri-infarct zone was analyzed for the IHD patients. Red staining represents the deposition of collagen **B.** Quantification of PSR staining in donor and HF samples **C.** Representative images of Wheat germ agglutinin (WGA) staining in NFC, DCM and IHD myocardium. Green staining (Alexa 488) represents the WGA, which, here, delineates cardiomyocytes. The nuclei are stained in blue (DAPI) **D.** Quantification of cardiomyocyte area in NFC, DCM and the peri-infarct zone of IHD patients. Data are represented as mean ± SEM. One-way ANOVA was performed with Tukey's multiple comparisons post-hoc test; *$p<0.05$, **$p<0.01$, ***$p<0.001$, ****$p<0.0001$

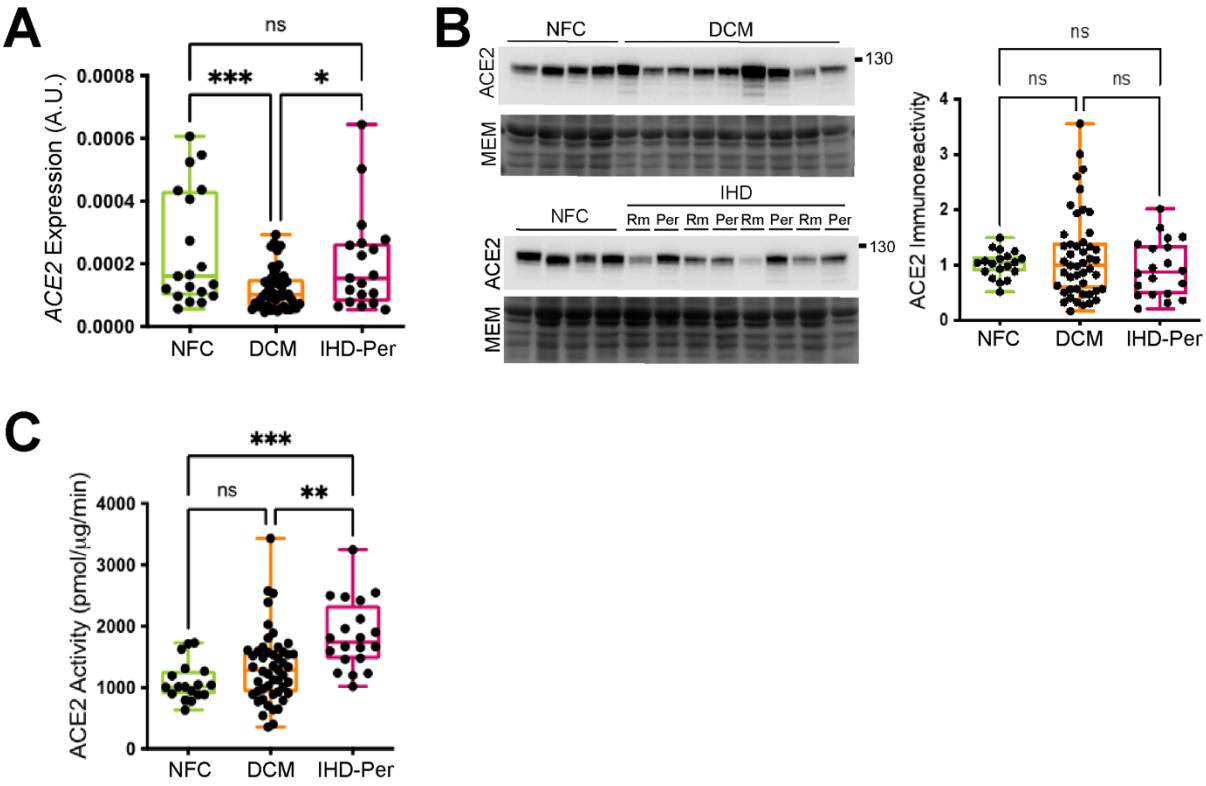

Figure 5.2. *Figure legend on next page*

Figure 5.2. ACE2 expression, protein levels and activity in NFC and HF.

A. *ACE2* expression of NFC, DCM and the peri-infarct (Per) zone of IHD patients in the LV myocardium. Expression levels were normalized to 18S as a housekeeping control **B.** Immunoblot and quantification of ACE2 protein levels in NFC, DCM and the IHD peri-infarct (Per) zone. Uncropped membranes and all replicated immunoblot membranes are shown in **Figure 5.6.** and **Figure 5.7. C.** ACE2 activity in the LV myocardium of NFC, DCM and the IHD peri-infarct (Per) zone. ACE2 activity assay was performed with a fluorogenic substrate in the presence and absence of specific ACE2 inhibitor, DX-600. A dose response curve was used to determine maximal inhibition by DX-600 in a subset of NFC and HF samples prior to analysis. Data are represented as mean ± SEM. One-way ANOVA was performed with Tukey's multiple comparisons post-hoc test; *p<0.05, **p<0.01, ***p<0.001, ****p<0.0001

5.4.4 ACE2 Regulation in HF

We assessed two modes of negative ACE2 regulation: candidate miRNAs (miRNA 125a-5p, miRNA 200c and miRNA 421) and proteolytic cleavage by ADAM17. miRNA 125a-5p expression was significantly downregulated in both DCM and IHD compared to NFC (**Figure 5.3A**). In contrast, miRNA 200c was significantly upregulated in DCM and unchanged in IHD compared to controls (**Figure 5.3B**). miRNA 421 was significantly reduced in DCM and IHD compared to controls (**Figure 5.3C**). We assessed proteolytic cleavage by measuring the protein levels and activity of ADAM17. ADAM17 protein levels were significantly increased in DCM and IHD patients compared to controls (**Figure 5.3D**). However, ADAM17 activity was unchanged in DCM compared to NFC and was reduced in IHD compared to NFC (**Figure 5.3E**). Here, the peri-infarct zone of IHD cases were used in comparisons to controls. When analyzing the miRNAs of peri-infarct and remote zones in IHD patients, miRNA 125a-5p was increased, miRNA 421 was unchanged, and miRNA 200c was reduced (**Figure 5.5A-C**). For ADAM17, the remote region had reduced protein levels and unchanged activity compared to the peri-infarct region (**Figure 5.5D-E**).

5.5 Discussion

Taken together, our data show a variable impact of the putative and known regulators of ACE2 in HF. Our findings of downregulated or unchanged *ACE2* expression in HF contrast previous studies, which found an approximately two-fold increase of *ACE2* expression in DCM and IHD compared to controls.[279] However, in the former study, the average age of controls was markedly younger and included pediatric cases (median 31 (range 3-51 years)) compared to DCM (median 51, (range 17-64 years)) and IHD (median 55.5 (range 48-62 years)).[279]

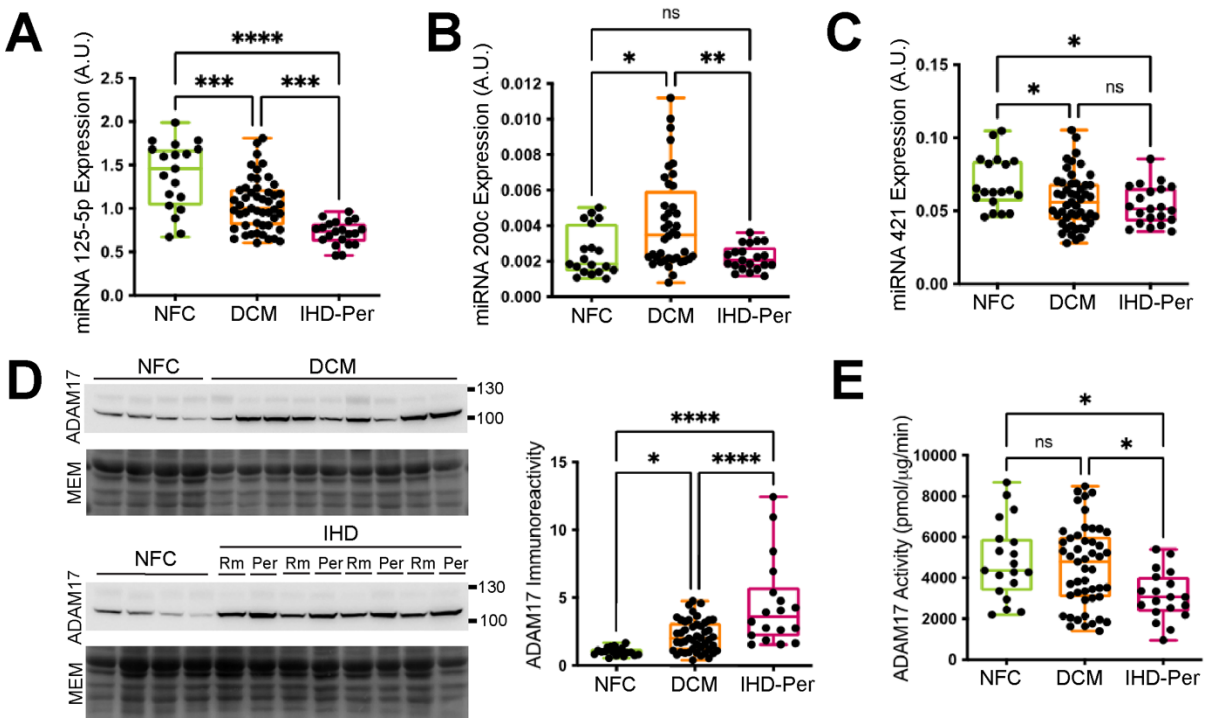

Figure 5.3. *Figure legend on next page*

Figure 5.3. Assessing modes of ACE2 regulation: miRNAs and ADAM17.

A. Expression of miRNA 125a-5p in NFC, DCM and the peri-infarct (Per) zone of IHD patients in the LV myocardium. miRNAs were normalized to miRNA 191 as a housekeeping control **B.** Expression of miRNA 200c in NFC, DCM and the peri-infarct zone of IHD patients in the LV myocardium. miRNAs were normalized to miRNA 191 as a housekeeping control **C.** Expression of miRNA 421 in NFC, DCM and the peri-infarct (Per) zone of IHD patients in the LV myocardium. miRNAs were normalized to miRNA 191 as a housekeeping control **D.** Immunoblot and quantification of ADAM17 protein levels in NFC, DCM and the IHD peri-infarct (Per) zone. Uncropped membranes and all replicated immunoblot membranes are shown in **Figure 5.8.** and **Figure 5.9. E.** ADAM17 activity in the LV myocardium of NFC, DCM and the IHD peri-infarct (Per) zone. ADAM17 activity assay was performed with a fluorogenic substrate in the presence and absence of ADAM17 inhibitor, TAPI-2. A dose response curve was used to determine maximal inhibition by TAPI-2 using recombinant human ADAM17. Data are represented as mean ± SEM. One-way ANOVA was performed with Tukey's multiple comparisons post-hoc test; *$p<0.05$, **$p<0.01$, ***$p<0.001$, ****$p<0.0001$

Given that *ACE2* expression is significantly lower in pediatric cases and increases until the age of 25 years,[280] the fact that nearly half of the controls (44%) are 25 years old or less may be a reason for the discrepancy between the former data and that of this study.[279] More recently, the integration of multiple data sets on *ACE2* expression found no differences between DCM and NFC by bulk RNA sequencing. However, cell-type specific expression of *ACE2* was dichotomous, with an increase in cardiomyocytes yet a reduction in fibroblasts, pericytes and vascular smooth muscle cells, indicating alterations in HF are cell-type specific.[2] Substantial variability was measured for ACE2 protein levels and activity, with only a moderate trend towards increased levels and activity with the exception of a significantly increased ACE2 activity in the IHD peri-infarct zone. Again, this contrasts with a previous publication that claimed a significant increase of ACE2 protein levels in HF, albeit in a small cohort (eight HF patients and eight controls), yet there was the absence of group demographics for comparison.[59]

The regulation modalities we investigated, namely miRNAs and proteolytic cleavage by ADAM17, were consistently heterogeneous. Overall, miRNAs negatively regulating ACE2 post-transcriptionally were downregulated in DCM and the IHD peri-infarct zone, namely miRNA 125a-5p and miRNA 421. miRNA 200c expression was upregulated in DCM and unchanged in the IHD peri-infarct zone; however, miRNA 200c was very lowly expressed at roughly 10-fold and 1000-fold lower than miRNA 421 and miRNA 125a-5p, respectively. Therefore, based on the overall pattern and expression levels, anticipated ACE2-regulating miRNAs are reduced in HF, albeit only miRNA 421 is demonstrated to reduce ACE2 protein levels in cardiac cells.[37] Cell-based assays are required to validate the ability of miRNA 125a-5p and miRNA 200c to reduce ACE2 protein levels as shown for miRNA 421,[37] as well as to determine the dose-

dependency of miRNA expression, and if synergism exists when these miRNAs are co-expressed.

ADAM17 protein levels and activity were discordant, with protein levels substantially elevated for both DCM and the IHD peri-infarct zone; rather, activity was unchanged and even reduced in the IHD peri-infarct. Modulating the activity levels of ADAM17 is achieved by a few mechanisms. Tissue inhibitors of metalloproteinases (TIMPs) are endogenous inhibitors of matrix metalloproteinases (MMPs) and ADAMs, including ADAM17. ADAM17 is selectively inhibited by TIMP3.[281] Although the N-terminus of TIMP4 inhibits ADAM17 *in vitro*, the full-length isoform does not; thus, the C-terminus must disrupt the inhibitory efficacy.[282,283] It is possible that the high protein levels and low activity of ADAM17 in HF are a result of inhibition by TIMP3. Variable evidence exists for the levels of TIMP3 in human HF resulting from DCM or IHD, with one study describing increased levels,[284] and another decreased.[285] Interestingly, TIMP3 deficient mice functionally phenocopy DCM, with increased cardiomyocyte hypertrophy, LV dilation, and impaired cardiac function.[286] Further, TIMP3 KO exacerbates cardiac dysfunction following myocardial infarction (MI),[287] and myocardial overexpression of TIMP3 is protective post-MI.[288] Despite evidence for the cardioprotective function of TIMP3 in animal models, the levels of TIMP3 in the human myocardium remains contested. Finally, ADAM17 activity can be modified by phosphorylation. Activation of the p38 MAPK pathway in response to Ang II activating the AT_1R phosphorylates and potentiates ADAM17 activity.[41] In all, these are a few known mechanisms that fine-tune ADAM17 activity, and further research is required to evaluate the contribution to human HF.

5.6 Conclusion

Understanding the regulation of ACE2 is critical to understanding physiology and pathophysiology, particularly in the context of ACE2-centric diseases such as CVD and COVID-19. Many putative miRNAs targeting ACE2 were downregulated in HF compared to NFCs, suggesting a mechanism to enhance ACE2 levels. The impact of proteolytic cleavage by ADAM17 was variable and may be unchanged or downregulated in HF. This pattern of reduced miRNA expression and neutral ADAM17 activity may explain the modest increase in ACE2 activity. However, it is challenging to tease apart the synergistic or antagonistic effects produced by these many modes of regulation, to determine if one is more predictive of final ACE2 protein levels or activity than others, or to determine if ACE2 regulation is distinct in disease settings. To extend the findings of this current study, applying a machine learning-based approach will be necessary to answer these critical questions and to inform strategies for the targeted increase of cardioprotective ACE2.

5.7 Acknowledgements

The authors acknowledge funding from the Canadian Institutes of Health Research (CIHR) and Heart and Stroke Foundation of Canada to GYO. The remaining authors have no funding sources to declare.

5.8 Disclosures

The authors have no conflict of interests to declare.

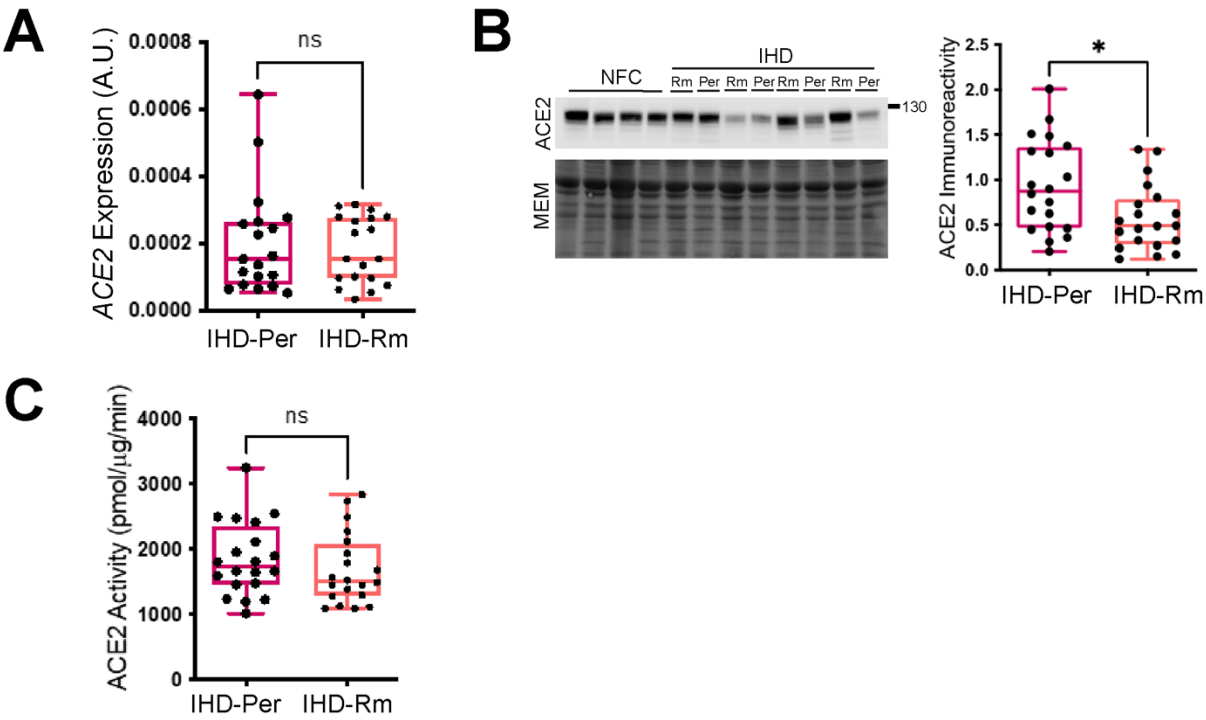

Figure 5.4. *Figure legend on next page*

Figure 5.4. Regional differences in ACE2 expression, protein levels and activity in IHD. **A.** ACE2 expression in the remote (Rm) and peri-infarct (Per) zone of IHD patients in the LV myocardium. Expression levels were normalized to 18S as a housekeeping control **B.** Immunoblot and quantification of ACE2 protein levels in remote (Rm) and peri-infarct (Per) zone of IHD patients **C.** ACE2 activity in the LV myocardium of in remote (Rm) and peri-infarct (Per) zone of IHD patients. ACE2 activity assay was performed with a fluorogenic substrate in the presence and absence of specific ACE2 inhibitor, DX-600. A dose response curve was used to determine maximal inhibition by DX-600 in a subset of NFC and HF samples prior to analysis. Data are represented as mean ± SEM. Unpaired students T-test was performed for comparison of the peri-infarct to the remote zones (IHD-Per to IHD-Rm); *$p<0.05$, **$p<0.01$, ***$p<0.001$, ****$p<0.0001$

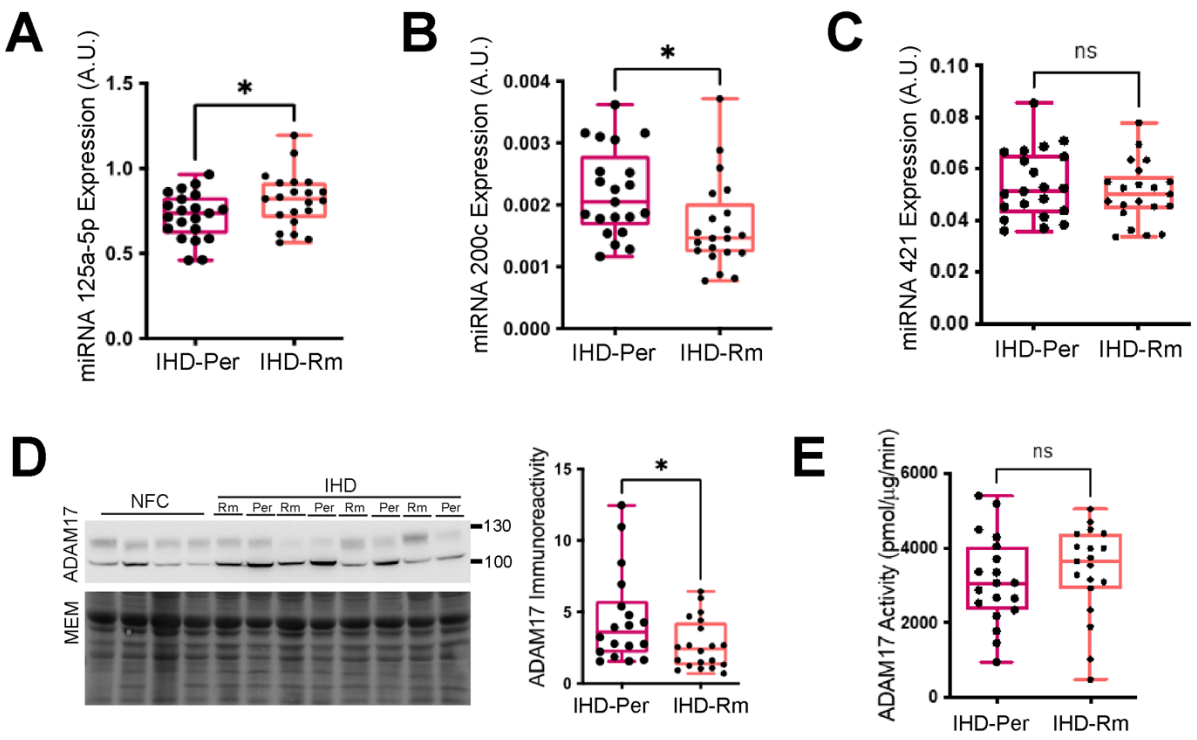

Figure 5.5. *Figure legend on next page*

Figure 5.5. Regional differences in the modes of ACE2 regulation in IHD patients.

A. Expression of miRNA 125a-5p in and the remote (Rm) and peri-infarct (Per) zone of IHD patients in the LV myocardium. miRNAs were normalized to miRNA 191 as a housekeeping control **B.** Expression of miRNA 200c in the remote (Rm) and peri-infarct (Per) zone of IHD patients in the LV myocardium. miRNAs were normalized to miRNA 191 as a housekeeping control **C.** Expression of miRNA 421 in the remote (Rm) and peri-infarct (Per) zone of IHD patients in the LV myocardium. miRNAs were normalized to miRNA 191 as a housekeeping control **D.** Immunoblot and quantification of ADAM17 protein levels in the remote (Rm) and peri-infarct (Per) zone of IHD patients in the LV myocardium. **E.** ADAM17 activity in the LV myocardium of the remote (Rm) and peri-infarct (Per) zone of IHD patients. ADAM17 activity assay was performed with a fluorogenic substrate in the presence and absence of ADAM17 inhibitor, TAPI-2. A dose response curve was used to determine maximal inhibition by TAPI-2 using recombinant human ADAM17. Data are represented as mean ± SEM. Unpaired students T-test was performed for comparison of the peri-infarct to the remote zones (IHD-Per to IHD-Rm); *p<0.05, **p<0.01, ***p<0.001, ****p<0.0001

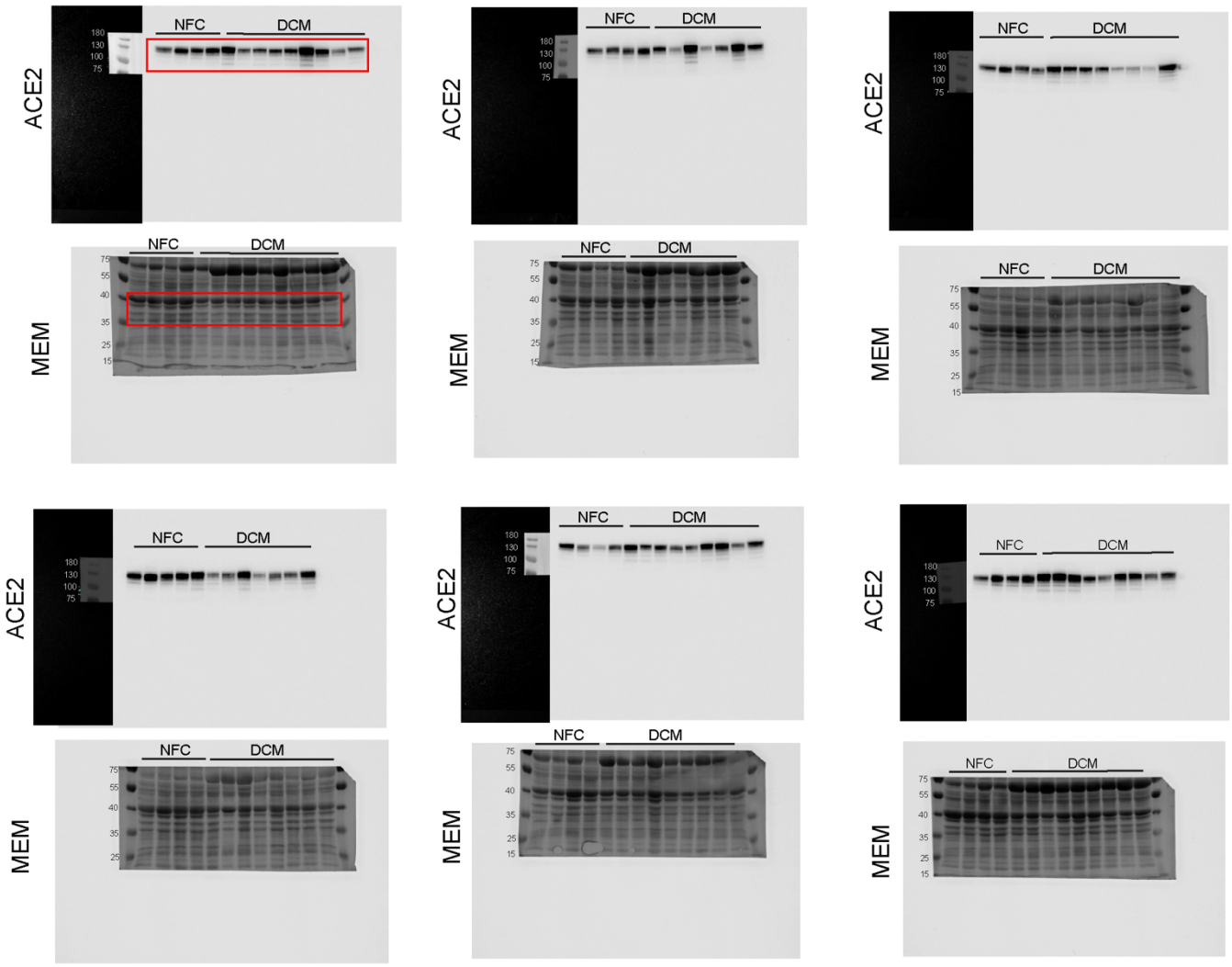

Figure 5.6. *Figure legend on next page*

Figure 5.6. Immunoblot for ACE2 in DCM.

Raw and uncropped western blot images from **Figure 5.2B**. Following transfer, the membrane was cut at 75 kDa to visualize ACE2 on the top (predicted molecular weight 130 kDa) and the bottom portion was stained with MemCode™ to quantify protein loading. Six gels were run with samples from NFC and DCM, with eight-nine DCM samples run alongside four sex- and age-matched NFCs. In total, nineteen biological replicates were analyzed for NFC and fourty-nine biological replicates for DCM. The red box denotes the portion of the blots that were cropped and used for the figure.

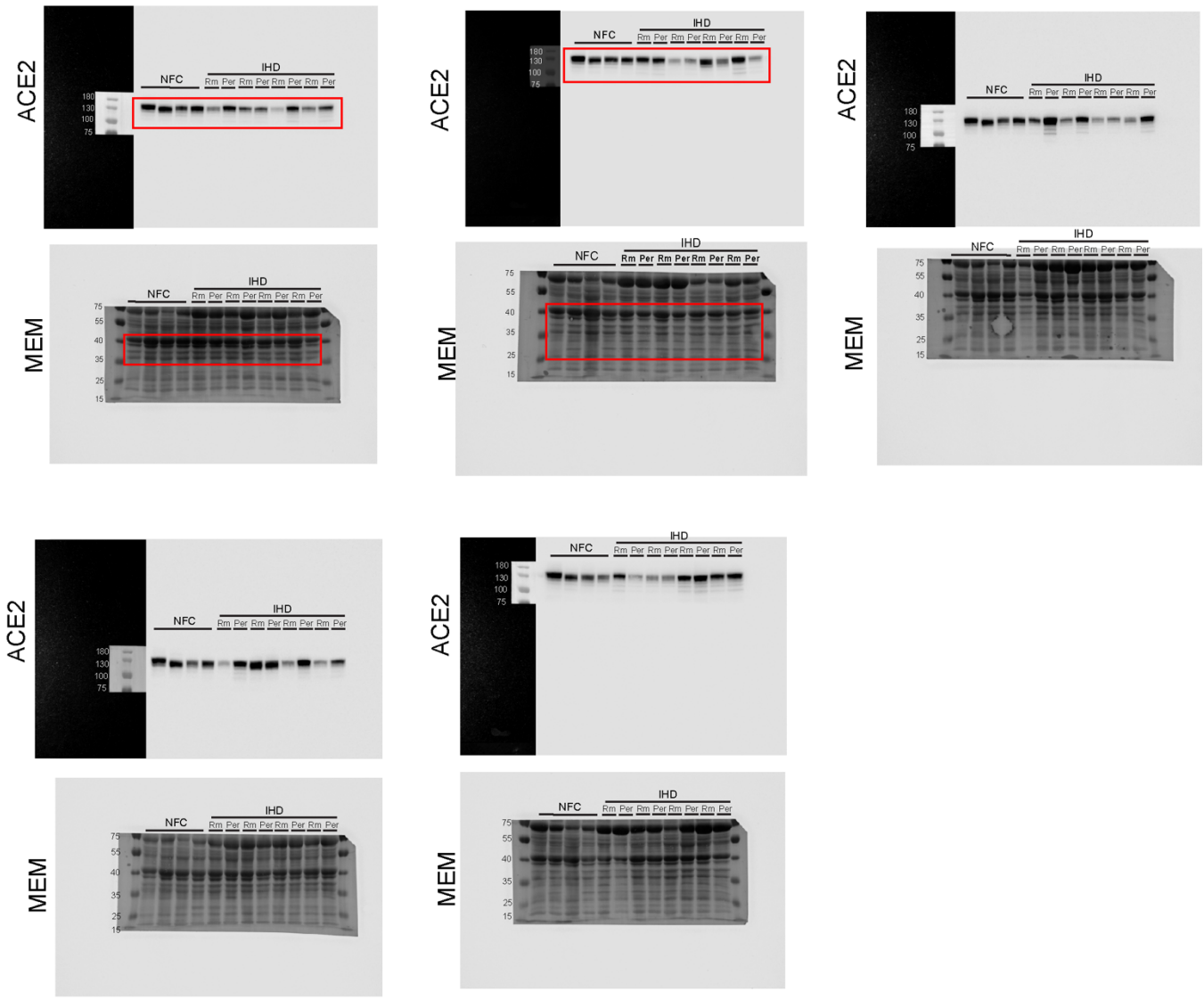

Figure 5.7. *Figure legend on next page*

Figure 5.7. Immunoblot for ACE2 in IHD.

Raw and uncropped western blot images from **Figure 5.2B** and **Figure 5.4**. Following transfer, the membrane was cut at 75 kDa to visualize ACE2 on the top (predicted molecular weight 130 kDa) and the bottom portion was stained with MemCode™ to quantify protein loading. Five gels were run with samples from NFC and IHD, with four IHD patient samples run alongside four sex- and age-matched NFCs in each gel. Samples from the IHD patients were divided into the remote (Rm) and peri-infarct (Per) region. In total, four biological replicates were analyzed for NFC and twenty-one biological replicates for IHD. The red box denotes the portion of the blots that were cropped and used for the figure.

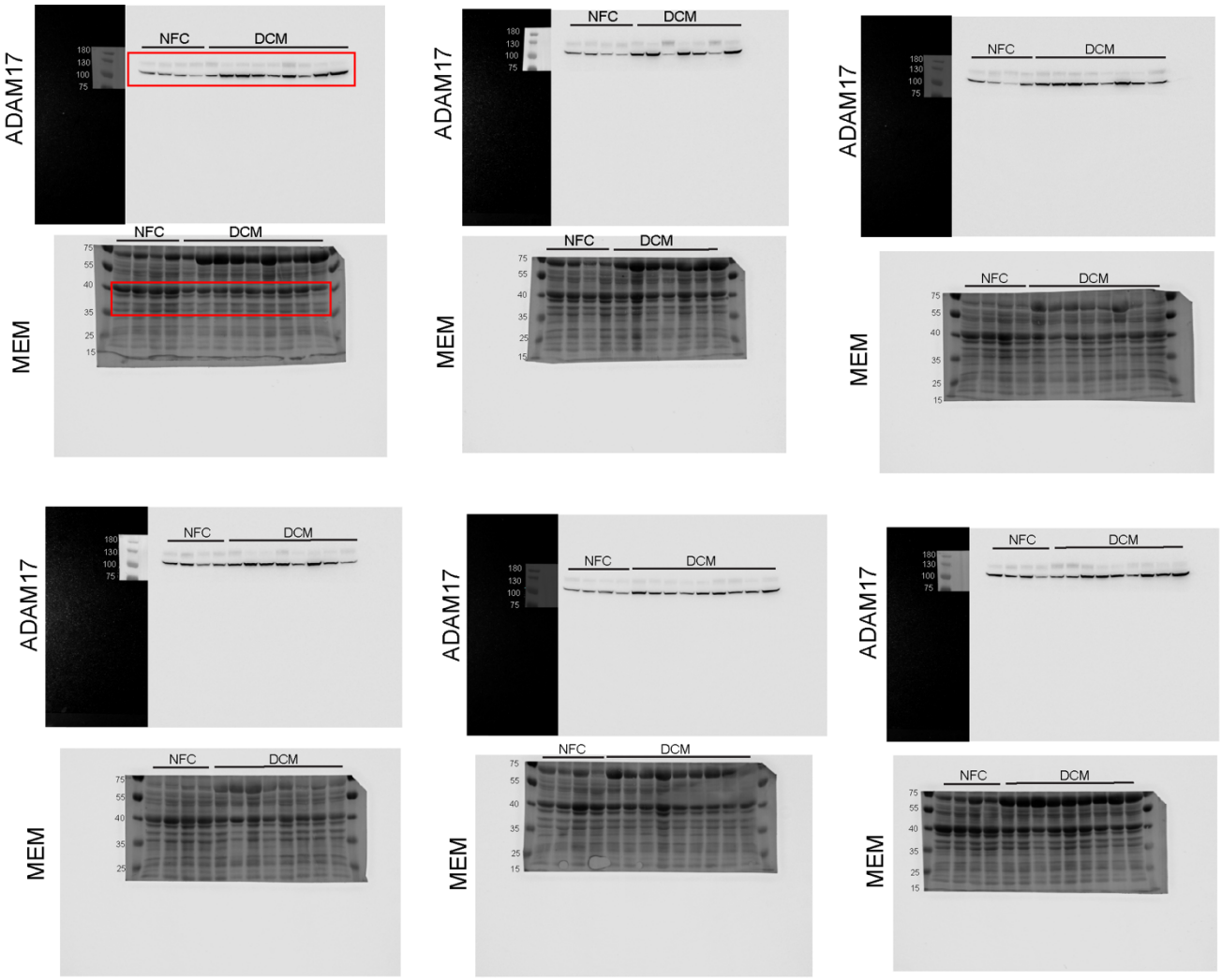

Figure 5.8. *Figure legend on next page*

Figure 5.8. Immunoblot for ADAM17 in DCM.

Raw and uncropped western blot images from **Figure 5.3D**. Following transfer, the membrane was cut at 75 kDa to visualize ADAM17 on the top (predicted molecular weight pro form: 120 kDa and mature form: 100 kDa) and the bottom portion was stained with MemCode™ to quantify protein loading. Six gels were run with samples from NFC and DCM, with eight-nine DCM samples run alongside four sex- and age-matched NFCs. In total, nineteen biological replicates were analyzed for NFC and fourty-nine biological replicates for DCM. The red box denotes the portion of the blots that were cropped and used for the figure.

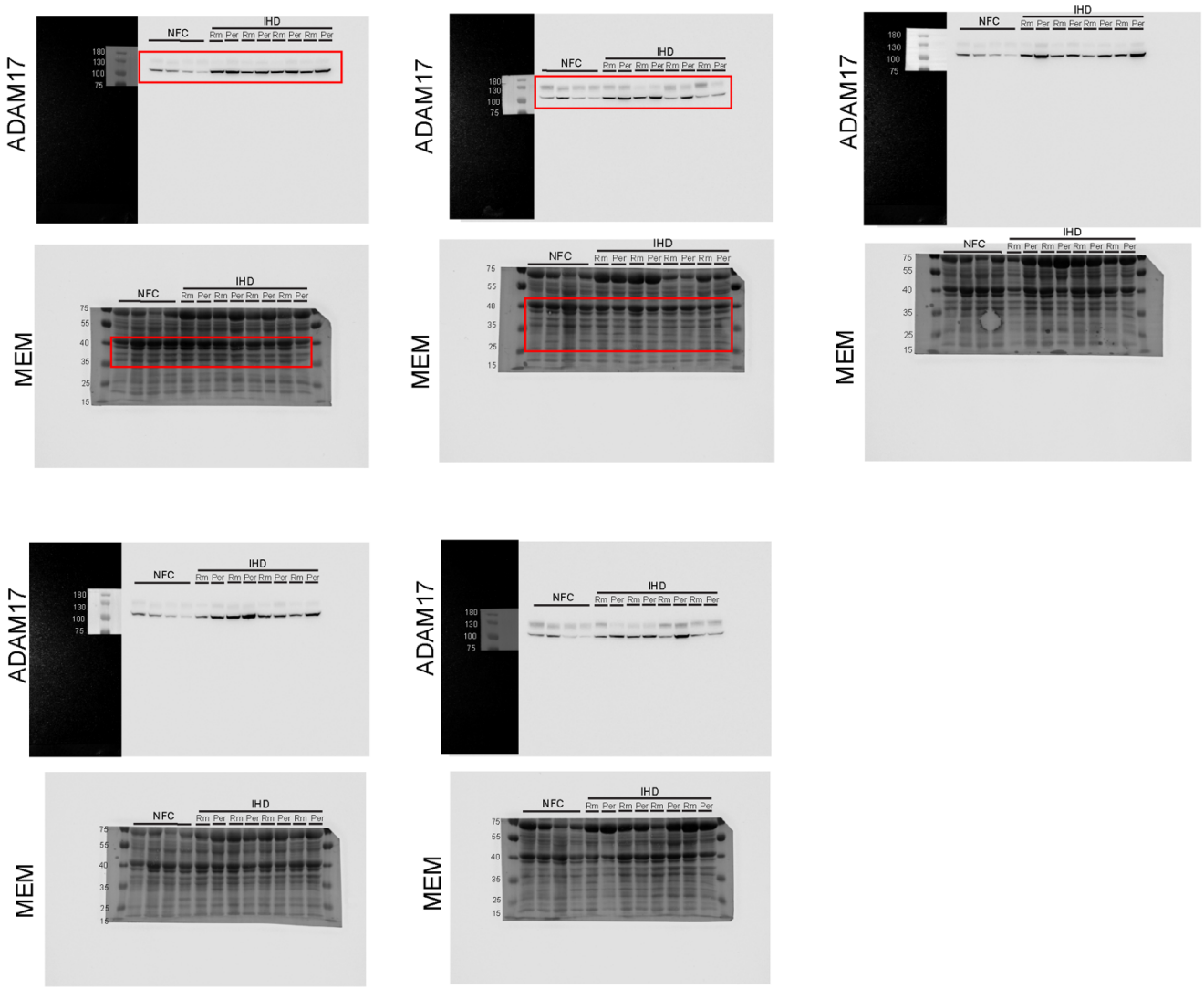

Figure 5.9. *Figure legend on next page*

Figure 5.9. Immunoblot for ADAM17 in IHD.

Raw and uncropped western blot images from **Figure 5.3D** and **Figure 5.5**. Following transfer, the membrane was cut at 75 kDa to visualize ADAM17 on the top (predicted molecular weight pro form: 120 kDa and mature form: 100 kDa) and the bottom portion was stained with MemCode™ to quantify protein loading. Samples from the IHD patients were divided into the remote (Rm) and peri-infarct (Per) region. In total, four biological replicates were analyzed for NFC and twenty-one biological replicates for IHD. The red box denotes the portion of the blots that were cropped and used for the figure.

Chapter 6

Phenotyping the Epicardial Adipose Tissue in Advanced Heart Failure: Novel Targets for Drug Discovery

Phenotyping the Epicardial Adipose Tissue in Advanced Heart Failure: Novel Targets for Drug Discovery

Anissa Viveiros[1,2]*, Kemar J. Brown[3,4]*, Huachen Chen[1,2], Anran Zhang[1,2], Mobin Khoramjoo[1], Yuri Kim[3], Jonathan G. Seidman[4], Christine E. Seidman[4,5], and Gavin Y. Oudit[1,2,6*]

[1]Department of Physiology, Faculty of Medicine and Dentistry, University of Alberta, Edmonton, Alberta, Canada
[2]Mazankowski Alberta Heart Institute, University of Alberta, Edmonton, Alberta, Canada
[3]Cardiac Unit, Massachusetts General Hospital, Boston, Massachusetts, United States
[4]Department of Genetics, Harvard Medical School, Boston, Massachusetts, United States
[5]Cardiovascular Division, Brigham and Women's Hospital, Boston, Massachusetts, United States
[6]Division of Cardiology, Department of Medicine, Faculty of Medicine and Dentistry, University of Alberta, Edmonton, Alberta, Canada

*indicates authors contributed equally to this work

A version of this chapter will be submitted to a peer-reviewed journal for consideration of publication as: ***Viveiros, A.****, *Joseph, K.B.**, *Chen, H., Zhang, A., Seidman, J.G., Seidman, C.E., Oudit, G.Y. Phenotyping the Epicardial Adipose Tissue in Heart Failure: Novel Targets for Drug Discovery.* This chapter has been modified from the article above.

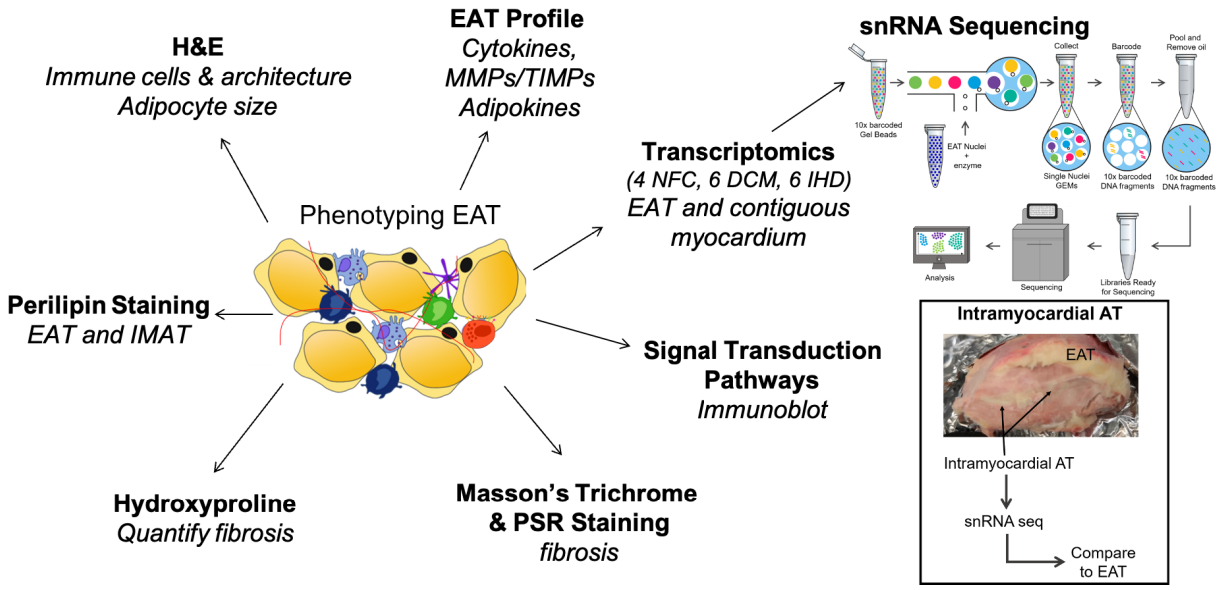

6.1 Abstract

The epicardial adipose tissue (EAT) is the true adipose tissue of the heart and is contiguous with the myocardium without barrier. As a highly bioactive secretory tissue depot of adipokines and cytokines, the EAT contributes to health and disease. There is a significant gap in knowledge in phenotyping the EAT and understanding its role in heart failure (HF), particular in HF with reduced ejection fraction (HFrEF) where we note a remarkable expansion of the EAT. Here, we employ single-nucleus RNA sequencing (snRNA Seq) and molecular techniques to phenotype the EAT in HFrEF caused by dilated cardiomyopathy (DCM) and ischemic heart disease (IHD). We identify signal transduction pathways and components of the local renin-angiotensin system (RAS) as potential targets to ameliorate EAT dysfunction in HF.

Keywords: Heart Failure, Epicardial Adipose Tissue, adipocyte, ACE2

6.2 Introduction

Adipose tissue (AT) was initially regarded as a neutral lipid storage organ; however, the role of AT as an endocrine organ in physiology and pathophysiology is increasingly recognized.[158,289] Specifically, visceral AT has a distinct secretasome that modulates the function of various organs. Here, we will focus on the epicardial adipose tissue (EAT) as the true AT depot of the heart. The EAT resides beneath the visceral pericardium and modulates the myocardium due to this physical proximity and through sharing of a common microcirculation.[158] The EAT serves as a regulator of fatty acid (FA) homeostasis, an energy source for the myocardium, and secretes anti-inflammatory adipokines.[147,154] However, the EAT becomes pathogenic in metabolic disorders, such as obesity and type 2 diabetes mellitus (T2DM), shifting the balance towards the aberrant release of FAs generating lipotoxicity, proinflammatory cytokine generation, and the infiltration of mast cells, macrophages, and neutrophils to potentiate a state of chronic low-grade inflammation.[147,158,165,166]

As such, the role of the EAT in the pathogenesis of obesity and heart failure with preserved ejection fraction (HFpEF) is established. Obesity increases EAT thickness and immune cell infiltration,[158] and increased EAT volume and expansion correlates with enhanced coronary artery calcification and predicts future coronary events.[290] In accordance, caloric excess drives adipocyte hypertrophy, adipocyte hypoxia, and consequent immune cell residency and inflammatory cytokine generation.[154,291] Adipocyte hypertrophy is a response for the storage of excess fatty acids, which is initially adaptive for nutrient buffering. However, adipocyte hypertrophy can be pathogenic when the capacity is exceeded, leading to adipocyte hypoxia and the accumulation of ectopic adipose tissue.[292]

Finally, the EAT contributes to dysfunction in HFpEF, a disease characterized by left ventricle (LV) diastolic dysfunction and preserved ejection fraction, with a high burden of comorbidities, including obesity and T2DM.[196,293] EAT expansion is a prognostic marker of poor outcomes in HF patients with mid-range or preserved LV ejection fraction (LVEF).[294] EAT accumulation is associated with impaired diastolic filling, increased vascular stiffness, and compromised coronary microcirculation.[202-204,289] Indeed, patients with HFpEF and concomitant obesity demonstrate increased EAT thickness and a proinflammatory cytokine profile, a phenotype that precedes the clinical diagnosis of HF. Therefore, the mechanistic connection between increased myocardial stiffness and EAT expansion fundamentally relies on EAT-mediated inflammation and fibrosis.[127]

Despite evidence for obesity and HFpEF, studies on the contribution of EAT expansion and inflammation in heart failure with reduced ejection fraction (HFrEF) are limited. Clinically, HFrEF is characterized by a reduced LVEF (<40%) that presents with dyspnea, peripheral edema and fatigue. HFrEF is further classified as non-ischemic, dilated cardiomyopathy (DCM) or ischemic heart disease (IHD) secondary to myocardial infarction or chronic CAD.[46-48] Data from imaging studies with cardiac magnetic resonance (CMR) indicates a reduction of EAT volume in HFrEF;[295,296] however, this contradicts echocardiography-based assessment, where EAT thickness was increased in CAD patients independent of obesity status.[297] There are many limitations of imaging techniques to quantify the EAT, namely in differentiating the EAT and pericardial adipose tissue (PAT).[298] As such, many studies erroneously identify the EAT as the PAT, and the nomenclature is used interchangeably to discuss the same tissue depot.[145,289] Further, measuring both the thickness and the total volume of EAT by CMR has the highest intra- and inter-observer variability, contributing to error.[298] Therefore, this further corroborates

the potential technical disadvantage of EAT analysis by CMR and the need for molecular insights that extend beyond imaging modalities.

Limited studies have assessed the transcriptomic signature of the EAT in HF. The analysis of adipocytes by single cell RNA sequencing (scRNA Seq) is challenged by the buoyancy and large size of adipocytes; thus, they are excluded from many scRNA Seq datasets.[299-301] To circumvent this challenge, a recent study examined the bulk RNA expression of fifteen adipose tissue depots from human donors, including the EAT.[302] Of the visceral AT, the EAT comprised a distinct expression pattern characterized by genes involved in myocardial function, apoptosis, coagulation, and immune signaling.[302] However, caution should be heeded in interpretation, as many of these donors succumbed to cardiac death or CVD was a significant comorbidity (MI or HF; 42%), there was a limited sample size (n=12), the samples were collected post-mortem, and the donors were of advanced age (median 84.5 (IQR 81.5-88.5)).[302] Nevertheless, this study highlights the unique features of the EAT that we sought to reveal further. We harnessed single nucleus RNA sequencing (snRNA Seq), which also curtails the challenges of scRNA Seq, as the nuclei are extracted prior to analysis. Here, we aimed to directly phenotype the EAT in human HFrEF using molecular, histological, and transcriptomic approaches to assess the contribution of this adipose tissue depot to disease pathogenesis.

6.3 Methods

Please refer to **2.2 Human Explanted Heart Protocol**, **2.3 Hematoxylin and Eosin**, **2.4 Trichrome Staining**, **2.7 Formalin-fixed Paraffin Embedded (FFPE) Immunofluorescent Staining**, **2.9 Immunoblot Analysis**, **2.15 Single-nucleus RNA Sequencing (snRNA Seq)**, **2.16 Genotyping**, **2.17 Quantification of Hydroxyproline Content**, **2.18 Removal of Excess**

Lipids (RELi) Protein Extraction, and **2.19 Multiplex Cytokine Assay** for specific methods relevant for this chapter.

6.4 Results

6.4.1 Study cohort

We studied the EAT from a total of ten non-failing control donors (NFC), thirty-two patients with dilated cardiomyopathy (DCM) and twenty-two patients with ischemic heart disease (IHD), for a total of fifty-four patients with HF. HF patients were sex, age, and body mass index (BMI) matched to the NFC donors. The median age of control donors was 54.0 years, 55.0 years for DCM patients, and 57.5 years for IHD patients. The median BMI for NFC, DCM and IHD was 25.0, 26.1, and 27.2, respectively. There was an approximately equal distribution of males and females across all groups, with 50% male for both NFC and DCM and 59% male for IHD patients (**Table 6.1**). DCM and IHD patients had significantly increased heart weights and a reduced LVEF compared to the NFCs, as would be anticipated for patients with HFrEF. There were no significant differences in the percentage of patients in each cohort with dyslipidemia, obesity, or hypertension; however, there was a significant increase in the number of patients with diabetes in the IHD group. The DCM cohort had higher kidney disease and atrial fibrillation incidence than controls (**Table 6.1**).

6.4.2 Region-associated cell type composition

We performed an initial pilot study using snRNA Seq to compare the cell-type abundance of the EAT to the contiguous LV (**Figure 6.1A**). For this analysis, the sixteen hearts included in the snRNA Seq data, representing an equal proportion of males and females, and independent of

etiology, were pooled and analyzed (**Figure 6.1B**). Integrated data across samples were projected using Uniform Manifold Approximation and Projections (UMAPs). As reported previously, in the combined object, clustering identified the major cells types, including ventricular cardiomyocytes (CMs), pericytes and smooth muscle cells (Mural, MCs), endothelial cells (ECs), immune cells (lymphoid, Lym; myeloid, Mye), fibroblasts (FBs), neuronal cells (NCs), adipocytes (ADs), and mast cells (**Figure 6.1C**).[245] As expected, the adipocyte population is markedly expanded when the EAT samples are combined into the LV object (**Figure 6.1D**). The EAT is primarily comprised of adipocytes, fibroblasts and myeloid cells, with a lower proportion of the remaining cell types including lymphoid, mural cells and neuronal cells. The EAT is virtually devoid of cardiomyocytes, and the small proportion likely represents contamination from the LV (**Figure 6.1D-E**). Besides adipocytes, the EAT is enriched for myeloid cells, fibroblasts, and lymphoid cells. The EAT is relatively devoid of cardiomyocytes and contains a lower proportion of mural and neuronal cells than the LV. The EAT and LV have a similar proportion of endothelial cells (**Figure 6.1E**).

6.4.3 The EAT in HF

The EAT is significantly expanded in HF and extends beyond the atrioventricular and interventricular grooves – a finding independent of HF etiology and obesity status (**Figure 6.2A**). To explore increased ectopic adipose tissue accumulation on failing hearts and to understand the impact of this phenotype, we further subgrouped the snRNA Seq analysis into those with HF or controls (**Figure 6.2B**). Global cell-type expression revealed the HF cohort contains a different proportion of the major cell types, with a higher proportion of adipocytes and fewer fibroblasts (**Figure 6.2C**).

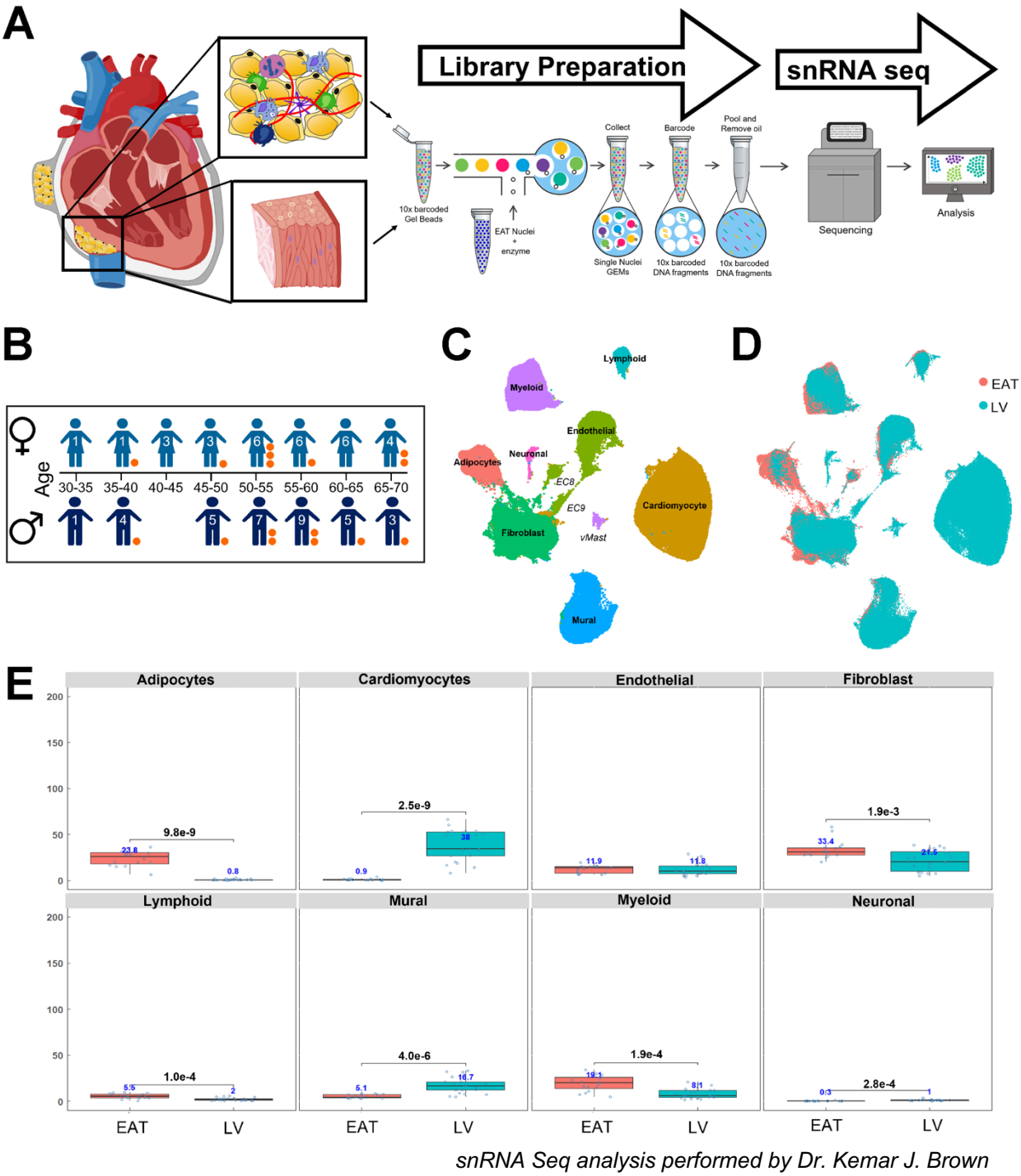

snRNA Seq analysis performed by Dr. Kemar J. Brown

Figure 6.1. *Figure legend on next page*

Figure 6.1. Pilot single-nucleus RNA sequencing study in the EAT and contiguous LV. **A.** Schematic workflow of the collection and snRNA Seq of the EAT with the contiguous LV. **B.** Pooled male and female paired myocardial and EAT samples utilized for this study. The samples used specifically for the snRNA Seq analysis are indicated by the orange circles. Each circles represents a single patient or donor. **C.** Uniform Manifold Approximation and Projection (UMAP) of the combined EAT and LV object with annotated cell-types. **D.** Uniform Manifold Approximation and Projection (UMAP) of the combined EAT and LV object separated by region. Nuclei originating from the EAT are labeled in pink and nuclei from the LV are indicated in blue. **E.** Comparison of the cell-type distribution between the EAT (pink) and the LV (blue). Data are represented as mean ± SEM. Unpaired students T-test was performed for comparison of the EAT to the LV. p-values were adjusted for multiple testing using Bonferroni correction.

6.4.4 HF possesses unique adipocyte cell states

The adipocytes were further subclustered into cell states (**Figure 6.2D**). These cell states contain a common transcriptional profile that identifies them as within the adipocytes; however, also as clusters that express distinct genes that imply a unique biological impact. The analysis of adipocytes was robust in our dataset, as previous studies captured a limited number of cells since the LV does not harbour a substantial number of adipocytes.[245] We annotated the same three states identified in DCM and control LVs previously:[243,245] canonical AD1, expressing lipid and lipoprotein metabolism and lipolytic genes, stromal AD2, expressing ECM genes such as *DCN*, and immune responsive AD3, expressing *OSMR* and inflammatory and cytokine-responsive genes (**Figure 6.2D**). We did not identify AD1.1, which was found almost exclusive to DCM hearts and expressed alterations in genes involved in fatty acid metabolism, such as a downregulation in *DGAT2*.[245]

However, a fourth cell state, AD3.1, was identified and abundant in diseased EAT. Differentially expressed genes (DEGs) in AD3.1 suggests proliferating and adipogenic adipocytes expressing *JUN* and *FOSB* (**Figure 6.2E**).[303-305] *ANXA1* was also highly expressed in AD3.1 (**Figure 6.2E**). In the EAT from HF patients compared to controls, we observed a trend towards increased AD3.1 and AD2 (**Figure 6.2F**). The proportion of adipocytes that reside in the myocardium in HF favoured AD1 over AD2, matching the profile of the EAT from HF and NFC. Rather, the myocardial adipocytes in NFC were predominantly AD2, suggesting a different biological origin and function of the adipocytes of the LV in healthy and disease (**Figure 6.2F**).

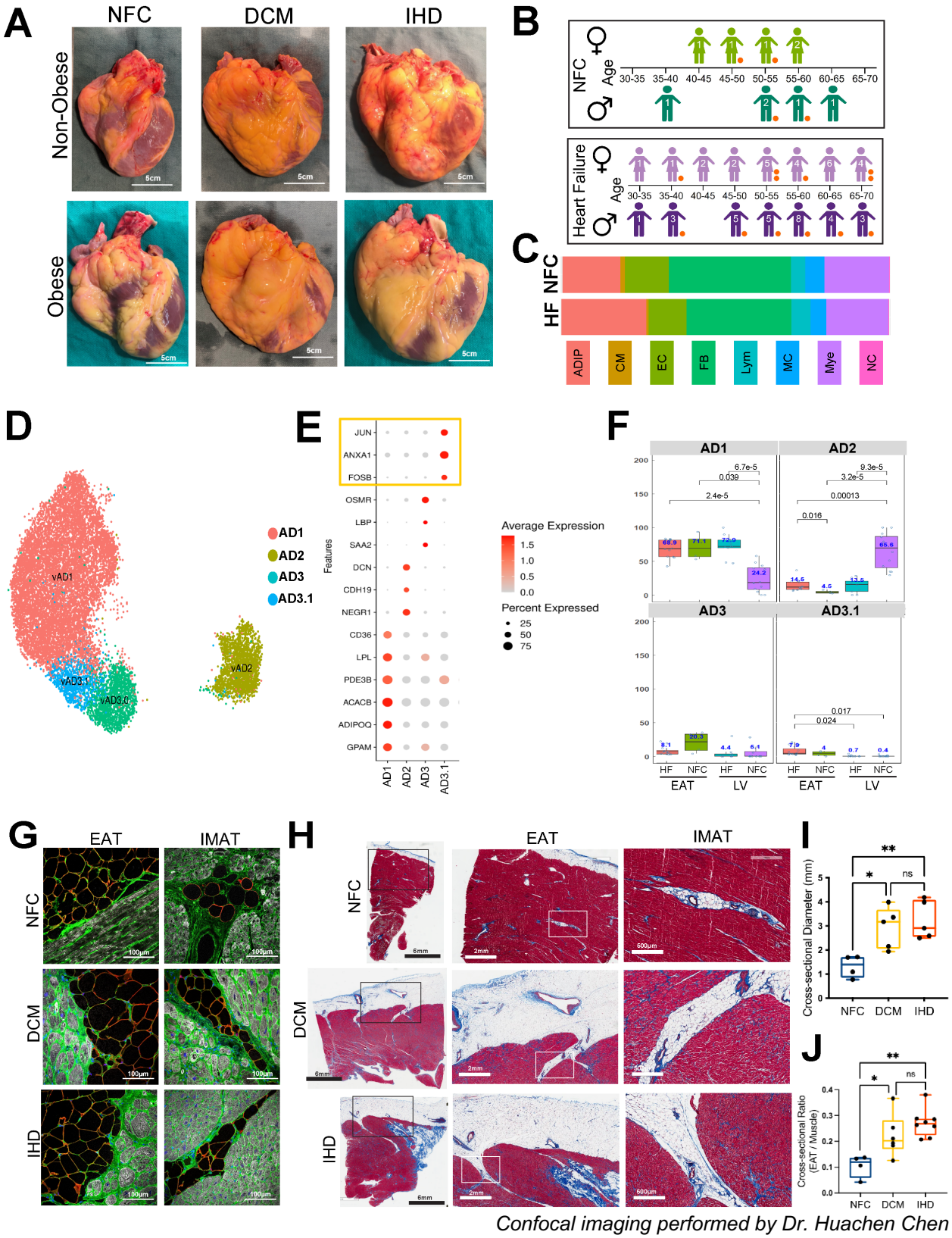

Confocal imaging performed by Dr. Huachen Chen

Figure 6.2. *Figure legend on next page*

Figure 6.2. Unique properties of the intramyocardial adipose tissue (IMAT) in HF.

A. Global EAT expansion in HFrEF independent of obesity status. Hearts from non-failing controls (NFC), dilated cardiomyopathy (DCM), and ischemic cardiomyopathy (ICM) in non-obese and obese donors. Pictures of the hearts were captured following cardioplegic arrest and removal prior to dissection. EAT in NFC donors resides preferentially in the atrioventricular and interventricular grooves; however, expands to cover the entire myocardial surface in both DCM and ICM patients. **B.** Cohort of NFC (top, green), and HF (bottom, purple) patients included in the study. The samples incorporated into the snRNA Seq data set are indicated with an orange circle. Each orange circle represents a single patient or donor. **C.** Cell-type composition of the EAT from NFC donors and HF patients. Adipocytes are labeled in salmon (ADIP), cardiomyocytes in mustard (CM), endothelial cells in chartreuse (EC), fibroblasts in emerald (FB), lymphocytes in teal (Lym), mural cells in blue (MCs), myeloid cells in purple (Mye), and neuronal cells in magenta (NCs) **D.** Cell state analysis of adipocytes. The adipocytes were further subclustered into AD1 (salmon), AD2 (olive), AD3 (emerald) and AD3.1 (blue). **E.** Top differentially expressed genes (DEGs) that identifies each unique subcluster. We highlight the DEGs in the novel EAT cluster with a yellow rectangle. **F.** Cell state abundance by region and etiology. The EAT from HF patients is labeled in salmon and the EAT from NFC donors in chartreuse. The adipocytes from the LV myocardium are labeled in blue for HF and in purple for NFC donors. Data are represented as mean ± SEM. One-way ANOVA was performed with Tukey's multiple comparisons post-hoc test; *$p<0.05$, **$p<0.01$, ***$p<0.001$, ****$p<0.0001$. **G.** Confocal images from the hearts of NFC, DCM and IHD donors and patients depicting the EAT and the intramyocardial adipose tissue (IMAT). Adipocytes were stained with perilipin (PLIN, Alexa 568 pseudocoloured red), wheat-germ agglutinin staining was used to delineate cells

(WGA, Alexa 488 pseudocoloured green), and cardiac troponin T staining for the cardiomyocytes (cTnT, Alexa 647 pseudocoloured grey). **H.** Masson's trichrome stained sections from NFC, DCM and IHD hearts at various magnifications to highlight the EAT and the IMAT. **I.** Quantification of the cross-sectional diameter of the EAT in NFC, DCM and IHD hearts. **J.** Quantification of the cross-sectional ratio between the EAT and the muscle in NFC, DCM and IHD hearts. Data are represented as mean ± SEM. One-way ANOVA was performed with Tukey's multiple comparisons post-hoc test; *$p<0.05$, **$p<0.01$.

6.4.5 Infiltrative epicardial adipose tissue in HF

Following initial analysis of the transcriptomic profile and the observation that different adipocyte cell states characterize the myocardial adipocytes of DCM and NFC, we aimed to phenotype further the intramyocardial adipose tissue (IMAT) and the EAT. We stained transmural LV sections, including the EAT's entire cross-section, with two primary markers: perilipin-1 and cardiac troponin T to identify the adipocytes and the cardiomyocytes, respectively. The IMAT in NFC samples appeared to reside predominantly adjacent to or surrounding the vasculature. Rather, the IMAT in DCM and IHD patients appeared to penetrate the myocardium from the EAT and create a fissure between cardiomyocytes (**Figure 6.2G**). To explore this further, we employed a full-slide scan of Masson's trichrome-stained sections to obtain lower-magnification images. We corroborated the predominantly perivascular deposition of AT in the myocardium of controls, whereas the IMAT in HF infiltrates from the EAT preferentially (**Figure 6.2H**). Using this modality, we aimed to retrospectively quantify the expansion of the EAT in HF. The thickness of the EAT was increased for both DCM and IHD compared to NFCs (**Figure 6.2I-J**).

6.4.6 Phenotyping the EAT

To further phenotype the EAT and tease apart the effects of obesity from that of HF, we employed traditional methods of AT characterization using Hematoxylin and Eosin (H&E) staining.

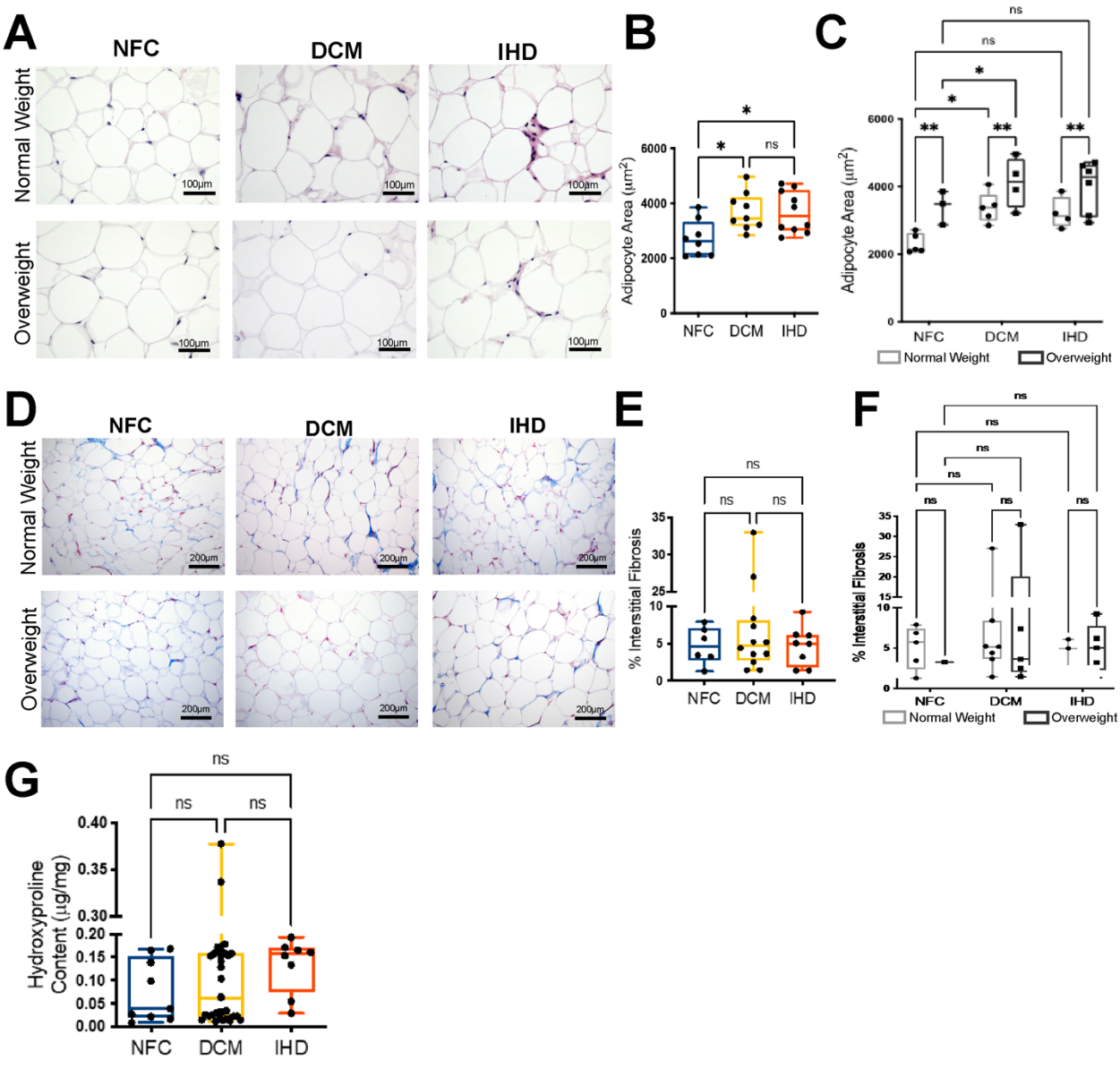

Hydroxyproline assay performed by Abby Ewasiuk

Figure 6.3. *Figure legend on next page*

Figure 6.3. Adipocyte hypertrophy and adipose tissue fibrosis in the EAT.

A. Hematoxylin & Eosin stained EAT from NFC, DCM and IHD cases. The cases were divided into normal weight (BMI<25) or overweight (BMI≥25). **B.** Quantification of adipocyte area in NFC, DCM and IHD cases. Greater than 200 adipocytes were measured for each patient or donor from 10-20 images captured for each slide. **C.** Quantification of adipocyte area with each group (NFC, DCM and IHD) divided based on BMI. A BMI<25 was considered normal weight and a BMI≥25 as overweight. **D.** Masson's trichrome stained EAT from NFC, DCM and IHD cases. The cases were divided into normal weight (BMI<25) or overweight (BMI≥25). **E.** Quantification of blue-stained collagen in NFC, DCM and IHD cases. 10-20 images were captured and quantified for each patient. **F.** Quantification of blue-stained area (representing collagen deposition) with each group (NFC, DCM and IHD) divided based on BMI. A BMI<25 was considered normal weight and a BMI≥25 as overweight. **G.** Hydroxyproline content quantification as a surrogate measure of collagen content in NFC, DCM and IHD donors or patients. Data are represented as mean ± SEM. One-way ANOVA was performed with Tukey's multiple comparisons post-hoc test for comparison of three groups. Two-way ANOVA with Tukey's multiple comparisons post-hoc test was used when considering both etiology and BMI; *p<0.05, **p<0.01, ***p<0.001, ****p<0.0001.

Adipocyte cross-sectional area was significantly increased in DCM and IHD EAT compared to NFC (**Figure 6.3A-B**). BMI (***; p=0.0007) and etiology (**; p=0.0057) were significant predictors of adipocyte size. Therefore, patients with HF possessed significantly larger adipocytes independent of overweight or obesity status (**Figure 6.3C**). Neither Masson's trichrome staining nor hydroxyproline assay revealed differences in EAT fibrosis between groups (**Figure 6.3D-E, Figure 6.3G**), nor were there differences in fibrosis if dividing cohorts based on BMI (**Figure 6.3F**).

6.4.7 Assessing the molecular signature of the EAT

We next examined the cytokine, adipokine and ECM remodeling protein signature of the EAT in HF compared to controls. Hierarchical clustering based on the molecular signature of the EAT demonstrated a similar trajectory within the DCM and control groups, and only a few samples clustered apart from their respective groups (**Figure 6.4A**). In contrast to the DCM results, the trajectory of molecules in IHD was variable, and samples clustered primarily into two separate groups based on their molecular signature (**Figure 6.4B**). The significantly elevated molecules in DCM amounted to thirty-three, with seven upregulated and twenty-six downregulated when a fold change (FC) threshold of |1.5| was applied to the DCM EAT compared to controls. Interestingly, most downregulated molecules were proinflammatory cytokines, such as interleukin-6 (IL-6), monocyte chemoattractant protein-1 (MCP-1), and resistin, for example (**Figure 6.4C**). When an FC cut-off of 1.5 was applied, five molecules remained upregulated, with the majority downregulated in IHD. Mirroring the DCM comparison, IHD patients' EAT had significantly lower proinflammatory cytokine levels, such as IL-6, resistin, and MCP-4 (**Figure 6.4D**). To visually compare the differences between all groups, we performed

unsupervised principal component analysis (PCA) on the merged dataset of all significantly changed or unchanged molecules. The NFCs appear to separate further from the DCM and IHD cohorts, although there is substantial overlap between HF cohorts (**Figure 6.4E**).

6.4.8 Computational PPI Network construction and pathway analysis

A protein-protein interaction network was constructed using Search Tool for the Retrieval of Interacting Genes/Proteins (STRING) 11.0 open access online database (https://string-db.org/). The protein-protein interaction network diagram was constructed on the upregulated cytokines that passed the threshold for fold change (FC>1.5) and statistical significance ($p<0.05$). Notably, six of the seven upregulated molecules in DCM compared to controls demonstrate relationships, namely TNF-related apoptosis-inducing ligand (TRAIL) (*TNFSF10*), interferon-gamma-inducible protein 10 (IP-10) (*CXCL10*), monokine induced by interferon-gamma (MIG/CXCL9) (*CXCL9*), Eotaxin-2 (*CCL24*), Macrophage-derived chemokine (MDC) (*CCL22*), and cutaneous T-cell-attracting chemokine (CTACK) (*CCL27*). One molecule, Adipsin (*CFD*), did not have a direct relationship with the others (**Figure 6.4F**). For the IHD patients, similarly upregulated molecules were incorporated into the network, including IP-10 (*CXCL10*), MIG/CXCL9 (*CXCL9*), and MDC (*CCL22*), with Adipsin (*CFD*) commonly residing peripheral to the network. One additional molecule that was upregulated in IHD and demonstrated a relationship with the former three was interferon-alpha 2 (*IFNA2*) (**Figure 6.4G**).

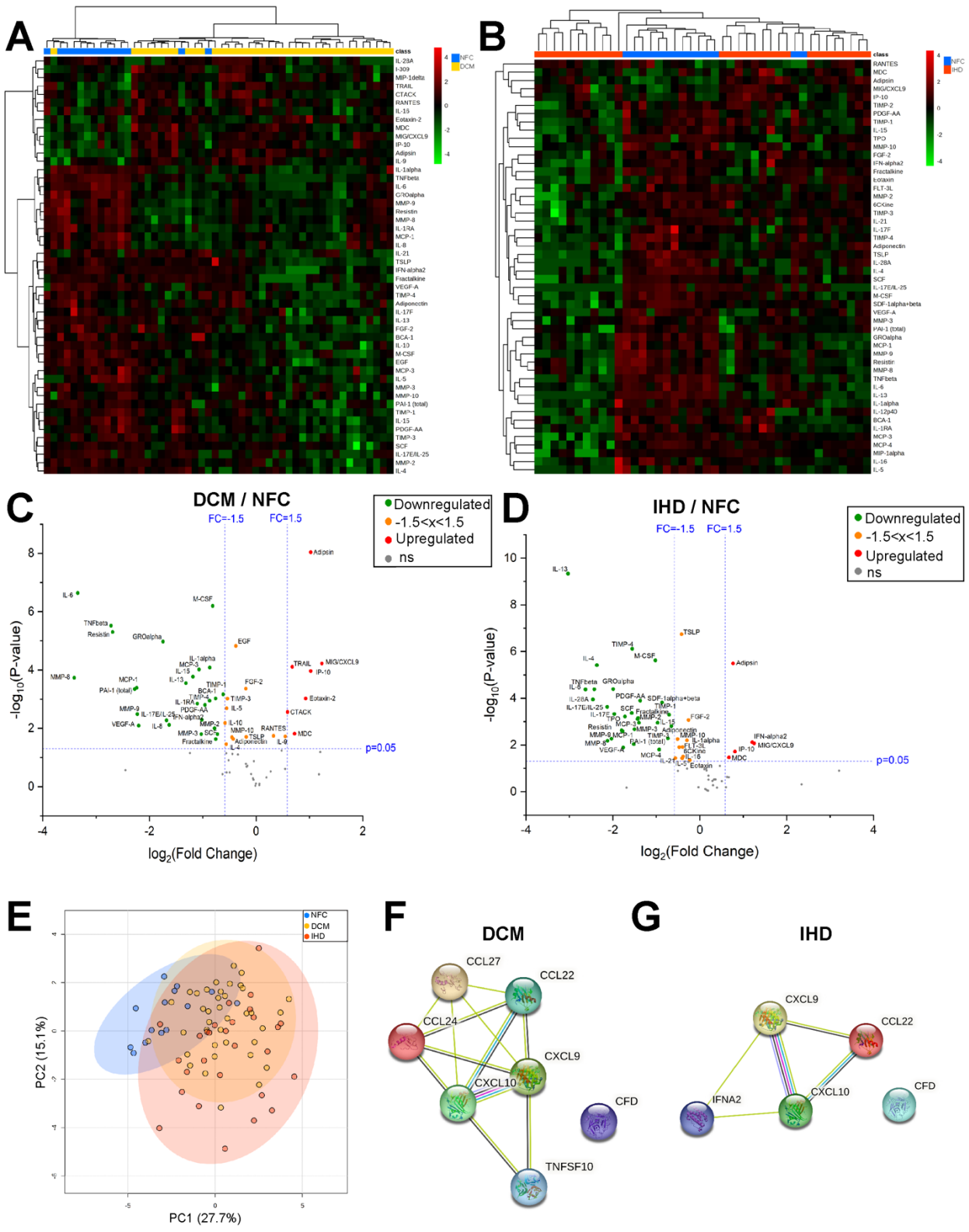

Figure 6.4. *Figure legend on next page*

Figure 6.4. Phenotyping the EAT in HF using a multiplexed cytokine analysis.

A. Heatmap in DCM EAT compared to NFCs of the top fifty cytokines, adipokines, and ECM remodeling target molecules analyzed by a multiplexed-cytokine assay. Samples and molecules were both subject to hierarchical clustering using the Ward's linkage method. DCM samples are labeled in yellow, and NFC are labeled in blue. Each column represents a single patient or donor. Each row represents a single molecule. Increased molecules are labeled in red, whereas decreased molecules are labeled in green, as indicated by the key **B.** Heatmap in IHD EAT compared to NFCs of the top fifty cytokines, adipokines, and ECM remodeling target molecules analyzed by a multiplexed-cytokine assay. Samples and molecules were both subject to hierarchical clustering using the Ward's linkage method. IHD samples are labeled in orange, and NFC samples are labeled in blue. Each column represents a single patient or donor. Each row represents a single molecule. Increased molecules are labeled in red, whereas decreased molecules are labeled in green, as indicated by the key **C.** Volcano plot of all significantly changed and unchanged molecules in DCM compared to NFC. Molecules that were significantly downregulated and exceeded a fold change (FC) cut-off of 1.5 are labeled with green dots. Molecules that were significantly upregulated and exceeded a FC cut-off of 1.5 are labeled with red dots. Molecules that were significantly changed but did not exceed a FC cut-off of |1.5| are indicated as yellow dots. Unchanged molecules are shown as grey dots. **D.** Volcano plot of all significantly changed and unchanged molecules in IHD compared to NFC. Molecules that were significantly downregulated and exceeded a fold change (FC) cut-off of 1.5 are labeled with green dots. Molecules that were significantly upregulated and exceeded a FC cut-off of 1.5 are labeled with red dots. Molecules that were significantly changed but did not exceed a FC cut-off of |1.5| are indicated as yellow dots. Unchanged molecules are shown as grey dots. **E.** Principal

component analysis (PCA) plot of NFC (blue), DCM (yellow) and IHD (orange) **F.** STRING interaction network of significantly upregulated molecules in DCM patients compared to NFC. Light blue lines indicated known interactions from curated databases. Magenta lines indicate experimentally determined interactions. Black lines indicate predicted interactions as putative homologs are co-expressed in other organisms. Light green lines indicate predicted interactions when putative homologs are mentioned together in other organisms (textmining Pubmed database). **G.** STRING interaction network of significantly upregulated molecules in IHD patients compared to NFC. Light blue lines indicated known interactions from curated databases. Magenta lines indicate experimentally determined interactions. Black lines indicate predicted interactions as putative homologs are co-expressed in other organisms. Light green lines indicate predicted interactions when putative homologs are mentioned together in other organisms (textmining Pubmed database).

Pathway analysis was performed with the Kyoto Encyclopedia of Genes and Genomes (KEGG) and Gene Ontology (GO). KEGG pathways were shared between DCM and IHD, with viral protein interactions, cytokine receptor interactions, and toll-like receptor signaling as commonly enriched (**Tables 6.2-6.3**). The top two biological processes and molecular functions enriched by GO and upregulated in DCM were the immune response, humoral immune response, chemokine activity, and cytokine activity (**Table 6.4**). The top two biological processes and molecular functions enriched by GO and upregulated in IHD consisted of the humoral immune response, response to virus, cytokine activity, and cytokine receptor binding (**Table 6.5**).

6.4.9 MAPK pathway activation in the EAT

We next probed the mitogen-activated protein kinase (MAPK) pathways in the EAT due to their involvement as upstream activators of the AP-1 family of transcription factors, including *JUN* and F*OSB*, which were found to be upregulated by snRNA Seq.[306] We examined the p38 pathway (p38α, β, γ, δ), extracellular signal-related kinases 1/2 (ERK1/2), and c-Jun amino (N)-terminal kinases 1/2/3 (JNK 1/2/3). In the DCM samples, phosphorylated-p38 (p-p38) was upregulated overall. However, patients with a pathogenic variant in lamin A/C (*LMNA*) and pathogenic variant negative (PV_{neg}) patients had increased p-p38, but not in patients with a pathogenic variant in titin (*TTN*) (**Figure 6.5A**). p-ERK was moderately increased in DCM EAT compared to controls; however, it did not reach statistical significance (p=0.059) nor showed genotype-specific variation (**Figure 6.5B**). p-JNK demonstrated substantial variation between samples and was not significantly upregulated in DCM compared to NFC EAT (p= 0.265) nor demonstrated genotype-specific variation (**Figure 6.5C**). In IHD, all MAPK pathways studied were significantly upregulated in the EAT compared to controls (**Figure 6.5D-F**).

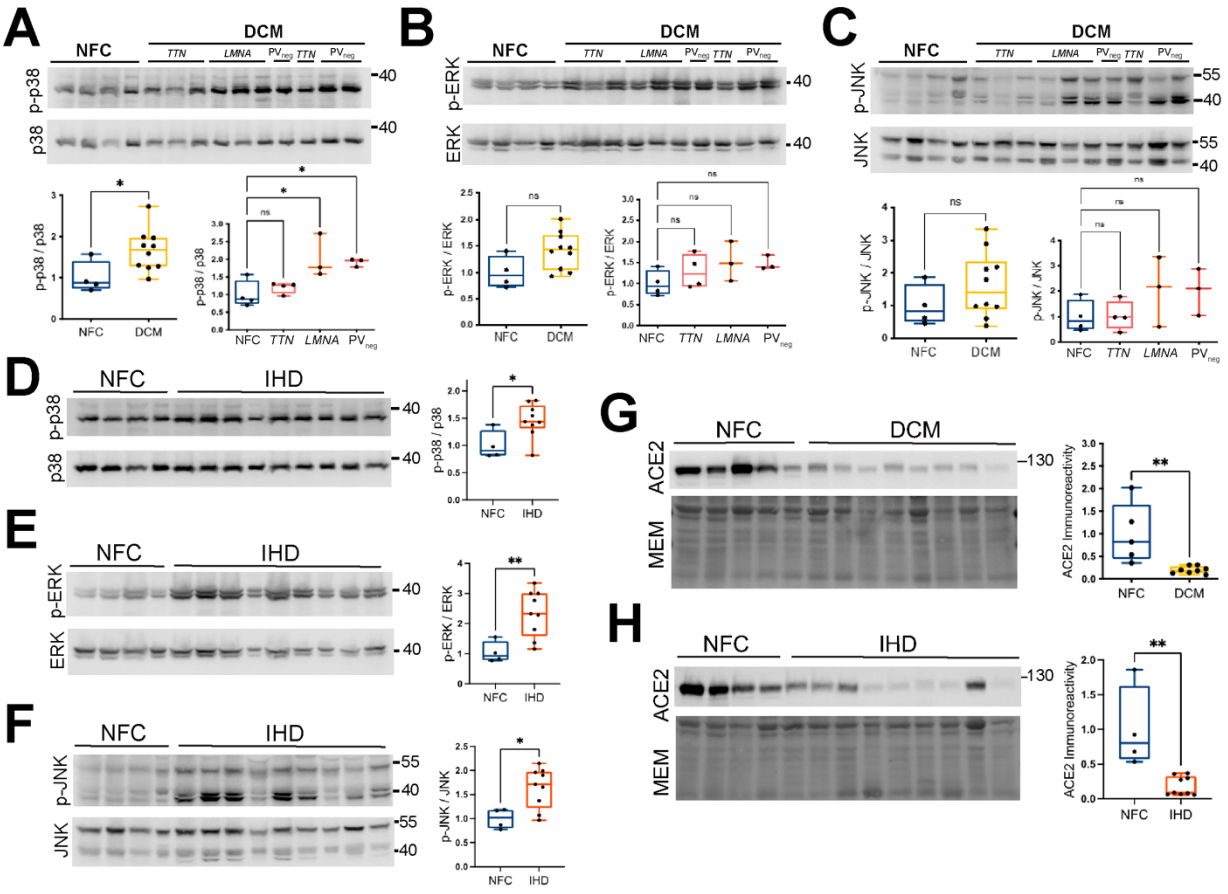

Figure 6.5. *Figure legend on next page*

Figure 6.5. Assessing putative altered EAT pathways in HF.

A. Immunoblot for p-p38 (top) and p-38 (bottom) MAPK in DCM and NFC EAT. Immunoreactivity was quantified and reported as a ratio of p-p38 over total p38. NFC are labeled in blue, and DCM in yellow (left). Quantification of the p-38/p38 ratio was also reported in a genotype-specific manner (right). NFC is labeled in blue. DCM patients with a mutation in titin (*TTN*) are labeled in pink. DCM patients with a mutation in lamin A/C (*LMNA*) are labeled in orange. DCM patients with no identified pathogenic variant (PV_{neg}) are labeled in dark orange. **B.** Immunoblot for p-ERK (top) and ERK (bottom) MAPK in DCM and NFC EAT. Immunoreactivity was quantified and reported as a ratio of p-ERK over total ERK. NFC are labeled in blue, and DCM in yellow (left). Quantification of the p-ERK/ERK ratio was also reported in a genotype-specific manner (right). NFC is labeled in blue. DCM patients with a mutation in titin (*TTN*) are labeled in pink. DCM patients with a mutation in lamin A/C (*LMNA*) are labeled in orange. DCM patients with no identified pathogenic variant (PV_{neg}) are labeled in dark orange. **C.** Immunoblot for p-JNK (top) and JNK (bottom) MAPK in DCM and NFC EAT. Immunoreactivity was quantified and reported as a ratio of p-JNK over total JNK. NFC are labeled in blue, and DCM in yellow (left). Quantification of the p-JNK/JNK ratio was also reported in a genotype-specific manner (right). NFC is labeled in blue. DCM patients with a mutation in titin (*TTN*) are labeled in pink. DCM patients with a mutation in lamin A/C (*LMNA*) are labeled in orange. DCM patients with no identified pathogenic variant (PV_{neg}) are labeled in dark orange. **D.** Immunoblot for p-p38 (top) and p-38 (bottom) MAPK in IHD and NFC EAT. Immunoreactivity was quantified and reported as a ratio of p-p38 over total p38. NFC are labeled in blue, and IHD in red. **E.** Immunoblot for p-ERK (top) and ERK (bottom) MAPK in IHD and NFC EAT. Immunoreactivity was quantified and reported as a ratio of p-ERK over total ERK.

NFC are labeled in blue, and IHD in red. **F.** Immunoblot for p-JNK (top) and JNK (bottom) MAPK in IHD and NFC EAT. Immunoreactivity was quantified and reported as a ratio of p-JNK over total JNK. NFC are labeled in blue, and IHD in red. **G.** Immunoblot for ACE2 in DCM and NFC EAT. Immunoreactivity was quantified and reported as a ratio over the MemCode™ total protein stain (MEM). NFC are labeled in blue, and DCM in yellow. **H.** Immunoblot for ACE2 in IHD and NFC EAT. Immunoreactivity was quantified and reported as a ratio over the MemCode™ total protein stain (MEM). NFC are labeled in blue, and IHD in red. Raw and uncropped immunoblots are shown in **Figure 6.6**. One-way ANOVA was performed with Tukey's multiple comparisons post-hoc test for comparison of more than two groups. Unpaired students T-test was used when only two groups were compared; *$p<0.05$, **$p<0.01$, ***$p<0.001$, ****$p<0.0001$.

6.4.10 Examining the RAS in HF EAT

Based on the evidence of an AT RAS and its involvement in obesity,[217,218] and the relevance of pathological RAS activation in HF,[307-309] we next asked if ACE2 levels are altered in the EAT of our HF cohort. There was a significant reduction of EAT ACE2 in DCM patients compared to controls (**Figure 6.5G**). Similarly, a significant decrease in EAT ACE2 was observed in IHD patients (**Figure 6.5H**).

6.5 Discussion

Our analyses of snRNA Seq and molecular phenotyping of the EAT and contiguous myocardium illuminated a unique cell-type distribution. They highlighted the EAT's distinct transcriptomic signature and molecular profile in HF secondary to DCM or IHD. Compared to control donors, the EAT of patients with HF demonstrated differences in the proportion of cell types, cell states, cytokine profile and signal transduction, considerably expanding the insights achieved by imaging modalities[295-297] and limited transcriptomic studies.[302]

6.5.1 Different origins of IMAT in NFC and HF

We noted an expansion in the EAT extending to cover nearly the entire myocardium and a significantly increased EAT diameter in both DCM and IHD, independent of overall adiposity. Interestingly, histology and immunofluorescent staining revealed a key difference between controls and HF hearts in the EAT and IMAT: the IMAT and EAT were distinct entities in NFC, whereas the EAT in HF were analogous. Histologically, the IMAT in HF resulted from infiltration of the EAT into the myocardium, whereas the IMAT in NFCs resides predominately perivascular within the myocardium. This observation was further corroborated by the snRNA

Seq data, as the LV adipocytes derived from HF patients favoured AD1, mirroring the dominant adipocyte cell state of the EAT. Rather, the LV adipocytes of the NFC hearts were predominately AD2, suggesting a difference in the origin or cellular localization of the LV adipocytes of HF and NFC and supporting our histological observations.

6.5.2 Perivascular IMAT in NFC

Previous studies have shown that the perivascular and periventricular EAT have distinct molecular signatures.[241] Further, genetic lineage tracing of perivascular adipocytes revealed that fibroblastic progenitor cells mediate PVAT formation in the thoracic aorta. However, the aortic adventitia of adult mice is devoid of fibroblastic preadipocytes and instead harbours smooth muscle cells that contribute to adipogenesis.[310] In support, it has been described that PVAT adipocytes share common progenitors with vascular smooth muscle cells (VSMCs) in the artery.[311,312] However, the origin of PVAT adipocytes is location-specific and originates from different precursors in a depot-specific manner.[311] Among its myriad of recently ascribed functions, the first recognized role of the PVAT was to provide structural support for vessels.[289] A collagen-rich extracellular matrix (ECM) exists external to the outermost layer of the vessel wall, the tunica adventitia, which supports the vessel against rupture at high pressures.[313] Due to the proximity of the PVAT and the requirement of this ECM support, and the enrichment of the ECM gene-enriched AD2 population in the IMAT of NFC hearts; it is reasonable to suspect that these adipocytes may play a role in the secretion of collagen to support the vasculature. Consistently, adipocytes secrete collagen and other ECM components in the process of adipocyte differentiation.[314]

6.5.3 Infiltrative IMAT in HF

In contrast to this possible physiological role of the IMAT in NFC donors, the accumulation of infiltrative IMAT in HF is likely pathogenic. In a seminal study investigating the EAT expansion in obesity, most cases had a clear demarcation between the EAT and the myocardium in the LV, despite cases of penetrative EAT in the RV;[315] thus, highlighting this phenomenon is selective for HF and not dependent exclusively on increased visceral adiposity and moderate EAT expansion. Informed by the cancer field, invasion requires remodeling of the extracellular matrix (ECM) for cell migration and metastasis.[316] However, we did not observe differences in adipose tissue fibrosis, and many matrix metalloproteinases (MMPs) and tissue inhibitors of MMPs (TIMPs) were downregulated in HF EAT. In the LV, aberrant cardiac remodeling and an imbalance of ECM turnover is characteristic of HF, independent of the etiology.[317] The balance of MMPs and TIMPs is perturbed in the myocardium of DCM and IHD patients, with a reduction of TIMP1 and TIMP3 expression and protein levels with a corresponding increase in MMP-2, MMP-3 and MMP-9 protein levels and activity.[285,317,318] Although a confounding study saw increases in TIMP1 and TIMP2, MMP activity was still significantly upregulated in end-stage DCM;[319] thus, differences may be based on HF duration.[317] Therefore, we predict that MMP activation in the myocardium is permissive for adipocyte infiltration from the EAT, leading to the veins of IMAT that invade the myocardium.

The biological consequence of this penetrative phenotype is still largely unknown. Atrial adipose tissue invasion, coined intraatrial fat, predicted atrial fibrillation (AF) risk in patients.[320] Although EAT expansion is associated with paroxysmal and persistent AF, it is not correlated with the development of AF.[320,321] To our knowledge, no studies exist investigating the impact of infiltrative EAT into the myocardium; yet, it is reasonable to suspect that alterations in

conduction and myocyte coordinated contraction would be consequent. Further studies are necessary to explore the enrichment of AD2 adipocytes in the PVAT and its role in vasculature homeostasis as distinct from the pathogenic, invasive pattern of IMAT derived from the EAT in HF.

6.5.4 Cytokine profile in HF EAT

When examining the cytokine profile of the EAT in HF compared to controls, we were surprised to note a reduction in many proinflammatory cytokines. As we are studying advanced heart failure, we may have missed the window for measuring elevated tissue cytokines. Consistently, the peak cytokine expression in both DCM and IHD precedes the diagnosis of HF.[322,323] Previous studies have shown elevated expression and protein levels of inflammatory mediators in the EAT of patients with critical CAD undergoing coronary bypass surgery.[156] Although most proinflammatory cytokines were down, we did see an increase in a few molecules commonly upregulated in DCM and IHD. Adipsin, or complement factor D (CFD), activates the alternative pathway of complement activation. The complement system is part of the innate immune system and provides a host defence against microbes. However, aberrant complement activation favours tissue damage and is involved in the pathogenesis of various diseases, such as myocardial ischemia-reperfusion injury, atherosclerosis formation, and HF.[324,325] The alternative complement pathway is dysregulated in HF, with increased plasma CFD associated with increased systemic inflammation and impaired cardiac function.[326] Finally, an array of chemokines were commonly upregulated in both DCM and IHD, namely CXCL9, MDC (CCL22) and IP-10 (CXCL10). These cytokines recruit activated T-cells and macrophages through the CXC chemokine receptor 3 (CXCR3), contributing to cardiac inflammation and

atherogenesis.[327,328] Therefore, the EAT may contribute to chronic systemic inflammation in HF, even at advanced stages.

6.5.5 Enhanced Adipogenesis in HF EAT

The EAT in HF was characterized by an expansion in AD3.1 with the upregulation of *ANXA1, JUN*, and *FOSB*. *ANXA1* codes for annexin A1, an anti-inflammatory phospholipid-binding molecule localized to the plasma membrane.[329] Adipose tissue-derived mesenchymal stem cells (MSCs) highly express *ANXA1* and have detectable protein levels.[330] Further, based on the upregulation of *JUN* and *FOSB* expression in HF compared to controls, we pointed our attention toward the MAPK pathways as upstream inducers of FosB and Jun.[331,332] Although the pleiotropic effects of the MAPK pathways complicate interpretation, we will discuss the potential implications of upregulated p38 activity and a trend towards an increase in ERK activity in DCM and increased activity of p38, ERK and JNK in IHD.

6.5.6 p38 pathway

In the DCM EAT, we noted an upregulation in phosphorylated p38 preferentially in patients with a mutation in *LMNA* or in patients with no identified pathogenic variant (PV_{neg}). This result is consistent with previous studies that found upregulated p38 activity in biopsies from hearts of adult patients with DCM caused by a mutation in *LMNA*,[333] and is the basis for the clinical trials in p38 inhibition that showed a positive signal in phase 2 clinical trials (Clinicaltrials.gov NCT02057341), and is now recruiting patients for phase 3 trials (REALM-DCM; Clinicaltrials.gov NCT03439514).[334] In the adipose tissue, p38 activation has been associated with variable, likely isoform-specific, effects. Activating β3-adrenergic receptors by p38 or JNK

stimulates hormone-sensitive lipase-mediated lipolysis and increases proinflammatory cytokine expression.[335] Further, p38α/β phosphorylates C/EBPβ (CCAAT-enhancer-binding protein beta) to promote adipogenesis.[336] Work from the same group found that constitutively active MKK6, the upstream activator of p38, initiates adipogenesis of 3T3-L1 cells; however, prolonged activation of p38 triggered cell death.[337] Moving beyond cell lines into animal studies, p38 activity was higher in preadipocytes than in adipocytes. An inhibitory role of p38 activity was confirmed using pharmacological inhibition of p38 MAPK and genetic knockout in cell lines, which saw enhanced adipocyte differentiation through relieving the inhibition of C/EBPβ and PPARγ (peroxisome proliferator-activated receptor gamma) transcriptional activity.[338] Finally, opposing the murine study, pharmacological inhibition of p38 reduces differentiation in human preadipocytes harvested from subcutaneous and visceral adipose tissues by decreasing the phosphorylation of C/EBPβ and reducing PPARγ protein levels, limiting the ability of human preadipocytes to accumulate lipids.[339] These results suggest species differences in p38 MAPK signaling in the adipocyte differentiation program.

6.5.7 ERK pathway

In our study, we measured an increase in markers of ERK activation in IHD and a trend toward an increase in activation in DCM. The role of extracellular signal-regulated kinase (ERK) is complex yet highly studied. In preadipocyte cell lines, ERK was found crucial for the differentiation of 3T3-L1 cells to adipocytes by an antisense oligonucleotide strategy.[340] However, PPARγ is a substrate for ERK, so the signaling must be delimited to prevent phosphorylation and reduced transcriptional activity that blocks adipocyte differentiation.[341] Although preadipocyte cell lines allow studying terminal differentiation exclusively, the model

of embryonic stem cells also recapitulates early adipogenesis.[342] Early events in adipocyte differentiation of embryonic stem cells activates the ERK pathway exclusively, and pharmacological inhibition markedly impairs adipocyte formation, thus, implicating ERK signaling for the early, proliferative phase of adipogenesis.[342,343] Genetic knockout of ERK isoform 1 ($ERK1^{-/-}$) in mice exhibited reduced adiposity compared to wild-type animals and protected from diet-induced obesity.[344] Adult preadipocytes isolated and cultured from $ERK1^{-/-}$ animals demonstrated impaired adipogenesis without a synergistic effect from a pan ERK inhibitor; thus, ERK1 rather than ERK2 is implicated in dictating adiposity.[344] In agreement, basal ERK activity is enhanced in adipocytes isolated from biopsies of subcutaneous adipose tissue of patients with type 2 diabetes.[345]

6.5.8 JNK pathway

Our study saw increased JNK activation in IHD, yet no difference in DCM compared to controls. In contrast to the critical roles of p38 and ERK signaling in adipogenesis, there is no current evidence that JNK participates in adipocyte differentiation. The predominant result of JNK activation is to exacerbate obesity. JNK1 knockout animals, but not JNK2, were resistant to diet-induced obesity and genetic obesity (ob/ob background).[346] Further, JNK is significantly increased in the adipose tissue of T2DM patients or animal models of obesity and diabetes and is involved in insulin resistance.[346,347] Therefore, JNK likely plays a more prominent role in the context of obesity and T2DM rather than specific to the etiology of HF. Overall, the enhanced activation state of p38 and ERK in the HF EAT suggests enhanced adipogenesis and increased proliferation, which supports the increased number of adipocytes in HF compared to NFC from

the snRNA Seq data. Further, the enrichment of *ANXA1* as a MSC signature suggests that the AD3.1 adipocyte cell state may be an early stage of adipocyte differentiation.[330]

6.5.9 RAS in the EAT

ACE2 protein levels were significantly reduced in the EAT of HF patients compared to controls in this study. Further, we noted adipocyte hypertrophy in the EAT of HF patients independent of overall adiposity, a mechanism that may be attributed to local Ang II actions on the adipocytes to promote lipid storage.[233] Interestingly, patients with DCM have elevated myocardial Ang II levels despite RAS inhibition (ACEi).[348] Another source of myocardial Ang II may be through the production by the EAT, which harbours chymase as an alternative enzyme that generates Ang II.[206] Further studies are required to implicate the EAT in the generation of Ang II and the inability to deactivate systemic or local Ang II. Nevertheless, to our knowledge, our results are the first to suggest an imbalance in the adipose tissue RAS of the EAT in HF.

6.6 Conclusion

In all, the proximity of the EAT places it in a unique position to directly modulate the myocardium. As a tissue depot that can harbour immune cells, release cytokines and adipokines, and possibly generate RAS peptides, it is critical to profile the EAT to target it for the treatment of HF. Tackling the expansion of the EAT and preventing myocardial invasion is essential for the proper functioning of the heart and probably the ability of cardiomyocytes to perform coordinated contraction. Further, as the adipose tissue RAS may be a local source of Ang II that may impact the myocardium, targeting the downregulation of ACE2 will be essential to ameliorate cardiac dysfunction. Therefore, targeting the pathogenic expansion of the EAT,

myocardial EAT infiltration, and the possible RAS activation are critical towards developing novel therapeutic strategies in HF.

6.7 Acknowledgements

The authors acknowledge funding from the Canadian Institutes of Health Research (CIHR) and Heart and Stroke Foundation of Canada to GYO. The remaining authors have no funding sources to declare.

6.8 Disclosures

The authors have no conflict of interests to declare.

Table 6.1. Baseline clinical table of included non-failing control donors and patients with advanced Heart Failure.

	NFC (n=10)	DCM (n=32)		IHD (n=22)	
			p-value		p-value
Demographics					
Age, y	54.0 (49.0-57.8)	55.0 (48.0-60.7)	0.668	57.5 (52.5-64.5)	0.172
BMI, kg/m^2	25.0 (24.5-28.2)	26.1 (23.0-30.3)	0.711	27.2 (25.1-30.7)	0.515
Male (%)	5 (50.0)	16 (50.0)	>0.999	13 (59.1)	0.712
Cardiac Parameters					
VAD	0 (0.0)	19 (59.4)		15 (68.2)	
Heart Weight	323.0 (308.5-385.0)	419.0 (372.0-474.0)	0.030*	548.0 (413.0-573.0)	0.0002*
LVEF	60 (56.2-60)	20 (14.7-28.9)	<0.0001*	20 (13.7-31.2)	<0.0001*
Comorbidities					
AF (%)	0 (0.0)	11 (37.9)	0.037*	2 (10.0)	0.540
Obesity (%)	1 (10.0)	10 (31.3)	0.245	7 (31.8)	0.380
Dyslipidemia (%)	1 (10.0)	7 (24.1)	0.653	10 (47.6)	0.055
DM (%)	0 (0.0)	4 (13.8)	0.556	8 (38.1)	0.032*
CKD (%)	0 (0.0)	13 (44.8)	0.017*	7 (33.3)	0.066
HTN (%)	3 (30.0)	6 (20.7)	0.669	7 (33.3)	>0.999
Medications					
ACE Inhibitors (%)	0 (0.0)	16 (51.6)		9 (42.9)	
ARB (%)	0 (0.0)	9 (29.0)		2 (9.52)	
β-Blocker (%)	0 (0.0)	27 (84.4)		13 (61.9)	
Loop diuretics (%)	0 (0.0)	28 (87.5)		13 (65.0)	
MRA (%)	0 (0.0)	22 (68.7)		11 (55.0)	
Statin (%)	0 (0.0)	13 (40.6)		14 (66.7)	
Antiarrhythmic (%)	0 (0.0)	17 (53.1)		4 (20.0)	

Obesity is defined as a BMI ≥30 kg/m^2. Chronic kidney disease (CKD) is defined as a estimated glomerular filtration rate (eGFR) of <60 mL/min/1.73 m^2. BMI: body mass index; VAD: ventricular assist device; LVEF: left ventricular ejection fraction; AF: atrial fibrillation; CKD: chronic kidney disease; HTN: hypertension; ARB: angiotensin-receptor blockers; MRA: mineralocorticoid receptor antagonist. Categorical variables are reported by count with

percentage in parenthesis: sex, comorbidities, devices, and medications. Continuous variables are reported by median with the interquartile range in parenthesis: age, BMI, heart weight. Statistical comparison was performed using Mann-Whitney U test compared to non-failing controls; *$p<0.05$.

Table 6.2. KEGG pathways upregulated in DCM EAT compared to NFC.

#term ID	term description	observed gene count	background gene count	strength	FDR	matching proteins in network
hsa04061	Viral protein interaction with cytokine and cytokine receptor	6	96	2.24	4.04E-11	CCL22, TNFSF10, CCL27,CXCL10 CXCL9, CCL24
hsa04060	Cytokine-cytokine receptor interaction	6	282	1.77	1.12E-08	CCL22, TNFSF10, CCL27,CXCL10 CXCL9, CCL24
hsa04062	Chemokine signaling pathway	5	186	1.88	1.94E-07	CCL22,CCL27 CXCL10, CXCL9, CCL24
hsa04620	Toll-like receptor signaling pathway	2	101	1.74	0.0476	CXCL10, CXCL9

Table 6.3. KEGG pathways upregulated in IHD EAT compared to NFC.

#term ID	term description	observed gene count	background gene count	strength	FDR	matching proteins in network
hsa04060	Cytokine-cytokine receptor interaction	4	282	1.74	7.42E-05	CCL22,CXCL10 ,CXCL9,IFNA2
hsa04061	Viral protein interaction with cytokine and cytokine receptor	3	96	2.09	2.10E-04	CCL22,CXCL10 ,CXCL9
hsa04620	Toll-like receptor signaling pathway	3	101	2.07	2.10E-04	CXCL10,CXCL9 ,IFNA2
hsa04062	Chemokine signaling pathway	3	186	1.8	0.00073	CCL22,CXCL10 ,CXCL9

Table 6.4. Gene Ontology pathways upregulated in DCM EAT compared to NFC.

Biological Process						
#term ID	term description	observed gene count	background gene count	strength	FDR	matching proteins in network
GO:0006955	Immune response	7	1588	1.09	5.20E-05	CCL22,TNFSF10, CCL27,CXCL10, CFD, CXCL9,CCL24
GO:0006959	Humoral immune response	5	275	1.71	5.20E-05	CCL22,CCL27,CX CL10,CFD,CXCL9
GO:0030593	Neutrophil chemotaxis	4	74	2.18	5.20E-05	CCL22,CXCL10, CXCL9,CCL24
GO:0031640	Killing of cells of other organism	4	91	2.09	5.20E-05	CCL22,CCL27,CX CL10,CXCL9
GO:0061844	Antimicrobial humoral immune response mediated by antimicrobial peptide	4	113	2	5.20E-05	CCL22,CCL27,CX CL10,CXCL9
GO:0070098	Chemokine-mediated signaling pathway	4	80	2.15	5.20E-05	CCL22,CXCL10,CX CL9,CCL24
GO:0007267	Cell-cell signaling	6	1145	1.17	0.00021	CCL22,TNFSF10,C CL27,CXCL10, CXCL9, CCL24
GO:0051707	Response to other organism	6	1256	1.13	0.0003	CCL22,CCL27,CX CL10,CFD,CXCL9, CCL24
GO:0048247	Lymphocyte chemotaxis	3	50	2.22	0.00035	CCL22,CXCL10,C CL24
GO:0098542	Defense response to other organism	5	900	1.19	0.0019	CCL22,CXCL10,CF D,CXCL9,CCL24
GO:0002687	Positive regulation of leukocyte migration	3	144	1.77	0.0057	CCL27,CXCL10,C CL24
GO:0048584	Positive regulation of response to stimulus	6	2257	0.87	0.0058	CCL22,TNFSF10,C CL27,CXCL10,CFD ,CCL24
GO:0006954	Inflammatory response	4	515	1.34	0.0061	CCL22,CXCL10,CX CL9,CCL24

GO:0007166	Cell surface receptor signaling pathway	6	2325	0.86	0.0064	CCL22,TNFSF10,CXCL10,CFD,CXCL9,CCL24
GO:0010819	Regulation of T cell chemotaxis	2	17	2.52	0.0065	CCL27,CXCL10
GO:0007186	G protein-coupled receptor signaling pathway	5	1255	1.05	0.0069	CCL22,CCL27,CXCL10,CXCL9, CCL24
GO:1901739	Regulation of myoblast fusion	2	22	2.41	0.0094	CXCL10,CXCL9
GO:0071677	Positive regulation of mononuclear cell migration	2	27	2.32	0.0132	CCL27,CXCL10
GO:2000406	Positive regulation of t cell migration	2	31	2.26	0.0154	CCL27,CXCL10
GO:0007165	Signal transduction	7	4876	0.6	0.0157	CCL22,TNFSF10,CCL27,CXCL10,CFD,CXCL9,CCL24
GO:0051281	Positive regulation of release of sequestered calcium ion into cytosol	2	42	2.12	0.0254	CXCL10,CXCL9
GO:0002548	Monocyte chemotaxis	2	43	2.11	0.0261	CCL22,CCL24
GO:0009615	Response to virus	3	293	1.46	0.0268	CCL22,CXCL10, CXCL9
GO:0002684	Positive regulation of immune system process	4	949	1.07	0.0378	CCL27,CXCL10, CFD,CCL24
GO:0045661	Regulation of myoblast differentiation	2	55	2.01	0.0378	CXCL10,CXCL9
Molecular Function						
#term ID	term description	observed gene count	background gene count	strength	FDR	matching proteins in network
GO:0008009	Chemokine activity	5	48	2.46	8.12E-09	CCL22, CCL27, CXCL10, CCL24
GO:0005125	Cytokine activity	6	233	1.86	2.44E-08	CCL22, TNFSF10, CCL27, CXCL10, CXCL9, CCL24

GO:0005126	Cytokine receptor binding	6	264	1.8	3.65E-08	CCL22, TNFSF10, CCL27, CXCL10, CXCL9, CCL24
GO:0048020	CCR chemokine receptor binding	3	47	2.25	0.0002	CCL22, CCL27, CCL24
GO:0031728	CCR3 chemokine receptor binding	2	5	3.05	0.00068	CCL27, CCL24
GO:0048248	CXCR3 chemokine receptor binding	2	5	3.05	0.00068	CXCL10, CXCL9

Table 6.5. Gene Ontology pathways upregulated in IHD EAT compared to NFC.

Biological Process						
#term ID	term description	observed gene count	background gene count	strength	FDR	matching proteins in network
GO:0006959	Humoral immune response	5	275	1.85	7.43E-06	CCL22, CXCL10 CFD,CXCL9, IFNA2
GO:0009615	Response to virus	4	293	1.73	1.30E-03	CCL22, CXCL10 CXCL9, IFNA2
GO:0098542	Defense response to other organism	5	900	1.34	1.30E-03	CCL22, CXCL10 CFD,CXCL9, IFNA2
GO:0006954	Inflammatory response	4	515	1.48	1.90E-03	CCL22, CXCL10 CXCL9, IFNA2
GO:0030593	Neutrophil chemotaxis	3	74	2.2	1.90E-03	CCL22, CXCL10 CXCL9
GO:0031640	Killing of cells of other organism	3	91	2.11	1.90E-03	CCL22, CXCL10 CXCL9
GO:0061844	Antimicrobial humoral immune response mediated by antimicrobial peptide	3	113	2.02	0.0019	CCL22, CXCL10 CXCL9
GO:0070098	Chemokine-mediated signaling pathway	3	80	2.17	0.0019	CCL22, CXCL10 CXCL9
GO:0019221	Cytokine-mediated signaling pathway	4	678	1.36	0.004	CCL22, CXCL10 CXCL9, IFNA2
GO:0051607	Defense response to virus	3	210	1.75	0.0062	CXCL10, CXCL9 IFNA2
GO:1901739	Regulation of myoblast fusion	2	22	2.55	0.0068	CXCL10, CXCL9
GO:0007166	Cell surface receptor signaling pathway	5	2325	0.93	0.0106	CCL22, CXCL10 CFD,CXCL9, IFNA2
GO:0002252	Immune effector process	4	969	1.21	0.0121	CXCL10, CFD, CXCL9, IFNA2

GO:0051281	Positive regulation of release of sequestered calcium ion into cytosol	2	42	2.27	0.0177	CXCL10, CXCL9
GO:0007267	Cell-cell signaling	4	1145	1.14	0.0196	CCL22, CXCL10 CXCL9, IFNA2
GO:0048247	Lymphocyte chemotaxis	2	50	2.19	0.0233	CCL22, CXCL10
GO:0045661	Regulation of myoblast differentiation	2	55	2.15	0.0273	CXCL10, CXCL9
Molecular Function						
#term ID	term description	observed gene count	background gene count	strength	FDR	matching proteins in network
GO:0005125	Cytokine activity	4	233	1.83	0.00034	CCL22, CXCL10 CXCL9, IFNA2
GO:0005126	Cytokine receptor binding	4	264	1.77	0.00034	CCL22, CXCL10 CXCL9, IFNA2
GO:0008009	Chemokine activity	3	48	2.39	0.00034	CCL22, CXCL10 CXCL9
GO:0048248	CXCR3 chemokine receptor binding	2	5	3.19	0.00071	CXCL10, CXCL9
GO:0005125	Cytokine activity	4	233	1.83	0.00034	CCL22, CXCL10 CXCL9, IFNA2

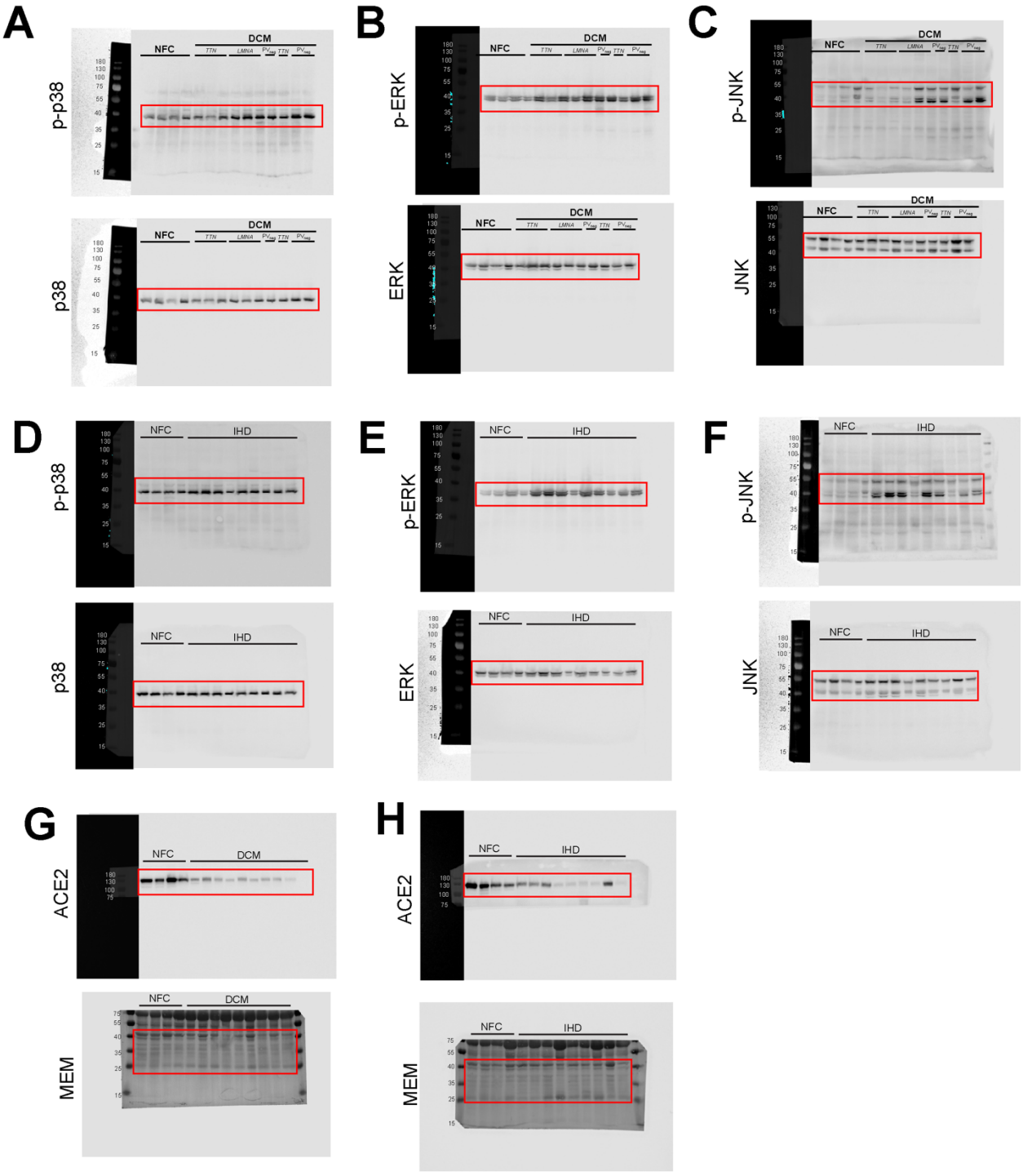

Figure 6.6. *Figure legend on next page*

Figure 6.6. Raw and uncropped western blot images from **Figure 6.5. A-F.**

For the MAPK pathways (p38, ERK and JNK), the blot was first probed for the phosphorylated protein (p-p38, p-ERK or p-JNK). The membrane was then stripped using Restore™ Western Blot Stripping Buffer (Thermo Fisher Scientific, Montreal, Quebec, Canada) and probed for the total MAPK protein (p38, ERK or JNK). The red rectangle represents the area cropped for the corresponding figure. **G-H.** Following transfer, the membrane was cut at 75 kDa to visualize ACE2 on the top (predicted molecular weight 130 kDa) and the bottom portion was stained with MemCode™ to quantify protein loading. One gel was run with EAT from NFC and DCM donors and patients, with ten DCM samples run alongside four sex- and age-matched NFCs. For IHD, four NFC samples were run alongside nine patient samples. In total, four biological replicates were analyzed for NFC, ten for DCM and nine for IHD. The red box denotes the portion of the blots that were cropped and used for the figure.

Chapter 7

Discussion and Future Directions

7.1 Discussion and Research Impact

Taken together, we explored the role of ACE2 beyond its ability to deactivate the pressor response of the canonical RAS, rather as the indispensable receptor for SARS-CoV-2 and as a modulator of lipid storage in adipose tissue. We further began elucidating the regulation of ACE2 in physiology and disease- specifically in heart failure (HF). We started with exploring the physiological regulation of ACE2 by age and sex in multiple organs. Our rationale was to begin to understand SARS-CoV-2's multi-organ injury and increased morbidity and mortality in older males.[25,40,349] As elevated viral load was associated with worse clinical outcomes;[255,261] we anticipated that older males would have higher ACE2 levels across organs to facilitate increased susceptibility.

We corroborated that the highest expression, protein levels, and activity of ACE2 resided in the small intestine, followed by the kidneys, heart, and lungs. In mice, we found higher ACE2 protein levels in the kidney of males of all age groups and the lungs of aged males compared to females. No sex differences were noted in murine hearts; however, in humans, aged males had significantly higher ACE2 levels and activity than females. Finally, ACE2 protein levels and activity were discordant with *ACE2* expression data. This study informs SARS-CoV-2 tropism and the finding that aged males have enhanced susceptibility to severe COVID-19, likely due to increased ACE2 protein levels at the tissue level. Further, this study moves away from the current reliance on expression data, highlighting that post-transcriptional and post-translational processes highly regulate protein levels and activity of ACE2.

In the following chapter, we moved to an animal model of COVID-19: the Syrian gold hamster infected with unmodified SARS-CoV-2 of the wild-type and Delta strains. We used this model in conjunction with human autopsy heart samples from patients who died of COVID-19 to

assess the impact of SARS-CoV-2 infection on myocardial ACE2 and inflammation. Based on a study that found myocardial ACE2 downregulation and macrophage infiltration in autopsied hearts from SARS patients,[21] we anticipated a similar downregulation of ACE2 and myeloid-dominant immune cell infiltrates in the heart. Indeed, we noted a significant reduction in ACE2 levels in hamsters infected with SARS-CoV-2 and patients with COVID-19. A consistent neutrophil and macrophage dominant myocardial immune cell infiltration pattern was recognized. Although the enhanced severity of human patients with COVID-19 was evident, this is expected as the hamsters infected with SARS-CoV-2 survived and recovered. The mechanism by which ACE2 is reduced is anticipated to be secondary to ADAM17-mediated proteolytic cleavage as with SARS-CoV,[95,274] although this has yet to be demonstrated for SARS-CoV-2. Therefore, the Syrian hamster model of SARS-CoV-2 infection presents a valuable tool for studying and targeting myocardial ACE2 downregulation and inflammation. This study justifies the need to assess ADAM17 activation in COVID-19 and possibly to administer temporary ADAM17 inhibition in acute SARS-CoV-2 infection.

Based on our findings and that of others of incongruent *ACE2* expression and protein levels, as well as the understanding that ADAM17 activity mediates ectodomain shedding of ACE2 in SARS and possibly COVID-19, our next goal was to begin exploring the regulation of ACE2 in physiology and in another disease paradigm: heart failure (HF). Loss of ACE2 is linked to the pathogenesis of HF;[13,51] thus, we assessed miRNAs and proteolytic cleavage as two mechanisms that negatively regulate ACE2.[349] ADAM17-mediated proteolytic cleavage of ACE2 is aberrantly activated in cardiovascular disease, particularly in myocardial inflammation, fibrosis, and impaired cardiac function.[41,350,351] Therefore, we anticipated that ADAM17 activity may be the most predictive of ACE2 protein levels in HF, and miRNAs may dictate ACE2

protein levels in non-failing control hearts. Consistent with our hypothesis, we noted significantly higher expression of miRNAs that are demonstrated, or are expected, to regulate ACE2 levels in NFC hearts compared to DCM or IHD. Further, we found significantly increased ADAM17 protein levels in DCM and IHD samples. However, the activity of ADAM17 did not reflect the higher protein levels. The relative contribution of these two modes of regulation, namely miRNAs and proteolytic cleavage by ADAM17, on the final ACE2 protein levels is difficult to determine. Therefore, this study is a foundation for assessing the relative contribution of miRNAs and proteolytic cleavage, by which we can employ computational approaches to see the predictive power of each. Our work highlights the complexity of the regulation of ACE2 and requires further assessment to bridge the gap between the modes of regulation and final ACE2 levels.

Due to the close anatomical proximity and a marked expansion of the EAT in HF, we next aimed to phenotype this adipose tissue depot and profile its inflammatory status and local RAS. We assessed the cell type distribution of the EAT in HF and found significantly higher adipocyte proportion, as well as differences in adipocyte cell states that favoured HF. Specifically, AD3.1, the newly identified cell state, was more proliferative and adipogenic based on enriched markers. The IMAT and the EAT demonstrated similar cell states in HF, yet in NFCs the cell states of the IMAT and the EAT were substantially different. Consistently, we noted an infiltrative pattern of the EAT into the myocardium preferentially in disease; rather, the IMAT of NFCs surrounded the myocardial vasculature by histology. This pattern reflects a different biological origin of the IMAT as opposed to the EAT in the control state. Unexpectedly, many proinfloammatory cytokines were reduced in the EAT of HF patients compared to NFC. Of the upregulated molecules, pathways in immune cell chemotaxis, viral

responses, and toll-like receptor signaling were enriched. Based on the proliferative adipocyte cell state markers enriched in DCM and IHD, we probed the MAPK pathways. Consistently, active p38 MAPK and ERK pathways were upregulated in HF, which promote adipogenesis.[336,342,344] ACE2 was significantly reduced in the EAT of DCM and IHD patients. As Ang II activity in adipose tissue is anti-lipolytic and pro-lipogenic,[233] impaired deactivation of Ang II may explain why HF etiology was a significant predictor of adipocyte hypertrophy even in the absence of increased BMI. To our knowledge, this is the first systematic investigation of the EAT of the heart, encompassing basic phenotyping, assessing inflammatory status, and assessing the local RAS. This study could inform novel therapeutic approaches to ameliorate EAT dysfunction. Overall, this compilation of research efforts showcases a comprehensive assessment of ACE2 in HF and COVID-19, highlighting some of the novel functions of ACE2 that extend beyond deactivation of the canonical RAS (**Figure 7.1**).

7.2 Limitations

Although the analysis of human tissue is invaluable in our pursuit of understanding human HF, there are some shortcomings that must be acknowledged. Our NFC hearts were obtained from brain-dead donors (DBD) whose organ was declined for transplantation due to blood type (ABO) and/or human leukocyte antigen (HLA) mismatch. All donors selected for this study had a normal antemortem echocardiography, yet may not represent truly healthy hearts for reasons including, but not limited to, their cause of death, extensive downtime to resuscitation (DTR), delay in organ procurement (as transplanted organs are harvested first), an adrenergic storm that occurs with brain death, and supportive treatments that may affect the heart, as donors spend an average of seven days in hospital prior to DBD declaration.

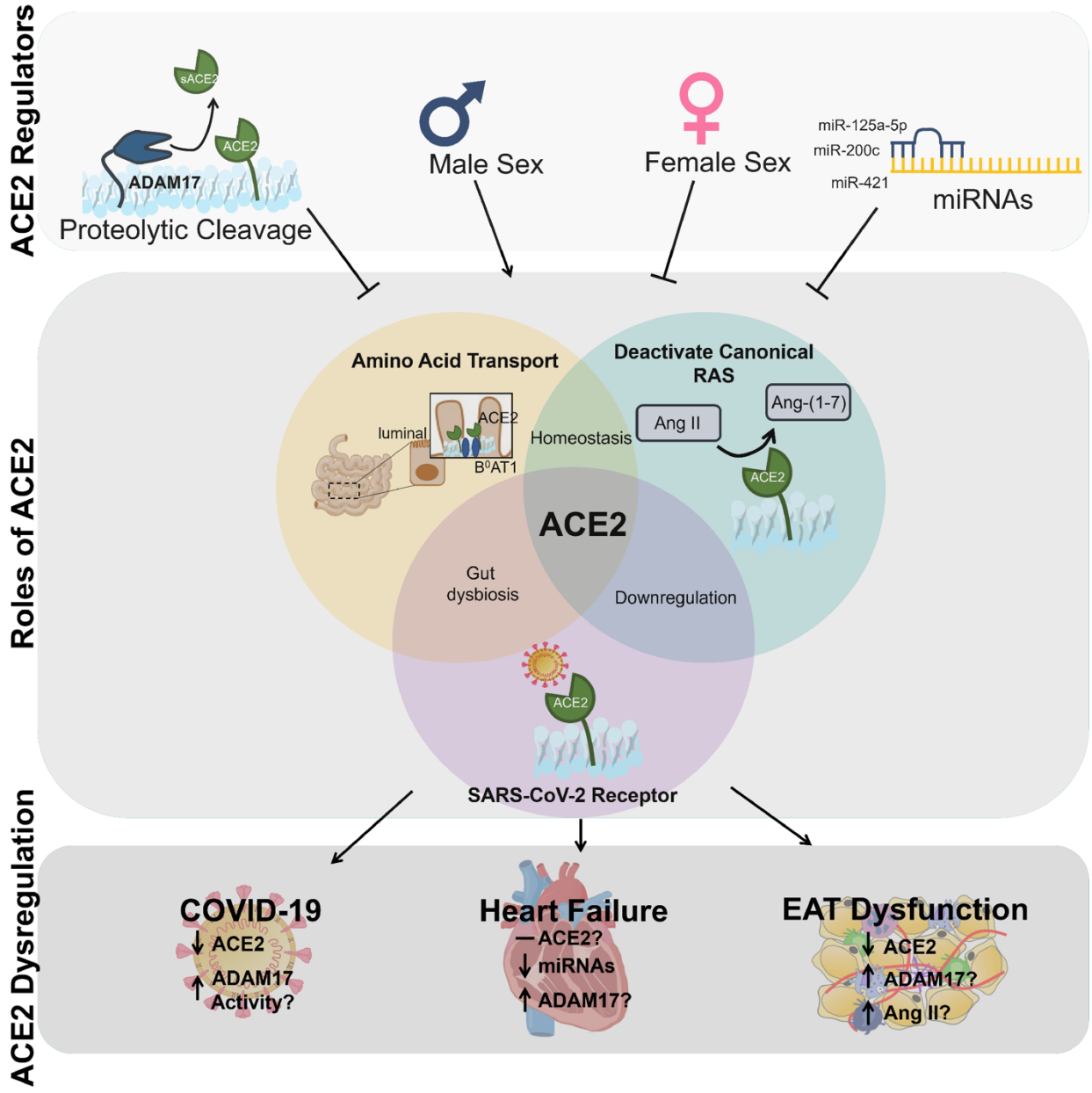

Figure 7.1. *Figure legend on next page*

Figure 7.1. Overview of thesis research and key findings.

This work investigated the impact of sex and aging on the ACE2 protein levels, expression, and activity (**Chapter 3**). We examined putative and known regulators of ACE2 protein levels, namely miRNAs and ADAM17-mediated proteolytic cleavage in non-failing and failing human hearts. miRNAs appeared to be reduced in heart failure (HF) and ADAM17 protein levels were increased in most patients' samples; however, ADAM17 activity was only increased in certain cases. Further work is necessary to delineate the impact of multiple regulatory mechanisms on ACE2 (**Chapter 5**). The biological role of ACE2 is to promote homeostasis in the renin-angiotensin system (RAS) and facilitating the transport of neutral acids in the gut. We explored the additional roles of ACE2 beyond deactivation of the canonical RAS, particularly as the receptor for SARS-CoV-2. The downstream impact of SARS-CoV-2 infection is intimately linked with the roles of ACE2, such as promoting gut dysbiosis due to the dominant role of ACE2 in the gut. In the heart, we noted a significant ACE2 downregulation as an anticipated result of enhanced ADAM17 activity, although the latter needs formal proof in the context of COVID-19 (**Chapter 4**). Finally, we broadly phenotyped the epicardial adipose tissue (EAT) in NFC and HF. We noted a significant reduction in ACE2 in the EAT in HF. We will explore if ADAM17 activity is upregulated to facilitate this loss. Further, we will measure Ang II peptide levels in the EAT to determine in the local RAS may contribute to detrimental outcomes in HF (**Chapter 6**).

Therefore, due to the nature of unpredictable time of organ procurement, the general heterogeneity of human patients, and limited clinical information available from donors, the non-failing controls (NFC) incorporated in our study may not be truly "healthy". This is challenged further for the EAT project, as we could only include donor's hearts containing sufficient adipose tissue for analysis. Thus, we analyzed NFC hearts from patients with higher visceral adipose tissue distribution and generally more comorbidities. However, this spectrum serves as an advantage, as we did not bias our control group to be absent of disease. Instead, these donors possessed comorbidities including hypertension, diabetes, and obesity, such that it reflects the true population and assures the differences observed in HF are etiology-specific.

Additionally, as samples from patients with HF were captured at explant, we were restricted to analyzing advanced disease at a single time point. Obtaining surgical samples would aid in studying earlier in the disease course; however, we would be further limited in the arbitrary sample collection, small tissue section, and challenges in maintaining consistency that are all remedied with the HELP team collecting explanted tissue. Heterogeneity is intrinsic to human studies, as analysis is subject to influence by comorbidities, diet, lifestyle, and pharmaceutical interventions that cannot be controlled for as in a laboratory setting. Our access to extensive clinical data mitigates this inherent challenge.

As our study is retrospective and not interventional, the modes of regulation of ACE2 and the pathways upregulated in HF EAT should ultimately be tested and targeted in preclinical models. However, specifically for the EAT project, murine models do not accumulate extensive adipose tissue on the heart as do humans, apart from minimal amounts in the dorsal and dorsoventral atrioventricular grooves.[148,352] Therefore, studying interventions for EAT

dysfunction would require a larger animal that accumulates cardiac adipose tissue, such as in ovine or porcine models.[353]

7.3 Future directions

Combating the ongoing COVID-19 pandemic requires the advent and implementation of universal therapeutic strategies effective against all current and future SARS-CoV-2 variants. Inference of the data from **Chapter 3** and **Chapter 4** suggests that increased ACE2 may enhance susceptibility to severe COVID-19, yet loss of myocardial ACE2 following the infectious phase may be detrimental to the homeostasis of multiple organs where ACE2 is tissue-protective.[349] As all SARS-CoV-2 variants invariably bind ACE2, exploiting the SARS-CoV-2 receptor binding domain (RBD)-ACE2 interaction is central to many therapeutic strategies. rhACE2 infusion has already been deemed safe and tolerable in phase 1 and 2 clinical trials.[354-356] Studies in human blood vessel and kidney organoids demonstrate a strong neutralization capacity of ACE2 decoys, such as rhACE2, to dramatically limit viral replication.[57] However, the clinical utility of this approach is challenged as the treatment is not orally bioavailable. Therefore, testing of nasally instilled ACE2 mimics or orally bioavailable ACE2 analogues may be of interest and could be tested in preclinical COVID-19 animal models such as the SARS-CoV-2 infected Syrian hamsters which we employed in this study.

Further analysis of the regulation of ACE2 is required to tease apart the influence of many contributing factors. In **Chapter 5**, we demonstrated preliminary alterations in regulators of ACE2 and are in the process of employing a machine learning approach to determine the most predictive modes of regulation, either miRNAs or ADAM17-mediated proteolytic cleavage, in dictating final ACE2 protein levels and activity. We will harness the machine learning algorithm

to answer a few critical questions: 1) is the enhanced severity of HF associated with lower ACE2 levels? 2) are the modes of ACE2 regulation physiology or HF pathophysiology-specific? and 3) is ACE2 regulation distinct between the etiologies of HF (DCM and IHD)? To answer these questions, we will incorporate extensive clinical parameters into the algorithm, including sex, age, BMI, comorbidities, LVEF and additional echocardiography parameters, etc., to capture a broad spectrum of disease, relevant contributing factors, and markers of severity. A recent study used ensemble machine learning in the interrogation of which matrix-related biomarkers predicted HFpEF;[357] thus, we will utilize this as a framework for analysis and data presentation.

The EAT project presented in **Chapter 6** serves as a foundation for pursuing many avenues to extend current findings. We will incorporate further snRNA sequencing analysis and include the cell state evaluation of the endothelial cells, fibroblasts, myeloid cells, lymphoid cells, mural cells, and neuronal cells, as has been done in similar studies.[245] We will also increase our sample size and incorporate the analysis of the right ventricle (RV) EAT (**Figure 7.2**). Exploring the RAS in the EAT is warranted to explain the loss of ACE2; thus, assessing RAS activation and ADAM17 activation is critical. We will incorporate immunoblot and activity measurement of ACE and chymase to determine if there is an imbalance in the canonical and counter-regulatory arms of the RAS. To take this a step further, we will assess local EAT aldosterone, Ang I, Ang II, and Ang 1-7 by profiling levels of angiotensin peptides using liquid chromatography-tandem mass spectrometry (LC-MS/MS), as has been performed previously.[60,358]

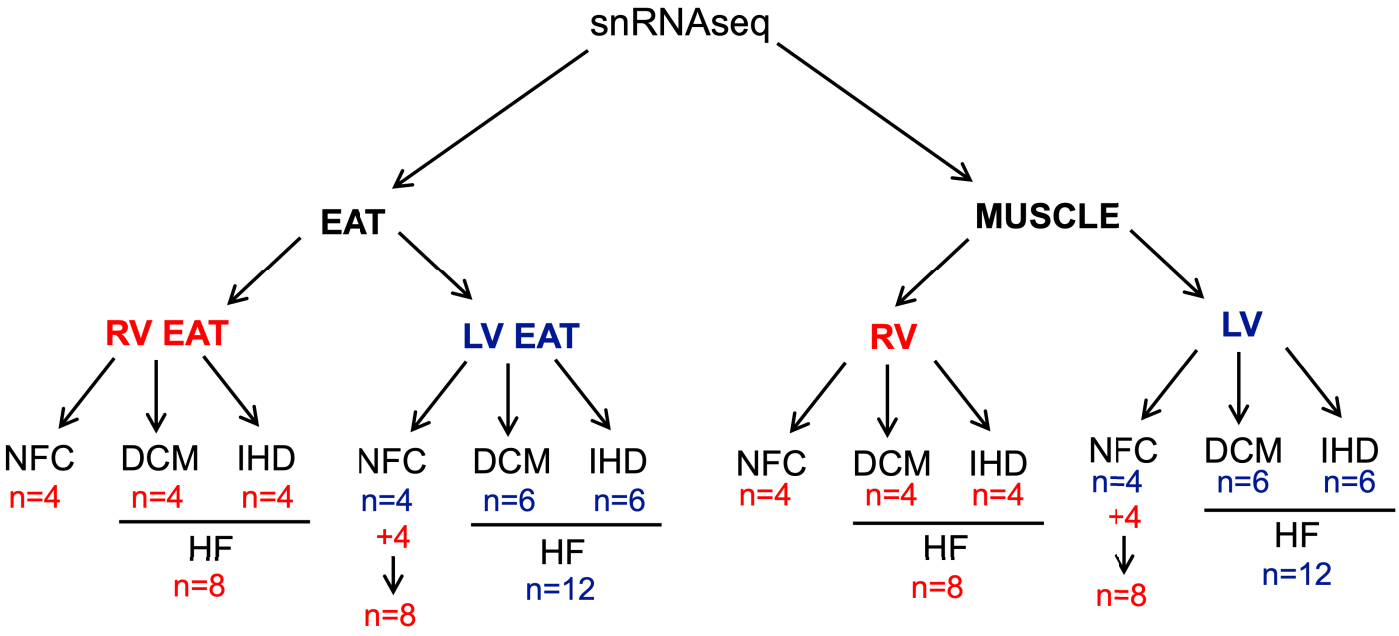

Figure 7.2. *Figure legend on next page*

Figure 7.2. snRNA sequencing current samples and future directions.

Flow chart depicting the current and future samples that will be analyzed using snRNA Seq. The samples incorporated in the current snRNA Seq object presented in this thesis (**Chapter 6**) consist of four NFC, six DCM, and six IHD donors and patients. All samples captured are of the epicardial adipose tissue (EAT) and the paired, contiguous left ventricle (LV). We are in the process of annotating a third version of the EAT object that includes the snRNA Seq data from an additional four NFC LV EAT samples. We have further included samples from the right ventricle (RV). We harvested and sequenced the EAT of the RV from four NFC, four DCM, and four IHD donor and patient samples. As with the LV, we have paired the analysis of the RV EAT with the contiguous RV muscle. In total, with the addition of all the new samples into the object, we will have: RV EAT: n=4 NFC, n=4 DCM, and n=4 IHD (n=8 HF); LV EAT: n=8 NFC, n=6 DCM, and n=6 IHD (n=12 HF); RV: n=4 NFC, n=4 DCM, and n=4 IHD (n=8 HF); LV: n=8 NFC, n=6 DCM, and n=6 IHD (n=12 HF).

Interestingly, p38 and ERK phosphorylate the intracellular Thr735 residue of ADAM17, liberating it from TIMP3 inhibition.[41,359,360] Therefore, as ADAM17 promotes ectodomain shedding of ACE2,[274] and we measured the upregulated activity of p38 and ERK pathways in the DCM and IHD EAT, this further provides a putative connection to the loss of ACE2 in the EAT.

Aldosterone is another novel adipokine critically relevant to HF. Aldosterone is implicated in the pathophysiology of HFrEF to promote sodium retention, magnesium and potassium loss, increased sympathetic tone, and myocardial and vascular fibrosis.[308,309,361,362] Accordingly, spironolactone and eplerenone, two mineralocorticoid receptor antagonists (MRAs) which block aldosterone from interacting with its receptor, improve morbidity and mortality in HFrEF (RALES and EMPHASIS-HF trails, respectively).[363,364] Adipocytes were discovered to basally secrete aldosterone, which was increased with Ang II supplementation and in T2DM and obesity.[365] Aldosterone synthase (*Cyp11b2* expression and protein levels) are detectable in 3T3-L1 cells and mature mouse adipocytes, and human adipocytes harvested from abdominal and subcutaneous adipose tissue express *CYP11B2*.[365] Therefore, systemic neurohumoral activation in HFrEF is likely exacerbated by adipocyte-derived aldosterone production. Further, if the EAT of HFrEF patients is characterized by increased aldosterone production, this would lead to detrimental consequences due to the close anatomic proximity of the EAT to the myocardium in conjunction with the role of aldosterone in promoting myocardial fibrosis and vascular damage.[366]

This work provides novel avenues for therapeutic intervention. Targeting p38 overactivation using inhibitors already in clinical trials[334] may be beneficial as a precision medicine-based approach for patients with a mutation in *LMNA* or PV_{neg} patients with DCM, as well as for patients with IHD. As for the reduced ACE2 levels in the EAT, and if we conclude

that an imbalance in the RAS does exist, trialing recombinant human ACE2 (rhACE2) administration may be beneficial to alleviate EAT dysfunction. Studies have demonstrated that despite treatment with ACE inhibitors, HF patients maintain increased myocardial Ang II levels,[348] a mechanism that could be attributed to local production by the EAT.[206] rhACE2 hydrolyzes Ang II to Ang-(1-7) in plasma from patients with HF *in vitro*,[348] and rhACE2 administration leads to a reduced proinflammatory and oxidative stress biomarker profile.[355,356,367] Thus, rhACE2 could be a beneficial treatment option to ameliorate myocardial canonical RAS imbalance in HF that could be attributed to, in part, by EAT dysregulation. Finally, blocking adipocyte-derived aldosterone production could be another novel HFrEF treatment indirectly targeting adipose tissue dysfunction. Aldosterone synthase inhibitor, Baxdrostat, is currently in phase 2 clinical trials in treatment-resistant hypertension.[368] Therefore, if the EAT is implicated in aberrant aldosterone production in our study, we could pursue the use of aldosterone synthase inhibitors rather than traditional MRAs, as MR-independent effects also contribute to cardiovascular damage.[366]

7.4 Conclusion

In summary, ACE2 serves as the critical entry gate for SARS-CoV-2 and as a cardioprotective enzyme to deactivate the canonical RAS explored extensively in HF. However, a gap of knowledge still exists in fully uncovering the pathways that regulate ACE2 levels and expression and the contribution of the local RAS in tissue depots. Our work begins to delineate the impact of sex on ACE2 protein levels that may account for increased susceptibility to severe COVID-19, myocardial inflammation and downregulation of ACE2 in COVID-19, the etiology-specific regulation of ACE2, as well as the local EAT RAS. Although many drugs are on the market as

HF treatment, current pharmacological interventions are primarily symptomatic, targeting neurohumoral activation (ACEi, ARBs, β-blockers, MRAs), and treating volume overload (diuretics). However, to date, disease-modifying treatments are not readily available. Here, we aimed to elucidate novel and innovative pathways in the treatment of HF, such as targeting EAT dysfunction and COVID-19-mediated ACE2 downregulation with rhACE2. Interventions such as these now need to be robustly tested in clinical trials to tackle the major public health concerns that are COVID-19 and HF.

References

1. Muus, C., Luecken, M.D., Eraslan, G., Sikkema, L., Waghray, A., Heimberg, G., Kobayashi, Y., Vaishnav, E.D., Subramanian, A., Smillie, C., et al. (2021). Single-cell meta-analysis of SARS-CoV-2 entry genes across tissues and demographics. Nat Med *27*, 546-559. 10.1038/s41591-020-01227-z.
2. Tucker, N.R., Chaffin, M., Bedi, K.C., Jr., Papangeli, I., Akkad, A.D., Arduini, A., Hayat, S., Eraslan, G., Muus, C., Bhattacharyya, R.P., et al. (2020). Myocyte-Specific Upregulation of ACE2 in Cardiovascular Disease: Implications for SARS-CoV-2-Mediated Myocarditis. Circulation *142*, 708-710. 10.1161/CIRCULATIONAHA.120.047911.
3. Sungnak, W., Huang, N., Becavin, C., Berg, M., Queen, R., Litvinukova, M., Talavera-Lopez, C., Maatz, H., Reichart, D., Sampaziotis, F., et al. (2020). SARS-CoV-2 entry factors are highly expressed in nasal epithelial cells together with innate immune genes. Nat Med *26*, 681-687. 10.1038/s41591-020-0868-6.
4. Corvol, P., Williams, T.A., and Soubrier, F. (1995). Peptidyl dipeptidase A: angiotensin I-converting enzyme. Methods Enzymol *248*, 283-305. 10.1016/0076-6879(95)48020-x.
5. Crackower, M.A., Sarao, R., Oudit, G.Y., Yagil, C., Kozieradzki, I., Scanga, S.E., Oliveira-dos-Santos, A.J., da Costa, J., Zhang, L., Pei, Y., et al. (2002). Angiotensin-converting enzyme 2 is an essential regulator of heart function. Nature *417*, 822-828. 10.1038/nature00786.

6. Carey, R.M., and Padia, S.H. (2009). Physiology and Regulation of the Renin-Angiotensin-Aldosterone System. Textbook of Nephro-Endocrinology, 147-165. Doi 10.1016/B978-0-12-373870-7.00012-0.

7. Sparks, M.A., Crowley, S.D., Gurley, S.B., Mirotsou, M., and Coffman, T.M. (2014). Classical Renin-Angiotensin system in kidney physiology. Compr Physiol *4*, 1201-1228. 10.1002/cphy.c130040.

8. Wang, K., Gheblawi, M., and Oudit, G.Y. (2020). Angiotensin Converting Enzyme 2: A Double-Edged Sword. Circulation. 10.1161/CIRCULATIONAHA.120.047049.

9. Gheblawi, M., Wang, K., Viveiros, A., Nguyen, Q., Zhong, J.C., Turner, A.J., Raizada, M.K., Grant, M.B., and Oudit, G.Y. (2020). Angiotensin Converting Enzyme 2: SARS-CoV-2 Receptor and Regulator of the Renin-Angiotensin System. Circ Res. 10.1161/CIRCRESAHA.120.317015.

10. Sampaio, W.O., Souza dos Santos, R.A., Faria-Silva, R., da Mata Machado, L.T., Schiffrin, E.L., and Touyz, R.M. (2007). Angiotensin-(1-7) through receptor Mas mediates endothelial nitric oxide synthase activation via Akt-dependent pathways. Hypertension *49*, 185-192. 10.1161/01.HYP.0000251865.35728.2f.

11. Benter, I.F., Yousif, M.H., Al-Saleh, F.M., Raghupathy, R., Chappell, M.C., and Diz, D.I. (2011). Angiotensin-(1-7) blockade attenuates captopril- or hydralazine-induced cardiovascular protection in spontaneously hypertensive rats treated with NG-nitro-L-arginine methyl ester. J Cardiovasc Pharmacol *57*, 559-567. 10.1097/FJC.0b013e31821324b6.

12. Santos, R.A.S., Sampaio, W.O., Alzamora, A.C., Motta-Santos, D., Alenina, N., Bader, M., and Campagnole-Santos, M.J. (2018). The ACE2/Angiotensin-(1–7)/MAS Axis of the

Renin-Angiotensin System: Focus on Angiotensin-(1–7). Physiological Reviews *98*, 505-553. 10.1152/physrev.00023.2016.

13. Oudit, G.Y., Kassiri, Z., Patel, M.P., Chappell, M., Butany, J., Backx, P.H., Tsushima, R.G., Scholey, J.W., Khokha, R., and Penninger, J.M. (2007). Angiotensin II-mediated oxidative stress and inflammation mediate the age-dependent cardiomyopathy in ACE2 null mice. Cardiovasc Res *75*, 29-39. 10.1016/j.cardiores.2007.04.007.

14. Wu, C.-H., Mohammadmoradi, S., Chen, J.Z., Sawada, H., Daugherty, A., and Lu, H.S. (2018). Renin-Angiotensin System and Cardiovascular Functions. Arteriosclerosis, thrombosis, and vascular biology *38*, e108-e116. 10.1161/ATVBAHA.118.311282.

15. Vickers, C., Hales, P., Kaushik, V., Dick, L., Gavin, J., Tang, J., Godbout, K., Parsons, T., Baronas, E., Hsieh, F., et al. (2002). Hydrolysis of biological peptides by human angiotensin-converting enzyme-related carboxypeptidase. J Biol Chem *277*, 14838-14843. 10.1074/jbc.M200581200.

16. Liu, S., Liu, J., Miura, Y., Tanabe, C., Maeda, T., Terayama, Y., Turner, A.J., Zou, K., and Komano, H. (2014). Conversion of Abeta43 to Abeta40 by the successive action of angiotensin-converting enzyme 2 and angiotensin-converting enzyme. J Neurosci Res *92*, 1178-1186. 10.1002/jnr.23404.

17. Sodhi, C.P., Wohlford-Lenane, C., Yamaguchi, Y., Prindle, T., Fulton, W.B., Wang, S., McCray, P.B., Jr., Chappell, M., Hackam, D.J., and Jia, H. (2018). Attenuation of pulmonary ACE2 activity impairs inactivation of des-Arg(9) bradykinin/BKB1R axis and facilitates LPS-induced neutrophil infiltration. Am J Physiol Lung Cell Mol Physiol *314*, L17-L31. 10.1152/ajplung.00498.2016.

18. Camargo, S.M., Singer, D., Makrides, V., Huggel, K., Pos, K.M., Wagner, C.A., Kuba, K., Danilczyk, U., Skovby, F., Kleta, R., et al. (2009). Tissue-specific amino acid transporter partners ACE2 and collectrin differentially interact with hartnup mutations. Gastroenterology *136*, 872-882. 10.1053/j.gastro.2008.10.055.

19. Hashimoto, T., Perlot, T., Rehman, A., Trichereau, J., Ishiguro, H., Paolino, M., Sigl, V., Hanada, T., Hanada, R., Lipinski, S., et al. (2012). ACE2 links amino acid malnutrition to microbial ecology and intestinal inflammation. Nature *487*, 477-481. 10.1038/nature11228.

20. Kowalczuk, S., Broer, A., Tietze, N., Vanslambrouck, J.M., Rasko, J.E., and Broer, S. (2008). A protein complex in the brush-border membrane explains a Hartnup disorder allele. FASEB J *22*, 2880-2887. 10.1096/fj.08-107300.

21. Oudit, G.Y., Kassiri, Z., Jiang, C., Liu, P.P., Poutanen, S.M., Penninger, J.M., and Butany, J. (2009). SARS-coronavirus modulation of myocardial ACE2 expression and inflammation in patients with SARS. Eur J Clin Invest *39*, 618-625. 10.1111/j.1365-2362.2009.02153.x.

22. Wang, Q., Zhang, Y., Wu, L., Niu, S., Song, C., Zhang, Z., Lu, G., Qiao, C., Hu, Y., Yuen, K.Y., et al. (2020). Structural and Functional Basis of SARS-CoV-2 Entry by Using Human ACE2. Cell *181*, 894-904 e899. 10.1016/j.cell.2020.03.045.

23. Yan, R., Zhang, Y., Li, Y., Xia, L., Guo, Y., and Zhou, Q. (2020). Structural basis for the recognition of SARS-CoV-2 by full-length human ACE2. Science *367*, 1444-1448. 10.1126/science.abb2762.

24. Tukiainen, T., Villani, A.C., Yen, A., Rivas, M.A., Marshall, J.L., Satija, R., Aguirre, M., Gauthier, L., Fleharty, M., Kirby, A., et al. (2017). Landscape of X chromosome inactivation across human tissues. Nature *550*, 244-248. 10.1038/nature24265.

25. Viveiros, A., Rasmuson, J., Vu, J., Mulvagh, S.L., Yip, C.Y.Y., Norris, C.M., and Oudit, G.Y. (2021). Sex differences in COVID-19: candidate pathways, genetics of ACE2, and sex hormones. Am J Physiol Heart Circ Physiol *320*, H296-H304. 10.1152/ajpheart.00755.2020.

26. Qiao, Y., Wang, X.M., Mannan, R., Pitchiaya, S., Zhang, Y., Wotring, J.W., Xiao, L., Robinson, D.R., Wu, Y.M., Tien, J.C., et al. (2020). Targeting transcriptional regulation of SARS-CoV-2 entry factors ACE2 and TMPRSS2. Proc Natl Acad Sci U S A. 10.1073/pnas.2021450118.

27. Dalpiaz, P.L., Lamas, A.Z., Caliman, I.F., Ribeiro, R.F., Jr., Abreu, G.R., Moyses, M.R., Andrade, T.U., Gouvea, S.A., Alves, M.F., Carmona, A.K., and Bissoli, N.S. (2015). Sex Hormones Promote Opposite Effects on ACE and ACE2 Activity, Hypertrophy and Cardiac Contractility in Spontaneously Hypertensive Rats. PLoS One *10*, e0127515. 10.1371/journal.pone.0127515.

28. Liu, J., Ji, H., Zheng, W., Wu, X., Zhu, J.J., Arnold, A.P., and Sandberg, K. (2010). Sex differences in renal angiotensin converting enzyme 2 (ACE2) activity are 17beta-oestradiol-dependent and sex chromosome-independent. Biol Sex Differ *1*, 6. 10.1186/2042-6410-1-6.

29. Sato, T., Suzuki, T., Watanabe, H., Kadowaki, A., Fukamizu, A., Liu, P.P., Kimura, A., Ito, H., Penninger, J.M., Imai, Y., and Kuba, K. (2013). Apelin is a positive regulator of

ACE2 in failing hearts. The Journal of clinical investigation *123*, 5203-5211. 10.1172/JCI69608.

30. Chatterjee, P., Gheblawi, M., Wang, K., Vu, J., Kondaiah, P., and Oudit, G.Y. (2020). Interaction between the apelinergic system and ACE2 in the cardiovascular system: therapeutic implications. Clin Sci (Lond) *134*, 2319-2336. 10.1042/CS20200479.

31. Cedar, H., and Bergman, Y. (2009). Linking DNA methylation and histone modification: patterns and paradigms. Nat Rev Genet *10*, 295-304. 10.1038/nrg2540.

32. Fan, R., Mao, S.Q., Gu, T.L., Zhong, F.D., Gong, M.L., Hao, L.M., Yin, F.Y., Dong, C.Z., and Zhang, L.N. (2017). Preliminary analysis of the association between methylation of the ACE2 promoter and essential hypertension. Mol Med Rep *15*, 3905-3911. 10.3892/mmr.2017.6460.

33. Pinto, B.G.G., Oliveira, A.E.R., Singh, Y., Jimenez, L., Goncalves, A.N.A., Ogava, R.L.T., Creighton, R., Schatzmann Peron, J.P., and Nakaya, H.I. (2020). ACE2 Expression Is Increased in the Lungs of Patients With Comorbidities Associated With Severe COVID-19. J Infect Dis *222*, 556-563. 10.1093/infdis/jiaa332.

34. Li, Y., Li, H., and Zhou, L. (2020). EZH2-mediated H3K27me3 inhibits ACE2 expression. Biochem Biophys Res Commun *526*, 947-952. 10.1016/j.bbrc.2020.04.010.

35. Nersisyan, S., Shkurnikov, M., Turchinovich, A., Knyazev, E., and Tonevitsky, A. (2020). Integrative analysis of miRNA and mRNA sequencing data reveals potential regulatory mechanisms of ACE2 and TMPRSS2. PLoS One *15*, e0235987. 10.1371/journal.pone.0235987.

36. Fernandes, T., Hashimoto, N.Y., Magalhaes, F.C., Fernandes, F.B., Casarini, D.E., Carmona, A.K., Krieger, J.E., Phillips, M.I., and Oliveira, E.M. (2011). Aerobic exercise training-induced left ventricular hypertrophy involves regulatory MicroRNAs, decreased angiotensin-converting enzyme-angiotensin ii, and synergistic regulation of angiotensin-converting enzyme 2-angiotensin (1-7). Hypertension *58*, 182-189. 10.1161/HYPERTENSIONAHA.110.168252.

37. Lambert, D.W., Lambert, L.A., Clarke, N.E., Hooper, N.M., Porter, K.E., and Turner, A.J. (2014). Angiotensin-converting enzyme 2 is subject to post-transcriptional regulation by miR-421. Clin Sci (Lond) *127*, 243-249. 10.1042/CS20130420.

38. Shen, H., Zhang, J., Wang, C., Jain, P.P., Xiong, M., Shi, X., Lei, Y., Chen, S., Yin, Q., Thistlethwaite, P.A., et al. (2020). MDM2-Mediated Ubiquitination of Angiotensin-Converting Enzyme 2 Contributes to the Development of Pulmonary Arterial Hypertension. Circulation *142*, 1190-1204. 10.1161/CIRCULATIONAHA.120.048191.

39. Deshotels, M.R., Xia, H., Sriramula, S., Lazartigues, E., and Filipeanu, C.M. (2014). Angiotensin II mediates angiotensin converting enzyme type 2 internalization and degradation through an angiotensin II type I receptor-dependent mechanism. Hypertension *64*, 1368-1375. 10.1161/HYPERTENSIONAHA.114.03743.

40. Gheblawi, M., Wang, K., Viveiros, A., Nguyen, Q., Zhong, J.C., Turner, A.J., Raizada, M.K., Grant, M.B., and Oudit, G.Y. (2020). Angiotensin-Converting Enzyme 2: SARS-CoV-2 Receptor and Regulator of the Renin-Angiotensin System: Celebrating the 20th Anniversary of the Discovery of ACE2. Circ Res *126*, 1456-1474. 10.1161/CIRCRESAHA.120.317015.

41. Patel, V.B., Clarke, N., Wang, Z., Fan, D., Parajuli, N., Basu, R., Putko, B., Kassiri, Z., Turner, A.J., and Oudit, G.Y. (2014). Angiotensin II induced proteolytic cleavage of myocardial ACE2 is mediated by TACE/ADAM-17: a positive feedback mechanism in the RAS. J Mol Cell Cardiol *66*, 167-176. 10.1016/j.yjmcc.2013.11.017.

42. Badawi, S., and Ali, B.R. (2021). ACE2 Nascence, trafficking, and SARS-CoV-2 pathogenesis: the saga continues. Hum Genomics *15*, 8. 10.1186/s40246-021-00304-9.

43. Reich, H.N., Oudit, G.Y., Penninger, J.M., Scholey, J.W., and Herzenberg, A.M. (2008). Decreased glomerular and tubular expression of ACE2 in patients with type 2 diabetes and kidney disease. Kidney Int *74*, 1610-1616. 10.1038/ki.2008.497.

44. Roger, V.L. (2021). Epidemiology of Heart Failure: A Contemporary Perspective. Circ Res *128*, 1421-1434. 10.1161/CIRCRESAHA.121.318172.

45. Heidenreich, P.A., Bozkurt, B., Aguilar, D., Allen, L.A., Byun, J.J., Colvin, M.M., Deswal, A., Drazner, M.H., Dunlay, S.M., Evers, L.R., et al. (2022). 2022 AHA/ACC/HFSA Guideline for the Management of Heart Failure: A Report of the American College of Cardiology/American Heart Association Joint Committee on Clinical Practice Guidelines. Circulation *145*, e895-e1032. 10.1161/CIR.0000000000001063.

46. Rossignol, P., Hernandez, A.F., Solomon, S.D., and Zannad, F. (2019). Heart failure drug treatment. Lancet *393*, 1034-1044. 10.1016/S0140-6736(18)31808-7.

47. Metra, M., and Teerlink, J.R. (2017). Heart failure. Lancet *390*, 1981-1995. 10.1016/S0140-6736(17)31071-1.

48. Braunwald, E. (2013). Heart failure. JACC Heart Fail *1*, 1-20. 10.1016/j.jchf.2012.10.002.

49. Cohn, J.N., Ferrari, R., and Sharpe, N. (2000). Cardiac remodeling--concepts and clinical implications: a consensus paper from an international forum on cardiac remodeling. Behalf of an International Forum on Cardiac Remodeling. J Am Coll Cardiol *35*, 569-582. 10.1016/s0735-1097(99)00630-0.

50. McNally, E.M., and Mestroni, L. (2017). Dilated Cardiomyopathy: Genetic Determinants and Mechanisms. Circ Res *121*, 731-748. 10.1161/CIRCRESAHA.116.309396.

51. Zhong, J., Basu, R., Guo, D., Chow, F.L., Byrns, S., Schuster, M., Loibner, H., Wang, X.H., Penninger, J.M., Kassiri, Z., and Oudit, G.Y. (2010). Angiotensin-converting enzyme 2 suppresses pathological hypertrophy, myocardial fibrosis, and cardiac dysfunction. Circulation *122*, 717-728, 718 p following 728. 10.1161/CIRCULATIONAHA.110.955369.

52. Narula, S., Yusuf, S., Chong, M., Ramasundarahettige, C., Rangarajan, S., Bangdiwala, S.I., van Eikels, M., Leineweber, K., Wu, A., Pigeyre, M., and Pare, G. (2020). Plasma ACE2 and risk of death or cardiometabolic diseases: a case-cohort analysis. Lancet *396*, 968-976. 10.1016/S0140-6736(20)31964-4.

53. Chirinos, J.A., Cohen, J.B., Zhao, L., Hanff, T., Sweitzer, N., Fang, J., Corrales-Medina, V., Anmar, R., Morley, M., Zamani, P., et al. (2020). Clinical and Proteomic Correlates of Plasma ACE2 (Angiotensin-Converting Enzyme 2) in Human Heart Failure. Hypertension *76*, 1526-1536. 10.1161/HYPERTENSIONAHA.120.15829.

54. Li, W., Moore, M.J., Vasilieva, N., Sui, J., Wong, S.K., Berne, M.A., Somasundaran, M., Sullivan, J.L., Luzuriaga, K., Greenough, T.C., et al. (2003). Angiotensin-converting

enzyme 2 is a functional receptor for the SARS coronavirus. Nature *426*, 450-454. 10.1038/nature02145.

55. Kuba, K., Imai, Y., Rao, S., Gao, H., Guo, F., Guan, B., Huan, Y., Yang, P., Zhang, Y., Deng, W., et al. (2005). A crucial role of angiotensin converting enzyme 2 (ACE2) in SARS coronavirus-induced lung injury. Nat Med *11*, 875-879. 10.1038/nm1267.

56. Hoffmann, M., Kleine-Weber, H., Schroeder, S., Kruger, N., Herrler, T., Erichsen, S., Schiergens, T.S., Herrler, G., Wu, N.H., Nitsche, A., et al. (2020). SARS-CoV-2 Cell Entry Depends on ACE2 and TMPRSS2 and Is Blocked by a Clinically Proven Protease Inhibitor. Cell. 10.1016/j.cell.2020.02.052.

57. Monteil, V., Kwon, H., Prado, P., Hagelkruys, A., Wimmer, R.A., Stahl, M., Leopoldi, A., Garreta, E., Hurtado Del Pozo, C., Prosper, F., et al. (2020). Inhibition of SARS-CoV-2 Infections in Engineered Human Tissues Using Clinical-Grade Soluble Human ACE2. Cell *181*, 905-913 e907. 10.1016/j.cell.2020.04.004.

58. Gawish, R., Starkl, P., Pimenov, L., Hladik, A., Lakovits, K., Oberndorfer, F., Cronin, S.J., Ohradanova-Repic, A., Wirnsberger, G., Agerer, B., et al. (2022). ACE2 is the critical in vivo receptor for SARS-CoV-2 in a novel COVID-19 mouse model with TNF- and IFNgamma-driven immunopathology. Elife *11*. 10.7554/eLife.74623.

59. Chen, L., Li, X., Chen, M., Feng, Y., and Xiong, C. (2020). The ACE2 expression in human heart indicates new potential mechanism of heart injury among patients infected with SARS-CoV-2. Cardiovasc Res *116*, 1097-1100. 10.1093/cvr/cvaa078.

60. Wang, K., Gheblawi, M., Nikhanj, A., Munan, M., MacIntyre, E., O'Neil, C., Poglitsch, M., Colombo, D., Del Nonno, F., Kassiri, Z., et al. (2022). Dysregulation of ACE (Angiotensin-Converting Enzyme)-2 and Renin-Angiotensin Peptides in SARS-CoV-2

Mediated Mortality and End-Organ Injuries. Hypertension *79*, 365-378. 10.1161/HYPERTENSIONAHA.121.18295.

61. Norris, C.M., Yip, C.Y.Y., Nerenberg, K.A., Clavel, M.A., Pacheco, C., Foulds, H.J.A., Hardy, M., Gonsalves, C.A., Jaffer, S., Parry, M., et al. (2020). State of the Science in Women's Cardiovascular Disease: A Canadian Perspective on the Influence of Sex and Gender. J Am Heart Assoc *9*, e015634. 10.1161/JAHA.119.015634.

62. Agarwala, A., Michos, E.D., Samad, Z., Ballantyne, C.M., and Virani, S.S. (2020). The Use of Sex-Specific Factors in the Assessment of Women's Cardiovascular Risk. Circulation *141*, 592-599. 10.1161/Circulationaha.119.043429.

63. Eisenberg, E., Di Palo, K.E., and Pina, I.L. (2018). Sex differences in heart failure. Clin Cardiol *41*, 211-216. 10.1002/clc.22917.

64. Beale, A.L., Meyer, P., Marwick, T.H., Lam, C.S.P., and Kaye, D.M. (2018). Sex Differences in Cardiovascular Pathophysiology: Why Women Are Overrepresented in Heart Failure With Preserved Ejection Fraction. Circulation *138*, 198-205. 10.1161/CIRCULATIONAHA.118.034271.

65. Lichtman, J.H., Leifheit, E.C., Safdar, B., Bao, H., Krumholz, H.M., Lorenze, N.P., Daneshvar, M., Spertus, J.A., and D'Onofrio, G. (2018). Sex Differences in the Presentation and Perception of Symptoms Among Young Patients With Myocardial Infarction: Evidence from the VIRGO Study (Variation in Recovery: Role of Gender on Outcomes of Young AMI Patients). Circulation *137*, 781-790. 10.1161/CIRCULATIONAHA.117.031650.

66. Maric, C. (2005). Sex differences in cardiovascular disease and hypertension: involvement of the renin-angiotensin system. Hypertension *46*, 475-476. 10.1161/01.HYP.0000178600.88820.b2.

67. Karlberg, J., Chong, D.S., and Lai, W.Y. (2004). Do men have a higher case fatality rate of severe acute respiratory syndrome than women do? Am J Epidemiol *159*, 229-231. 10.1093/aje/kwh056.

68. World Health Organization (2007). Addressing sex and gender in epidemic-prone infectious diseases. World Health Organization.

69. Scully, E.P., Haverfield, J., Ursin, R.L., Tannenbaum, C., and Klein, S.L. (2020). Considering how biological sex impacts immune responses and COVID-19 outcomes. Nat Rev Immunol. 10.1038/s41577-020-0348-8.

70. Takahashi, T., Ellingson, M.K., Wong, P., Israelow, B., Lucas, C., Klein, J., Silva, J., Mao, T., Oh, J.E., Tokuyama, M., et al. (2020). Sex differences in immune responses that underlie COVID-19 disease outcomes. Nature. 10.1038/s41586-020-2700-3.

71. Basso, C., Leone, O., Rizzo, S., De Gaspari, M., van der Wal, A.C., Aubry, M.C., Bois, M.C., Lin, P.T., Maleszewski, J.J., and Stone, J.R. (2020). Pathological features of COVID-19-associated myocardial injury: a multicentre cardiovascular pathology study. Eur Heart J *41*, 3827-3835. 10.1093/eurheartj/ehaa664.

72. Bois, M.C., Boire, N.A., Layman, A.J., Aubry, M.C., Alexander, M.P., Roden, A.C., Hagen, C.E., Quinton, R.A., Larsen, C., Erben, Y., et al. (2021). COVID-19-Associated Nonocclusive Fibrin Microthrombi in the Heart. Circulation *143*, 230-243. 10.1161/CIRCULATIONAHA.120.050754.

73. Zhu, N., Zhang, D., Wang, W., Li, X., Yang, B., Song, J., Zhao, X., Huang, B., Shi, W., Lu, R., et al. (2020). A Novel Coronavirus from Patients with Pneumonia in China, 2019. N Engl J Med *382*, 727-733. 10.1056/NEJMoa2001017.

74. Botly, L.C.P., Martin-Rhee, M., BMath, A.K., Swartz, R.H., Mulvagh, S.L., Lindsay, P., Goia, C., Smith, E.E., Hill, M.D., Fileld, T.S., et al. (2020). COVID-19 Pandemic: Global Impact and Potential Implications for Cardiovascular Disease in Canada. CJC Open.

75. Fried, J.A., Ramasubbu, K., Bhatt, R., Topkara, V.K., Clerkin, K.J., Horn, E., Rabbani, L., Brodie, D., Jain, S.S., Kirtane, A., et al. (2020). The Variety of Cardiovascular Presentations of COVID-19. Circulation
. 10.1161/CIRCULATIONAHA.120.047164.

76. South, A.M., Diz, D.I., and Chappell, M.C. (2020). COVID-19, ACE2, and the cardiovascular consequences. Am J Physiol Heart Circ Physiol *318*, H1084-H1090. 10.1152/ajpheart.00217.2020.

77. Ackermann, M., Verleden, S.E., Kuehnel, M., Haverich, A., Welte, T., Laenger, F., Vanstapel, A., Werlein, C., Stark, H., Tzankov, A., et al. (2020). Pulmonary Vascular Endothelialitis, Thrombosis, and Angiogenesis in Covid-19. N Engl J Med. 10.1056/NEJMoa2015432.

78. Verdecchia, P., Cavallini, C., Spanevello, A., and Angeli, F. (2020). COVID-19: ACE2centric Infective Disease? Hypertension *76*, 294-299. 10.1161/HYPERTENSIONAHA.120.15353.

79. Del Valle, D.M., Kim-Schulze, S., Huang, H.H., Beckmann, N.D., Nirenberg, S., Wang, B., Lavin, Y., Swartz, T.H., Madduri, D., Stock, A., et al. (2020). An inflammatory cytokine

signature predicts COVID-19 severity and survival. Nat Med. 10.1038/s41591-020-1051-9.

80. Abou-Raya, S., Abou-Raya, A., Naim, A., and Abuelkheir, H. (2007). Chronic inflammatory autoimmune disorders and atherosclerosis. Ann N Y Acad Sci *1107*, 56-67. 10.1196/annals.1381.007.

81. Klein, S.L., and Flanagan, K.L. (2016). Sex differences in immune responses. Nat Rev Immunol *16*, 626-638. 10.1038/nri.2016.90.

82. Mann, D.L., Topkara, V.K., Evans, S., and Barger, P.M. (2010). Innate immunity in the adult mammalian heart: for whom the cell tolls. Trans Am Clin Climatol Assoc *121*, 34-50; discussion 50-31.

83. Mann, D.L. (2011). The emerging role of innate immunity in the heart and vascular system: for whom the cell tolls. Circ Res *108*, 1133-1145. 10.1161/CIRCRESAHA.110.226936.

84. Patel, V.B., Zhong, J.C., Grant, M.B., and Oudit, G.Y. (2016). Role of the ACE2/Angiotensin 1-7 Axis of the Renin-Angiotensin System in Heart Failure. Circ Res *118*, 1313-1326. 10.1161/CIRCRESAHA.116.307708.

85. Patel, V.B., Zhong, J.C., Fan, D., Basu, R., Morton, J.S., Parajuli, N., McMurtry, M.S., Davidge, S.T., Kassiri, Z., and Oudit, G.Y. (2014). Angiotensin-converting enzyme 2 is a critical determinant of angiotensin II-induced loss of vascular smooth muscle cells and adverse vascular remodeling. Hypertension *64*, 157-164. 10.1161/HYPERTENSIONAHA.114.03388.

86. Oudit, G.Y., and Pfeffer, M.A. (2020). Plasma angiotensin-converting enzyme 2: novel biomarker in heart failure with implications for COVID-19. Eur Heart J *41*, 1818-1820. 10.1093/eurheartj/ehaa414.

87. Chappell, M.C., Marshall, A.C., Alzayadneh, E.M., Shaltout, H.A., and Diz, D.I. (2014). Update on the Angiotensin converting enzyme 2-Angiotensin (1-7)-MAS receptor axis: fetal programing, sex differences, and intracellular pathways. Front Endocrinol (Lausanne) *4*, 201. 10.3389/fendo.2013.00201.

88. Yancy, C.W., Jessup, M., Bozkurt, B., Butler, J., Casey, D.E., Jr., Colvin, M.M., Drazner, M.H., Filippatos, G.S., Fonarow, G.C., Givertz, M.M., et al. (2017). 2017 ACC/AHA/HFSA Focused Update of the 2013 ACCF/AHA Guideline for the Management of Heart Failure: A Report of the American College of Cardiology/American Heart Association Task Force on Clinical Practice Guidelines and the Heart Failure Society of America. Circulation *136*, e137-e161. 10.1161/CIR.0000000000000509.

89. Santema, B.T., Ouwerkerk, W., Tromp, J., Sama, I.E., Ravera, A., Regitz-Zagrosek, V., Hillege, H., Samani, N.J., Zannad, F., Dickstein, K., et al. (2019). Identifying optimal doses of heart failure medications in men compared with women: a prospective, observational, cohort study. Lancet *394*, 1254-1263. 10.1016/S0140-6736(19)31792-1.

90. Gerdts, E., and Regitz-Zagrosek, V. (2019). Sex differences in cardiometabolic disorders. Nat Med *25*, 1657-1666. 10.1038/s41591-019-0643-8.

91. Totura, A.L., and Baric, R.S. (2012). SARS coronavirus pathogenesis: host innate immune responses and viral antagonism of interferon. Curr Opin Virol *2*, 264-275. 10.1016/j.coviro.2012.04.004.

92. Rettew, J.A., Huet-Hudson, Y.M., and Marriott, I. (2008). Testosterone reduces macrophage expression in the mouse of toll-like receptor 4, a trigger for inflammation and innate immunity. Biol Reprod *78*, 432-437. 10.1095/biolreprod.107.063545.

93. Ribero, M.S., Jouvenet, N., Dreux, M., and Nisole, S. (2020). Interplay between SARS-CoV-2 and the type I interferon response. Plos Pathog *16*. ARTN e1008737 10.1371/journal.ppat.1008737.

94. Sharma, S.K., Stevens, B.R., Obukhov, A.G., Grant, M.B., Oudit, G.Y., Richards, E.M., Pepine, C.J., and Raizada, M.K. (2020). Angiotensin Converting Enzyme 2 in Cardiopulmonary Diseases: Ramifications for the Control of SARS-CoV-2. Hypertension, In Press.

95. Haga, S., Yamamoto, N., Nakai-Murakami, C., Osawa, Y., Tokunaga, K., Sata, T., Yamamoto, N., Sasazuki, T., and Ishizaka, Y. (2008). Modulation of TNF-alpha-converting enzyme by the spike protein of SARS-CoV and ACE2 induces TNF-alpha production and facilitates viral entry. Proc Natl Acad Sci U S A *105*, 7809-7814. 10.1073/pnas.0711241105.

96. Gooz, M. (2010). ADAM-17: the enzyme that does it all. Crit Rev Biochem Mol Biol *45*, 146-169. 10.3109/10409231003628015.

97. Schurz, H., Salie, M., Tromp, G., Hoal, E.G., Kinnear, C.J., and Moller, M. (2019). The X chromosome and sex-specific effects in infectious disease susceptibility. Hum Genomics *13*, 2. 10.1186/s40246-018-0185-z.

98. Pisitkun, P., Deane, J.A., Difilippantonio, M.J., Tarasenko, T., Satterthwaite, A.B., and Bolland, S. (2006). Autoreactive B cell responses to RNA-related antigens due to TLR7 gene duplication. Science *312*, 1669-1672. 10.1126/science.1124978.

99. Berghofer, B., Frommer, T., Haley, G., Fink, L., Bein, G., and Hackstein, H. (2006). TLR7 ligands induce higher IFN-alpha production in females. J Immunol *177*, 2088-2096. 10.4049/jimmunol.177.4.2088.

100. Wang, W., Patel, V.B., Parajuli, N., Fan, D., Basu, R., Wang, Z., Ramprasath, T., Kassiri, Z., Penninger, J.M., and Oudit, G.Y. (2014). Heterozygote loss of ACE2 is sufficient to increase the susceptibility to heart disease. J Mol Med (Berl) *92*, 847-858. 10.1007/s00109-014-1149-y.

101. Chen, K., Bi, J., Su, Y., Chappell, M.C., and Rose, J.C. (2016). Sex-Specific Changes in Renal Angiotensin-Converting Enzyme and Angiotensin-Converting Enzyme 2 Gene Expression and Enzyme Activity at Birth and Over the First Year of Life. Reprod Sci *23*, 200-210. 10.1177/1933719115597760.

102. Hannah, M.F., Bajic, V.B., and Klein, S.L. (2008). Sex differences in the recognition of and innate antiviral responses to Seoul virus in Norway rats. Brain Behav Immun *22*, 503-516. 10.1016/j.bbi.2007.10.005.

103. Channappanavar, R., Fett, C., Mack, M., Ten Eyck, P.P., Meyerholz, D.K., and Perlman, S. (2017). Sex-Based Differences in Susceptibility to Severe Acute Respiratory

Syndrome Coronavirus Infection. J Immunol *198*, 4046-4053. 10.4049/jimmunol.1601896.

104. Robinson, D.P., Lorenzo, M.E., Jian, W., and Klein, S.L. (2011). Elevated 17beta-estradiol protects females from influenza A virus pathogenesis by suppressing inflammatory responses. Plos Pathog *7*, e1002149. 10.1371/journal.ppat.1002149.

105. Hao, S., Zhao, J., Zhou, J., Zhao, S., Hu, Y., and Hou, Y. (2007). Modulation of 17beta-estradiol on the number and cytotoxicity of NK cells in vivo related to MCM and activating receptors. Int Immunopharmacol *7*, 1765-1775. 10.1016/j.intimp.2007.09.017.

106. Ji, H., Menini, S., Zheng, W., Pesce, C., Wu, X., and Sandberg, K. (2008). Role of angiotensin-converting enzyme 2 and angiotensin(1-7) in 17beta-oestradiol regulation of renal pathology in renal wrap hypertension in rats. Exp Physiol *93*, 648-657. 10.1113/expphysiol.2007.041392.

107. Gupte, M., Thatcher, S.E., Boustany-Kari, C.M., Shoemaker, R., Yiannikouris, F., Zhang, X., Karounos, M., and Cassis, L.A. (2012). Angiotensin converting enzyme 2 contributes to sex differences in the development of obesity hypertension in C57BL/6 mice. Arterioscler Thromb Vasc Biol *32*, 1392-1399. 10.1161/ATVBAHA.112.248559.

108. Okumura, M., Iwai, M., Ide, A., Mogi, M., Ito, M., and Horiuchi, M. (2005). Sex difference in vascular injury and the vasoprotective effect of valsartan are related to differential AT2 receptor expression. Hypertension *46*, 577-583. 10.1161/01.HYP.0000178564.14464.80.

109. Ji, H., de Souza, A.M.A., Bajaj, B., Zheng, W., Wu, X., Speth, R.C., and Sandberg, K. (2020). Sex-Specific Modulation of Blood Pressure and the Renin-Angiotensin System by ACE (Angiotensin-Converting Enzyme) 2. Hypertension *76*, 478-487. 10.1161/HYPERTENSIONAHA.120.15276.

110. Farrar, J., and Gupta, G.R. (2020). Why we need women's leadership in the COVID-19 response. https://www.weforum.org/agenda/2020/04/women-female-leadership-gender-coronavirus-covid19-response/.

111. United Nations (2020). Policy Brief: The Impact of COVID-19 on Women. https://www.un.org/sites/un2.un.org/files/policy_brief_on_covid_impact_on_women_9_april_2020.pdf.

112. Zheng, S., Fan, J., Yu, F., Feng, B., Lou, B., Zou, Q., Xie, G., Lin, S., Wang, R., Yang, X., et al. (2020). Viral load dynamics and disease severity in patients infected with SARS-CoV-2 in Zhejiang province, China, January-March 2020: retrospective cohort study. BMJ *369*, m1443. 10.1136/bmj.m1443.

113. Global Health 5050 (2020). COVID-19 sex-disaggregated data tracker. https://globalhealth5050.org/the-sex-gender-and-covid-19-project/.

114. Kannel, W.B., and McGee, D.L. (1979). Diabetes and Glucose Tolerance as Risk Factors for Cardiovascular Disease: The Framingham Study. Diabetes Care *2*, 120-126. 10.2337/diacare.2.2.120.

115. Fowler, M.J. (2008). Microvascular and Macrovascular Complications of Diabetes. Clinical Diabetes *26*, 77-82. 10.2337/diaclin.26.2.77.

116. Eckel, R.H., York, D.A., Rossner, S., Hubbard, V., Caterson, I., St Jeor, S.T., Hayman, L.L., Mullis, R.M., Blair, S.N., and American Heart, A. (2004). Prevention Conference VII:

Obesity, a worldwide epidemic related to heart disease and stroke: executive summary. Circulation *110*, 2968-2975. 10.1161/01.CIR.0000140086.88453.9A.

117. Murphy, N.F., MacIntyre, K., Stewart, S., Hart, C.L., Hole, D., and McMurray, J.J. (2006). Long-term cardiovascular consequences of obesity: 20-year follow-up of more than 15 000 middle-aged men and women (the Renfrew-Paisley study). Eur Heart J *27*, 96-106. 10.1093/eurheartj/ehi506.

118. Prospective Studies, C., Whitlock, G., Lewington, S., Sherliker, P., Clarke, R., Emberson, J., Halsey, J., Qizilbash, N., Collins, R., and Peto, R. (2009). Body-mass index and cause-specific mortality in 900 000 adults: collaborative analyses of 57 prospective studies. Lancet *373*, 1083-1096. 10.1016/S0140-6736(09)60318-4.

119. Russo, C., Jin, Z., Homma, S., Rundek, T., Elkind, M.S., Sacco, R.L., and Di Tullio, M.R. (2011). Effect of obesity and overweight on left ventricular diastolic function: a community-based study in an elderly cohort. J Am Coll Cardiol *57*, 1368-1374. 10.1016/j.jacc.2010.10.042.

120. Savji, N., Meijers, W.C., Bartz, T.M., Bhambhani, V., Cushman, M., Nayor, M., Kizer, J.R., Sarma, A., Blaha, M.J., Gansevoort, R.T., et al. (2018). The Association of Obesity and Cardiometabolic Traits With Incident HFpEF and HFrEF. JACC Heart Fail *6*, 701-709. 10.1016/j.jchf.2018.05.018.

121. Guilherme, A., Virbasius, J.V., Puri, V., and Czech, M.P. (2008). Adipocyte dysfunctions linking obesity to insulin resistance and type 2 diabetes. Nat Rev Mol Cell Biol *9*, 367-377. 10.1038/nrm2391.

122. Richardson, V.R., Smith, K.A., and Carter, A.M. (2013). Adipose tissue inflammation: Feeding the development of type 2 diabetes mellitus. Immunobiology *218*, 1497-1504. https://doi.org/10.1016/j.imbio.2013.05.002.

123. Shimizu, I., Yoshida, Y., Katsuno, T., and Minamino, T. (2013). Adipose tissue inflammation in diabetes and heart failure. Microbes and Infection *15*, 11-17. https://doi.org/10.1016/j.micinf.2012.10.012.

124. Kohlgruber, A., and Lynch, L. (2015). Adipose tissue inflammation in the pathogenesis of type 2 diabetes. Current diabetes reports *15*, 92. 10.1007/s11892-015-0670-x.

125. Fitzgibbons, T.P., and Czech, M.P. (2014). Epicardial and Perivascular Adipose Tissues and Their Influence on Cardiovascular Disease: Basic Mechanisms and Clinical Associations. J Am Heart Assoc *3*. 10.1161/jaha.113.000582.

126. Marchington, J.M., Mattacks, C.A., and Pond, C.M. (1989). Adipose tissue in the mammalian heart and pericardium: structure, foetal development and biochemical properties. Comp Biochem Physiol B *94*, 225-232. 10.1016/0305-0491(89)90337-4.

127. Patel, V.B., Shah, S., Verma, S., and Oudit, G.Y. (2017). Epicardial adipose tissue as a metabolic transducer: role in heart failure and coronary artery disease. Heart Fail Rev *22*, 889-902. 10.1007/s10741-017-9644-1.

128. Aghamohammadzadeh, R., Withers, S., Lynch, F., Greenstein, A., Malik, R., and Heagerty, A. (2012). Perivascular adipose tissue from human systemic and coronary vessels: the emergence of a new pharmacotherapeutic target. British journal of pharmacology *165*, 670-682. 10.1111/j.1476-5381.2011.01479.x.

129. Withers, S.B., Bussey, C.E., Saxton, S.N., Melrose, H.M., Watkins, A.E., and Heagerty, A.M. (2014). Mechanisms of adiponectin-associated perivascular function in vascular disease. Arterioscler Thromb Vasc Biol *34*, 1637-1642. 10.1161/atvbaha.114.303031.

130. Saxton, S.N., Withers, S.B., and Heagerty, A.M. (2019). Emerging Roles of Sympathetic Nerves and Inflammation in Perivascular Adipose Tissue. Cardiovascular drugs and therapy *33*, 245-259. 10.1007/s10557-019-06862-4.

131. Soltis, E.E., and Cassis, L.A. (1991). Influence of perivascular adipose tissue on rat aortic smooth muscle responsiveness. Clinical and experimental hypertension. Part A, Theory and practice *13*, 277-296. 10.3109/10641969109042063.

132. Lohn, M., Dubrovska, G., Lauterbach, B., Luft, F.C., Gollasch, M., and Sharma, A.M. (2002). Periadventitial fat releases a vascular relaxing factor. Faseb j *16*, 1057-1063. 10.1096/fj.02-0024com.

133. Greenstein, A.S., Khavandi, K., Withers, S.B., Sonoyama, K., Clancy, O., Jeziorska, M., Laing, I., Yates, A.P., Pemberton, P.W., Malik, R.A., and Heagerty, A.M. (2009). Local inflammation and hypoxia abolish the protective anticontractile properties of perivascular fat in obese patients. Circulation *119*, 1661-1670. 10.1161/circulationaha.108.821181.

134. Galvez, B., de Castro, J., Herold, D., Dubrovska, G., Arribas, S., Gonzalez, M.C., Aranguez, I., Luft, F.C., Ramos, M.P., Gollasch, M., and Fernandez Alfonso, M.S. (2006). Perivascular adipose tissue and mesenteric vascular function in spontaneously hypertensive rats. Arterioscler Thromb Vasc Biol *26*, 1297-1302. 10.1161/01.ATV.0000220381.40739.dd.

135. Gao, Y.J., Takemori, K., Su, L.Y., An, W.S., Lu, C., Sharma, A.M., and Lee, R.M. (2006). Perivascular adipose tissue promotes vasoconstriction: the role of superoxide anion. Cardiovasc Res *71*, 363-373. 10.1016/j.cardiores.2006.03.013.

136. Gao, Y.J., Lu, C., Su, L.Y., Sharma, A.M., and Lee, R.M. (2007). Modulation of vascular function by perivascular adipose tissue: the role of endothelium and hydrogen peroxide. British journal of pharmacology *151*, 323-331. 10.1038/sj.bjp.0707228.

137. Verlohren, S., Dubrovska, G., Tsang, S.Y., Essin, K., Luft, F.C., Huang, Y., and Gollasch, M. (2004). Visceral periadventitial adipose tissue regulates arterial tone of mesenteric arteries. Hypertension *44*, 271-276. 10.1161/01.HYP.0000140058.28994.ec.

138. Szasz, T., Bomfim, G.F., and Webb, R.C. (2013). The influence of perivascular adipose tissue on vascular homeostasis. Vascular health and risk management *9*, 105-116. 10.2147/vhrm.s33760.

139. Lehman, S.J., Massaro, J.M., Schlett, C.L., O'Donnell, C.J., Hoffmann, U., and Fox, C.S. (2010). Peri-aortic fat, cardiovascular disease risk factors, and aortic calcification: the Framingham Heart Study. Atherosclerosis *210*, 656-661. 10.1016/j.atherosclerosis.2010.01.007.

140. Fox, C.S., Massaro, J.M., Schlett, C.L., Lehman, S.J., Meigs, J.B., O'Donnell, C.J., Hoffmann, U., and Murabito, J.M. (2010). Periaortic fat deposition is associated with peripheral arterial disease: the Framingham heart study. Circulation. Cardiovascular imaging *3*, 515-519. 10.1161/circimaging.110.958884.

141. Rosito, G.A., Massaro, J.M., Hoffmann, U., Ruberg, F.L., Mahabadi, A.A., Vasan, R.S., O'Donnell, C.J., and Fox, C.S. (2008). Pericardial fat, visceral abdominal fat,

cardiovascular disease risk factors, and vascular calcification in a community-based sample: the Framingham Heart Study. Circulation *117*, 605-613. 10.1161/circulationaha.107.743062.

142. Mahabadi, A.A., Massaro, J.M., Rosito, G.A., Levy, D., Murabito, J.M., Wolf, P.A., O'Donnell, C.J., Fox, C.S., and Hoffmann, U. (2009). Association of pericardial fat, intrathoracic fat, and visceral abdominal fat with cardiovascular disease burden: the Framingham Heart Study. Eur Heart J *30*, 850-856. 10.1093/eurheartj/ehn573.

143. Owen, M.K., Noblet, J.N., Sassoon, D.J., Conteh, A.M., Goodwill, A.G., and Tune, J.D. (2014). Perivascular Adipose Tissue and Coronary Vascular Disease. Arteriosclerosis, Thrombosis, and Vascular Biology *34*, 1643-1649. doi:10.1161/ATVBAHA.114.303033.

144. Izgi, C. (2015). Epicardial adipose tissue: Just a predictor or a local player for coronary atherosclerosis? Anatol J Cardiol *15*, 360-362. 10.5152/akd.2015.0053.

145. Iacobellis, G. (2009). Epicardial and pericardial fat: close, but very different. Obesity (Silver Spring) *17*, 625; author reply 626-627. 10.1038/oby.2008.575.

146. Iacobellis, G., and Willens, H.J. (2009). Echocardiographic epicardial fat: a review of research and clinical applications. J Am Soc Echocardiogr *22*, 1311-1319; quiz 1417-1318. 10.1016/j.echo.2009.10.013.

147. Talman, A.H., Psaltis, P.J., Cameron, J.D., Meredith, I.T., Seneviratne, S.K., and Wong, D.T. (2014). Epicardial adipose tissue: far more than a fat depot. Cardiovasc Diagn Ther *4*, 416-429. 10.3978/j.issn.2223-3652.2014.11.05.

148. Iacobellis, G., Corradi, D., and Sharma, A.M. (2005). Epicardial adipose tissue: anatomic, biomolecular and clinical relationships with the heart. Nat Clin Pract Cardiovasc Med *2*, 536-543. 10.1038/ncpcardio0319.

149. Corradi, D., Maestri, R., Callegari, S., Pastori, P., Goldoni, M., Luong, T.V., and Bordi, C. (2004). The ventricular epicardial fat is related to the myocardial mass in normal, ischemic and hypertrophic hearts. Cardiovasc Pathol *13*, 313-316. 10.1016/j.carpath.2004.08.005.

150. Sacks, H.S., and Fain, J.N. (2007). Human epicardial adipose tissue: a review. Am Heart J *153*, 907-917. 10.1016/j.ahj.2007.03.019.

151. Sengul, C., and Ozveren, O. (2013). Epicardial adipose tissue: a review of physiology, pathophysiology, and clinical applications. Anadolu Kardiyol Derg *13*, 261-265. 10.5152/akd.2013.075.

152. Iacobellis, G., and Bianco, A.C. (2011). Epicardial adipose tissue: emerging physiological, pathophysiological and clinical features. Trends Endocrinol Metab *22*, 450-457. 10.1016/j.tem.2011.07.003.

153. Taguchi, R., Takasu, J., Itani, Y., Yamamoto, R., Yokoyama, K., Watanabe, S., and Masuda, Y. (2001). Pericardial fat accumulation in men as a risk factor for coronary artery disease. Atherosclerosis *157*, 203-209. Doi 10.1016/S0021-9150(00)00709-7.

154. Fitzgibbons, T.P., and Czech, M.P. (2014). Epicardial and perivascular adipose tissues and their influence on cardiovascular disease: basic mechanisms and clinical associations. J Am Heart Assoc *3*, e000582. 10.1161/JAHA.113.000582.

155. Iacobellis, G., Ribaudo, M.C., Assael, F., Vecci, E., Tiberti, C., Zappaterreno, A., Di Mario, U., and Leonetti, F. (2003). Echocardiographic epicardial adipose tissue is related to anthropometric and clinical parameters of metabolic syndrome: a new indicator of cardiovascular risk. J Clin Endocrinol Metab *88*, 5163-5168. 10.1210/jc.2003-030698.

156. Mazurek, T., Zhang, L., Zalewski, A., Mannion, J.D., Diehl, J.T., Arafat, H., Sarov-Blat, L., O'Brien, S., Keiper, E.A., Johnson, A.G., et al. (2003). Human epicardial adipose tissue is a source of inflammatory mediators. Circulation *108*, 2460-2466. 10.1161/01.CIR.0000099542.57313.C5.

157. Rabkin, S.W. (2007). Epicardial fat: properties, function and relationship to obesity. Obes Rev *8*, 253-261. 10.1111/j.1467-789X.2006.00293.x.

158. Cherian, S., Lopaschuk, G.D., and Carvalho, E. (2012). Cellular cross-talk between epicardial adipose tissue and myocardium in relation to the pathogenesis of cardiovascular disease. Am J Physiol Endocrinol Metab *303*, E937-949. 10.1152/ajpendo.00061.2012.

159. Lei, B., Lionetti, V., Young, M.E., Chandler, M.P., d'Agostino, C., Kang, E., Altarejos, M., Matsuo, K., Hintze, T.H., Stanley, W.C., and Recchia, F.A. (2004). Paradoxical downregulation of the glucose oxidation pathway despite enhanced flux in severe heart failure. J Mol Cell Cardiol *36*, 567-576. 10.1016/j.yjmcc.2004.02.004.

160. Stanley, W.C., Recchia, F.A., and Lopaschuk, G.D. (2005). Myocardial substrate metabolism in the normal and failing heart. Physiol Rev *85*, 1093-1129. 10.1152/physrev.00006.2004.

161. Marchington, J.M., and Pond, C.M. (1990). Site-specific properties of pericardial and epicardial adipose tissue: the effects of insulin and high-fat feeding on lipogenesis and the incorporation of fatty acids in vitro. Int J Obes *14*, 1013-1022.

162. Wozniak, S.E., Gee, L.L., Wachtel, M.S., and Frezza, E.E. (2009). Adipose tissue: the new endocrine organ? A review article. Dig Dis Sci *54*, 1847-1856. 10.1007/s10620-008-0585-3.

163. Iacobellis, G., Pistilli, D., Gucciardo, M., Leonetti, F., Miraldi, F., Brancaccio, G., Gallo, P., and di Gioia, C.R. (2005). Adiponectin expression in human epicardial adipose tissue in vivo is lower in patients with coronary artery disease. Cytokine *29*, 251-255. 10.1016/j.cyto.2004.11.002.

164. Yamauchi, T., Kamon, J., Minokoshi, Y., Ito, Y., Waki, H., Uchida, S., Yamashita, S., Noda, M., Kita, S., Ueki, K., et al. (2002). Adiponectin stimulates glucose utilization and fatty-acid oxidation by activating AMP-activated protein kinase. Nat Med *8*, 1288-1295. 10.1038/nm788.

165. Galli, S.J., Borregaard, N., and Wynn, T.A. (2011). Phenotypic and functional plasticity of cells of innate immunity: macrophages, mast cells and neutrophils. Nat Immunol *12*, 1035-1044. 10.1038/ni.2109.

166. Cildir, G., Akincilar, S.C., and Tergaonkar, V. (2013). Chronic adipose tissue inflammation: all immune cells on the stage. Trends Mol Med *19*, 487-500. 10.1016/j.molmed.2013.05.001.

167. Guzik, T.J., Skiba, D.S., Touyz, R.M., and Harrison, D.G. (2017). The role of infiltrating immune cells in dysfunctional adipose tissue. Cardiovasc Res *113*, 1009-1023. 10.1093/cvr/cvx108.

168. Gruzdeva, O., Uchasova, E., Dyleva, Y., Borodkina, D., Akbasheva, O., Antonova, L., Matveeva, V., Belik, E., Ivanov, S., Sotnikov, A., et al. (2019). Adipocytes Directly Affect Coronary Artery Disease Pathogenesis via Induction of Adipokine and Cytokine Imbalances. Front Immunol *10*, 2163. 10.3389/fimmu.2019.02163.

169. Cheng, K.H., Chu, C.S., Lee, K.T., Lin, T.H., Hsieh, C.C., Chiu, C.C., Voon, W.C., Sheu, S.H., and Lai, W.T. (2008). Adipocytokines and proinflammatory mediators from abdominal and epicardial adipose tissue in patients with coronary artery disease. Int J Obes (Lond) *32*, 268-274. 10.1038/sj.ijo.0803726.

170. Eiras, S., Teijeira-Fernandez, E., Shamagian, L.G., Fernandez, A.L., Vazquez-Boquete, A., and Gonzalez-Juanatey, J.R. (2008). Extension of coronary artery disease is associated with increased IL-6 and decreased adiponectin gene expression in epicardial adipose tissue. Cytokine *43*, 174-180. 10.1016/j.cyto.2008.05.006.

171. Gruzdeva, O.V., Akbasheva, O.E., Dyleva, Y.A., Antonova, L.V., Matveeva, V.G., Uchasova, E.G., Fanaskova, E.V., Karetnikova, V.N., Ivanov, S.V., and Barbarash, O.L. (2017). Adipokine and Cytokine Profiles of Epicardial and Subcutaneous Adipose Tissue in Patients with Coronary Heart Disease. Bull Exp Biol Med *163*, 608-611. 10.1007/s10517-017-3860-5.

172. Baker, A.R., Silva, N.F., Quinn, D.W., Harte, A.L., Pagano, D., Bonser, R.S., Kumar, S., and McTernan, P.G. (2006). Human epicardial adipose tissue expresses a pathogenic profile of adipocytokines in patients with cardiovascular disease. Cardiovasc Diabetol *5*, 1. 10.1186/1475-2840-5-1.

173. Wang, W., Shen, M., Fischer, C., Basu, R., Hazra, S., Couvineau, P., Paul, M., Wang, F., Toth, S., Mix, D.S., et al. (2019). Apelin protects against abdominal aortic aneurysm

and the therapeutic role of neutral endopeptidase resistant apelin analogs. Proc Natl Acad Sci U S A *116*, 13006-13015. 10.1073/pnas.1900152116.

174. Patel, V.B., Mori, J., McLean, B.A., Basu, R., Das, S.K., Ramprasath, T., Parajuli, N., Penninger, J.M., Grant, M.B., Lopaschuk, G.D., and Oudit, G.Y. (2016). ACE2 Deficiency Worsens Epicardial Adipose Tissue Inflammation and Cardiac Dysfunction in Response to Diet-Induced Obesity. Diabetes *65*, 85-95. 10.2337/db15-0399.

175. Mraz, M., Cinkajzlova, A., Klouckova, J., Lacinova, Z., Kratochvilova, H., Lips, M., Porizka, M., Kopecky, P., Lindner, J., Kotulak, T., et al. (2019). Dendritic Cells in Subcutaneous and Epicardial Adipose Tissue of Subjects with Type 2 Diabetes, Obesity, and Coronary Artery Disease. Mediators Inflamm *2019*, 5481725. 10.1155/2019/5481725.

176. Mraz, M., Cinkajzlova, A., Klouckova, J., Lacinova, Z., Kratochvilova, H., Lips, M., Porizka, M., Kopecky, P., Pierzynova, A., Kucera, T., et al. (2019). Coronary Artery Disease Is Associated with an Increased Amount of T Lymphocytes in Human Epicardial Adipose Tissue. Mediators Inflamm *2019*, 4075086. 10.1155/2019/4075086.

177. Hirata, Y., Tabata, M., Kurobe, H., Motoki, T., Akaike, M., Nishio, C., Higashida, M., Mikasa, H., Nakaya, Y., Takanashi, S., et al. (2011). Coronary atherosclerosis is associated with macrophage polarization in epicardial adipose tissue. J Am Coll Cardiol *58*, 248-255. 10.1016/j.jacc.2011.01.048.

178. Levitsky, A., Brismar, K., Hafstrom, I., Hambardzumyan, K., Lourdudoss, C., van Vollenhoven, R.F., and Saevarsdottir, S. (2017). Obesity is a strong predictor of worse clinical outcomes and treatment responses in early rheumatoid arthritis:

results from the SWEFOT trial. RMD Open *3*, e000458. 10.1136/rmdopen-2017-000458.

179. Maglio, C., Peltonen, M., Rudin, A., and Carlsson, L.M.S. (2017). Bariatric Surgery and the Incidence of Psoriasis and Psoriatic Arthritis in the Swedish Obese Subjects Study. Obesity (Silver Spring) *25*, 2068-2073. 10.1002/oby.21955.

180. Huppke, B., Ellenberger, D., Hummel, H., Stark, W., Robl, M., Gartner, J., and Huppke, P. (2019). Association of Obesity With Multiple Sclerosis Risk and Response to First-line Disease Modifying Drugs in Children. JAMA Neurol. 10.1001/jamaneurol.2019.1997.

181. Schieir, O., Tosevski, C., Glazier, R.H., Hogg-Johnson, S., and Badley, E.M. (2017). Incident myocardial infarction associated with major types of arthritis in the general population: a systematic review and meta-analysis. Ann Rheum Dis *76*, 1396-1404. 10.1136/annrheumdis-2016-210275.

182. Fernandez-Gutierrez, B., Perrotti, P.P., Gisbert, J.P., Domenech, E., Fernandez-Nebro, A., Canete, J.D., Ferrandiz, C., Tornero, J., Garcia-Sanchez, V., Panes, J., et al. (2017). Cardiovascular disease in immune-mediated inflammatory diseases: A cross-sectional analysis of 6 cohorts. Medicine (Baltimore) *96*, e7308. 10.1097/MD.0000000000007308.

183. Marrie, R.A., Garland, A., Schaffer, S.A., Fransoo, R., Leung, S., Yogendran, M., Kingwell, E., and Tremlett, H. (2019). Traditional risk factors may not explain increased incidence of myocardial infarction in MS. Neurology *92*, e1624-e1633. 10.1212/WNL.0000000000007251.

184. Lima-Martinez, M.M., Campo, E., Salazar, J., Paoli, M., Maldonado, I., Acosta, C., Rodney, M., Contreras, M., Cabrera-Rego, J.O., and Iacobellis, G. (2014). Epicardial fat thickness as cardiovascular risk factor and therapeutic target in patients with rheumatoid arthritis treated with biological and nonbiological therapies. Arthritis *2014*, 782850. 10.1155/2014/782850.

185. Wang, X., Guo, Z., Zhu, Z., Bao, Y., and Yang, B. (2016). Epicardial fat tissue in patients with psoriasis:a systematic review and meta-analysis. Lipids Health Dis *15*, 103. 10.1186/s12944-016-0271-y.

186. Uysal, F., Akbal, E., Akbal, A., Cevizci, S., Arik, K., and Gazi, E. (2016). Epicardial Adipose Tissue Is Increased in Patients With Inflammatory Bowel Disease. J Ultrasound Med *35*, 1859-1864. 10.7863/ultra.14.09040.

187. Song, D.K., Hong, Y.S., Lee, H., Oh, J.Y., Sung, Y.A., and Kim, Y. (2015). Increased Epicardial Adipose Tissue Thickness in Type 2 Diabetes Mellitus and Obesity. Diabetes Metab J *39*, 405-413. 10.4093/dmj.2015.39.5.405.

188. Packer, M. (2018). Epicardial Adipose Tissue May Mediate Deleterious Effects of Obesity and Inflammation on the Myocardium. J Am Coll Cardiol *71*, 2360-2372. 10.1016/j.jacc.2018.03.509.

189. Udell, J.A., Cavender, M.A., Bhatt, D.L., Chatterjee, S., Farkouh, M.E., and Scirica, B.M. (2015). Glucose-lowering drugs or strategies and cardiovascular outcomes in patients with or at risk for type 2 diabetes: a meta-analysis of randomised controlled trials. Lancet Diabetes Endocrinol *3*, 356-366. 10.1016/S2213-8587(15)00044-3.

190. Lima-Martinez, M.M., Paoli, M., Rodney, M., Balladares, N., Contreras, M., D'Marco, L., and Iacobellis, G. (2016). Effect of sitagliptin on epicardial fat thickness in subjects with type 2 diabetes and obesity: a pilot study. Endocrine *51*, 448-455. 10.1007/s12020-015-0710-y.

191. Packer, M. (2018). Have dipeptidyl peptidase-4 inhibitors ameliorated the vascular complications of type 2 diabetes in large-scale trials? The potential confounding effect of stem-cell chemokines. Cardiovascular Diabetology *17*. ARTN 9 10.1186/s12933-017-0648-x.

192. Iacobellis, G., Mohseni, M., Bianco, S.D., and Banga, P.K. (2017). Liraglutide causes large and rapid epicardial fat reduction. Obesity (Silver Spring) *25*, 311-316. 10.1002/oby.21718.

193. Pastel, E., McCulloch, L.J., Ward, R., Joshi, S., Gooding, K.M., Shore, A.C., and Kos, K. (2017). GLP-1 analogue-induced weight loss does not improve obesity-induced AT dysfunction. Clin Sci (Lond) *131*, 343-353. 10.1042/CS20160803.

194. Marso, S.P., Bain, S.C., Consoli, A., Eliaschewitz, F.G., Jodar, E., Leiter, L.A., Lingvay, I., Rosenstock, J., Seufert, J., Warren, M.L., et al. (2016). Semaglutide and Cardiovascular Outcomes in Patients with Type 2 Diabetes. N Engl J Med *375*, 1834-1844. 10.1056/NEJMoa1607141.

195. Marso, S.P., Daniels, G.H., Brown-Frandsen, K., Kristensen, P., Mann, J.F., Nauck, M.A., Nissen, S.E., Pocock, S., Poulter, N.R., Ravn, L.S., et al. (2016). Liraglutide and Cardiovascular Outcomes in Type 2 Diabetes. N Engl J Med *375*, 311-322. 10.1056/NEJMoa1603827.

196. Paulus, W.J., Tschope, C., Sanderson, J.E., Rusconi, C., Flachskampf, F.A., Rademakers, F.E., Marino, P., Smiseth, O.A., De Keulenaer, G., Leite-Moreira, A.F., et al. (2007). How to diagnose diastolic heart failure: a consensus statement on the diagnosis of heart failure with normal left ventricular ejection fraction by the Heart Failure and Echocardiography Associations of the European Society of Cardiology. European Heart Journal *28*, 2539-2550. 10.1093/eurheartj/ehm037.

197. Lam, C.S.P., Donal, E., Kraigher-Krainer, E., and Vasan, R.S. (2011). Epidemiology and clinical course of heart failure with preserved ejection fraction. Eur J Heart Fail *13*, 18-28. 10.1093/eurjhf/hfq121.

198. Komajda, M., and Lam, C.S. (2014). Heart failure with preserved ejection fraction: a clinical dilemma. Eur Heart J *35*, 1022-1032. 10.1093/eurheartj/ehu067.

199. Borlaug, B.A., and Paulus, W.J. (2011). Heart failure with preserved ejection fraction: pathophysiology, diagnosis, and treatment. Eur Heart J *32*, 670-679. 10.1093/eurheartj/ehq426.

200. Ponikowski, P., Voors, A.A., Anker, S.D., Bueno, H., Cleland, J.G.F., Coats, A.J.S., Falk, V., Gonzalez-Juanatey, J.R., Harjola, V.P., Jankowska, E.A., et al. (2016). 2016 ESC Guidelines for the diagnosis and treatment of acute and chronic heart failure: The Task Force for the diagnosis and treatment of acute and chronic heart failure of the European Society of Cardiology (ESC)Developed with the special contribution of the Heart Failure Association (HFA) of the ESC. Eur Heart J *37*, 2129-2200. 10.1093/eurheartj/ehw128.

201. Solomon, S.D., and Biering-Sorensen, T. (2017). LA Strain When Ejection Fraction Is Preserved: A New Measure of Diastolic Function? JACC Cardiovasc Imaging *10*, 744-746. 10.1016/j.jcmg.2016.09.018.

202. Ozturk, C., Balta, S., Demirkol, S., Celik, T., and Iyisoy, A. (2014). Epicardial adipose tissue thickness may be related diastolic dysfunction in obese adolescents. Eur Rev Med Pharmacol Sci *18*, 1109.

203. Nakanishi, K., Fukuda, S., Tanaka, A., Otsuka, K., Taguchi, H., and Shimada, K. (2017). Relationships Between Periventricular Epicardial Adipose Tissue Accumulation, Coronary Microcirculation, and Left Ventricular Diastolic Dysfunction. Can J Cardiol *33*, 1489-1497. 10.1016/j.cjca.2017.08.001.

204. Natale, F., Tedesco, M.A., Mocerino, R., de Simone, V., Di Marco, G.M., Aronne, L., Credendino, M., Siniscalchi, C., Calabro, P., Cotrufo, M., and Calabro, R. (2009). Visceral adiposity and arterial stiffness: echocardiographic epicardial fat thickness reflects, better than waist circumference, carotid arterial stiffness in a large population of hypertensives. Eur J Echocardiogr *10*, 549-555. 10.1093/ejechocard/jep002.

205. Iacobellis, G., Leonetti, F., Singh, N., and A, M.S. (2007). Relationship of epicardial adipose tissue with atrial dimensions and diastolic function in morbidly obese subjects. Int J Cardiol *115*, 272-273. 10.1016/j.ijcard.2006.04.016.

206. Karlsson, C., Lindell, K., Ottosson, M., Sjostrom, L., Carlsson, B., and Carlsson, L.M. (1998). Human adipose tissue expresses angiotensinogen and enzymes required for its conversion to angiotensin II. J Clin Endocrinol Metab *83*, 3925-3929. 10.1210/jcem.83.11.5276.

207. Engeli, S., Gorzelniak, K., Kreutz, R., Runkel, N., Distler, A., and Sharma, A.M. (1999). Co-expression of renin-angiotensin system genes in human adipose tissue. J Hypertens *17*, 555-560. 10.1097/00004872-199917040-00014.

208. Schling, P., Mallow, H., Trindl, A., and Loffler, G. (1999). Evidence for a local renin angiotensin system in primary cultured human preadipocytes. Int J Obes Relat Metab Disord *23*, 336-341. 10.1038/sj.ijo.0800821.

209. Frigolet, M.E., Torres, N., and Tovar, A.R. (2013). The renin-angiotensin system in adipose tissue and its metabolic consequences during obesity. J Nutr Biochem *24*, 2003-2015. 10.1016/j.jnutbio.2013.07.002.

210. Harp, J.B., and DiGirolamo, M. (1995). Components of the renin-angiotensin system in adipose tissue: changes with maturation and adipose mass enlargement. J Gerontol A Biol Sci Med Sci *50*, B270-276. 10.1093/gerona/50a.5.b270.

211. Al-Benna, S. (2020). Association of high level gene expression of ACE2 in adipose tissue with mortality of COVID-19 infection in obese patients. Obes Med *19*, 100283. 10.1016/j.obmed.2020.100283.

212. Martinez-Colon, G.J., Ratnasiri, K., Chen, H., Jiang, S., Zanley, E., Rustagi, A., Verma, R., Chen, H., Andrews, J.R., Mertz, K.D., et al. (2022). SARS-CoV-2 infection drives an inflammatory response in human adipose tissue through infection of adipocytes and macrophages. Sci Transl Med *14*, eabm9151. 10.1126/scitranslmed.abm9151.

213. El-Sayed Moustafa, J.S., Jackson, A.U., Brotman, S.M., Guan, L., Villicana, S., Roberts, A.L., Zito, A., Bonnycastle, L., Erdos, M.R., Narisu, N., et al. (2022). ACE2 expression in adipose tissue is associated with cardio-metabolic risk factors and cell type

composition-implications for COVID-19. Int J Obes (Lond) *46*, 1478-1486. 10.1038/s41366-022-01136-w.

214. Cassis, L.A. (2000). Fat cell metabolism: insulin, fatty acids, and renin. Curr Hypertens Rep *2*, 132-138. 10.1007/s11906-000-0072-5.

215. Cassis, L.A., Fettinger, M.J., Roe, A.L., Shenoy, U.R., and Howard, G. (1996). Characterization and regulation of angiotensin II receptors in rat adipose tissue. Angiotensin receptors in adipose tissue. Adv Exp Med Biol *396*, 39-47. 10.1007/978-1-4899-1376-0_5.

216. Bujak-Gizycka, B., Madej, J., Wolkow, P.P., Olszanecki, R., Drabik, L., Rutowski, J., and Korbut, R. (2007). Measurement of angiotensin metabolites in organ bath and cell culture experiments by liquid chromatography - electrospray ionization - mass spectrometry (LC-ESI-MS). J Physiol Pharmacol *58*, 529-540.

217. Tomono, Y., Iwai, M., Inaba, S., Mogi, M., and Horiuchi, M. (2008). Blockade of AT1 receptor improves adipocyte differentiation in atherosclerotic and diabetic models. Am J Hypertens *21*, 206-212. 10.1038/ajh.2007.50.

218. Kurata, A., Nishizawa, H., Kihara, S., Maeda, N., Sonoda, M., Okada, T., Ohashi, K., Hibuse, T., Fujita, K., Yasui, A., et al. (2006). Blockade of Angiotensin II type-1 receptor reduces oxidative stress in adipose tissue and ameliorates adipocytokine dysregulation. Kidney Int *70*, 1717-1724. 10.1038/sj.ki.5001810.

219. Frederich, R.C., Jr., Kahn, B.B., Peach, M.J., and Flier, J.S. (1992). Tissue-specific nutritional regulation of angiotensinogen in adipose tissue. Hypertension *19*, 339-344. 10.1161/01.hyp.19.4.339.

220. Hainault, I., Nebout, G., Turban, S., Ardouin, B., Ferre, P., and Quignard-Boulange, A. (2002). Adipose tissue-specific increase in angiotensinogen expression and secretion in the obese (fa/fa) Zucker rat. Am J Physiol Endocrinol Metab *282*, E59-66. 10.1152/ajpendo.2002.282.1.E59.

221. Van Harmelen, V., Ariapart, P., Hoffstedt, J., Lundkvist, I., Bringman, S., and Arner, P. (2000). Increased adipose angiotensinogen gene expression in human obesity. Obes Res *8*, 337-341. 10.1038/oby.2000.40.

222. Lu, H., Boustany-Kari, C.M., Daugherty, A., and Cassis, L.A. (2007). Angiotensin II increases adipose angiotensinogen expression. Am J Physiol Endocrinol Metab *292*, E1280-1287. 10.1152/ajpendo.00277.2006.

223. Massiera, F., Bloch-Faure, M., Ceiler, D., Murakami, K., Fukamizu, A., Gasc, J.M., Quignard-Boulange, A., Negrel, R., Ailhaud, G., Seydoux, J., et al. (2001). Adipose angiotensinogen is involved in adipose tissue growth and blood pressure regulation. FASEB J *15*, 2727-2729. 10.1096/fj.01-0457fje.

224. Jones, B.H., Standridge, M.K., and Moustaid, N. (1997). Angiotensin II increases lipogenesis in 3T3-L1 and human adipose cells. Endocrinology *138*, 1512-1519. 10.1210/endo.138.4.5038.

225. Crandall, D.L., Herzlinger, H.E., Saunders, B.D., Armellino, D.C., and Kral, J.G. (1994). Distribution of angiotensin II receptors in rat and human adipocytes. J Lipid Res *35*, 1378-1385.

226. Massiera, F., Seydoux, J., Geloen, A., Quignard-Boulange, A., Turban, S., Saint-Marc, P., Fukamizu, A., Negrel, R., Ailhaud, G., and Teboul, M. (2001). Angiotensinogen-deficient mice exhibit impairment of diet-induced weight gain with alteration in

adipose tissue development and increased locomotor activity. Endocrinology *142*, 5220-5225. 10.1210/endo.142.12.8556.

227. Yvan-Charvet, L., Even, P., Bloch-Faure, M., Guerre-Millo, M., Moustaid-Moussa, N., Ferre, P., and Quignard-Boulange, A. (2005). Deletion of the angiotensin type 2 receptor (AT2R) reduces adipose cell size and protects from diet-induced obesity and insulin resistance. Diabetes *54*, 991-999. 10.2337/diabetes.54.4.991.

228. Kouyama, R., Suganami, T., Nishida, J., Tanaka, M., Toyoda, T., Kiso, M., Chiwata, T., Miyamoto, Y., Yoshimasa, Y., Fukamizu, A., et al. (2005). Attenuation of diet-induced weight gain and adiposity through increased energy expenditure in mice lacking angiotensin II type 1a receptor. Endocrinology *146*, 3481-3489. 10.1210/en.2005-0003.

229. Shiuchi, T., Iwai, M., Li, H.S., Wu, L., Min, L.J., Li, J.M., Okumura, M., Cui, T.X., and Horiuchi, M. (2004). Angiotensin II type-1 receptor blocker valsartan enhances insulin sensitivity in skeletal muscles of diabetic mice. Hypertension *43*, 1003-1010. 10.1161/01.HYP.0000125142.41703.64.

230. Goossens, G.H., Blaak, E.E., Arner, P., Saris, W.H., and van Baak, M.A. (2007). Angiotensin II: a hormone that affects lipid metabolism in adipose tissue. Int J Obes (Lond) *31*, 382-384. 10.1038/sj.ijo.0803388.

231. Goossens, G.H., Blaak, E.E., Saris, W.H., and van Baak, M.A. (2004). Angiotensin II-induced effects on adipose and skeletal muscle tissue blood flow and lipolysis in normal-weight and obese subjects. J Clin Endocrinol Metab *89*, 2690-2696. 10.1210/jc.2003-032053.

232. Boschmann, M., Ringel, J., Klaus, S., and Sharma, A.M. (2001). Metabolic and hemodynamic response of adipose tissue to angiotensin II. Obes Res *9*, 486-491. 10.1038/oby.2001.63.

233. Yvan-Charvet, L., and Quignard-Boulange, A. (2011). Role of adipose tissue renin-angiotensin system in metabolic and inflammatory diseases associated with obesity. Kidney Int *79*, 162-168. 10.1038/ki.2010.391.

234. Liu, C., Lv, X.H., Li, H.X., Cao, X., Zhang, F., Wang, L., Yu, M., and Yang, J.K. (2012). Angiotensin-(1-7) suppresses oxidative stress and improves glucose uptake via Mas receptor in adipocytes. Acta Diabetol *49*, 291-299. 10.1007/s00592-011-0348-z.

235. Benter, I.F., Yousif, M.H., Cojocel, C., Al-Maghrebi, M., and Diz, D.I. (2007). Angiotensin-(1-7) prevents diabetes-induced cardiovascular dysfunction. Am J Physiol Heart Circ Physiol *292*, H666-672. 10.1152/ajpheart.00372.2006.

236. Gálvez-Prieto, B., Bolbrinker, J., Stucchi, P., Heras, A.I.d.l., Merino, B., Arribas, S., Ruiz-Gayo, M., Huber, M., Wehland, M., Kreutz, R., and Fernandez-Alfonso, M.S. (2008). Comparative expression analysis of the renin–angiotensin system components between white and brown perivascular adipose tissue. Journal of Endocrinology *197*, 55-64. 10.1677/JOE-07-0284.

237. Rosei, C.A., Withers, S.B., Belcaid, L., De Ciuceis, C., Rizzoni, D., and Heagerty, A.M. (2015). Blockade of the renin-angiotensin system in small arteries and anticontractile function of perivascular adipose tissue. Journal of hypertension *33*, 1039-1045. 10.1097/hjh.0000000000000506.

238. Sakaue, T., Suzuki, J., Hamaguchi, M., Suehiro, C., Tanino, A., Nagao, T., Uetani, T., Aono, J., Nakaoka, H., Kurata, M., et al. (2017). Perivascular Adipose Tissue

Angiotensin II Type 1 Receptor Promotes Vascular Inflammation and Aneurysm Formation. Hypertension *70*, 780-789. doi:10.1161/HYPERTENSIONAHA.117.09512.

239. Nóbrega, N., Araújo, N.F., Reis, D., Facine, L.M., Miranda, C.A.S., Mota, G.C., Aires, R.D., Capettini, L.d.S.A., Cruz, J.d.S., and Bonaventura, D. (2019). Hydrogen peroxide and nitric oxide induce anticontractile effect of perivascular adipose tissue via renin angiotensin system activation. Nitric Oxide *84*, 50-59. https://doi.org/10.1016/j.niox.2018.12.011.

240. Roubicek, T., Dolinkova, M., Blaha, J., Haluzikova, D., Bosanska, L., Mraz, M., Kremen, J., and Haluzik, M. (2008). Increased angiotensinogen production in epicardial adipose tissue during cardiac surgery: possible role in a postoperative insulin resistance. Physiol Res *57*, 911-917. 10.33549/physiolres.931315.

241. Gaborit, B., Venteclef, N., Ancel, P., Pelloux, V., Gariboldi, V., Leprince, P., Amour, J., Hatem, S.N., Jouve, E., Dutour, A., and Clement, K. (2015). Human epicardial adipose tissue has a specific transcriptomic signature depending on its anatomical peri-atrial, peri-ventricular, or peri-coronary location. Cardiovasc Res *108*, 62-73. 10.1093/cvr/cvv208.

242. Epelman, S., Tang, W.H., Chen, S.Y., Van Lente, F., Francis, G.S., and Sen, S. (2008). Detection of soluble angiotensin-converting enzyme 2 in heart failure: insights into the endogenous counter-regulatory pathway of the renin-angiotensin-aldosterone system. J Am Coll Cardiol *52*, 750-754. 10.1016/j.jacc.2008.02.088.

243. Litvinukova, M., Talavera-Lopez, C., Maatz, H., Reichart, D., Worth, C.L., Lindberg, E.L., Kanda, M., Polanski, K., Heinig, M., Lee, M., et al. (2020). Cells of the adult human heart. Nature *588*, 466-472. 10.1038/s41586-020-2797-4.

244. Nadelmann, E.R., Gorham, J.M., Reichart, D., Delaughter, D.M., Wakimoto, H., Lindberg, E.L., Litvinukova, M., Maatz, H., Curran, J.J., Ischiu Gutierrez, D., et al. (2021). Isolation of Nuclei from Mammalian Cells and Tissues for Single-Nucleus Molecular Profiling. Curr Protoc *1*, e132. 10.1002/cpz1.132.

245. Reichart, D., Lindberg, E.L., Maatz, H., Miranda, A.M.A., Viveiros, A., Shvetsov, N., Gartner, A., Nadelmann, E.R., Lee, M., Kanemaru, K., et al. (2022). Pathogenic variants damage cell composition and single cell transcription in cardiomyopathies. Science *377*, eabo1984. 10.1126/science.abo1984.

246. Li, H., and Durbin, R. (2009). Fast and accurate short read alignment with Burrows-Wheeler transform. Bioinformatics *25*, 1754-1760. 10.1093/bioinformatics/btp324.

247. Van der Auwera, G.A., Carneiro, M.O., Hartl, C., Poplin, R., Del Angel, G., Levy-Moonshine, A., Jordan, T., Shakir, K., Roazen, D., Thibault, J., et al. (2013). From FastQ data to high confidence variant calls: the Genome Analysis Toolkit best practices pipeline. Curr Protoc Bioinformatics *43*, 11 10 11-11 10 33. 10.1002/0471250953.bi1110s43.

248. Landrum, M.J., Lee, J.M., Benson, M., Brown, G.R., Chao, C., Chitipiralla, S., Gu, B., Hart, J., Hoffman, D., Jang, W., et al. (2018). ClinVar: improving access to variant interpretations and supporting evidence. Nucleic Acids Res *46*, D1062-D1067. 10.1093/nar/gkx1153.

249. Hofman, K., Hall, B., Cleaver, H., and Marshall, S. (2011). High-throughput quantification of hydroxyproline for determination of collagen. Anal Biochem *417*, 289-291. 10.1016/j.ab.2011.06.019.

250. Neuman, R.E., and Logan, M.A. (1950). The determination of hydroxyproline. J Biol Chem *184*, 299-306.

251. Diaz Marin, R., Crespo-Garcia, S., Wilson, A.M., and Sapieha, P. (2019). RELi protocol: Optimization for protein extraction from white, brown and beige adipose tissues. MethodsX *6*, 918-928. 10.1016/j.mex.2019.04.010.

252. Xia, J., and Wishart, D.S. (2011). Web-based inference of biological patterns, functions and pathways from metabolomic data using MetaboAnalyst. Nat Protoc *6*, 743-760. 10.1038/nprot.2011.319.

253. Raudvere, U., Kolberg, L., Kuzmin, I., Arak, T., Adler, P., Peterson, H., and Vilo, J. (2019). g:Profiler: a web server for functional enrichment analysis and conversions of gene lists (2019 update). Nucleic Acids Res *47*, W191-W198. 10.1093/nar/gkz369.

254. Muus, C., Luecken, M.D., Eraslan, G., Sikkema, L., Waghray, A., Heimberg, G., Kobayashi, Y., Vaishnav, E.D., Subramanian, A., Smillie, C., et al. (2021). Single-cell meta-analysis of SARS-CoV-2 entry genes across tissues and demographics. Nat Med *27*, 546-559. 10.1038/s41591-020-01227-z.

255. Shenoy, S. (2021). SARS-CoV-2 (COVID-19), viral load and clinical outcomes; lessons learned one year into the pandemic: A systematic review. World J Crit Care Med *10*, 132-150. 10.5492/wjccm.v10.i4.132.

256. Stelzig, K.E., Canepa-Escaro, F., Schiliro, M., Berdnikovs, S., Prakash, Y.S., and Chiarella, S.E. (2020). Estrogen regulates the expression of SARS-CoV-2 receptor ACE2 in differentiated airway epithelial cells. Am J Physiol Lung Cell Mol Physiol *318*, L1280-L1281. 10.1152/ajplung.00153.2020.

257. Pendergrass, K.D., Pirro, N.T., Westwood, B.M., Ferrario, C.M., Brosnihan, K.B., and Chappell, M.C. (2008). Sex differences in circulating and renal angiotensins of hypertensive mRen(2). Lewis but not normotensive Lewis rats. Am J Physiol Heart Circ Physiol *295*, H10-20. 10.1152/ajpheart.01277.2007.

258. Ojeda, N.B., Grigore, D., Robertson, E.B., and Alexander, B.T. (2007). Estrogen protects against increased blood pressure in postpubertal female growth restricted offspring. Hypertension *50*, 679-685. 10.1161/HYPERTENSIONAHA.107.091785.

259. Lin, B., Ferguson, C., White, J.T., Wang, S., Vessella, R., True, L.D., Hood, L., and Nelson, P.S. (1999). Prostate-localized and androgen-regulated expression of the membrane-bound serine protease TMPRSS2. Cancer Res *59*, 4180-4184.

260. Sharma, R.K., Stevens, B.R., Obukhov, A.G., Grant, M.B., Oudit, G.Y., Li, Q., Richards, E.M., Pepine, C.J., and Raizada, M.K. (2020). ACE2 (Angiotensin-Converting Enzyme 2) in Cardiopulmonary Diseases: Ramifications for the Control of SARS-CoV-2. Hypertension *76*, 651-661. 10.1161/HYPERTENSIONAHA.120.15595.

261. Fajnzylber, J., Regan, J., Coxen, K., Corry, H., Wong, C., Rosenthal, A., Worrall, D., Giguel, F., Piechocka-Trocha, A., Atyeo, C., et al. (2020). SARS-CoV-2 viral load is associated with increased disease severity and mortality. Nat Commun *11*, 5493. 10.1038/s41467-020-19057-5.

262. Kragstrup, T.W., Singh, H.S., Grundberg, I., Nielsen, A.L., Rivellese, F., Mehta, A., Goldberg, M.B., Filbin, M.R., Qvist, P., and Bibby, B.M. (2021). Plasma ACE2 predicts outcome of COVID-19 in hospitalized patients. PLoS One *16*, e0252799. 10.1371/journal.pone.0252799.

263. Lu, D., Chatterjee, S., Xiao, K., Riedel, I., Wang, Y., Foo, R., Bar, C., and Thum, T. (2020). MicroRNAs targeting the SARS-CoV-2 entry receptor ACE2 in cardiomyocytes. J Mol Cell Cardiol *148*, 46-49. 10.1016/j.yjmcc.2020.08.017.

264. Munoz-Fontela, C., Dowling, W.E., Funnell, S.G.P., Gsell, P.S., Riveros-Balta, A.X., Albrecht, R.A., Andersen, H., Baric, R.S., Carroll, M.W., Cavaleri, M., et al. (2020). Animal models for COVID-19. Nature *586*, 509-515. 10.1038/s41586-020-2787-6.

265. Chan, J.F., Zhang, A.J., Yuan, S., Poon, V.K., Chan, C.C., Lee, A.C., Chan, W.M., Fan, Z., Tsoi, H.W., Wen, L., et al. (2020). Simulation of the Clinical and Pathological Manifestations of Coronavirus Disease 2019 (COVID-19) in a Golden Syrian Hamster Model: Implications for Disease Pathogenesis and Transmissibility. Clin Infect Dis *71*, 2428-2446. 10.1093/cid/ciaa325.

266. Huang, J., Hume, A.J., Abo, K.M., Werder, R.B., Villacorta-Martin, C., Alysandratos, K.D., Beermann, M.L., Simone-Roach, C., Lindstrom-Vautrin, J., Olejnik, J., et al. (2020). SARS-CoV-2 Infection of Pluripotent Stem Cell-Derived Human Lung Alveolar Type 2 Cells Elicits a Rapid Epithelial-Intrinsic Inflammatory Response. Cell Stem Cell *27*, 962-973 e967. 10.1016/j.stem.2020.09.013.

267. Tschope, C., Ammirati, E., Bozkurt, B., Caforio, A.L.P., Cooper, L.T., Felix, S.B., Hare, J.M., Heidecker, B., Heymans, S., Hubner, N., et al. (2021). Myocarditis and

inflammatory cardiomyopathy: current evidence and future directions. Nat Rev Cardiol *18*, 169-193. 10.1038/s41569-020-00435-x.

268. Angeles Montero-Fernandez, M., and Pardo-Garcia, R. (2021). Histopathology features of the lung in COVID-19 patients. Diagn Histopathol (Oxf) *27*, 123-127. 10.1016/j.mpdhp.2020.11.009.

269. Tavazzi, G., Pellegrini, C., Maurelli, M., Belliato, M., Sciutti, F., Bottazzi, A., Sepe, P.A., Resasco, T., Camporotondo, R., Bruno, R., et al. (2020). Myocardial localization of coronavirus in COVID-19 cardiogenic shock. Eur J Heart Fail *22*, 911-915. 10.1002/ejhf.1828.

270. Cheung, C.Y., Poon, L.L., Ng, I.H., Luk, W., Sia, S.F., Wu, M.H., Chan, K.H., Yuen, K.Y., Gordon, S., Guan, Y., and Peiris, J.S. (2005). Cytokine responses in severe acute respiratory syndrome coronavirus-infected macrophages in vitro: possible relevance to pathogenesis. J Virol *79*, 7819-7826. 10.1128/JVI.79.12.7819-7826.2005.

271. Del Valle, D.M., Kim-Schulze, S., Huang, H.H., Beckmann, N.D., Nirenberg, S., Wang, B., Lavin, Y., Swartz, T.H., Madduri, D., Stock, A., et al. (2020). An inflammatory cytokine signature predicts COVID-19 severity and survival. Nat Med *26*, 1636-1643. 10.1038/s41591-020-1051-9.

272. Han, H., Ma, Q., Li, C., Liu, R., Zhao, L., Wang, W., Zhang, P., Liu, X., Gao, G., Liu, F., et al. (2020). Profiling serum cytokines in COVID-19 patients reveals IL-6 and IL-10 are disease severity predictors. Emerg Microbes Infect *9*, 1123-1130. 10.1080/22221751.2020.1770129.

273. Hoffmann, M., Kleine-Weber, H., Schroeder, S., Kruger, N., Herrler, T., Erichsen, S., Schiergens, T.S., Herrler, G., Wu, N.H., Nitsche, A., et al. (2020). SARS-CoV-2 Cell Entry Depends on ACE2 and TMPRSS2 and Is Blocked by a Clinically Proven Protease Inhibitor. Cell *181*, 271-280 e278. 10.1016/j.cell.2020.02.052.

274. Lambert, D.W., Yarski, M., Warner, F.J., Thornhill, P., Parkin, E.T., Smith, A.I., Hooper, N.M., and Turner, A.J. (2005). Tumor necrosis factor-alpha convertase (ADAM17) mediates regulated ectodomain shedding of the severe-acute respiratory syndrome-coronavirus (SARS-CoV) receptor, angiotensin-converting enzyme-2 (ACE2). J Biol Chem *280*, 30113-30119. 10.1074/jbc.M505111200.

275. Viveiros, A., Gheblawi, M., Aujla, P.K., Sosnowski, D.K., Seubert, J.M., Kassiri, Z., and Oudit, G.Y. (2022). Sex- and age-specific regulation of ACE2: Insights into severe COVID-19 susceptibility. J Mol Cell Cardiol *164*, 13-16. 10.1016/j.yjmcc.2021.11.003.

276. Wang, Y., Wang, Y., Luo, W., Huang, L., Xiao, J., Li, F., Qin, S., Song, X., Wu, Y., Zeng, Q., et al. (2020). A comprehensive investigation of the mRNA and protein level of ACE2, the putative receptor of SARS-CoV-2, in human tissues and blood cells. Int J Med Sci *17*, 1522-1531. 10.7150/ijms.46695.

277. O'Brien, J., Hayder, H., Zayed, Y., and Peng, C. (2018). Overview of MicroRNA Biogenesis, Mechanisms of Actions, and Circulation. Front Endocrinol (Lausanne) *9*, 402. 10.3389/fendo.2018.00402.

278. Liu, Q., Du, J., Yu, X., Xu, J., Huang, F., Li, X., Zhang, C., Li, X., Chang, J., Shang, D., et al. (2017). miRNA-200c-3p is crucial in acute respiratory distress syndrome. Cell Discov *3*, 17021. 10.1038/celldisc.2017.21.

279. Goulter, A.B., Goddard, M.J., Allen, J.C., and Clark, K.L. (2004). ACE2 gene expression is up-regulated in the human failing heart. BMC Med *2*, 19. 10.1186/1741-7015-2-19.

280. Bunyavanich, S., Do, A., and Vicencio, A. (2020). Nasal Gene Expression of Angiotensin-Converting Enzyme 2 in Children and Adults. JAMA *323*, 2427-2429. 10.1001/jama.2020.8707.

281. Amour, A., Slocombe, P.M., Webster, A., Butler, M., Knight, C.G., Smith, B.J., Stephens, P.E., Shelley, C., Hutton, M., Knauper, V., et al. (1998). TNF-alpha converting enzyme (TACE) is inhibited by TIMP-3. FEBS Lett *435*, 39-44. 10.1016/s0014-5793(98)01031-x.

282. Fan, D., and Kassiri, Z. (2020). Biology of Tissue Inhibitor of Metalloproteinase 3 (TIMP3), and Its Therapeutic Implications in Cardiovascular Pathology. Front Physiol *11*, 661. 10.3389/fphys.2020.00661.

283. Lee, M.H., Rapti, M., and Murphy, G. (2005). Total conversion of tissue inhibitor of metalloproteinase (TIMP) for specific metalloproteinase targeting: fine-tuning TIMP-4 for optimal inhibition of tumor necrosis factor-alpha-converting enzyme. J Biol Chem *280*, 15967-15975. 10.1074/jbc.M500897200.

284. Polyakova, V., Loeffler, I., Hein, S., Miyagawa, S., Piotrowska, I., Dammer, S., Risteli, J., Schaper, J., and Kostin, S. (2011). Fibrosis in endstage human heart failure: severe changes in collagen metabolism and MMP/TIMP profiles. Int J Cardiol *151*, 18-33. 10.1016/j.ijcard.2010.04.053.

285. Li, Y.Y., Feldman, A.M., Sun, Y., and McTiernan, C.F. (1998). Differential expression of tissue inhibitors of metalloproteinases in the failing human heart. Circulation *98*, 1728-1734. 10.1161/01.cir.98.17.1728.

286. Fedak, P.W., Smookler, D.S., Kassiri, Z., Ohno, N., Leco, K.J., Verma, S., Mickle, D.A., Watson, K.L., Hojilla, C.V., Cruz, W., et al. (2004). TIMP-3 deficiency leads to dilated cardiomyopathy. Circulation *110*, 2401-2409. 10.1161/01.CIR.0000134959.83967.2D.

287. Kandalam, V., Basu, R., Abraham, T., Wang, X., Awad, A., Wang, W., Lopaschuk, G.D., Maeda, N., Oudit, G.Y., and Kassiri, Z. (2010). Early activation of matrix metalloproteinases underlies the exacerbated systolic and diastolic dysfunction in mice lacking TIMP3 following myocardial infarction. Am J Physiol Heart Circ Physiol *299*, H1012-1023. 10.1152/ajpheart.00246.2010.

288. Takawale, A., Zhang, P., Azad, A., Wang, W., Wang, X., Murray, A.G., and Kassiri, Z. (2017). Myocardial overexpression of TIMP3 after myocardial infarction exerts beneficial effects by promoting angiogenesis and suppressing early proteolysis. Am J Physiol Heart Circ Physiol *313*, H224-H236. 10.1152/ajpheart.00108.2017.

289. Rafeh, R., Viveiros, A., Oudit, G.Y., and El-Yazbi, A.F. (2020). Targeting perivascular and epicardial adipose tissue inflammation: therapeutic opportunities for cardiovascular disease. Clin Sci (Lond) *134*, 827-851. 10.1042/CS20190227.

290. Karastergiou, K., and Fried, S.K. (2013). Multiple adipose depots increase cardiovascular risk via local and systemic effects. Curr Atheroscler Rep *15*, 361. 10.1007/s11883-013-0361-5.

291. Ghaben, A.L., and Scherer, P.E. (2019). Adipogenesis and metabolic health. Nat Rev Mol Cell Biol *20*, 242-258. 10.1038/s41580-018-0093-z.

292. Muir, L.A., Neeley, C.K., Meyer, K.A., Baker, N.A., Brosius, A.M., Washabaugh, A.R., Varban, O.A., Finks, J.F., Zamarron, B.F., Flesher, C.G., et al. (2016). Adipose tissue fibrosis, hypertrophy, and hyperplasia: Correlations with diabetes in human obesity. Obesity (Silver Spring) *24*, 597-605. 10.1002/oby.21377.

293. Patel, V.B., Basu, R., and Oudit, G.Y. (2016). ACE2/Ang 1-7 axis: A critical regulator of epicardial adipose tissue inflammation and cardiac dysfunction in obesity. Adipocyte *5*, 306-311. 10.1080/21623945.2015.1131881.

294. van Woerden, G., van Veldhuisen, D.J., Manintveld, O.C., van Empel, V.P.M., Willems, T.P., de Boer, R.A., Rienstra, M., Westenbrink, B.D., and Gorter, T.M. (2022). Epicardial Adipose Tissue and Outcome in Heart Failure With Mid-Range and Preserved Ejection Fraction. Circ Heart Fail *15*, e009238. 10.1161/CIRCHEARTFAILURE.121.009238.

295. Doesch, C., Haghi, D., Fluchter, S., Suselbeck, T., Schoenberg, S.O., Michaely, H., Borggrefe, M., and Papavassiliu, T. (2010). Epicardial adipose tissue in patients with heart failure. J Cardiovasc Magn Reson *12*, 40. 10.1186/1532-429X-12-40.

296. Nerlekar, N., Muthalaly, R.G., Wong, N., Thakur, U., Wong, D.T.L., Brown, A.J., and Marwick, T.H. (2018). Association of Volumetric Epicardial Adipose Tissue Quantification and Cardiac Structure and Function. J Am Heart Assoc *7*, e009975. 10.1161/JAHA.118.009975.

297. Iacobellis, G., Lonn, E., Lamy, A., Singh, N., and Sharma, A.M. (2011). Epicardial fat thickness and coronary artery disease correlate independently of obesity. Int J Cardiol *146*, 452-454. 10.1016/j.ijcard.2010.10.117.

298. Nelson, A.J., Worthley, M.I., Psaltis, P.J., Carbone, A., Dundon, B.K., Duncan, R.F., Piantadosi, C., Lau, D.H., Sanders, P., Wittert, G.A., and Worthley, S.G. (2009). Validation of cardiovascular magnetic resonance assessment of pericardial adipose tissue volume. J Cardiovasc Magn Reson *11*, 15. 10.1186/1532-429X-11-15.

299. Vijay, J., Gauthier, M.F., Biswell, R.L., Louiselle, D.A., Johnston, J.J., Cheung, W.A., Belden, B., Pramatarova, A., Biertho, L., Gibson, M., et al. (2020). Single-cell analysis of human adipose tissue identifies depot and disease specific cell types. Nat Metab *2*, 97-109. 10.1038/s42255-019-0152-6.

300. Norreen-Thorsen, M., Struck, E.C., Oling, S., Zwahlen, M., Von Feilitzen, K., Odeberg, J., Lindskog, C., Ponten, F., Uhlen, M., Dusart, P.J., and Butler, L.M. (2022). A human adipose tissue cell-type transcriptome atlas. Cell Rep *40*, 111046. 10.1016/j.celrep.2022.111046.

301. Hildreth, A.D., Ma, F., Wong, Y.Y., Sun, R., Pellegrini, M., and O'Sullivan, T.E. (2021). Single-cell sequencing of human white adipose tissue identifies new cell states in health and obesity. Nat Immunol *22*, 639-653. 10.1038/s41590-021-00922-4.

302. Schleinitz, D., Krause, K., Wohland, T., Gebhardt, C., Linder, N., Stumvoll, M., Bluher, M., Bechmann, I., Kovacs, P., Gericke, M., and Tonjes, A. (2020). Identification of distinct transcriptome signatures of human adipose tissue from fifteen depots. Eur J Hum Genet *28*, 1714-1725. 10.1038/s41431-020-0681-1.

303. Stephens, J.M., Butts, M., Stone, R., Pekala, P.H., and Bernlohr, D.A. (1993). Regulation of transcription factor mRNA accumulation during 3T3-L1 preadipocyte differentiation by antagonists of adipogenesis. Mol Cell Biochem *123*, 63-71. 10.1007/BF01076476.

304. Stephens, J.M., Butts, M.D., and Pekala, P.H. (1992). Regulation of transcription factor mRNA accumulation during 3T3-L1 preadipocyte differentiation by tumour necrosis factor-alpha. J Mol Endocrinol *9*, 61-72. 10.1677/jme.0.0090061.

305. White, U.A., and Stephens, J.M. (2010). Transcriptional factors that promote formation of white adipose tissue. Mol Cell Endocrinol *318*, 10-14. 10.1016/j.mce.2009.08.023.

306. Eriksson, M., Taskinen, M., and Leppa, S. (2007). Mitogen activated protein kinase-dependent activation of c-Jun and c-Fos is required for neuronal differentiation but not for growth and stress response in PC12 cells. J Cell Physiol *210*, 538-548. 10.1002/jcp.20907.

307. Weber, K.T., and Brilla, C.G. (1991). Pathological hypertrophy and cardiac interstitium. Fibrosis and renin-angiotensin-aldosterone system. Circulation *83*, 1849-1865. 10.1161/01.cir.83.6.1849.

308. Dzau, V.J., Colucci, W.S., Hollenberg, N.K., and Williams, G.H. (1981). Relation of the renin-angiotensin-aldosterone system to clinical state in congestive heart failure. Circulation *63*, 645-651. 10.1161/01.cir.63.3.645.

309. Swedberg, K., Eneroth, P., Kjekshus, J., and Wilhelmsen, L. (1990). Hormones regulating cardiovascular function in patients with severe congestive heart failure

and their relation to mortality. CONSENSUS Trial Study Group. Circulation *82*, 1730-1736. 10.1161/01.cir.82.5.1730.

310. Angueira, A.R., Sakers, A.P., Holman, C.D., Cheng, L., Arbocco, M.N., Shamsi, F., Lynes, M.D., Shrestha, R., Okada, C., Batmanov, K., et al. (2021). Defining the lineage of thermogenic perivascular adipose tissue. Nat Metab *3*, 469-484. 10.1038/s42255-021-00380-0.

311. Chang, L., Garcia-Barrio, M.T., and Chen, Y.E. (2020). Perivascular Adipose Tissue Regulates Vascular Function by Targeting Vascular Smooth Muscle Cells. Arterioscler Thromb Vasc Biol *40*, 1094-1109. 10.1161/ATVBAHA.120.312464.

312. Chang, L., Villacorta, L., Li, R., Hamblin, M., Xu, W., Dou, C., Zhang, J., Wu, J., Zeng, R., and Chen, Y.E. (2012). Loss of perivascular adipose tissue on peroxisome proliferator-activated receptor-gamma deletion in smooth muscle cells impairs intravascular thermoregulation and enhances atherosclerosis. Circulation *126*, 1067-1078. 10.1161/CIRCULATIONAHA.112.104489.

313. Wagenseil, J.E., and Mecham, R.P. (2009). Vascular extracellular matrix and arterial mechanics. Physiol Rev *89*, 957-989. 10.1152/physrev.00041.2008.

314. Ojima, K., Oe, M., Nakajima, I., Muroya, S., and Nishimura, T. (2016). Dynamics of protein secretion during adipocyte differentiation. FEBS Open Bio *6*, 816-826. 10.1002/2211-5463.12091.

315. Smith, H.L., and Willius, F.A. (1933). Adiposity of the heart - A clinical and pathologic study of one hundred and thirty-six obese patients. Arch Intern Med *52*, 911-931. DOI 10.1001/archinte.1933.00160060085007.

316. Winkler, J., Abisoye-Ogunniyan, A., Metcalf, K.J., and Werb, Z. (2020). Concepts of extracellular matrix remodelling in tumour progression and metastasis. Nat Commun *11*, 5120. 10.1038/s41467-020-18794-x.

317. Kassiri, Z., and Khokha, R. (2005). Myocardial extra-cellular matrix and its regulation by metalloproteinases and their inhibitors. Thromb Haemost *93*, 212-219. 10.1160/TH04-08-0522.

318. Spinale, F.G., Coker, M.L., Heung, L.J., Bond, B.R., Gunasinghe, H.R., Etoh, T., Goldberg, A.T., Zellner, J.L., and Crumbley, A.J. (2000). A matrix metalloproteinase induction/activation system exists in the human left ventricular myocardium and is upregulated in heart failure. Circulation *102*, 1944-1949. 10.1161/01.cir.102.16.1944.

319. Thomas, C.V., Coker, M.L., Zellner, J.L., Handy, J.R., Crumbley, A.J., 3rd, and Spinale, F.G. (1998). Increased matrix metalloproteinase activity and selective upregulation in LV myocardium from patients with end-stage dilated cardiomyopathy. Circulation *97*, 1708-1715. 10.1161/01.cir.97.17.1708.

320. Tereshchenko, L.G., Rizzi, P., Mewton, N., Volpe, G.J., Murthy, S., Strauss, D.G., Liu, C.Y., Marchlinski, F.E., Spooner, P., Berger, R.D., et al. (2014). Infiltrated atrial fat characterizes underlying atrial fibrillation substrate in patients at risk as defined by the ARIC atrial fibrillation risk score. Int J Cardiol *172*, 196-201. 10.1016/j.ijcard.2014.01.012.

321. Shin, S.Y., Yong, H.S., Lim, H.E., Na, J.O., Choi, C.U., Choi, J.I., Kim, S.H., Kim, J.W., Kim, E.J., Park, S.W., et al. (2011). Total and interatrial epicardial adipose tissues are independently associated with left atrial remodeling in patients with atrial

fibrillation. J Cardiovasc Electrophysiol *22*, 647-655. 10.1111/j.1540-8167.2010.01993.x.

322. Liao, X., Shen, Y., Zhang, R., Sugi, K., Vasudevan, N.T., Alaiti, M.A., Sweet, D.R., Zhou, L., Qing, Y., Gerson, S.L., et al. (2018). Distinct roles of resident and nonresident macrophages in nonischemic cardiomyopathy. Proc Natl Acad Sci U S A *115*, E4661-E4669. 10.1073/pnas.1720065115.

323. Dewald, O., Zymek, P., Winkelmann, K., Koerting, A., Ren, G., Abou-Khamis, T., Michael, L.H., Rollins, B.J., Entman, M.L., and Frangogiannis, N.G. (2005). CCL2/Monocyte Chemoattractant Protein-1 regulates inflammatory responses critical to healing myocardial infarcts. Circ Res *96*, 881-889. 10.1161/01.RES.0000163017.13772.3a.

324. Aukrust, P., Gullestad, L., Lappegard, K.T., Ueland, T., Aass, H., Wikeby, L., Simonsen, S., Froland, S.S., and Mollnes, T.E. (2001). Complement activation in patients with congestive heart failure: effect of high-dose intravenous immunoglobulin treatment. Circulation *104*, 1494-1500. 10.1161/hc3801.096353.

325. Lappegard, K.T., Garred, P., Jonasson, L., Espevik, T., Aukrust, P., Yndestad, A., Mollnes, T.E., and Hovland, A. (2014). A vital role for complement in heart disease. Mol Immunol *61*, 126-134. 10.1016/j.molimm.2014.06.036.

326. Shahini, N., Michelsen, A.E., Nilsson, P.H., Ekholt, K., Gullestad, L., Broch, K., Dahl, C.P., Aukrust, P., Ueland, T., Mollnes, T.E., et al. (2017). The alternative complement pathway is dysregulated in patients with chronic heart failure. Sci Rep *7*, 42532. 10.1038/srep42532.

327. Altara, R., Mallat, Z., Booz, G.W., and Zouein, F.A. (2016). The CXCL10/CXCR3 Axis and Cardiac Inflammation: Implications for Immunotherapy to Treat Infectious and Noninfectious Diseases of the Heart. J Immunol Res *2016*, 4396368. 10.1155/2016/4396368.

328. Altara, R., Manca, M., Hessel, M.H., Gu, Y., van Vark, L.C., Akkerhuis, K.M., Staessen, J.A., Struijker-Boudier, H.A., Booz, G.W., and Blankesteijn, W.M. (2016). CXCL10 Is a Circulating Inflammatory Marker in Patients with Advanced Heart Failure: a Pilot Study. J Cardiovasc Transl Res *9*, 302-314. 10.1007/s12265-016-9703-3.

329. Arefanian, H., Ramji, Q., Gupta, N., Spigelman, A.F., Grynoch, D., MacDonald, P.E., Mueller, T.F., Gazda, L.S., Rajotte, R.V., and Rayat, G.R. (2022). Yield, cell composition, and function of islets isolated from different ages of neonatal pigs. Front Endocrinol (Lausanne) *13*, 1032906. 10.3389/fendo.2022.1032906.

330. Rackham, C.L., Vargas, A.E., Hawkes, R.G., Amisten, S., Persaud, S.J., Austin, A.L., King, A.J., and Jones, P.M. (2016). Annexin A1 Is a Key Modulator of Mesenchymal Stromal Cell-Mediated Improvements in Islet Function. Diabetes *65*, 129-139. 10.2337/db15-0990.

331. Hazzalin, C.A., Cuenda, A., Cano, E., Cohen, P., and Mahadevan, L.C. (1997). Effects of the inhibition of p38/RK MAP kinase on induction of five fos and jun genes by diverse stimuli. Oncogene *15*, 2321-2331. 10.1038/sj.onc.1201403.

332. Hoene, M., Franken, H., Fritsche, L., Lehmann, R., Pohl, A.K., Haring, H.U., Zell, A., Schleicher, E.D., and Weigert, C. (2010). Activation of the mitogen-activated protein kinase (MAPK) signalling pathway in the liver of mice is related to plasma glucose

levels after acute exercise. Diabetologia *53*, 1131-1141. 10.1007/s00125-010-1666-3.

333. Muchir, A., Wu, W., Choi, J.C., Iwata, S., Morrow, J., Homma, S., and Worman, H.J. (2012). Abnormal p38alpha mitogen-activated protein kinase signaling in dilated cardiomyopathy caused by lamin A/C gene mutation. Hum Mol Genet *21*, 4325-4333. 10.1093/hmg/dds265.

334. MacRae, C.A., Taylor, M.R.G., Mestroni, L., Moses, J., Ashley, E.A., Wheeler, M.T., Lakdawala, N.K., Hershberger, R.E., Sandor, V., Saunders, M.E., et al. (2022). Efficacy and Safety of ARRY-371797 in LMNA-Related Dilated Cardiomyopathy: A Phase 2 Study. Circ Genom Precis Med, e003730. 10.1161/CIRCGEN.122.003730.

335. Mottillo, E.P., Shen, X.J., and Granneman, J.G. (2010). beta3-adrenergic receptor induction of adipocyte inflammation requires lipolytic activation of stress kinases p38 and JNK. Biochim Biophys Acta *1801*, 1048-1055. 10.1016/j.bbalip.2010.04.012.

336. Engelman, J.A., Lisanti, M.P., and Scherer, P.E. (1998). Specific inhibitors of p38 mitogen-activated protein kinase block 3T3-L1 adipogenesis. J Biol Chem *273*, 32111-32120. 10.1074/jbc.273.48.32111.

337. Engelman, J.A., Berg, A.H., Lewis, R.Y., Lin, A., Lisanti, M.P., and Scherer, P.E. (1999). Constitutively active mitogen-activated protein kinase kinase 6 (MKK6) or salicylate induces spontaneous 3T3-L1 adipogenesis. J Biol Chem *274*, 35630-35638. 10.1074/jbc.274.50.35630.

338. Aouadi, M., Laurent, K., Prot, M., Le Marchand-Brustel, Y., Binetruy, B., and Bost, F. (2006). Inhibition of p38MAPK increases adipogenesis from embryonic to adult stages. Diabetes *55*, 281-289. 10.2337/diabetes.55.02.06.db05-0963.

339. Aouadi, M., Jager, J., Laurent, K., Gonzalez, T., Cormont, M., Binetruy, B., Le Marchand-Brustel, Y., Tanti, J.F., and Bost, F. (2007). p38MAP Kinase activity is required for human primary adipocyte differentiation. FEBS Lett *581*, 5591-5596. 10.1016/j.febslet.2007.10.064.

340. Sale, E.M., Atkinson, P.G., and Sale, G.J. (1995). Requirement of MAP kinase for differentiation of fibroblasts to adipocytes, for insulin activation of p90 S6 kinase and for insulin or serum stimulation of DNA synthesis. EMBO J *14*, 674-684. 10.1002/j.1460-2075.1995.tb07046.x.

341. Hu, E., Kim, J.B., Sarraf, P., and Spiegelman, B.M. (1996). Inhibition of adipogenesis through MAP kinase-mediated phosphorylation of PPARgamma. Science *274*, 2100-2103. 10.1126/science.274.5295.2100.

342. Bost, F., Aouadi, M., Caron, L., and Binetruy, B. (2005). The role of MAPKs in adipocyte differentiation and obesity. Biochimie *87*, 51-56. 10.1016/j.biochi.2004.10.018.

343. Bost, F., Caron, L., Marchetti, I., Dani, C., Le Marchand-Brustel, Y., and Binetruy, B. (2002). Retinoic acid activation of the ERK pathway is required for embryonic stem cell commitment into the adipocyte lineage. Biochem J *361*, 621-627. 10.1042/0264-6021:3610621.

344. Bost, F., Aouadi, M., Caron, L., Even, P., Belmonte, N., Prot, M., Dani, C., Hofman, P., Pages, G., Pouyssegur, J., et al. (2005). The extracellular signal-regulated kinase isoform ERK1 is specifically required for in vitro and in vivo adipogenesis. Diabetes *54*, 402-411. 10.2337/diabetes.54.2.402.

345. Carlson, C.J., Koterski, S., Sciotti, R.J., Poccard, G.B., and Rondinone, C.M. (2003). Enhanced basal activation of mitogen-activated protein kinases in adipocytes from type 2 diabetes: potential role of p38 in the downregulation of GLUT4 expression. Diabetes *52*, 634-641. 10.2337/diabetes.52.3.634.

346. Hirosumi, J., Tuncman, G., Chang, L., Gorgun, C.Z., Uysal, K.T., Maeda, K., Karin, M., and Hotamisligil, G.S. (2002). A central role for JNK in obesity and insulin resistance. Nature *420*, 333-336. 10.1038/nature01137.

347. Boden, G., Duan, X., Homko, C., Molina, E.J., Song, W., Perez, O., Cheung, P., and Merali, S. (2008). Increase in endoplasmic reticulum stress-related proteins and genes in adipose tissue of obese, insulin-resistant individuals. Diabetes *57*, 2438-2444. 10.2337/db08-0604.

348. Basu, R., Poglitsch, M., Yogasundaram, H., Thomas, J., Rowe, B.H., and Oudit, G.Y. (2017). Roles of Angiotensin Peptides and Recombinant Human ACE2 in Heart Failure. J Am Coll Cardiol *69*, 805-819. 10.1016/j.jacc.2016.11.064.

349. Oudit, G.Y., Wang, K., Viveiros, A., Kellner, M.J., and Penninger, J.M. (2023). Angiotensin-converting enzyme 2-at the heart of the COVID-19 pandemic. Cell *186*, 906-922. 10.1016/j.cell.2023.01.039.

350. Satoh, M., Nakamura, M., Saitoh, H., Satoh, H., Maesawa, C., Segawa, I., Tashiro, A., and Hiramori, K. (1999). Tumor necrosis factor-alpha-converting enzyme and tumor necrosis factor-alpha in human dilated cardiomyopathy. Circulation *99*, 3260-3265. 10.1161/01.cir.99.25.3260.

351. Satoh, M., Nakamura, M., Satoh, H., Saitoh, H., Segawa, I., and Hiramori, K. (2000). Expression of tumor necrosis factor-alpha--converting enzyme and tumor necrosis

factor-alpha in human myocarditis. J Am Coll Cardiol *36*, 1288-1294. 10.1016/s0735-1097(00)00827-5.

352. Yamaguchi, Y., Cavallero, S., Patterson, M., Shen, H., Xu, J., Kumar, S.R., and Sucov, H.M. (2015). Adipogenesis and epicardial adipose tissue: a novel fate of the epicardium induced by mesenchymal transformation and PPARgamma activation. Proc Natl Acad Sci U S A *112*, 2070-2075. 10.1073/pnas.1417232112.

353. McKenney, M.L., Schultz, K.A., Boyd, J.H., Byrd, J.P., Alloosh, M., Teague, S.D., Arce-Esquivel, A.A., Fain, J.N., Laughlin, M.H., Sacks, H.S., and Sturek, M. (2014). Epicardial adipose excision slows the progression of porcine coronary atherosclerosis. J Cardiothorac Surg *9*, 2. 10.1186/1749-8090-9-2.

354. Haschke, M., Schuster, M., Poglitsch, M., Loibner, H., Salzberg, M., Bruggisser, M., Penninger, J., and Krahenbuhl, S. (2013). Pharmacokinetics and pharmacodynamics of recombinant human angiotensin-converting enzyme 2 in healthy human subjects. Clin Pharmacokinet *52*, 783-792. 10.1007/s40262-013-0072-7.

355. Khan, A., Benthin, C., Zeno, B., Albertson, T.E., Boyd, J., Christie, J.D., Hall, R., Poirier, G., Ronco, J.J., Tidswell, M., et al. (2017). A pilot clinical trial of recombinant human angiotensin-converting enzyme 2 in acute respiratory distress syndrome. Crit Care *21*, 234. 10.1186/s13054-017-1823-x.

356. Hemnes, A.R., Rathinasabapathy, A., Austin, E.A., Brittain, E.L., Carrier, E.J., Chen, X., Fessel, J.P., Fike, C.D., Fong, P., Fortune, N., et al. (2018). A potential therapeutic role for angiotensin-converting enzyme 2 in human pulmonary arterial hypertension. Eur Respir J *51*. 10.1183/13993003.02638-2017.

357. Ward, M., Yeganegi, A., Baicu, C.F., Bradshaw, A.D., Spinale, F.G., Zile, M.R., and Richardson, W.J. (2022). Ensemble machine learning model identifies patients with HFpEF from matrix-related plasma biomarkers. Am J Physiol Heart Circ Physiol *322*, H798-H805. 10.1152/ajpheart.00497.2021.

358. Wang, K., Basu, R., Poglitsch, M., Bakal, J.A., and Oudit, G.Y. (2020). Elevated Angiotensin 1-7/Angiotensin II Ratio Predicts Favorable Outcomes in Patients With Heart Failure. Circ Heart Fail *13*, e006939. 10.1161/CIRCHEARTFAILURE.120.006939.

359. Xu, P., Liu, J., Sakaki-Yumoto, M., and Derynck, R. (2012). TACE activation by MAPK-mediated regulation of cell surface dimerization and TIMP3 association. Sci Signal *5*, ra34. 10.1126/scisignal.2002689.

360. Chemaly, M., McGilligan, V., Gibson, M., Clauss, M., Watterson, S., Alexander, H.D., Bjourson, A.J., and Peace, A. (2017). Role of tumour necrosis factor alpha converting enzyme (TACE/ADAM17) and associated proteins in coronary artery disease and cardiac events. Arch Cardiovasc Dis *110*, 700-711. 10.1016/j.acvd.2017.08.002.

361. Weber, K.T., and Villarreal, D. (1993). Aldosterone and antialdosterone therapy in congestive heart failure. Am J Cardiol *71*, 3A-11A. 10.1016/0002-9149(93)90238-8.

362. Barr, C.S., Lang, C.C., Hanson, J., Arnott, M., Kennedy, N., and Struthers, A.D. (1995). Effects of adding spironolactone to an angiotensin-converting enzyme inhibitor in chronic congestive heart failure secondary to coronary artery disease. Am J Cardiol *76*, 1259-1265. 10.1016/s0002-9149(99)80353-1.

363. Pitt, B., Zannad, F., Remme, W.J., Cody, R., Castaigne, A., Perez, A., Palensky, J., and Wittes, J. (1999). The effect of spironolactone on morbidity and mortality in patients

with severe heart failure. Randomized Aldactone Evaluation Study Investigators. N Engl J Med *341*, 709-717. 10.1056/NEJM199909023411001.

364. Zannad, F., McMurray, J.J., Krum, H., van Veldhuisen, D.J., Swedberg, K., Shi, H., Vincent, J., Pocock, S.J., Pitt, B., and Group, E.-H.S. (2011). Eplerenone in patients with systolic heart failure and mild symptoms. N Engl J Med *364*, 11-21. 10.1056/NEJMoa1009492.

365. Briones, A.M., Nguyen Dinh Cat, A., Callera, G.E., Yogi, A., Burger, D., He, Y., Correa, J.W., Gagnon, A.M., Gomez-Sanchez, C.E., Gomez-Sanchez, E.P., et al. (2012). Adipocytes produce aldosterone through calcineurin-dependent signaling pathways: implications in diabetes mellitus-associated obesity and vascular dysfunction. Hypertension *59*, 1069-1078. 10.1161/HYPERTENSIONAHA.111.190223.

366. Brown, N.J. (2013). Contribution of aldosterone to cardiovascular and renal inflammation and fibrosis. Nat Rev Nephrol *9*, 459-469. 10.1038/nrneph.2013.110.

367. Zoufaly, A., Poglitsch, M., Aberle, J.H., Hoepler, W., Seitz, T., Traugott, M., Grieb, A., Pawelka, E., Laferl, H., Wenisch, C., et al. (2020). Human recombinant soluble ACE2 in severe COVID-19. Lancet Respir Med *8*, 1154-1158. 10.1016/S2213-2600(20)30418-5.

368. Freeman, M.W., Halvorsen, Y.D., Marshall, W., Pater, M., Isaacsohn, J., Pearce, C., Murphy, B., Alp, N., Srivastava, A., Bhatt, D.L., et al. (2023). Phase 2 Trial of Baxdrostat for Treatment-Resistant Hypertension. N Engl J Med *388*, 395-405. 10.1056/NEJMoa2213169.